

DOCTORAL THESIS

Design and Development of Novel Partially Biodegradable Composite by Hybrid Manufacturing

Mayank Kumar Yadav

TALLINN UNIVERSITY OF TECHNOLOGY
DOCTORAL THESIS
34/2026

**Design and Development of Novel
Partially Biodegradable Composite
by Hybrid Manufacturing**

MAYANK KUMAR YADAV



TALLINN UNIVERSITY OF TECHNOLOGY

School of Engineering

Department of Mechanical and Industrial Engineering

This dissertation was accepted for the defence of the degree 18/05/2026

Supervisor:

Prof. Prashanth Konda Gokuldoss
Department of Mechanical and Industrial Engineering
Tallinn University of Technology
Tallinn, Estonia

Co-supervisor:

Assoc. Prof. Jayaraj Jayamani
Department of Mechanical and Materials Engineering
Karlstad University, Karlstad, Sweden.
Department of Mechanical Engineering
Dalarna University, Falun, Sweden.

Opponents:

Assoc. Prof. Dr. Ashish Ganvir
Department of Mechanical and Materials Engineering
University of Turku
Turku, Finland

Leading Researcher Dr.sc.ing. Arita Dubņika
Direction Leader "Materials in vitro"
Institute of Biomaterials and Bioengineering
Faculty of Natural Sciences and Technology
Riga Technical University
Riga, Latvia

Defence of the thesis: 18/06/2026, Tallinn

Declaration:

Hereby I declare that this doctoral thesis, my original investigation and achievement, submitted for the doctoral degree at Tallinn University of Technology has not been submitted for doctoral or equivalent academic degree.

Mayank Kumar Yadav

signature



European Union
European Regional
Development Fund



Investing
in your future

Copyright: Mayank Kumar Yadav, 2026

ISSN 2585-6898 (publication)

ISBN 978-9916-80-451-3 (publication)

ISSN 2585-6901 (PDF)

ISBN 978-9916-80-452-0 (PDF)

<https://doi.org/10.23658/taltech.34/2026>

Printed by Koopia Niini & Rauam

Yadav, M. K. (2026). *Design and development of novel partially biodegradable composite by hybrid manufacturing* [TalTech Press]. <https://doi.org/10.23658/taltech.34/2026>

TALLINNA TEHNIKAÜLIKOOL
DOKTORITÖÖ
34/2026

Uue osaliselt biolaguneva komposiidi projekteerimine ja väljatöötamine hübriidtootmise teel

MAYANK KUMAR YADAV



Dedicated to:

My beloved **“Parents”**, whose love, sacrifices, and guidance have shaped every step of my journey, and to my little niece, **“Tanishka”** the newest light of our family and a beautiful reminder of joy and new beginnings.

Contents

List of publications	9
Other publications (not included in thesis).....	10
Author's contribution to the publications	11
Introduction	12
Abbreviations	15
Terms	18
1 Literature review	20
1.1 Bone metabolism	20
1.1.1 Bone physiology.....	21
1.1.2 Types of cells in the bone	21
1.1.3 Mechanical properties of bone.....	21
1.2 Materials used for orthopedic implant applications: advantages and disadvantages	23
1.2.1 Ti and its alloys: The material of ultimate choice for implant applications	25
1.2.2 Ceramic-based biomaterials: Advantages and disadvantages	27
1.2.3 Emergence of biodegradable metals and alloys for biomedical applications.....	28
1.3 Development of porous orthopedic implants.....	29
1.3.1 Development of porous scaffolds using additive manufacturing	29
1.3.2 Development of porous scaffolds using SPS	33
1.3.3 Hybrid manufacturing of porous scaffold	36
1.4 Research gap	38
1.5 Objective of the thesis	39
2 Materials and experimental techniques	40
2.1 Raw materials.....	40
2.2 Sample fabrication method.....	41
2.2.1 SLM of Ti64.....	41
2.2.2 SPS of Ti64 and Zn	41
2.2.3 Hybrid manufacturing of composites.....	42
2.3 Characterization of composites	43
2.3.1 Phase and microstructural analysis.....	43
2.3.2 Mechanical testing	44
2.3.3 Biodegradation and electrochemical corrosion analysis	44
2.3.4 Biocompatibility assessment.....	45
3 SLM and SPS fabrication of Ti64 alloy : A comparative analysis	47
3.1 Phase analysis of Ti64 alloy	47
3.2 Microstructural analysis of Ti64 alloy	48
3.3 Mechanical behavior of Ti64 alloy	52
3.4 Fractography of fractured Ti64 samples	53
3.5 Cytocompatibility assessment of Ti64 alloy	54
3.6 Summary	56
4 Spark plasma sintering of biodegradable pure Zn	58
4.1 Densification of Zn after SPS	58
4.2 Phase analysis of Zn	59

4.3 Microstructural characterization of Zn	59
4.4 Mechanical behavior of Zn.....	61
4.5 <i>In-vitro</i> biodegradation analysis of Zn.....	62
4.6 Electrochemical corrosion analysis of Zn	63
4.7 Cytocompatibility assessment of Zn	66
4.8 Summary	69
5 Development of novel partially biodegradable Ti64-Zn MBMC by a hybrid manufacturing approach.....	70
5.1 Phase and microstructural analysis of Ti64-Zn MBMC.....	70
5.2 Mechanical behavior of Ti64-Zn MBMC.....	73
5.3 <i>In-vitro</i> biodegradation analysis of Ti64-Zn MBMC.....	75
5.4 Electrochemical corrosion behavior of Ti64-Zn MBMC	77
5.5 Cytocompatibility assessment of Ti64-Zn MBMC	79
5.6 Summary	82
6 Conclusion and outlook of the thesis.....	83
6.1 Conclusion.....	83
6.2 Outlook.....	83
References	84
Acknowledgements.....	99
Abstract.....	100
Lühikokkuvõte.....	101
Appendix	103
Curriculum vitae.....	215
Elulookirjeldus.....	216

List of publications

The list of author's publications, on the basis of which the thesis has been prepared:

- I M.K. Yadav, A. Yarlapati, Y.N. Aditya, K. Praveenkumar, V. Pandey, C.S. Perugu, A. Nain, K. Chatterjee, S. Suwas, J. Jayaraj, K.G. Prashanth, Processing and development of porous titanium for biomedical applications: a comprehensive review, *Journal of Manufacturing and Materials Processing* 9 (2025) 401. <https://doi.org/10.3390/jmmp9120401>.
- II M.K. Yadav, R.H. Shukla, K.G. Prashanth, A comprehensive review on development of waste derived hydroxyapatite (HAp) for tissue engineering application, *Materials Today: Proceedings* In press (2023). <https://doi.org/10.1016/j.matpr.2023.04.669>.
- III M.K. Yadav, R.H. Shukla, K. Praveenkumar, S. Nilawar, C.S. Perugu, P. Sellamuthu, K. Chatterjee, S. Suwas, J. Jayaraj, K.G. Prashanth, Microstructural, mechanical, corrosion, and biological behavior of spark plasma sintered commercially pure zinc for biomedical applications, *Materials Advances* 6 (2025) 3546-3560. <https://doi.org/10.1039/d5ma00092k>.
- IV M.K. Yadav, R.H. Shukla, L. Xi, Z. Wang, K.G. Prashanth, Metallic multimaterials fabricated by combining additive manufacturing and powder metallurgy, *Journal of Composites Science* 9 (2025) 80. <https://doi.org/10.3390/jcs9020080>.
- V M.K. Yadav, K. Praveenkumar, R.H. Shukla, S. Nilawar, C.S. Perugu, K. Chatterjee, S. Suwas, J. Jayaraj, K.G. Prashanth, Novel partially biodegradable Ti-6Al-4V/Zn composites fabricated through hybrid additive manufacturing and powder metallurgy, *Advanced Light Materials* 1 (2026) 1-18. <https://doi.org/10.1016/j.almate.2026.03.001>

Other publications (not included in thesis)

- VI S. Subramanian, M.K. Yadav, J. Jayaraj, F. Yangyang, L. Xi, K.G. Prashanth, Microstructural homogenization through laser remelting in an additively manufactured Ti-40Nb sample from elemental feedstock powders, *Journal of Materials Research Technology* 38 (2025) 4305-4320. <https://doi.org/10.1016/j.jmrt.2025.08.203>.
- VII S. Sahay, K. Praveenkumar, M.K. Yadav, S. Nilawar, G. Manivasagam, K. Chatterjee, High-pressure torsion affects mechanical properties, electrochemical behavior, and cellular response to a biomedical Ti-Nb-Zr-Ta alloy, *Materials Transactions* 66 (2025) 490-500. <https://doi.org/10.2320/matertrans.mt-mc2024013>.
- VIII K. Praveenkumar, J. Vishnu, S.C. Samuel, V. Gopal, M. Arivarasu, J.M. Lackner, B. Meier, D. Karthik, S. Suwas, S. Swaroop, K.G. Prashanth, M.K. Yadav, G. Manivasagam, High temperature dry sliding wear behaviour of selective laser melted Ti-6Al-4V alloy surfaces, *Journal of Materials Processing Technology* 329 (2024) 118439. <https://doi.org/10.1016/j.jmatprotec.2024.118439>.
- IX R.H. Shukla, M.K. Yadav, L.Y.C. Madruga, J. Jayaraj, K. Popat, Z. Wang, L. Xi, K.G. Prashanth, A novel Ti-eggshell-based composite fabricated by combined additive manufacturing–powder metallurgical routes as bioimplants, *Ceramics International* 51 (2025) 6281-6291. <https://doi.org/10.1016/j.ceramint.2024.12.073>.
- X A. Yarlapati, Y.N. Aditya, D. Kumar, R.J. Vikram, M.K. Yadav, K.S. Reddy, K.G. Prashanth, Recent advances in additive manufacturing of refractory high entropy alloys: A critical review, *Journal of Alloys and Metallurgical Systems* 8 (2024) 100120. <https://doi.org/10.1016/j.jalmes.2024.100120>.

Author's contribution to the publications

Contribution to the papers in this thesis are:

- I First Author: Conceptualization, methodology, literature review and analysis, writing—original draft preparation, and coordination of manuscript preparation.
- II First Author: Conceptualization, methodology, literature review and analysis, writing—original draft preparation, and coordination of manuscript preparation.
- III First Author: Conceptualization, formal analysis, methodology, Writing—original draft preparation.
- IV First Author: Methodology, formal analysis, investigation, data curation, writing—original draft preparation.
- V First Author: Methodology, formal analysis, investigation, data curation, writing—original draft preparation.

Introduction

The demand for orthopedic implants continues to increase due to population aging, trauma, and degenerative bone disorders. Load-bearing implants must provide sufficient mechanical strength, long-term stability, and biological compatibility to restore physiological function. Metallic biomaterials remain the primary choice because of their superior mechanical reliability and fracture resistance. Among them, Ti-6Al-4V (Ti64) is extensively used owing to its high strength, corrosion resistance, fatigue performance, and clinical reliability [1].

Despite these advantages, dense Ti64 implants exhibit limitations that affect long-term clinical performance. The elastic modulus of Ti64 (~110 GPa) is significantly higher than that of cortical bone (10-30 GPa). This mismatch alters physiological load transfer and results in stress shielding, where the implant carries a greater proportion of the applied load. Reduced mechanical stimulus at the bone-implant interface suppresses bone remodeling and initiates bone resorption, which may ultimately lead to implant loosening and failure [1,2]. In addition, Ti64 is biologically inert and nondegradable, and its permanent presence may lead to long-term complications or revision surgeries, increasing patient risk and healthcare costs.

To improve mechanical compatibility, porous titanium (Ti) structures have been developed to reduce effective stiffness and promote osseointegration. Additive manufacturing (AM), particularly selective laser melting (SLM), enables the fabrication of controlled lattice architectures with tailored mechanical properties and interconnected porosity [3]. However, increasing porosity reduces the load-bearing cross-section and may compromise strength and fatigue resistance under physiological loading. Furthermore, porous Ti structures remain permanent and do not provide functional adaptability during the healing process.

Biodegradable metals have been investigated as an alternative strategy to eliminate long-term material retention. Magnesium (Mg), iron (Fe), and zinc (Zn) are the principal biodegradable metallic systems studied for biomedical applications. Mg exhibits rapid corrosion and hydrogen evolution, which can cause premature mechanical failure [4]. Fe degrades very slowly and may remain in the body for extended periods. Zn has attracted significant attention due to its moderate degradation rate and essential physiological role in bone metabolism, but its relatively low mechanical strength limits its use in load-bearing applications [5].

These limitations indicate that neither permanent Ti implants nor fully biodegradable metals alone can simultaneously provide long-term structural integrity and controlled biological adaptation. This challenge has led to growing interest in hybrid systems that integrate a stable load-bearing phase with a degradable phase. Interpenetrating phase composites (IPCs) and metallic multimaterials (MMMs) represent such an approach, where at least one phase remains topologically continuous to maintain structural stability while the secondary phase provides functional degradation [6,7]. Bioinspired natural materials such as bone and nacre demonstrate how multi-phase architectures achieve optimized stiffness, toughness, and functional adaptability [8].

Several studies have explored metal-metal IPCs for biomedical applications, including Mg-Ti and Zn-Ti systems produced through infiltration or hybrid processing routes [8]. These studies demonstrate the potential of combining a permanent scaffold with a degradable phase to achieve progressive porosity and enhanced bone integration. However, significant challenges remain. Differences in melting temperature, thermal

expansion, and chemical reactivity between dissimilar metals often result in poor interfacial bonding, residual stresses, or the formation of brittle intermetallic phases. In addition, systematic studies linking processing routes with microstructure, mechanical performance, and degradation behavior in load-bearing Ti-based composite systems remain limited.

Hybrid manufacturing approaches that combine AM with powder metallurgy (PM) can provide a promising solution to these challenges. SLM enables the fabrication of complex Ti scaffolds with precise control over geometry and porosity, while powder consolidation techniques such as spark plasma sintering (SPS) allow rapid densification of secondary metallic phases with minimal thermal exposure and reduced interfacial reactions [9]. This integrated AM-PM route enables the fabrication of IPC-like architectures that cannot be achieved through conventional casting or single-process AM.

Based on the current state of research, a critical gap exists in the development of bioinspired, load-bearing, partially biodegradable Ti-based multimaterial systems fabricated through hybrid AM-PM processing. In particular, the feasibility of combining an SLM-fabricated Ti64 scaffold with a Zn phase to achieve desired mechanical performance and controlled degradation behavior has not been systematically established. Moreover, baseline studies on individual constituent materials processed by SLM and SPS are necessary to understand their processing-structure-property relationships before developing a hybrid system.

The goal of this thesis is to develop a bioinspired, partially biodegradable Ti64-Zn metallic bi-metal composite (MBMC) that provides long-term mechanical stability while enabling controlled degradation to support bone regeneration. It is hypothesized that a porous Ti64 architecture fabricated by SLM will act as a continuous load-bearing framework with reduced effective stiffness, thereby minimizing stress shielding. The incorporation of Zn using SPS is expected to introduce a degradable phase that gradually resorbs, creating additional space for bone ingrowth without compromising the structural integrity of the Ti64 scaffold.

To achieve this goal, the thesis is structured around a systematic workflow. First, bone physiology, implant functional requirements and their different possible manufacturing routes are reviewed. Second, Ti64 fabricated by SLM and SPS is comparatively evaluated to establish processing-structure-property relationships relevant to implant frameworks and to understand its high-temperature behavior during consolidation. Third, commercially pure Zn processed by SPS is compared with as-cast Zn to establish its microstructural characteristics, mechanical response, and degradation behavior under physiological conditions. Fourth, the feasibility of metallic multimaterials is investigated using SLM-fabricated lattices filled with secondary metal powders and consolidated by SPS, establishing a general hybrid manufacturing platform. Finally, these insights are integrated to develop the central system of the thesis, namely a Ti64-Zn MBMC.

The methodology combines hybrid manufacturing with multiscale characterization. SLM is used to fabricate architected Ti64 scaffolds, followed by SPS consolidation of Zn within the structure. The developed systems are evaluated through phase analysis, microstructural characterization, three-dimensional imaging, mechanical testing, electrochemical and immersion-based degradation studies, and biological assessment. This integrated approach enables the establishment of processing-structure-property-function relationships for bioinspired multimaterial systems.

The novelty of this thesis lies in the development of a bioinspired Ti64-Zn MBMC using a hybrid SLM-SPS route to achieve partial biodegradability in a load-bearing implant

system. The study demonstrates a design strategy that bridges the gap between permanent Ti implants and fully biodegradable metals by combining a bio-inspired Ti64 framework with a controlled degradable Zn phase. This approach enables independent control of architecture, mechanical compatibility, and degradation behavior within a single implant system and provides a new pathway for the design of next-generation multifunctional orthopedic implants.

The chapters of this thesis are arranged as follows: Chapter 1 presents a comprehensive literature review on bone physiology, implant requirements, biodegradable metals, and advanced manufacturing techniques for the development of reliable implants. Chapter 2 describes the materials selection, hybrid manufacturing routes (SLM and SPS), and experimental methodologies employed for structural, mechanical, corrosion, and biological evaluations. Chapter 3 comparatively investigates Ti64 fabricated via SLM and SPS processes. It highlights the influence of processing routes on the microstructure, mechanical, and in-vitro biological properties. Chapter 4 evaluates SPS-fabricated Zn against conventionally as-cast Zn. Material properties like microstructural, mechanical and degradation behaviour and biocompatibility were analyzed. Chapter 5 presents the development of a novel Ti64-Zn MBMC. The mechanical integrity, corrosion and biodegradation behavior under physiological conditions, and cytocompatibility are assessed for implant applications. Finally, Chapter 6 presents the conclusions and possible future work of this research.

Abbreviations

AM	Additive manufacturing
AZ31	Magnesium alloy containing approximately 3 wt.% aluminum and 1 wt.% Zinc
AZ91	Magnesium alloy containing approximately 9 wt.% aluminum and 1 wt.% Zinc
ASTM	American society for testing and materials
BCC	Body centered cubic
BJT	Binder jetting
BOR	Burger's orientation relationship
BSE	Back-scattered electron
CAD	Computer-aided design
CAM	Computer-aided manufacturing
CE	Conformité Européenne
CoF	Coefficient of friction
CoCrMo	Cobalt chromium molybdenum alloy
CoCr20Ni15Mo7	Cobalt-based alloy containing approximately 20 wt.% Cr, 15 wt.% Ni, and 7 wt.% Mo
Cp-Ti	Commercial pure titanium
CR	Corrosion rate
CYS	Compressive yield strength
DAPI	4',6-diamidino-2-phenylindole
DED	Direct energy deposition
E_{corr}	Corrosion potential
E_{bp}	Breakdown potential
E_{pp}	Passivation potential
EBM	Electron beam melting
EBSD	Electron backscatter diffraction
EDS	Energy dispersive spectroscopy
EIS	Electrochemical impedance spectroscopy
FBS	Fetal bovine serum
FCC	Face centered cubic
Fe20Mn	Iron-based alloy containing approximately 20 wt.% manganese
GNDs	Geometrically necessary dislocations
HAp	Hydroxyapatite
HCP	Hexagonal closed packing
HAGBs	High-angle grain boundaries
I_{corr}	Corrosion current density
I_p	Passivation current density
IPC	Interpenetrating phase composites

IPF	Inverse pole figure
IQ	Image quality
KAM	Kernel average misorientation
LAGBs	Low-angle grain boundaries
LDED	Laser-directed energy deposition
LENS	Laser-engineered net shaping
LPBF	Laser powder bed fusion
MEM	Minimum essential medium
MBMC	Metallic bimetal composite
MMMs	Metallic multimaterials
NS	Non-significant
OCP	Open circuit potential
OD	Optical density
OM	Optical microscopy
PBS	Phosphate buffered saline
PCL	Poly(ϵ -caprolactone), biodegradable polymer
PDP	Potentiodynamic polarization
PEEK	Polyetheretherketone
PL-SPS	Pressure less spark plasma sintering
PLA	Polylactic acid, biodegradable polymer
PLGA	Poly(lactic-co-glycolic acid), biodegradable polymer
PM	Powder metallurgy
RGR	Relative growth rate
RP	Rapid prototyping
SADP	Selected area diffraction pattern
SBF	Simulated body fluid
SCE	Standard calomel electrode
SE	Secondary electron
SEM	Scanning electron microscopy
SLM	Selective laser melting
SMAT	Surface mechanical attrition treatment
SPS	Spark plasma sintering
SS	Stainless steel
316L SS	Austenitic stainless steel 316L (low carbon)
TPMS	Triply periodic minimal surfaces
TEM	Transmission electron microscopy
Ti6Al4V	Titanium alloy containing 6 wt.% aluminum and 4 wt.% vanadium
Ti6Al4V ELI	Extra-Low Interstitial grade of Ti6Al4V alloy
Ti6Al7Nb	Titanium alloy containing 6 wt.% aluminum and 7 wt.% niobium

Ti5Al2.5Fe	Titanium alloy containing 5 wt.% aluminum and 2.5 wt.% iron
Ti13Nb13Zr	Titanium alloy containing 13 wt.% niobium and 13 wt.% zirconium
Ti12Mo6Zr2Fe	Titanium alloy containing 12 wt.% molybdenum, 6 wt.% zirconium, and 2 wt.% iron
Ti35Nb7Zr5Ta	Titanium alloy containing 35 wt.% niobium, 7 wt.% zirconium, and 5 wt.% tantalum
Ti29Nb13Ta4.6Zr	Titanium alloy containing 29 wt.% niobium, 13 wt.% tantalum, and 4.6 wt.% zirconium
Ti35Nb5Ta7Zr	Titanium alloy containing 35 wt.% niobium, 5 wt.% tantalum, 7 wt.%
Ti15Mo5Zr3Al	Titanium alloy containing 15 wt.% molybdenum, 5 wt.% zirconium, and 3 wt.% aluminum
TiMo	Titanium molybdenum alloy system (β -type titanium alloy depending on Mo content)
TYS	Tensile yield strength
UCS	Ultimate compressive strength
UHMWPE	Ultra-high molecular weight polyethylene
UTS	Ultimate tensile strength
WST	Water soluble tetrazolium
XRD	X-ray diffraction
YS	Yield strength
μ -CT/CT	Micro computed tomography/ computed tomography
σ_y	Yield strength of the materials.
ZnAlCu	Zinc, aluminum, copper alloy

Terms

Bio-implant	A bio-implant is a biocompatible material designed to replace, support, or restore the function of damaged biological tissues or organs within the body.
Biomaterials	Materials used for bio-implant applications
Bioactivity	The ability of a material to interact with biological tissues, often promoting healing or tissue regeneration.
Biodegradation	The natural breakdown of materials by biological agents, enabling safe absorption or removal from the body.
Bioinert	Materials that remain stable and non-reactive in the body, avoiding any interaction with surrounding tissues.
Bioresorbable	Materials that dissolve in a controlled manner, providing the therapeutic agent (e.g., Ca^{+2} , PO_4^{-3}) during degradation.
Dislocation	A linear crystalline defect around which there is atomic misalignment.
Ca/P	It refers to the calcium-to-phosphorus atomic ratio, commonly used to evaluate the composition and quality of calcium phosphate or hydroxyapatite layers in biomaterials.
CE approval	CE approval indicates that a product meets the European Union's safety, health, and environmental protection standards.
Elastic modulus	It is a measure of a material's stiffness, defined as the ratio of stress to strain within the elastic (reversible deformation) region of the stress-strain curve.
Gyroid	It is a triply periodic minimal surface with a complex, continuous 3D structure that provides a high strength-to-weight ratio and interconnected porosity.
<i>In-vitro</i>	It refers to experiments conducted outside a living organism, typically in controlled environments such as test tubes, petri dishes, or culture media.
<i>In-vivo</i>	It refers to experiments performed within a living organism, such as animal models or human subjects, to study biological responses in real physiological conditions.
MC3T3-E1 pre-osteoblast cells	These are mouse-derived cell lines commonly used in bone biology research, which can proliferate and differentiate into osteoblasts under appropriate conditions.
Osseointegration	The direct bonding between living bone and an implant, creating a stable and lasting connection.
Patient-specific implant	These are medical implants custom-designed and manufactured to match the unique anatomy of an individual patient.
Stiffness	Stiffness is the resistance of a material or structure to deformation when a force is applied.
Torsional loading	It is a type of mechanical load in which a twisting force (torque) is applied to an object around its longitudinal axis, causing it to rotate or twist.
Triply periodic minimal surface	It is a mathematically defined 3D surface that repeats periodically along three axes and has zero mean curvature,

	creating smooth, continuous, and porous structures ideal for lightweight and biomimetic designs.
Widmanstätten structure	It is a distinctive interlocking microstructural pattern found in titanium.
0.7 T _m	It refers to 0.7 times the melting temperature of a metal.

1 Literature review

The literature review forms a critical foundation of this thesis by synthesizing existing knowledge and positioning the present work within the broader scientific context. It encompasses a comprehensive overview of prior studies on Ti and its alloys, advanced manufacturing techniques such as SLM and SPS, the development of biodegradable systems, and emerging concepts of metallic multimaterials. In addition, special emphasis is placed on bone metabolism and its interaction with implant materials, as this understanding is essential for evaluating the biological relevance of the developed systems. By analyzing these contributions, the review not only highlights the progress made in the field but also justifies the necessity and novelty of the current investigation.

1.1 Bone metabolism

Understanding bone metabolism is crucial for designing implants because it governs how bone tissue grows, remodels, and responds to foreign materials. Bone is a dynamic tissue that continuously undergoes formation and resorption, and any imbalance in this cycle can lead to implant failure. An implant material must not only provide mechanical support but also interact favorably with the surrounding bone environment to promote osseointegration, minimize adverse immune responses, and, in the case of biodegradable systems, degrade in accordance with new bone formation. Without considering bone metabolism, implants risk causing poor integration, excessive bone loss, or a mismatch between degradation rate and tissue regeneration. Bone is a hard, living tissue that supports the body under mechanical loads and protects the vital organs within the human body [10,11]. To understand bone metabolism, it is necessary to grasp bone physiology and its mechanical properties. The different structural levels of bone are shown in Figure 1.1, illustrating that the bone tissue comprises collagen fibers at the nanoscale.

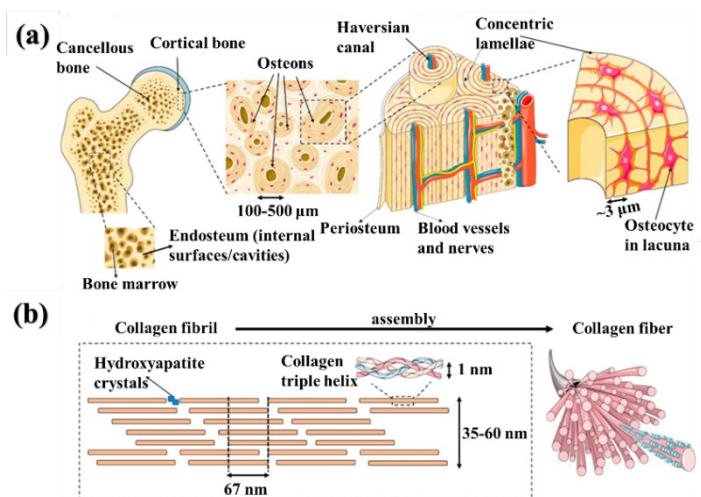


Figure 1.1. Bone showing a hierarchical structure spanning multiple length scales (a) a macro-to-microscopic view of cancellous and cortical bones, (b) a nanoscale view of bone tissue comprising collagen fibers with mineral components. Reproduced with permission from [13].

1.1.1 Bone physiology

At the microscopic scale, bone can be categorized into two types according to the organization of its fibers: woven bone and lamellar bone [11]. Woven bones are regarded as an immature form of bone tissue and generally exhibit a mineral grain size in the range of 10-15 nm. This type of bone is characterized by coarse collagen fibers that are randomly distributed throughout the structure. Consequently, the nonuniform orientation of collagen fibers gives rise to the direction-independent mechanical behavior observed in woven bone [11]. Similarly, lamellar bone represents another form of bone structure that can be identified at the microscopic scale. In contrast to woven bone, it is composed of a mineralized matrix primarily consisting of hydroxyapatite (HAp) with the chemical formula $\text{Ca}_{10}(\text{PO}_4)_6(\text{OH})_2$. In the human femur, HAp crystals are typically observed to be approximately 20-80 nm in length and 2-5 nm in thickness. As the name suggests, lamellar bone is arranged in well-defined layers, with collagen fibers oriented along the principal stress directions, which gives rise to anisotropic mechanical behavior. Furthermore, based on their structural organization, both woven and lamellar bones are classified into trabecular and cortical bone types [11].

Trabecular bones are highly porous, having 50-90% porosity and large pores up to several millimeters in diameter. Therefore, these bones are also known as spongy bones or cancellous bones. The trabecular bone bears compressive forces under physiological loading conditions [11]. The distal end radius is an example of a trabecular bone. Similarly, cortical bones are less porous and possess small pores of up to 1 mm in diameter. Therefore, it is also known as compact bone, contributing to 80% of the weight of the human skeleton. It is harder, stronger, and stiffer than trabecular bone due to less porosity. The humerus and femur are examples of cortical bone [11,12].

Bone is mainly composed of approximately 70% inorganic constituents, 20% organic matter, and 10% water. The inorganic phase is mainly crystalline HAp, while approximately 90% of the organic fraction consists of Type I collagen, with the remaining 10% comprising non-collagenous proteins, lipids, and other macromolecules [11].

1.1.2 Types of cells in the bone

Bones comprise four types of cells: osteoblasts, osteoclasts, osteocytes, and osteogenic cells. Figure 1.2 provides a schematic diagram of these cell types. Osteoblast cells are also known as bone-forming cells because they synthesize new bone. Osteocytes are fully differentiated bone cells derived from osteoblasts. Osteoclasts are bone-resorbing cells responsible for bone remodeling and calcium regulation. Osteoprogenitor cells, also known as osteogenic cells, are stem cells found in bone tissue that play a vital role in bone formation and regeneration. Located within the bone marrow, they serve as precursors to more specialized bone cells, including osteoblasts and osteocytes [11,14].

1.1.3 Mechanical properties of bone

The primary function of bone is to provide structural support under mechanical loading and to protect vital organs. Wolff's law of bone remodeling (1892) states that mechanical load can affect bone architecture [15–17] and hence promote bone remodeling and fracture healing [18]. In cases of trauma or diseased biological structures, implants often replace the affected organ. Thus, essential properties including Young's modulus, fracture toughness, hardness, yield strength, ultimate tensile strength, stiffness, ductility, time-dependent deformation, and creep should be considered while designing implants. Table 1.1 lists the mechanical properties of human bone and common materials used for orthopedic implant applications.

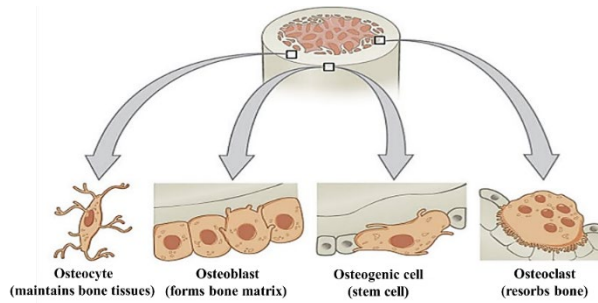


Figure 1.2. Schematic representation of the classification of the four types of bone cells. Reproduced with permission from [14].

Table 1.1. Physical and mechanical properties of metallic, ceramic, and polymeric biomaterials, where ρ -Density in g/cm^3 , E -Young's modulus in GPa, YS -Yield strength in MPa, UTS -Ultimate tensile strength in MPa, UCS -Ultimate compressive strength in MPa, and FS -Fatigue strength in MPa, 107 cycles.

Materials	ρ	E	YS	UTS	UCS	FS	Ref.
Natural bone							
Cortical bone	1.8-2.0	7-30	-	164-240	100-230	27-35	[19]
Cancellous bone	1.0-1.4	0.01-3.0	-	-	2-12	-	
Metals and alloys							
Ti6Al4V (cast)	4.43	114	760-880	895-930	-	600-700	[19]
Ti6Al4V (wrought)	4.43	114	827-1103	860-965	896-1172	500-800	
Ti6Al7Nb	4.52	105	880	900	-	-	[1]
316L SS	8.0	193	170-310	540-1000	480-620	240-480	[19]
Fe20Mn	7.73	207	420	700	-	-	[20]
ZnAlCu	5.79	90	171	210	-	-	[19]
CoCrMo	8.3	240	500-1500	900-1540	-	500-900	
CoCr20Ni15Mo7	7.8	195-230	240-450	450-960	-	-	
Pure Mg (cast)	1.74	41	21	87	40	-	
Pure Mg (wrought)	1.74	41	100	180	100-140	-	
AZ31 (Mg-based alloy)	1.78	45	185	263	-	-	
AZ91 (Mg-based alloy)	1.81	45	160	150	-	-	

1.2 Materials used for orthopedic implant applications: advantages and disadvantages

Metals, polymers, and ceramics are commonly used for implants; therefore, this section includes a brief discussion of these materials. The selection of suitable material depends on the application. Table 1.2 summarizes the advantages, disadvantages, and applications of different materials used as implants.

Ceramics are inorganic oxides of non-metals known for their excellent corrosion resistance, biocompatibility, and in some cases bioactivity. They are composed primarily of ionic bonds with some covalent character, making them brittle with low fracture toughness and a high elastic modulus. There are two main types of bio-ceramics: bioinert ceramics, such as zirconia, possess excellent chemical inertness, enabling their application in biomedical fields [21]. Bioresorbable ceramics, like HAp and β -tricalcium phosphate, are designed to gradually dissolve and be replaced by natural bone [22–24]. However, owing to their inferior mechanical strength, monolithic ceramics are not suitable for load-bearing applications in long bones, as they are prone to failure under mechanical loading. Nevertheless, ceramics are effectively utilized in bone filler applications and in the field of dentistry [25,26].

Polymers are organic oxides of non-metals; they can be used as an implant material in low-load-bearing fracture sites. Polymers have emerged as promising materials for orthopedic use due to their mechanical properties, which are comparable to those of trabecular bone, and their biodegradability has further heightened interest in their application [27]. Polymer like ultra-high molecular weight polyethylene (UHMWPE) owns properties like high impact strength, low friction coefficient, and low density. However, the application of UHMWPE is limited due to long-term radicals in the bulk resulting from the ionizing radiation employed in the sterilization process. Natural polysaccharide polymers like starch, cellulose, and alginate are also used in biomedical applications [25,27]. The main problem associated with the use of polymers in orthopedic applications is the overproduction of wear debris, which leads to inflammatory reactions between adjacent tissue and implant. This adverse tissue reaction causes osteolysis, bone resorption, and implant failure [28].

Metals and their alloys are preferred over ceramics and polymers for implant applications due to their excellent mechanical properties and biocompatibility [29]. Commonly used metals include Ti and its alloys, medical-grade SS, Co-Cr, and Mg alloys. However, these metals may contain elements such as Co, Cr, Al, Cu, V, and Ni, classified as allergenic. Elements like Ni, Co, and Cr are released from 316L SS and Co-Cr alloy due to corrosion in the physiological environment [30–33]. The toxicity of Ni causes skin-related diseases like dermatitis, and the release of Co causes carcinogenicity [1,32,33]. Young's modulus of 316L SS and Co-Cr alloy is much higher than that of natural bone, causing nonuniform load transfer between bone and implant, leading to bone resorption and implant loosening.

However, due to the low cost of 316L SS compared to all other metallic alloys, 316L SS has maintained its demand in fixation devices like bone plates, bone screws, etc. Mg and its alloys, due to their biodegradability and potential for avoiding revision surgery, have increased the attention of the general orthopedic community for surgical fixation of injured musculoskeletal tissue [34–36]. It is believed that when Mg-based alloys are introduced in a biological environment, it degrades to Mg chloride, oxide, sulfate, or phosphate, and these ions do not cause any adverse effect on local tissues [37,38].

Despite many advantages, there are certain limitations to using Mg-based alloys. The high corrosion rate of Mg-based alloys is one of the major problems [39]. Corrosion causes the evolution of hydrogen gas, which creates the balloon effect *in-vivo* [40]. Due to the high corrosion rate, the pH value of the surrounding surface also increases [41].

Table 1.2. Table furnishing a comprehensive list of biomaterials along with their advantages, disadvantages, and applications [42].

Materials	Advantages	Disadvantages	Applications
316L SS	Widely available and cost-effective, with excellent mechanical properties, and biocompatible	High elastic modulus, inadequate resistance to corrosion, low wear resistance, potential to trigger allergic reactions with surrounding tissues, stress shielding, which can lead to bone resorption	Bone plates, bone screws, pins, wires, etc.
Co-Cr alloy	Excellent resistance to corrosion, fatigue, and wear, high mechanical strength, and sustained biocompatibility over the long term	High cost, limited machinability, induction of stress shielding, and potential biological toxicity from the release of Co, Cr, and Ni ions	Shorter-term implants, bone plates and wires, total hip replacements, stem or hard-on-hard bearing system
Mg alloy	Biocompatible, biodegradable, bioresorbable, similar density and Young's modulus to that of natural bone, lightweight	Hydrogen evolution, during degradation, less corrosion resistance	Bone screws, bone plates, bone pins, etc.
Ti alloy	Excellent resistance to corrosion, lower modulus, stronger than SS, lightweight, and biocompatible	Poor wear resistance, poor bending ductility, and expensive	Fracture fixation devices such as plates, nails, rods, screws, fasteners, and wires, femoral hip stems, total Joint replacement (TJR) systems, arthroplasty procedures, particularly for hip and knee joints

Alumina (Al ₂ O ₃)	Biocompatibility and bioinert behavior elevated hardness, strength, and resistance to abrasion, minimal formation of fibrous tissue at the implant tissue interface	Low fracture toughness, brittle, limited ductility, radiopacity	Porous coatings for femoral stems, femoral head, bone screws and plates, and knee prosthesis
Zirconia (ZrO ₂)	Excellent fracture toughness, high flexural strength, low Young's modulus, closely matching bone, bioinert nature, good biocompatibility, non-toxic behavior within the biological environment	Phase transformation, Brittle, low toughness	Femoral head, artificial knee, bone screws, plates
Bio-glass	Biocompatibility, bioactivity, promoting integration with surrounding tissue, and non-toxicity	Brittleness may limit load-bearing applications, low tensile strength, and poor fatigue resistance	Artificial bone, dental implants
Hydroxyapatite (HAp)	Bioresorbable, Bioactive, Biocompatible, similar composition to bone, good osteoconductive properties	Brittleness may limit load-bearing applications, low tensile strength, and poor fatigue resistance	Femoral knee, femoral hips, tibial components, acetabular cup

1.2.1 Ti and its alloys: The material of ultimate choice for implant applications

Ti is a transition metal with atomic number 22 with an incomplete valence shell. It can form a substitutional solid solution with an element having a size factor of $\pm 20\%$. The melting point of Ti is 1678 °C, and the crystal structure of Ti is hexagonally closed-packed (hcp), α -Ti up to the beta transus temperature (882.5 °C), transforming to a body-centered cubic structure (bcc) β -Ti above this temperature, as shown in Figure 1.3 [43,44].

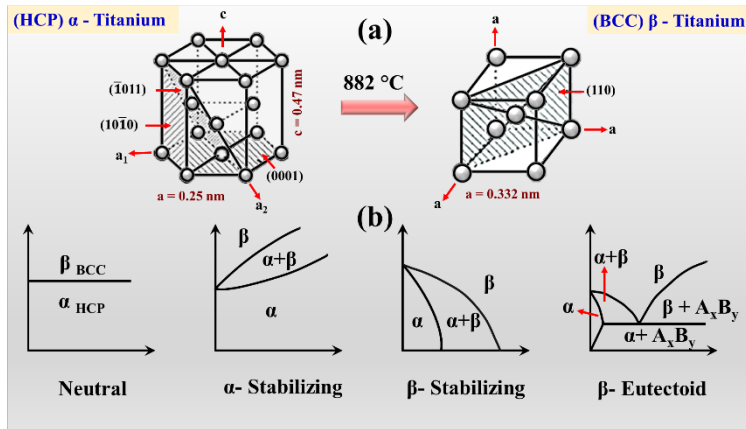


Figure 1.3. Schematic representations illustrating (a) the allotropic forms of titanium (Ti), hexagonal close-packed α -Ti, stable up to 882 °C, and body-centered cubic β -Ti, stable at temperatures above this transition, and (b) classification of Ti phase diagrams based on different alloying additions. Reproduced with permission from [44].

The nature of the alloying element decides the microstructure (α to β transformation temperature) of Ti-based alloy. Elements like Al, O, N, etc., are commonly known as α stabilizers because they stabilize the α phase by increasing the β transus temperature. Similarly, elements like V, Mo, Nb, Fe, Cr, etc., stabilize β transus temperature and are known as β stabilizers. The addition of these elements depresses the β transus temperature. Figure 1.4 highlights the various biomedical applications of Ti and its alloys.

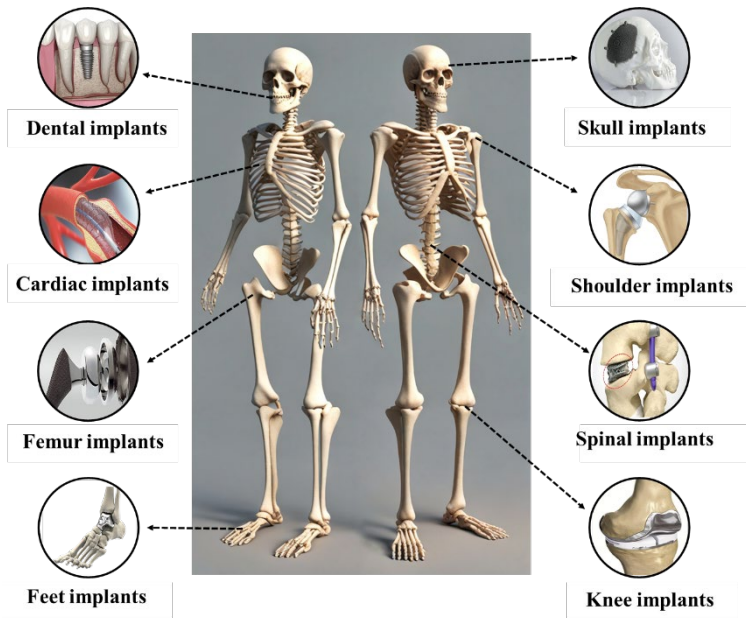


Figure 1.4. Graphical representation illustrating the different titanium-based implants used in biomedical applications. Reproduced with permission from [42].

Ti alloys are generally classified based on the α and β phases. They are classified as α , near- α , ($\alpha+\beta$), and metastable β alloys. The α alloy consists of only the α phase. Near α alloys are a special class of α alloys comprising 1-2% β stabilizers and about 5-10% β phase. Similarly, $\alpha+\beta$ alloys contain 10-30% of the β phase, and alloys with higher β -stabilizers where the β phase is formed by fast cooling are known as metastable β alloys. Generally, $\alpha+\beta$ and metastable β alloys are employed in biomedical applications. Among all these alloys, α and ($\alpha+\beta$) alloys are considered first-generation Ti alloys and possess a high Young's modulus (110 GPa). The development of a second-generation Ti-based alloy (β alloys) was established in 1990 [45]. Due to their lower Young's modulus (55-90 GPa), β alloys are the material of choice for orthopedic applications. Different Ti alloys and their mechanical properties used for biomedical applications are listed in Table 1.3.

Table 1.3. List furnishing the mechanical properties of titanium and its alloys (where E-Modulus in GPa and UTS-Ultimate tensile strength in MPa) [1].

Material	Standard*	E	UTS	Alloy composition
First-generation biomaterials (1950-1990)				
Commercially pure Ti (CP grade 1-4)	ASTM 1341	100	240-550	α
Ti6Al4V ELI wrought	ASTM F136	110	860-965	$\alpha+\beta$
Ti6Al4V ELI standard grade	ASTM F1472	112	895-930	$\alpha+\beta$
Ti6Al7Nb wrought	ASTM 1295	110	900-1050	$\alpha+\beta$
Ti5Al2.5Fe	-	110	1020	$\alpha+\beta$
Second-generation biomaterials (1990 to present)				
Ti13Nb13Zr wrought	ASTM F1713	79-84	973-1037	Metastable β
Ti12Mo6Zr2Fe (TMZF)	ASTM F1813	74-85	1060-1100	β
Ti35Nb7Zr5Ta (TNZT)	-	55	596	β
Ti29Nb13Ta4.6Zr	-	65	911	β
Ti35Nb5Ta7Zr0.40 (TNZTO)	-	66	1010	β
Ti15Mo5Zr3Al	-	22	-	β
*The listed ASTM standards are technically equivalent or harmonized with their corresponding EN/ISO standards, ensuring consistency in testing methodology, acceptance criteria, and data interpretation.				

1.2.2 Ceramic-based biomaterials: Advantages and disadvantages

As discussed in Section 1.2, ceramics are widely explored for biomedical applications due to their excellent corrosion resistance, superior biocompatibility, and inherent bioactivity. For effective bone regeneration, ceramic-based scaffolds must possess an interconnected microporous network, an appropriate surface texture to enhance cell adhesion, and adequate mechanical strength to provide structural support. Among various ceramic biomaterials, HAp with the chemical formula $\text{Ca}_{10}((\text{PO})_4)_6(\text{OH})_2$ stands out as one of the most promising candidates because of its bioactivity, biocompatibility, osseointegration, osteoconduction, and non-toxicity [46,47]. Figure 1.5 shows the growth of the apatite layer on the surface of the HAp-based porous scaffold. HAp is a

bioactive calcium phosphate ceramic that closely mimics the mineral composition of natural bone, facilitating direct bonding with host tissue. Synthetic HAp, produced via methods such as mechanochemical reactions, wet chemical precipitation, hydrothermal conversion, emulsion, and sol-gel techniques, is often considered superior to natural HAp in terms of purity and tunable properties. A review article [24] provides the different methods of producing HAp using waste animal bones.

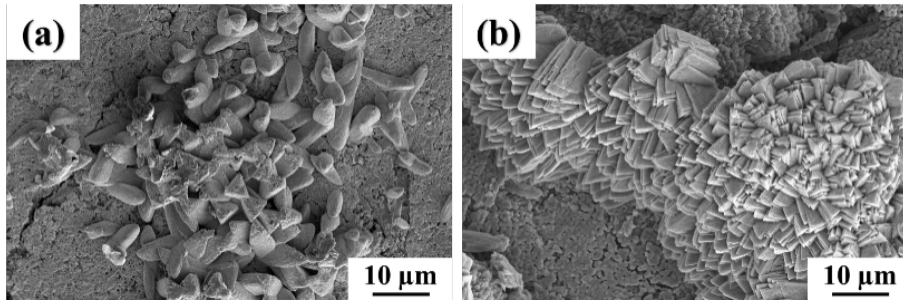


Figure 1.5. Scanning electron microscopy images of the hydroxyapatite-based scaffold showing the formation and progressive growth of an apatite layer on the scaffold surface after incubation in simulated body fluid for (a) 7 and (b) 14 days. Reproduced with permission from [24]

Despite its remarkable bioactivity, HAp exhibits certain drawbacks that limit its standalone application in load-bearing implants. It is brittle in nature and possesses low tensile and fatigue strength, which restricts its ability to withstand dynamic physiological loads [48]. Furthermore, HAp shows a slow degradation rate, as it dissolves primarily through ion exchange and surface dissolution in physiological fluids [24]. Highly crystalline HAp is almost non-resorbable over extended periods, while less crystalline or doped variants degrade faster, but still not at a rate matching natural bone healing. This partial biodegradability allows gradual replacement by natural bone, making HAp ideal as a coating material or composite filler to enhance the osteoconductivity of metallic or polymeric implants rather than as a bulk implant material. While ceramic-based biomaterials offer superior bioactivity and biocompatibility, but their brittleness and slow degradation behavior underscore the need for alternative materials with controllable mechanical and degradation characteristics, leading to the emergence of biodegradable metals and alloys for biomedical applications.

1.2.3 Emergence of biodegradable metals and alloys for biomedical applications

Considering the challenges experienced by conventional permanent metallic implants made up of Ti and SS, global research efforts have focused on the development of biodegradable metallic implants. Such materials are designed to provide temporary mechanical support during the healing process and gradually degrade within the body, thereby eliminating the need for secondary surgical procedures to remove the implant. This approach has the potential to improve patient quality of life, reduce healthcare costs, and minimize the complications associated with permanent implants.

Biodegradable metals represent a unique class of biomaterials designed to gradually degrade in the human body while eliciting a favorable host response. Ideally, they fully resorb after fulfilling their tissue-regenerative function, leaving no residual material. As these metals corrode progressively *in-vivo*, their degradation by-products are

metabolized, assimilated, or excreted by the host, ensuring safe dissolution once the healing process is complete [49]. In terms of nomenclature, “biodegradable metals” are synonymous with “absorbable metallic materials” as defined by ASTM F3160 [50–52]. Biodegradable metals can be categorized into three primary groups: Mg, Fe, and Zn. Each of these elements offers distinct advantages: Fe provides the highest mechanical strength and ease of fabrication, Mg exhibits superior biocompatibility with mechanical behavior close to that of natural bone, and Zn has a corrosion rate intermediate between Mg and Fe, near the ideal range for biomedical use [50,51].

Applications of biodegradable metals are particularly promising for temporary implants such as vascular stents, bone fixation devices, and bone grafting scaffolds, where the surrounding tissue has the intrinsic ability to regenerate. Over the past two decades, significant progress has been achieved toward clinical translation of biodegradable systems. For instance, early clinical use of Mg-based scaffolds was reported in 2004, when Witte described their application in 20 patients with inferior genicular artery conditions [53]. This milestone was followed by the commercial release of the Magmaris Mg coronary stent by Biotronik, Germany, in 2016, which received CE approval as the first clinically validated biodegradable metallic scaffold [19,54]. The device was fabricated from an Mg-RE alloy (WE43) and is expected to become widely available [50]. Additionally, Lifetech Scientific (China) initiated the first human trial of Fe-based biodegradable stents in 2018. Clinical cases of Mg-based biodegradable bone screws have also been reported in Germany [55], Korea [56], and China [19].

Despite these benefits, research into biodegradable metals for bone grafting remains underdeveloped, largely due to challenges in manufacturing porous scaffolds with patient-specific architectures. Such scaffolds are highly desirable because they provide tunable mechanical strength, appropriate porosity, and sufficient permeability for cell infiltration and tissue ingrowth. Conventional fabrication methods, including casting, sintering, foaming, and chemical vapor deposition, have been explored, but these techniques offer limited control over pore size, shape, and distribution. Furthermore, they lack the flexibility to produce patient-customized geometries that align precisely with anatomical requirements. To date, no biodegradable metallic porous scaffold has reached clinical use.

1.3 Development of porous orthopedic implants

In the previous sections, the fundamentals of bone metabolism and various materials suitable for orthopedic implant applications were discussed. In the present section, a comprehensive review of the different manufacturing processes used for developing orthopedic implants is presented. Techniques such as additive manufacturing (AM), spark plasma sintering (SPS), and hybrid manufacturing techniques are reviewed.

1.3.1 Development of porous scaffolds using additive manufacturing

AM, also known as rapid prototyping (RP), is a computer-assisted advanced fabrication technique that utilizes computer-aided design (CAD) and computer-aided manufacturing (CAM) models to construct predefined micro and macrostructures and precisely controlled hierarchical architectures [57,58]. As the demand of the manufacturing sector is more focused on precision and specific design, the AM technique has emerged as a strong tool for mitigating the problems associated with conventional PM techniques like material loss during post-processing, difficulty in producing complex shapes, etc. [59–62]. AM has been extensively utilized in the medical field by creating patient-specific

components based on patients' medical imaging. AM techniques can be categorized based on energy-powder interaction and consolidation mechanisms, including methods such as electron beam melting (EBM), selective laser melting (SLM), laser engineered net shaping (LENS), and binder jetting (BJT) [63,64]. Though there are several AM processes, only a few techniques, including SLM/LPBF and EBM, are widely used and can fabricate a wide variety of materials. Other AM processes, like directed energy deposition (DED), are widely used for higher deposition rates and large-scale manufacturing [65].

A unique feature of AM is the precise control it offers over scaffold architecture, including pore size, shape, volume, and interconnectivity. It is a layer-by-layer fabrication process in which the selected part is built in a CAD file and the file is sliced along the Z-axis in a virtual environment, and a machine-specific tool path is generated for each slice. This approach provides flexibility to design and fabricate porous scaffolds with tailored pore geometry and interconnectivity, thereby enabling structures that closely replicate the architecture of natural bone. Apart from this, AM offers specific advantages like site-specific deposition with higher cooling rates and can easily produce intricate shapes [66]. Apart from fabricating intricate shapes, the AM structures also exhibit improved properties because of hierarchical microstructures resulting from higher cooling rates observed during the process [67–69].

AM-fabricated porous Ti alloys exhibit relatively better mechanical properties due to interconnected structures. Good interconnectivity of the porous implants enables uniform load distribution among the structures, while poorly connected porous structures typically fail prematurely at the joints. Ample evidence in the literature suggests premature failure for porous metallic implants [70,71]. Biomedical implant dimensions and requirements vary from patient to patient, making other routes challenging. Porous Ti implants are usually used for orthopedic implants owing to their outstanding mechanical and biological properties. The elastic modulus of bone ranges between 10-20 GPa and is mostly composed of inner cancellous and outer cortical bone. Meanwhile, dense Ti alloys have an elastic modulus of around 110 GPa. However, it is worth mentioning that metallic alloys fabricated via AM tend to possess a lower elastic modulus than regular Ti-based alloys, making them comparable to bone [72]. In addition, porous Ti also possesses high rigidity and good fatigue properties, making it a suitable candidate for biomedical implants.

Figure 1.6 shows the Ti femoral implant and the hip ball and socket joints [42]. Pelvic injury is prevalent in trauma patients, caused by impact, rolling, steep falls, and other injuries. Recently, AM has often been employed for preoperative examination and simulated surgery, treating pelvic fractures. Investigations demonstrate the possibility of employing AM-fabricated Ti alloys for pelvic implants [73,74]. Wong et al. [75] manufactured pelvic-specific implants from Ti alloy and evaluated their performance. Broekhuis et al. [76] used AM to customize and create metallic pelvic prostheses for acetabular repair following tumor resections.



Figure 1.6. Image showing (a) medical-grade titanium (Ti) alloy femoral implant, (b) 3D-printed Ti hip ball-and-socket implant, and (c) the first trabecular Ti hip cup used in biomedical application. Reproduced with permission from [42].

In 2017, the United States FDA (Food and Drug Administration) authorized two alloys of Ti for spinal implants made by AM. One example of an additively manufactured vertebral implant is the HAWKEYE Ti, while another is the NEXXT MATRIX 3D-printed spinal implant. Hollander et al. [77] employed AM technology to fabricate spinal implants with tailored porosity and demonstrated that their surface characteristics supported the adhesion and proliferation of human osteoblasts. Figure 1.7. shows ATEC's IdentiTi posterior curved porous titanium interbody implant placed in the human spinal column. Lin et al. [78] utilized the SLM method to achieve a porosity of approximately 55%, resulting in an elastic modulus close to that of natural human bone (~3 GPa) and developed titanium interbody fusion cage.

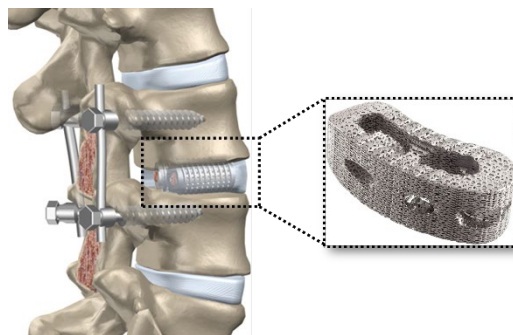


Figure 1.7. Schematic representation of the human spinal column showing the location of ATEC's IdentiTi posterior curved porous titanium interbody implant (indicated in black). Reproduced with permission from [42].

Figure 1.8 shows the cranial implant developed by Novax DMA [42] for a patient requiring a large metallic implant. In the case of a skull implant, external variables, particularly the implant itself, should be promoted rather than hindering the healing process. Most significantly, the implant should fit as perfectly as feasible, as offered by AM. The manufacturing technique, which uses a laser for building up a material (Ti) layer-by-layer, allows for maximum customization in terms of form and size. Because of the large hole in the patient's bone structure, integrating biological activities and minimizing heat loss into the brain tissue were given high priority. A Ti construction may also be impermeable to brain tissue fluid. Only permeable construction may satisfy the requirements.

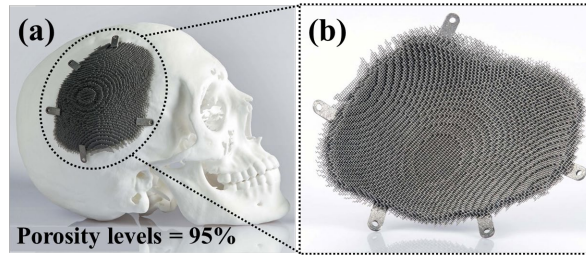


Figure 1.8. (a) Titanium-based highly porous cranial implant developed by Novax DMA designed to match complex anatomical geometries, and (b) magnified image of the porous titanium cranial implants with porosity levels of 95%. Reproduced with permission from [42].

A lattice-structured implant with skull-integrated, screw-in fasteners allows fluids to pass through and combine with the skull's bone. Furthermore, such a construction would provide insulation, reducing heat transfer entering the cranial cavity. The pore spaces are around 1 mm, whereas the cell links are about 0.2 mm thick. Murr et al. [79] described a reticular skull implant developed through EBM. Mazzoli et al. [80] used μ -CT imaging, computer modeling, and AM to produce a biocompatible Ti skull implant. Yan et al. [81] employed EBM to create a mandibular prosthetic implant that had a 3D mesh and a porosity of 81.3%, which fits the parameters for implantation in the human body (Figure 1.9). Moiduddin et al. [82] also utilized a Ti-based alloy to fabricate cheekbones.

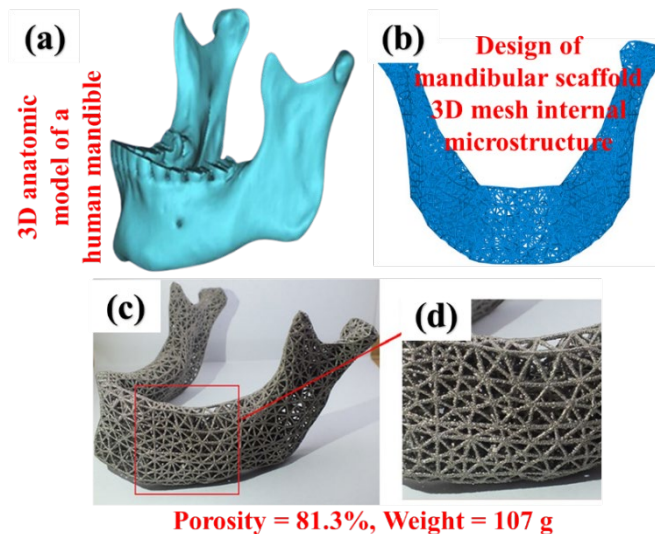


Figure 1.9. Design and fabrication of a patient-specific mandibular scaffold demonstrating the integration of anatomical modeling and additive manufacturing (a) 3-dimensional anatomic model of a human mandible prosthetic, (b) design of mandibular scaffold 3-dimensional mesh internal microstructure, (c) titanium alloy scaffolds produced by additive manufacturing process, and (d) higher magnification image of additive manufactured Ti6Al4V scaffold showing pore characteristics. Reproduced with permission from [81].

Yanez et al. [83] studied the gyroid-based porous Ti structures, where triply periodic minimal surfaces (TPMS) have been used as an effective approach for developing porous biomaterials. They developed a variety of porous Ti structures with varying degrees of porosity using EBM to investigate mechanical characteristics under compression and torsion loads, as illustrated in Figure 1.10. Compression testing indicated that deformed gyroid structures possess significant strength and stiffness when subjected to axial loading, particularly when a reinforcing shell is incorporated.

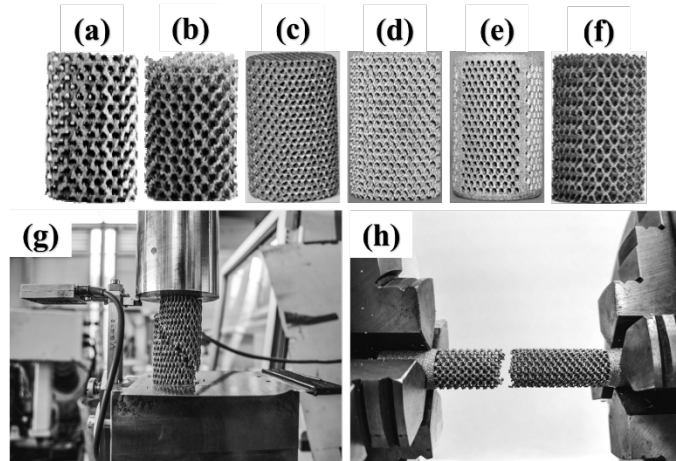


Figure 1.10. Representative images of six gyroid-structured porous titanium (Ti) designs (a) gyroid 75, (b) gyroid 90, (c) deformed gyroid 75, (d) deformed gyroid 90, (e) deformed gyroid with shell reinforcement, and (f) double deformed gyroid, (g) experimental setup illustrating compressive mechanical testing of a gyroid porous Ti specimen and, (h) torsional testing configuration showing a porous Ti sample subjected to rotational loading. Reproduced with permission from [83].

1.3.2 Development of porous scaffolds using SPS

The conventional sintering or pressureless sintering process involves heating Ti and its alloys at an elevated temperature of 1200 °C to 1400 °C (but below the melting point of the material) and a high vacuum of the order of 4×10^{-4} Pa to 6×10^{-6} Pa for a long time of about 24 h to 48 h for densification and homogenization [84,85]. Even after this lengthy procedure, achieving a porous homogeneous microstructure is challenging [85]. SPS is an advanced consolidation technique that uses pressure-assisted pulsed current to sinter and can produce pore-free samples. In this process, the powder is loaded in an electrically conducting die, which acts as a heating source when subjected to a pulsed direct current. Thus, the powdered samples will be heated from both sides under uniaxial pressure [86,87], and due to this fast heating, enhanced mass transfer and rapid powder consolidation will occur [88]. Two theories explain the consolidation mechanism of commercially pure (CP) Ti. According to the first hypothesis, the surface of the powder particles is cleaned and activated by spark discharges generated between metallic powdered particles, thus promoting mass transport for sintering [89,90]. Another hypothesis suggests that the densification of powder is due to particle deformation because, as the temperature increases, the yield strength of the powder particles decreases [91]. The properties of porous Ti synthesized using SPS from various studies are presented in Table 1.4.

SPS is also referred to by several alternative names, including field-assisted consolidation, electrical field-activated sintering, plasma-activated sintering, and electrical discharge compaction [90]. Ibrahim et al. [92] synthesized porous Ti and its alloy using SPS. During this process, porous Ti with different porosities was successfully synthesized by NH_4HCO_3 as a space holder and TiH_2 as a foaming agent. The experimental results showed that pure Ti samples achieved full relative density at a relatively low temperature of 750 °C and a pressure of 16 MPa. The porosity of 53% and Young's modulus of 40 GPa were achieved in the case of pressureless sintering at a temperature of 1000 °C.

Kashimbetova et al. [93] reported the fabrication of porous Ti structures using pressure-less spark plasma sintering (PL-SPS). Their study focused on examining how different sintering temperatures influence the microstructural features and mechanical performance. Figure. 1.11 (a,d,g). display the porous strands formed at 1400 °C, where bonding occurred primarily at contact points between adjacent Ti particles in the early sintering stage. At 1500 °C, more developed sintering necks between particles were observed, as shown in Figure 1.11-(b,e,h), indicating enhanced densification with limited grain growth. Further sintering at 1600 °C brought the structures into the mid-stage of sintering, marked by significant pore shrinkage, though overall porosity was maintained (Figure 1.11-(c,f,i)).

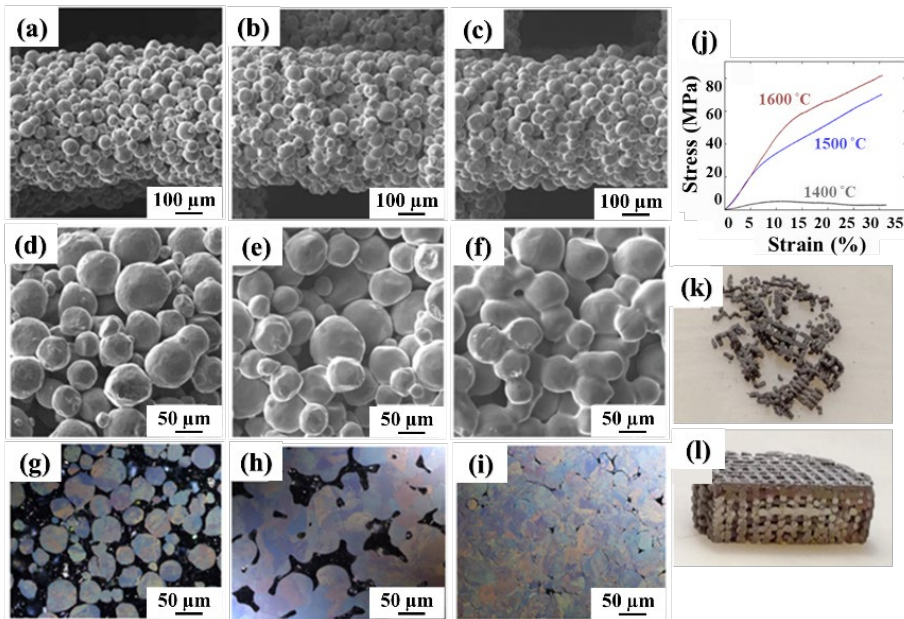


Figure 1.11. Images depicting porous titanium (Ti) fabricated using pressureless spark plasma sintering as a function of varying sintering temperatures (a,d,g) 1400 °C, (b,e,h) 1500 °C, and (c,f,i) 1600 °C. Images (d-f) show higher-magnification views of (a-c), respectively. Images (g-i) present metallographic cross-section microstructures of the corresponding samples. (j) Compressive stress-strain curves of porous Ti as a function of different sintering temperatures. Images of the (k) fragments of broken samples sintered at 1400 °C, and (l) lateral view of compacted samples sintered at 1600 °C. Reproduced with permission from [93].

Table 1.4. Processing conditions and mechanical properties of porous titanium prepared by spark plasma sintering, hot pressing, and microwave sintering (where ST-Sintering temperature in °C, TP-Time and pressure in min and MPa respectively, P-Porosity in %, PS-Pore size (µm), E-Young's modulus (GPa), YS-Yield strength in MPa, UCS-Ultimate compressive strength in MPa, and UTS-Ultimate tensile strength in MPa).

Material type	ST	TP	P	PS	E	YS	UCS	UTS	Ref.
Pure Ti	750	16	0	-	~1 25	-	-	-	[92]
Pure Ti	1000	Pressur e less	53	-	40	-	-	-	
Ti5Mn alloy	950	Pressur e less	56	-	35	-	-	-	
Ti5Mn alloy	1100	Pressur e less	21	-	52	-	-	-	
Pure Ti	700	-	30-70	125 - 800	6- 36	27- 94	-	-	[94]
β-alloy Ti- 45Nb (Gas atomized)	1000	10, 30	0.5	-	72	550	-	-	[95]
β-alloy Ti- 45Nb (Milled)	1000	10, 30	4.0	-	72	867	-	-	[95]
Ti6Al4V	700	3, 30	32	-	-	-	125	-	[96]
Pure Ti	600	3, 30	32	-	-	-	113	-	[96]
CP Ti (Grade 1) powder	900	5, 60	-	-	-	340	-	445	[97,98]
Cryo-milled nanocrystalli ne CP Ti (Grade 2) powder	850	-	-	-	-	770	-	840	
CP Ti (Grade 3) powder	900	5, 60	-	-	-	595	-	720	
Wrought titanium grade 4	-	3, 80 MPa	-	-	-	480 - 635	-	655 - 690	

Increased densification at higher temperatures had a direct effect on compressive yield strength (CYS) (Figure 1.11-(j)). At 1400 °C, the weakly bonded particles resulted in a low yield strength of 4.7 MPa. This increased to 26.7 MPa at 1500 °C due to the growth of sintering necks and reached 52.6 MPa at 1600 °C as a result of further densification. The samples sintered at 1500 °C and 1600 °C exhibited elastic deformation followed by strain hardening during compression. In contrast, the structure sintered at 1400 °C reached peak stress shortly after yielding and then fractured instantaneously, as shown

in Figure 1.11-(k). The compressed sample sintered at 1600 °C maintained its pore geometry as shown in Figure 1.11-(l).

1.3.3 Hybrid manufacturing of porous scaffold

As discussed in the previous sections, major causes of implant failure, such as stress shielding and implant loosening, can be mitigated by reducing the Young's modulus of metallic implants through the introduction of porosity using different fabrication techniques. However, these modifications inevitably reduce the strength and fatigue resistance of the implants compared with their dense counterparts [99–102]. To overcome this limitation and simultaneously enhance the mechanical and biological performance, researchers have explored strategies to integrate a secondary bioactive phase into the 3D-printed porous framework [103]. One promising approach involves the development of next-generation metallic composites known as interpenetrating phase composites (IPCs). IPCs represent a distinctive class of multi-material composites in which at least one phase forms a topologically continuous network, while the second phase is uniformly distributed throughout the structure [6]. A key advantage of IPCs is their inherent structural redundancy: even if one phase undergoes degradation, the remaining continuous phase can maintain mechanical integrity and load-bearing capability [104,105]. Inspired by natural materials, bio-inspired IPC architectures have been proposed to improve strength, toughness, and damage tolerance [106–108]. Although such architectures have been successfully realized in polymer-based systems due to their greater fabrication flexibility [109–111], replicating similarly complex designs in metallic systems remains a considerable challenge. In this regard, AM provides a promising route for producing intricate metallic architectures with controlled porosity and geometry that mimic biological structures [112–116]. Nevertheless, the development of multi-phase IPCs using AM is still in its early stages, as most existing studies focus on single-material systems, and integrating multiple metallic phases significantly increases processing complexity.

Several studies have attempted to fabricate IPC by combining AM-fabricated porous metallic scaffolds with secondary functional phases by the conventional route. For instance, Zhang et al. [8] developed a Mg-Ti composite by pressureless infiltration of Mg into an AM-fabricated Ti64 scaffold. Since the constituents of the composite were continuous and mutually interpenetrated in the 3D space, the composite was termed IPC. These porous structures were designed to mimic the bioinspired architecture structure as shown in Figure 1.12. The composite shows effective stress transfer, delocalized damage, and arrest cracking. Similarly, Dou et al. [103] fabricated partially degradable IPC by first creating a pure Ti-based dodecahedral cellular structure with pore sizes ranging from 400-500 μm using SLM, followed by pressureless infiltration of pure Mg into the porous framework. The developed composite possesses a higher strength (yield strength of 64 MPa and ultimate compressive strength of 275 MPa) and lower modulus (47.3 GPa) than cast pure Mg and Ti. Also, the degradation of the Mg supports the ingrowth of bone tissue and biological fixation between the host and implant. *In-vitro* and *in-vivo* studies of these composites revealed that the composite exhibits accelerated corrosion compared to pure Mg. Still, it remains non-cytotoxic and does not induce adverse reactions following implantation. In a similar approach, Rahmani et al. [117] reported the addition of three different types of wollastonite (CaSiO_3)-based bio-ceramic via SPS in an AM fabricated Ti64 lattice as shown in Figure 1.12. The produced composite exhibited higher wear resistance, damage tolerance, and mechanical properties, which

can improve the durability of the bones. In another study, Rahmani et al. [117] reported improved impact and osteoinductivity by manufacturing hybrid wollastonite and Ti64 for craniofacial implants, as shown in Figure 1.13.

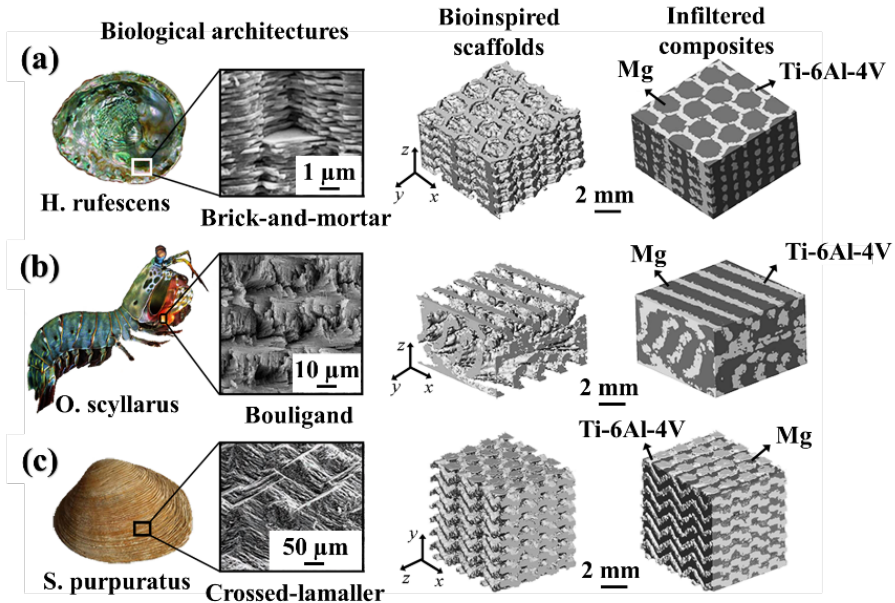


Figure 1.12. Bioinspired architecture comprising additively manufactured Ti6Al4V (Ti64) infiltrated with magnesium (Mg) via a pressureless infiltration route. The developed Ti64-Mg composite exhibits a different bioinspired interpenetrating (a) *H. Rufescens*, (b) *O. Scyllarus*, and (c) *S. Purpuratus* architecture. Reproduced with permission from [8].

However, the classification of such composites as IPCs strongly depends on the fabrication route and the resulting phase architecture. When IPCs are produced using solidification-based casting approaches, the secondary phase is typically infiltrated into a porous precursor with or without the application of external pressure. During this process, the infiltrated melts penetrate and interconnect with the porous precursor, resulting in mutually interpenetrating continuous phases and forming IPC structures. Therefore, the terminology IPC is well-suited for composites fabricated through infiltration-based casting, as illustrated in Figure 1.12. In contrast, when composites are fabricated using powder metallurgical approaches, the processing mechanism differs significantly. In such cases, neither infiltration nor interpenetration of the secondary phase occurs; instead, the secondary phase is manually added to the precursor matrix like the processing of conventional composites. Consequently, a new scientific terminology is required to clearly classify and describe these types of composites. If the secondary phase is incorporated into the precursor matrix using powder metallurgy-based approaches, similar to conventional composite processing, the secondary phases typically surround the precursor matrix without forming an interpenetrating network during consolidation. Therefore, such materials may be more appropriately classified as metallic multimaterials (MMMs) rather than IPCs. When two phases are involved, these systems may be specifically referred to as metallic bimaterials. Furthermore, if both the matrix and reinforcement phases are metallic, the resulting composites can be defined

as metallic bimetal composites (MBMCs) [6]. The detailed investigation on the development of MMMs and MBMCs is presented in Chapter 5 of this thesis.

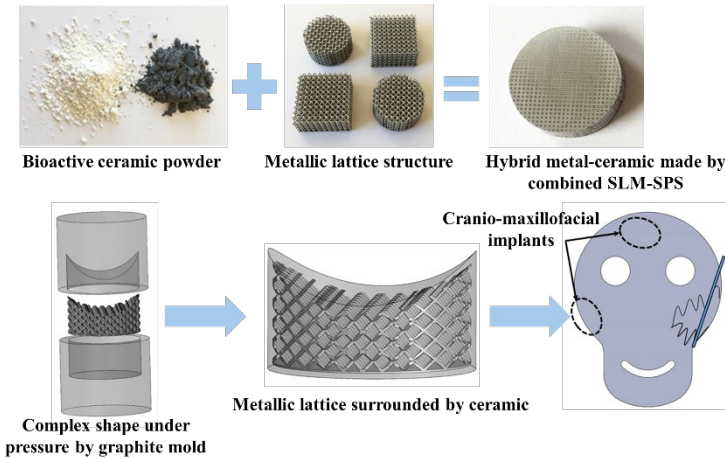


Figure 1.13. Processing step for designing cranio-maxillofacial implant by infiltrating wollastonite, hydroxyapatite-based nanoscale bioceramics inside titanium alloys with arbitrary lattice structures. Reproduced with permission from [118].

1.4 Research gap

Orthopedic implants are generally based on non-biodegradable metallic materials such as Ti alloys, which provide excellent mechanical strength and corrosion resistance but remain permanently in the biological system. In contrast, biodegradable metals such as Zn exhibit controlled degradation behavior and good biocompatibility. But their insufficient mechanical strength restricts their usage in load-bearing applications. To address these challenges, porous Ti structures fabricated using AM have been developed to reduce stiffness mismatch and enhance osseointegration. Nevertheless, increasing porosity reduces the effective load-bearing capacity, while the material remains non-biodegradable. Consequently, porous architecture alone cannot simultaneously achieve mechanical integrity and functional degradation. In this context, partially biodegradable systems combining a stable structural phase with a degradable phase have emerged as a promising approach. IPCs have been explored to realize such systems, yet their fabrication is largely restricted to conventional processing routes, limiting control over complex geometries. This limitation has driven the need for hybrid manufacturing strategies integrating AM and PM, although systematic investigations in this area remain limited. For the successful development of such hybrid systems, the selection of an appropriate load-bearing phase is critical. Ti64 alloys processed via SLM and SPS have been widely investigated. However, these studies are predominantly independent, and a systematic comparison of their microstructural evolution, mechanical performance, corrosion behavior, and biological response under physiological conditions is lacking. Such a comparison is essential to identify the most suitable processing route for the structural phase in hybrid partially biodegradable systems. Furthermore, the development of bio-inspired MMMs through hybrid processing remains underexplored, resulting in a limited understanding of viable material combinations that can be effectively fabricated. In particular, the feasibility of integrating an SLM-fabricated

porous Ti64 scaffold with SPS-infiltrated Zn to develop a partially biodegradable implant has not been established. Moreover, the influence of such hybrid architecture on microstructural evolution, interfacial integrity, mechanical performance, corrosion, biodegradation behavior, and *in-vitro* biological response under physiological conditions remains unaddressed.

1.5 Objective of the thesis

The overall aim of this doctoral research is to develop a partially biodegradable Ti64-Zn MBMC using a hybrid manufacturing method for biomedical implant applications. To achieve this aim, the following specific objectives were defined and systematically addressed:

- Evaluate the effect of fabrication route by comparing SLM and SPS processed Ti64 in terms of microstructure, mechanical, and biological performance under a physiological environment.
- Evaluate the degradation behavior and *in-vitro* biological performance of SPS-processed pure Zn in comparison with conventionally used as-cast Zn.
- Design and fabrication of Ti64-Zn MBMC with a bioinspired Ti64 porous scaffold as the permanent phase and Zn as the degradable phase. The developed composite will be systematically evaluated in terms of phase composition, mechanical integrity, corrosion, and biodegradation behavior, and *in-vitro* cytocompatibility.

2 Materials and experimental techniques

2.1 Raw materials

This study employs a range of metallic raw materials selected to investigate hybrid manufacturing and multimaterial composite development. The primary materials include Ti64 alloy powders, Zn powders, and conventionally as-cast Zn. This section briefly outlines the characteristics of these materials relevant to the present work. Gas-atomized Ti64 alloy powder, commercially sourced from SLM Solutions with a particle size range of 20-63 μm , was employed as the feedstock material. The morphology of the as-received powder, shown in Figure 2.1-(a,b), reveals predominantly spherical particles accompanied by smaller satellite particles adhering to their surfaces. These satellites typically form due to collisions between solidifying droplets under turbulent flow within the atomization chamber. At higher magnification, as shown in Figure 2.1-(b), some particles display a distinctive “clamshell” structure, which can be attributed to rapid solidification and prior β as-cast grain formation at elevated temperatures [119]. The particle size distribution curve shown in Figure 2.1-(c) indicates an average diameter of 30 ± 10 μm . Elemental composition was further analyzed using energy-dispersive spectroscopy (EDS) at higher magnification (Figure 2.1-(d)), confirming a homogeneous distribution of Al and V within the Ti matrix.

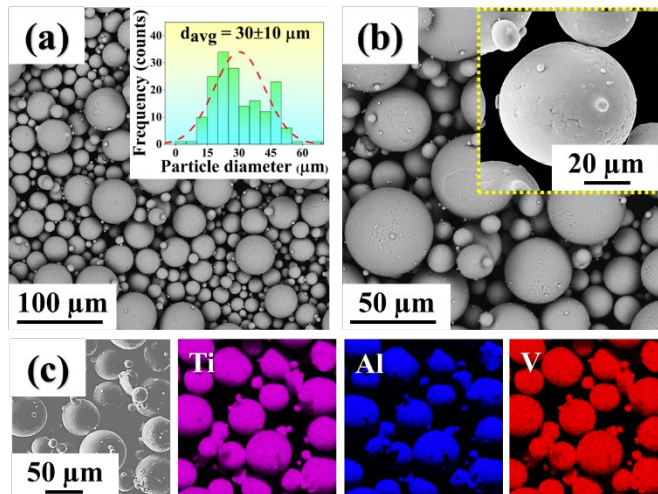


Figure 2.1. Scanning electron microscopy images of the (a,b) as-received powder at different magnifications, the inset figures in (a) show the particle size distribution curve, and (b) shows the morphology of a single particle, (c) energy dispersive spectroscopy map obtained from the high-magnification region in (b).

Similarly, commercially pure gas-atomized Zn powder with a particle size range of 10-25 μm was employed, along with commercially pure Zn blocks (>99.9%) procured from Vedanta Ltd. (Mumbai, India). To ensure microstructural uniformity, the cast Zn blocks were subjected to recrystallization at 300 $^{\circ}\text{C}$ for 4 h under ambient conditions. The morphology of the Zn powder, as shown in Figure 2.2-(a,b), reveals nearly spherical particles with faceted surfaces, often accompanied by smaller satellite particles adhering to the larger ones. The particle size distribution curve (Figure 2.2-(c)) indicates an average

particle size of $11 \pm 6 \mu\text{m}$, while the X-ray diffraction (XRD) pattern (Figure 2.2-(d)) confirms the presence of peaks corresponding to the hexagonal close-packed (hcp) structure of Zn.

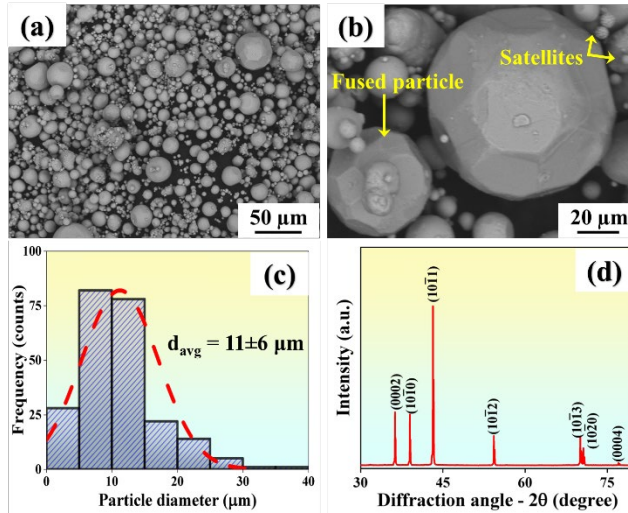


Figure 2.2. Scanning electron microscopy images depicting the morphology of pure zinc (Zn) powder at (a) low and (b) high magnification, (c) shows the particle size distribution curve of the pure Zn powder, and (d) X-ray diffraction pattern of pure Zn powder. Reproduced with permission from [120].

2.2 Sample fabrication method

2.2.1 SLM of Ti64

The SLM samples were fabricated from pre-alloyed elemental powder using the LPBF technique on an SLM280 system (SLM Solutions GmbH, Luebeck, Germany). Fabrication was carried out on a Ti and 316L SS based substrate under an argon atmosphere, to prevent oxidation during the LPBF process. A 90° hatch rotation strategy was applied between successive layers to minimize thermal gradients and alleviate residual stresses induced by rapid solidification. A summary of the optimized processing parameters for SLM is presented in Table 2.1.

2.2.2 SPS of Ti64 and Zn

Both Ti64 and Zn powders were consolidated into cylindrical pellets with a height of approximately 6-7 mm using an HPD 10-GB SPS system (FCT System GmbH, Effelder-Rauenstein, Germany) equipped with a graphite die of 20 mm inner diameter. To prevent adhesion of the powders to the die and to ensure uniform electrical conductivity during sintering, 0.5 mm thick graphite paper was placed between the powder and the graphite punches. The sintered pellets were subsequently machined on all surfaces to remove any residual graphite contamination. The sintering parameters for both materials are summarized in Table 2.1. The SPS cycle consisted of three main stages: (i) initial compaction, during which the pressure was gradually increased from 5 MPa to 50 MPa; (ii) heating, where the temperature was raised from 50°C to the designated sintering temperature at a rate of $50^\circ\text{C}/\text{min}$ and maintained for a dwell time of 10 min; and (iii)

cooling, during which the temperature was reduced from the elevated sintering temperature to 50 °C at the same rate.

2.2.3 Hybrid manufacturing of composites

The hybrid manufacturing of MMMs and Ti64-Zn MBMC was carried out in two stages: AM of a bioinspired Ti64 honeycomb structure, followed by consolidation of the secondary phase using SPS. The honeycomb lattice was produced using the parameters discussed in Section 2.2.1. The CAD model of the bioinspired honeycomb structure is shown in Figure 2.3, highlighting the dimensions of hexagon unit. The optimized processing parameters for SLM are shown in Table 2.1. The developed parts were cleaned using the standard procedure followed by ultrasonication in ethanol for 15 minutes before further use. The cleaned lattice of 6 mm thickness was manually filled with Zn spherical powder inside a 20 mm diameter graphite die as discussed in Section 2.2.2. The optimized SPS parameters for MMMs and MBMC are listed in Table 2.1. A schematic illustration of the two-step fabrication route for Ti64-Zn MBMC is shown in Figure 2.4.

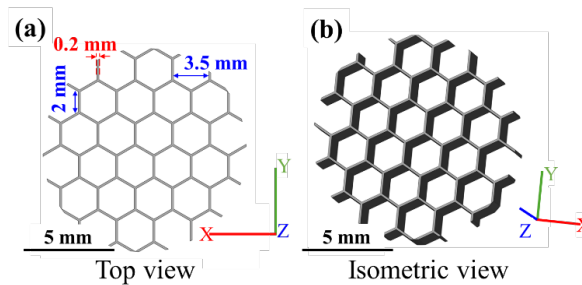


Figure 2.3. Computer-aided design model of the bioinspired Ti6Al4V hexagonal lattice (a) top view with cell/strut dimensions and (b) isometric 3-dimensional view. Reproduced with permission from [121].

Table 2.1. Process parameters used to fabricate composites using the combination of selective laser melting and spark plasma sintering processes for different material systems.

Selective laser melting parameters					
Material	Laser power (W)	Scan speed (mm/sec)	Hatch distance (mm)	Layer thickness (mm)	Energy density (J/mm ³)
Ti64 Bulk	400	1000	0.12	0.05	66.66
Ti64 Hexagons	400	1000	0.12	0.05	66.66
Spark plasma sintering parameters					
Material	Sintering temperature (°C)		Holding time (min)	Compaction load (MPa)	
Pure Zinc	300		10	50	
Ti64-Zn (MBMC)	375		30	50	

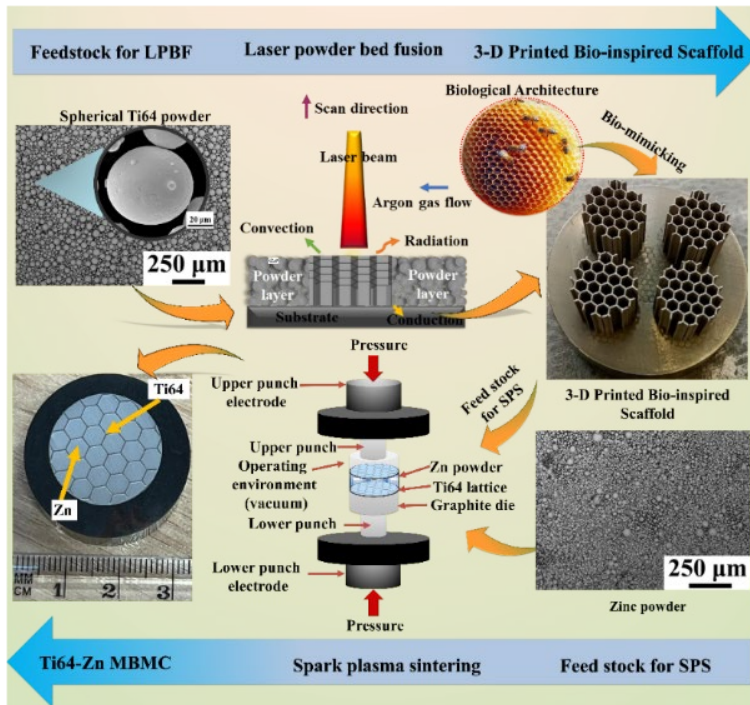


Figure 2.4. Schematic representation of the two-step fabrication route for Ti6Al4V-Zinc (Ti64-Zn) metallic bimetal composites (MBMCs). In Step 1, a bioinspired Ti64 hexagonal lattice architecture is produced via selective laser melting. In Step 2, Zn powder was infiltrated into the Ti64 lattice and consolidated through spark plasma sintering, leading to the development of Ti64-Zn MBMC. Reproduced with permission from [121].

2.3 Characterization of composites

2.3.1 Phase and microstructural analysis

The phase composition of Ti and Zn powders, as well as their bulk-processed counterparts and Ti64-Zn composite, was analyzed using a Rigaku Smart Lab X-ray diffractometer with Cu-K α radiation ($\lambda = 1.5406 \text{ \AA}$) in Bragg-Brentano mode. For all the samples, scans were performed over a 2θ range of 25° - 90° , with a step size of 0.01° and a scan rate of $3^\circ/\text{min}$. The crystallographic texture of the Ti64 and Zn bulk samples was further examined on the XY surface using Schulz reflection geometry, with the X-ray source operated at 45 kV and 30 mA. This approach allowed for the identification of phase formation, detection of secondary phases, and assessment of texture in developed samples.

The microstructure of powders, bulk Ti64 and Zn, and Ti64-Zn MBMC were examined using optical microscopy (OM Leica Microsystems), scanning electron microscopy (Zeiss Gemini SEM 450), and electron backscatter diffraction (EDAX detector). All samples were prepared following standard metallographic procedures, including mounting and sequential grinding up to 4000-grit paper.

For Ti64, electropolishing was performed in a standard A3 electrolyte for 20 s, followed by sonication in deionized water to remove residual contaminants. Zn samples were manually electropolished at 20 V for 35 s in an electrolyte consisting of

orthophosphoric acid and ethanol (3:5) to achieve a mirror-like surface and subsequently etched for 10 s in 10% nital (10% nitric acid mixed with alcohol) to reveal grain morphology. In the Ti64-Zn composite, the Ti64-rich regions were treated using the A3 electrolyte for 20 s, while the Zn-rich regions were electropolished at 20 V for 35 s in the orthophosphoric acid and ethanol mixture. The polished surfaces of all materials were then examined using an SEM equipped with an EDAX EBSD detector. To analyse the substructural features that differentiate the SPS and SLM processing routes, transmission electron microscopy (TEM; Tecnai ST20, 200 keV, Germany) was employed.

2.3.2 Mechanical testing

The mechanical behavior of the developed samples was evaluated through hardness, compression, and tensile testing, followed by SEM and EBSD analysis of the fractured samples. Vickers microhardness was measured using a micro-indentation tester (Future-Tech FM-810) under a load of 0.1 kgf with a dwell time of 10 s. Tensile and compressive properties were determined at room temperature using a screw-driven universal testing machine (Instron 5567) at a strain rate of 10^{-3} s^{-1} . Post-deformation analysis of the fractured samples was performed using SEM (Zeiss Gemini SEM 450), and electron backscatter diffraction (EDAX detector) to examine microstructural evolution where necessary. All experiments were conducted in triplicate to ensure consistency, reliability, and reproducibility of the results.

2.3.3 Biodegradation and electrochemical corrosion analysis

The *in-vitro* biodegradation behavior of the composite was evaluated by immersing the samples in SBF for 7, 14, and 21 days. The SBF solution was prepared following the procedure described in [122]. Prior to immersion, all samples were polished using the same procedure described earlier and then subjected to ultrasonication for 30 min to remove any surface contaminants. The samples were then incubated at 37 °C with a 5% CO₂ supply for the designated periods. After immersion, the samples were retrieved and treated with 200 g/L CrO₃ solution for 10 min to remove surface oxidation and corrosion products. This was followed by ultrasonic cleaning in alcohol for 30 min. Once dried, the mass change was recorded to determine the degradation rate. Additionally, the surface morphology of the degraded samples was analyzed using SEM (Zeiss Gemini SEM 450) to assess the effect of immersion on the samples. All experiments were conducted in triplicate to ensure reproducibility of the results.

The electrochemical corrosion behavior of the SPS-processed Zn, SLM-processed Ti64 samples, and Ti64-Zn composite was evaluated using a standard three-electrode cell setup connected to a potentiostat (C.H. Instruments, CHI604E, USA). In this setup, a standard calomel electrode (SCE) and a platinum (Pt) electrode served as the reference and counter electrodes, respectively, while the thoroughly polished samples (exposure area: 1 cm²) acted as the working electrode. SBF was used as an electrolyte to simulate physiological conditions. Potentiodynamic polarization (PDP) tests were performed at a potential range of -2000 mV to +2000 mV vs. SCE, at a scan rate of 1 mV/s. All electrochemical tests were conducted three times to ensure repeatability and reliability. To understand the resistance and capacitance of oxide films in Zn samples after 1 h and 24 h of immersion, the electrochemical impedance spectroscopy (EIS) information was recorded. The EIS measurement was performed in the frequency range of 10 kHz to 0.01 kHz by applying a 10 mV perturbation to OCP values. Following these, the samples were cleaned according to ISO 8407:2009 standards, and their corroded surface morphology

was examined using SEM (Zeiss Gemini SEM 450). The corrosion rate (CR) in mm/year was calculated according to Eq. 2.1.

$$CR = \frac{I_{corr} \cdot 1000}{n \cdot F \cdot A} \quad (\text{Eq. 2.1})$$

where I_{corr} represents the current density, n denotes the number of electrons (2 in the present case), F signifies the Faraday's constant (96500 C/mol), and A stands for the atomic weight of the metal (65.38 g/mol). Electrochemical corrosion experiments were conducted in triplicate to ensure the reproducibility of the results.

2.3.4 Biocompatibility assessment

Cytotoxicity of the developed samples was evaluated by an indirect method using MC3T3-E1 subclone 4 mouse calvarial pre-osteoblast cells (ATCC, USA; CRL-2593). Fresh culture medium served as the control. disc-shaped samples (20 mm diameter, 2 mm thickness) were uniformly polished, sterilized in ethanol, and exposed to UV radiation for 1 h. To eliminate residual ethanol, the samples were washed three times with a PBS solution containing 1% antibiotics. Since Zn degrades in the solution medium, the potential effect of leachates from the material on cellular response was examined by preparing a conditioned medium. The conditioned medium was prepared by incubating sterilized samples in complete culture medium (α -MEM supplemented with 10% FBS (Gibco, Life Technologies) and 1% antibiotic (Sigma Aldrich)) at 37 °C with 5% CO₂ for 24 h and 72 h, respectively. A fixed volume of 15 μ L/mm² of complete medium was used for conditioning. Following incubation, the samples were removed, and the conditioned medium was centrifuged at 5000 rpm for 20 min to eliminate debris. MC3T3-E1 cells were cultured in a complete medium on a 48-well plate at a density of 3 x 10³ cells per well and allowed to adhere for 24 h at 37 °C with 5% CO₂. After 24 h, the culture medium was replaced with a conditioned medium and incubated for an additional 24 and 72 h. The conditioned medium from all samples was tested at two different dilutions 1X dilution (i.e.100% conditioned medium) and 8X dilution (i.e., 12.5% conditioned medium, with the remaining volume supplemented with complete medium). For positive control, cells were cultured in a fresh medium and incubated for the same period as the conditioned medium sample. After 1 and 3 days of incubation, the conditioned medium was aspirated, and the cells were rinsed with PBS. Cell viability was assessed using the WST-1 assay (Invitrogen) by incubating cells in WST-1 solution (1:10 dilution) for 3 h. The optical density (OD) of the resultant medium was measured using a plate reader (Biotek Gen 5, Santa Clara, CA, USA) at 440 nm. The relative growth rate (RGR) was calculated according to Eq. 2.2:

$$RGR = \left(\frac{OD_{sample}}{OD_{control}} \right) \cdot 100 \quad (\text{Eq. 2.2})$$

where OD_{sample} is the optical density of the sample, and $OD_{control}$ is the optical density of the control determined with a plate reader. The data obtained from the WST-1 assay were analyzed using analysis of variance (ANOVA) with Tukey's test, and statistical significance was considered at $p < 0.05$. All data are reported as mean \pm standard deviation from at least four independent samples. To further evaluate cell viability, a live-dead assay was performed by staining the cells with calcein AM (Thermo Fisher Scientific, India) for live cells and Ethidium Homodimer (Thermo Fisher Scientific, India) for dead cells. The stained cells were then visualized using an inverted epi-fluorescence microscope (Olympus IX-53, Tokyo, Japan). For cell morphology analysis, the cells were fixed with 3.7% formaldehyde in PBS at room temperature for 30 min, followed by PBS washing. The cell membrane was permeabilized by incubating in 0.2% Triton X-100

solution (Sigma, Germany) for 8 min, followed by another PBS wash. To stain actin filaments, the washed cells were incubated with 25 µg/mL Alexa Fluor 488 (Invitrogen) at room temperature for 30 min. The cell nuclei were stained using 0.2 µg/mL DAPI (Invitrogen) at room temperature for 3 min. The stained cells were examined using an inverted epi-fluorescence microscope. All experiments were conducted in triplicate to ensure the reproducibility of the results.

3 SLM and SPS fabrication of Ti64 alloy : A comparative analysis

The objective of this chapter is to address the existing research gap by systematically comparing Ti64 fabricated through SLM and SPS, with emphasis on differences in their microstructural, mechanical, and biological performance. A comprehensive methodology is adopted to examine microstructural features using SEM and EBSD, enabling detailed assessment of grain morphology, phase distribution, and texture evolution. The mechanical behavior was systematically characterized via tensile and compressive testing, encompassing parameters such as ultimate strength, yield strength, and strain to failure. Fractographic analysis was employed to elucidate failure mechanisms and evaluate structural integrity under mechanical loading. . In addition, in-vitro biocompatibility will be evaluated by investigating cell adhesion, proliferation, and potential cytotoxicity, providing insights into cell-material interactions. By integrating these multidisciplinary analyses, the study aims to identify the processing route that yields optimal mechanical stability, and biofunctionality, thereby enhancing the clinical applicability of Ti64 implants. Beyond this comparison, the findings also contribute to the broader objective of developing advanced, high-performance biomaterials for next-generation implant systems.

3.1 Phase analysis of Ti64 alloy

Figure 3.1-(a) shows the XRD patterns of as-received Ti64 powder and the SPS and SLM-processed compacts, highlighting the phase differences under the three conditions. The Ti64 powder exhibited peaks corresponding to α -Ti without any impurity signals, confirming its high purity. In the SLM-processed samples, the diffraction pattern shows the presence of hexagonal close-packed (HCP) α/α' martensite. The absence of β Ti is attributed to its low volume fraction (3-5 vol%) and the extremely rapid cooling rates during laser melting, which transform most of the β phase into fine α/α' -martensite, consistent with earlier studies [123,124]. However, it is important to note that XRD alone cannot reliably distinguish between α (HCP) and α' (HCP), since their c-axis lattice parameters differ by approximately 0.1% [125]. The broader diffraction peaks in the SLM samples indicate the presence of residual stresses, micro-strain, and subgrain refinement, reflecting non-equilibrium solidification. In contrast, the SPS compact retained the α Ti phase while also showing β Ti reflections at 2θ values of 39° and 75° , which can be attributed to the relatively slower cooling rates during sintering that allow partial stabilization of the β phase.

The crystallographic texture of SPS and SLM-processed Ti64 is illustrated in the inverse pole figure (IPF) plot in Figure 3.1-(b,c). The SPS sample exhibited a pronounced texture strongly aligned along [0001] with a weaker [1120] component, which can be linked to the growth of coarse columnar laths favored by slower cooling rates. In contrast, the SLM sample revealed a comparatively weaker [1120] texture with more random grain orientations. This weak texture is associated with the rapid thermal cycles in SLM, which suppress the growth of preferred orientations and promote orientation randomness. These observations are consistent with EBSD microtexture analysis, which is discussed later.

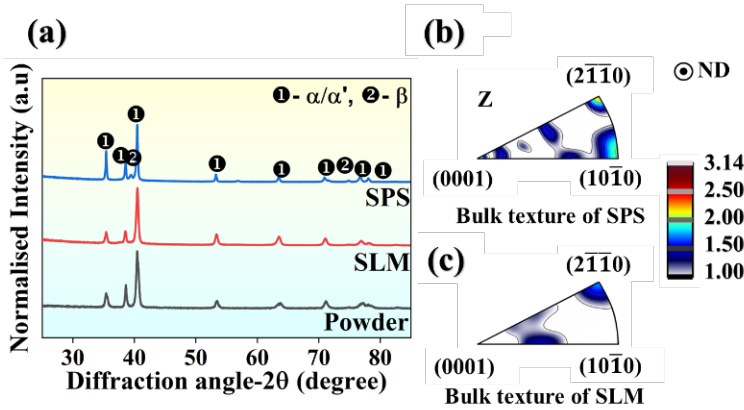


Figure 3.1. (a) X-ray diffraction patterns for the as-received Ti6Al4V (Ti64) powder, and Ti64 samples fabricated by selective laser melting (SLM) and spark plasma sintering (SPS) processes. Inverse pole figure plots obtained using an X-ray texture goniometer for (b) SPS, and (c) SLM processed samples.

3.2 Microstructural analysis of Ti64 alloy

The microstructural characteristics of Ti64 alloys fabricated via SPS and SLM were systematically investigated using SEM, EBSD, and transmission electron microscopy (TEM). The integration of these techniques provided critical insights into how processing routes influence phase morphology, crystallographic orientation, and substructural features.

Figure 3.2-(a,b) shows the microstructure of SPS-processed Ti64, while Figure 3.2-(c,d) presents that of the SLM fabricated samples, highlighting the distinct grain morphologies produced by the two processing routes. The SPS microstructure is characterized by a bimodal grain distribution with coarse prior β grains and lamellar $\alpha+\beta$ colonies forming a basketweave-like Widmanstätten structure [43]. During SPS, the elevated processing temperature (1200 °C) and applied load (50 MPa) enable β -phase growth along α boundaries, leading to a coarser lamellar structure. Above the β -transus, Ti64 exists in the β (BCC) phase, which on cooling transforms into a mixture of α and β phases depending on the thermal trajectory. The relatively slower cooling rate in SPS preserves large polygonal prior β grains, within which colonies of alternating α (grey) and β (white) lamellae are observed, with a spacing of 1-2 μm . Such morphologies arise from diffusional transformations under near-equilibrium conditions, consistent with previous findings [43].

In contrast, the SLM-processed samples exhibit a fine acicular α' martensitic structure, as shown in Figure 3.2-(c,d). Rapid solidification during SLM suppresses diffusional transformations, instead promoting a diffusionless $\beta \rightarrow \alpha'$ martensitic transformation. Both α and α' phases retain a hexagonal close packed (HCP) structure with nearly identical lattice parameters, although α' is a metastable supersaturated phase enriched with Al and V stabilizers [126]. This supersaturation alters the lattice constants, introducing significant residual stresses and micro-strain. The α' laths typically nucleate at prior- β grain boundaries and grow along Burger's orientation relationship (BOR) defined planes. Among the twelve possible α' orientation variants, $\{110\}\beta // \{0001\}\alpha'$ and $\langle 111 \rangle \beta // \langle 1120 \rangle \alpha$ are most favorable, producing laths inclined at $\sim 45^\circ$ [127].

Moreover, hierarchical martensitic laths are evident in SLM samples. Long primary laths coexist with shorter secondary and tertiary laths, formed through sequential nucleation during repeated thermal cycling inherent to SLM processing. Yang et al. [128] reported that this multi-scale martensitic morphology arises from partial reheating of primary martensite during layer deposition, triggering further martensitic transformation. This repeated transformation, combined with high cooling rates, also introduces high dislocation densities and martensitic twinning, which accommodates transformation strain and provides additional nucleation sites for fine-scale variants.

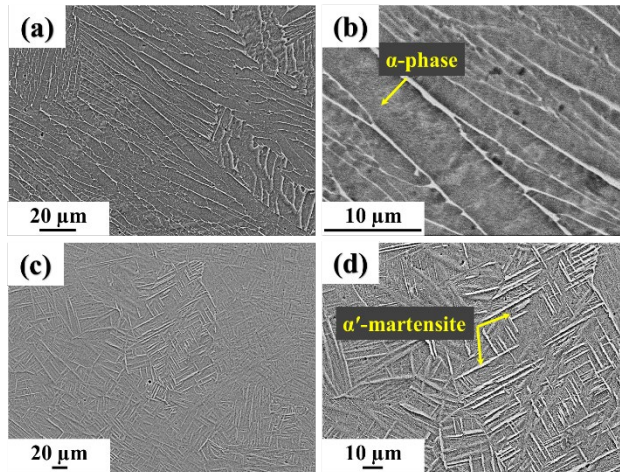


Figure 3.2. Scanning electron microscopy images of Ti6Al4V (a,b) spark plasma sintered samples at low and high magnifications, showing the presence of prior β grain boundaries with α phase (yellow arrow), and (c,d) selective laser melted samples highlighting the acicular α' martensitic needles (yellow arrow) within the microstructure.

To further analyze the crystallographic features and phase evolution of Ti64 samples, EBSD was employed. The EBSD maps of SPS and SLM processed samples are shown in Figure 3.3-(a-c) and Figure 3.3-(d-g), respectively. The IPF, phase distribution, and kernel average misorientation (KAM) maps collectively provide insight into crystallographic orientation, phase constitution, and strain distribution as influenced by the distinct thermal histories of the two processing routes.

The IPF maps of the SPS sample (Figure 3.3-(a)) reveal large α colonies containing fine lamellar prior β , with minimal variation in intergranular orientation. This suggests a slow, diffusion-controlled $\beta \rightarrow \alpha + \beta$ transformation, where variant selection is primarily thermodynamically driven to minimize interfacial energy. In contrast, the IPF map of the SLM sample shown in Figure 3.3-(d) displays highly fragmented α/α' orientations, characteristics of a non-equilibrium transformation. The absence of strong variant selection results in a higher fraction of low-angle grain boundaries (LAGBs), reflecting rapid solidification kinetics.

Phase maps Figure 3.3-(b,e) show notable differences in α and β phase fractions. SPS-processed Ti64 retained 5.2% β phase, mostly localized at interlamellar boundaries, enriched with V and Fe, and present as continuous networks or small globules. Conversely, the SLM sample contained only approximately 2.1% retained β , sparsely

distributed due to extremely high cooling rates ($>10^6$ K/s). These differences in α/β balance directly influence the mechanical response, including strength and ductility.

The KAM map shown in Figure 3.3-(c,f) highlights strain distribution within the microstructures. The SPS specimen exhibits relatively low KAM values, indicative of a strain-free or minimally strained microstructure. In contrast, the SLM sample shows significantly higher KAM values, particularly along inter-martensitic lath boundaries. These elevated misorientations stem from the rapid, diffusionless $\beta \rightarrow \alpha'$ transformation during SLM, which introduces a high density of defects such as dislocations and stacking faults, contributing to localized strain accumulation and heterogeneity in grain orientation [129].

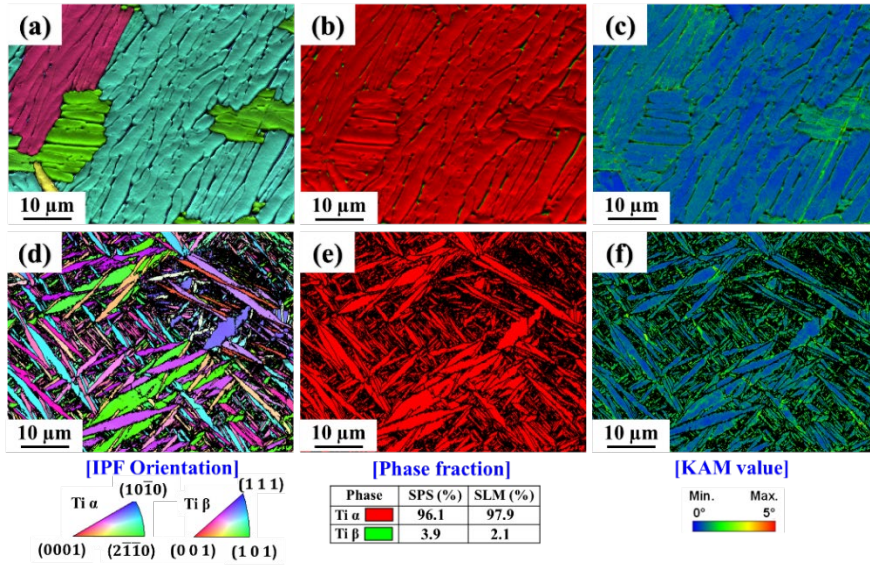


Figure 3.3. Electron backscatter diffraction maps of Ti6Al4V processed by (a-c) spark plasma sintering and (d-f) selective laser melting, showing the (a,d) inverse pole figure, (b,e) phase maps, and (c,f) kernel average misorientation maps.

TEM images shown in Figures 3.4 and 3.5 provide deeper insight into the microstructural distinctions between SPS and SLM-processed Ti6Al4V. Figure 3.4-(a-c) shows TEM micrographs of the SPS samples, where dislocations within the α phase are sparse and isolated (red arrows), suggesting that residual strain is accommodated primarily through elastic rather than plastic mechanisms. As discussed previously, SPS microstructures consist of lamellar $\alpha+\beta$ colonies. The β phase, shown in Figure 3.4-(b), exhibits a coarse morphology with well-defined interfaces and an average lamellar width of 350 nm, consistent with diffusion-controlled transformations. High-magnification TEM images in Figure 3.4-(b,c) reveal that strain is largely concentrated at α/β interfaces, where interfacial misfit dislocation arrays form to accommodate the crystallographic mismatch between HCP α and BCC β during cooling. The selected area diffraction pattern (SADP) of SPS samples confirms the α phase with a zone axis of $[4\bar{5}\bar{1}3]$. The absence of diffraction anomalies such as streaking or splitting excludes significant twinning or stacking faults, supporting a predominantly displacive transformation during sintering.

In contrast, the SLM microstructure shown in Figure 3.5-(a-c) is dominated by densely packed α' martensitic needles with heavily entangled dislocations, reflecting rapid, non-equilibrium solidification.

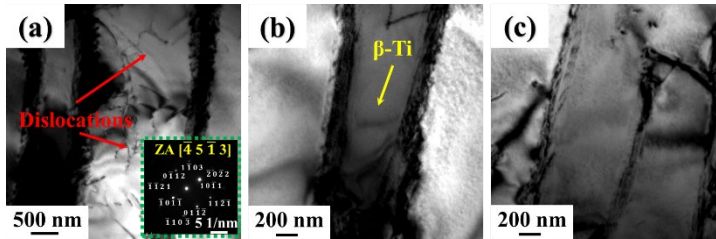


Figure 3.4. Transmission electron microscopy (TEM) images showing the detailed microstructure (a) bright-field TEM image showing dislocations within the lamellar structure, the inset presents the indexed selected area electron diffraction pattern, (b) higher magnification image highlighting the presence of β -Ti phase, and (c) higher magnification image illustrating the lamellar morphology and interfacial features.

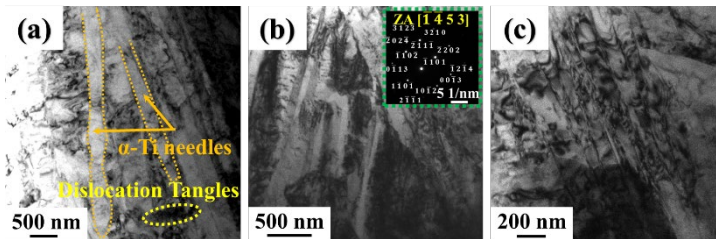


Figure 3.5. Transmission electron microscopy (TEM) images showing the detailed microstructure (a) bright-field TEM image revealing α -titanium (Ti) needle-like features and regions of dislocation tangles, (b,c) higher magnification TEM images illustrating the distribution of α -Ti needles and associated dislocation structures, the inset in (b) shows the indexed selected area electron diffraction pattern.

The α' laths align preferentially along specific crystallographic planes, consistent with the diffusionless $\beta \rightarrow \alpha'$ transformation widely observed in Ti64. SADP patterns along the $[\bar{1}453]$ zone axis confirms the HCP structure, though they cannot clearly distinguish between α and α' due to imaging along a higher-index zone axis, where c/a ratios are difficult to extract. However, TEM images clearly reveal α' martensite morphology. The presence of dark contrast regions and diffuse diffraction intensities indicates localized lattice distortions and significant residual stresses. Additionally, widespread dislocation tangles within martensitic laths suggest a high density of geometrically necessary dislocations (GNDs), generated during rapid solidification and cyclic reheating inherent to SLM. These α' needles hinder dislocation mobility, leading to strain localization via dislocation pileups. While this mechanism contributes to strengthening through Orowan looping, it may also promote crack initiation under cyclic loading or corrosive environments.

3.3 Mechanical behavior of Ti64 alloy

The mechanical behavior of the developed composites was characterized using hardness, tensile, and compressive tests conducted according to ASTM standards. The SLM specimens exhibited higher hardness values ($412 \pm 17 \text{ HV}_{0.1}$) as compared to its SPS counterpart ($361 \pm 20 \text{ HV}_{0.1}$). Similarly, SLM samples achieved superior strength, with CYS of $1428 \pm 5.5 \text{ MPa}$ and ultimate compressive strength (UCS) of $1828 \pm 13 \text{ MPa}$ as shown in Figure 3.6-(a). In contrast, SPS samples showed lower CYS ($946 \pm 5.3 \text{ MPa}$) and UCS ($1732 \pm 68 \text{ MPa}$). Although SLM demonstrated higher strength, SPS specimens exhibited greater plastic deformation before failure. The calculated values of mechanical properties are presented in Table 3.1.

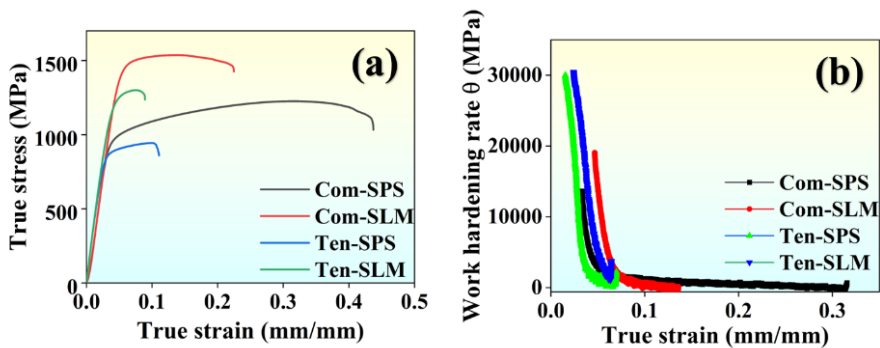


Figure 3.6. (a) True tensile/compressive stress-strain curves, and (b) corresponding strain hardening rate plot for Ti6Al4V samples fabricated by spark plasma sintering and selective laser melting.

The UCS and UTS values obtained for SLM samples are consistent with earlier reports by Gupta et al. [130] and Sabban et al. [131]. Microstructural differences, particularly the refinement of α' martensitic laths and slight compositional variations, account for these trends. Galarraga et al. [123] noted that an increase in finer α' laths enhances alloy strength, in accordance with the Hall-Petch relationship. However, the dense arrangement of α' laths in SLM Ti64 restricted ductility, as rapid solidification introduces significant internal strain and limits dislocation slip within differently oriented laths [130]. In contrast, SPS samples displayed enhanced plasticity. This is attributed to the decomposition of metastable α' into equilibrium α and β phases during high-temperature sintering at $1200 \text{ }^\circ\text{C}$ [132]. Vanadium diffusion during slow cooling promotes α lath coarsening, reducing internal stresses and facilitating greater plastic deformation.

Strain hardening behavior under compressive and tensile loading is shown in Figure 3.6-(b). For compression, SPS specimens exhibited a higher strain hardening rate compared to SLM. However, the SPS sample also showed a sharper decline in hardening (faster softening), while SLM maintained a slightly extended curve, suggesting greater resistance to softening. Under tensile loading, both samples showed comparable strain hardening trends, but at higher strains, the SPS specimens softened more rapidly than their SLM counterparts. This trend is consistent with the observations from compression tests.

Table 3.1. Mechanical properties of sintered and additively manufactured Ti6Al4V samples.

Samples	Hardness (HV)	CYS (MPa) σ_{yc}	UCS (MPa)	TYS (MPa) σ_{yt}	UTS (MPa)	Fracture strain (%)	σ_{yt}/σ_{yc}
SPS	361±20	946±5.3	1732±68	520±7	865±20	34±1	0.54
SLM	412±17	1428±5.5	1828±13	799±6	1211±12	12±2	0.55

3.4 Fractography of fractured Ti64 samples

Tensile and compressive fracture morphologies of SPS and SLM samples are shown in Figure 3.7 and Figure 3.8, respectively. The SPS specimens display a quasi-ductile failure mode, characterized by surfaces with large dimples, reflecting a mixed fracture mechanism involving both ductile and intergranular brittle features. This fracture behavior explains the significant elongation observed during tensile testing (Figure 3.7-(a-d)). However, the SLM samples (Figure 3.7-(e-h)) exhibit a distinctly different profile, with rough fracture surfaces at the center and relatively flat regions along the edges. Shallow dimples were observed near the edge regions (Figure 3.7-(h)). Secondary cracks are visible on the fracture surface (Figure 3.7-(f)), likely originating from the coalescence of pre-existing pores under increasing stress [133]. Moreover, step-like fracture features (Figure 3.7-(g)) suggest crack propagation across differently oriented laths. These observations are consistent with the mechanical property data reported in Table 3.1. Overall, the SLM samples reveal dominant brittle fracture characteristics with limited plasticity, whereas the SPS samples demonstrate a more typical ductile fracture mode, in agreement with earlier reports. A similar trend was evident in the compressive fracture surfaces, as shown in Figure 3.8-(a-f).

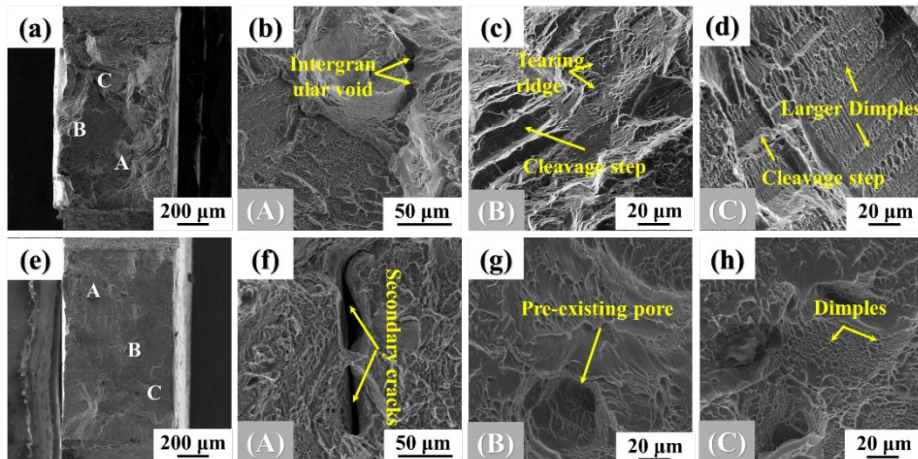


Figure 3.7. Scanning electron microscopy images of fractured tensile samples of (a-d) spark plasma sintered, and (e-h) selective laser melted Ti6Al4V samples at different locations (A, B, and C).

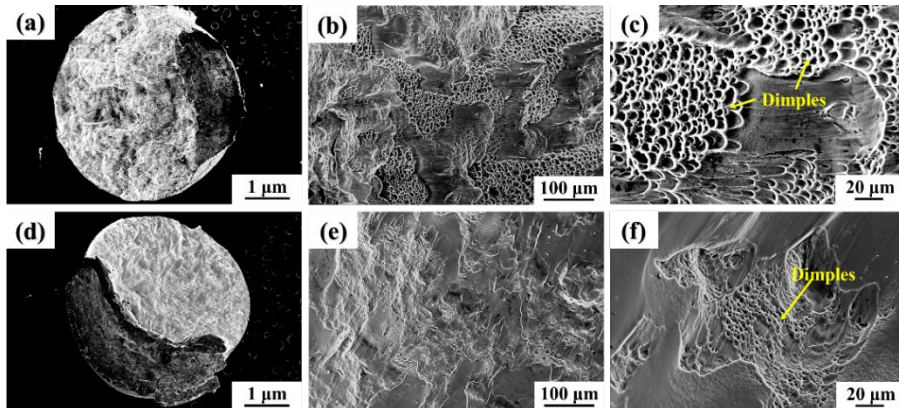


Figure 3.8. Scanning electron microscopy images of fractured compression samples of (a-c) spark plasma sintered, and (d-f) selective laser melted Ti6Al4V samples at different magnifications.

3.5 Cytocompatibility assessment of Ti64 alloy

The cytocompatibility of SPS and SLM samples was assessed by culturing MC3T3-E1 cells for 1, 3, and 5 days, as shown in Figure 3.9. Cell proliferation was quantified through the RGR. Both materials demonstrated >80% cell viability across all time points, confirming good cytocompatibility in accordance with ISO 10993-5 [134]. The SLM samples, used as the control due to their extensive prior evaluation [130], showed a slightly higher RGR compared to the SPS specimens.

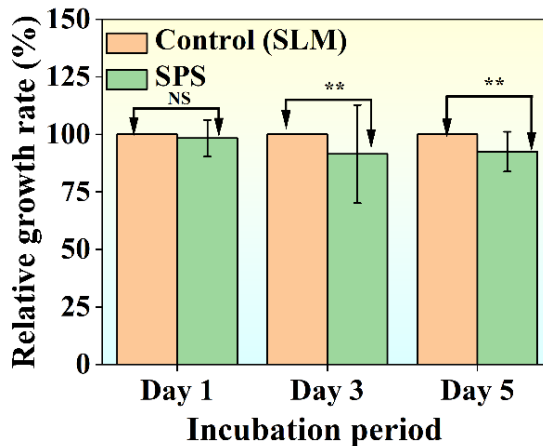


Figure 3.9. Relative growth rate measured by water-soluble tetrazolium assay for MC3T3-E1 cells cultured on Ti6Al4V (Ti64) samples for 1, 3, and 5 days. Selective laser melted Ti64 samples were taken as the control for each day. The significance level is taken as $p=0.05$, i.e., $p<0.05$ (*), $p<0.01$ (**), $p<0.001$ (***), $p<0.0001$ (****) and $p>0.05$, non-significant (ns), $n=4$.

This improved cell response in AM samples can be associated with their finer-grain microstructure, as discussed earlier. Grain refinement is well known to influence surface

properties, particularly hydrophilicity, which enhances protein adsorption and cell attachment. In this study, AM Ti64 exhibited a more hydrophilic surface than SPS Ti64, contributing to better osteoblast adhesion and proliferation. These findings are consistent with Medvedev et al. [135], who reported superior osteogenic performance in ultrafine-grained Ti compared to coarse-grained Ti, and Tong et al. [136], who demonstrated enhanced cytocompatibility in β Ti alloys after microstructural refinement.

Fluorescence microscopy images of both conditions (Figure 3.10) confirm these results. At day 1, cells were uniformly attached to both surfaces, but by days 3 and 5, cell density was markedly higher on AM Ti64, reaching full confluence earlier than on SPS.

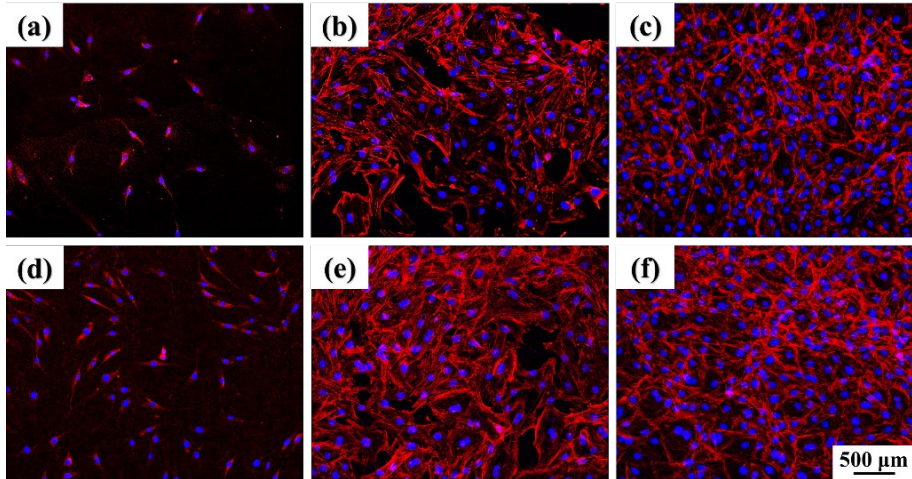


Figure 3.10. Fluorescence images of MC3T3-E1 cells cultured on Ti6Al4V samples after 1, 3, and 5 days of incubation, showing actin filaments (red) and nuclei (blue). (a-c) Cells cultured on spark plasma sintered samples and (d-f) cells cultured on selective laser melted samples, (a,d) correspond to day 1, (b,e) correspond to day 3, and (c,f) correspond to day 5.

Further evidence is provided by SEM micrographs of cell adhesion (Figure 3.11). On day 1, cells on both surfaces appeared rounded with limited spreading. By day 3, cells exhibited elongated morphologies with extended filopodia, forming interconnected networks that became more pronounced by day 5, particularly on the AM samples. This enhanced spreading suggests a more favorable microenvironment for osteoblast proliferation, likely arising from the finer grain size and higher surface wettability of the SLM samples. Overall, these findings confirm that SLM-processed Ti64 exhibits superior cytocompatibility compared to SPS-processed Ti64, primarily due to its refined microstructure and enhanced surface characteristics.

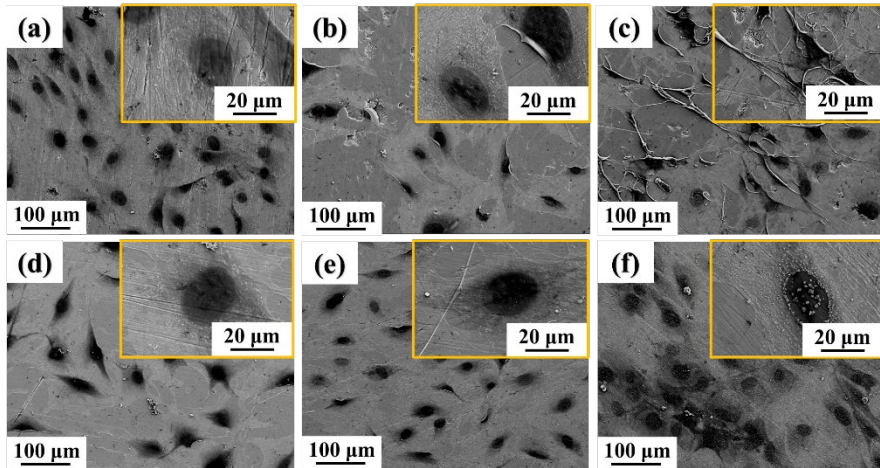


Figure 3.11. Scanning electron microscopy images showing the morphology and attachment of MC3T3-E1 cells cultured on Ti6Al4V samples fabricated by spark plasma sintering (SPS) and selective laser melting (SLM). (a-c) Cells cultured on SPS and (d-f) cells cultured on SLM samples (a,d) correspond to day 1, (b,e) correspond to day 3, and (c,f) correspond to day 5. Insets show higher-magnification views of representative cell-surface interactions.

3.6 Summary

This chapter systematically compared the microstructural, mechanical, and biological responses of Ti64 processed via SPS and SLM. The findings highlight that the processing route strongly dictates the resulting phase constitution, grain morphology, and crystallographic texture, which in turn govern material performance. SLM processing produced a fine α' martensitic microstructure with high dislocation density, resulting in superior hardness and compressive strength but at the expense of ductility due to restricted slip within densely packed laths. In contrast, SPS yielded a lamellar $\alpha+\beta$ structure with coarser grains, which allowed for greater plastic deformation through diffusional transformations and reduced internal stresses. Cytocompatibility studies confirmed that both processing routes produced biocompatible Ti64, with >80% cell viability in accordance with ISO 10993-5. However, SLM samples demonstrated slightly enhanced osteoblast adhesion, proliferation, and spreading, which can be attributed to their finer grain size and greater surface hydrophilicity. Overall, SLM Ti64 exhibited higher strength and better biological response, while SPS Ti64 offered improved ductility. These complementary characteristics underscore the importance of tailoring processing routes to achieve balanced performance, depending on the specific biomedical application.

Overall, the findings highlight the influence of manufacturing routes on the functional performance of Ti64 and establish an important baseline for understanding the behavior of titanium in biomedical applications. However, as discussed earlier, due to the bioinert nature of titanium and its alloys, they remain nondegradable, and their long-term presence in the body may lead to issues such as stress shielding and the need for revision surgeries. Therefore, the subsequent chapter focuses on biodegradable metallic systems, specifically pure Zn processed through SPS and conventional casting. This investigation

aims to understand how different processing routes influence the microstructure, mechanical properties, degradation behavior, and biocompatibility of Zn, thereby providing the necessary foundation for incorporating a degradable phase in the development of hybrid Ti-based multimaterial implant systems explored in the later chapters of this thesis.

4 Spark plasma sintering of biodegradable pure Zn

The objective of this chapter is to investigate the potential of Zn as a biodegradable material and to evaluate the influence of processing routes on its performance. Zn produced through two different processing routes is systematically examined. Particular emphasis is placed on the structure-property relationship by correlating the resulting microstructural features with mechanical properties, degradation behavior, and biological response. This analysis provides a comprehensive understanding of how processing methods influence the structure and functional performance of Zn-based biomaterials. Microstructural evolution and crystallographic characteristics are examined using OM, SEM, and EBSD to understand grain morphology, texture development, and recrystallization behavior. Mechanical performance is evaluated through compressive testing to determine the influence of grain refinement and deformation mechanisms on strength and ductility. In addition, the biodegradation behavior of the materials is investigated through immersion and electrochemical corrosion tests in SBF, providing insights into their degradation kinetics and corrosion mechanisms under physiological conditions. Furthermore, the biological response of Zn is assessed through *in-vitro* cytocompatibility studies to examine the effect of degradation products on cell viability and proliferation. Through these detailed studies, this chapter aims to establish an effective processing route for refining Zn microstructure and tailoring its performance for biomedical applications. The outcomes of this study provide a foundational understanding of Zn behavior and serve as a critical step toward its integration with Ti-based systems for the development of partially biodegradable metallic composites in subsequent chapters.

4.1 Densification of Zn after SPS

The density of the SPS-processed Zn samples was found to be 7.1 g/cm^3 , corresponding to a relative density of 99.4%, indicating near-complete densification of the powder during sintering. Abedi et al. [137] reported that metallic systems typically achieve a more uniform temperature distribution compared to ceramics, which contributes to higher consolidation efficiency. The sintering profile, presented in Figure 4.1 (piston displacement vs. time and temperature vs. time), highlights three distinct stages leading to final densification.

In Stage I, an external pressure of 50 MPa was applied at room temperature, which promoted particle rearrangement and reduction of pore volume. This stage exhibited a significant piston displacement at an average rate of 0.35 mm/min. Stage II corresponded to the heating phase, where rapid temperature rise facilitated plasma generation between powder particles, surface cleaning, and thermally activated densification [138]. During this stage, the piston displacement decreased to 0.1 mm/min as the temperature increased from 50 °C to 300 °C at a rate of 50 °C/min, followed by a 10 min dwell, enabling grain boundary diffusion, neck formation, and pore closure. Finally, Stage III involved cooling from 300 °C to 50 °C at the same rate (50 °C/min). The piston displacement further decreased to 0.01 mm/min, which was attributed to thermal shrinkage of the compact rather than densification [139].

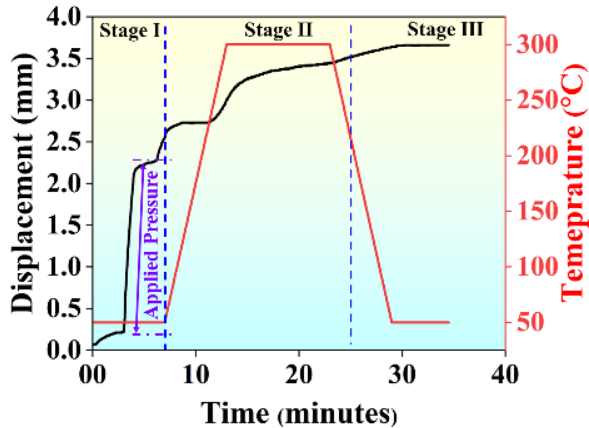


Figure 4.1. Plot showing the spark plasma sintering cycles observed due to piston displacement and temperature as a function of time for the zinc samples. Reproduced with permission from [120].

4.2 Phase analysis of Zn

Figure 4.2 presents the XRD patterns of pure Zn powder and SPS-processed samples. Both patterns reveal a single-phase microstructure with peaks corresponding to the hcp crystal structure, and no additional peaks are detected within measurable limits, confirming the absence of oxide formation during sintering. For Zn powder, the highest intensity peak appears at $(10\bar{1}1)$, whereas for the bulk samples, the dominant peak is observed at (0002) . This shift in peak intensity indicates the development of preferred orientation, where crystallites in a polycrystalline material tend to align along specific crystallographic planes during processing [140–142].

In SPS, the combined effect of high temperature and applied pressure promotes particle bonding and densification, during which crystallites may reorient in a particular direction. Factors such as sintering parameters, particle morphology, applied stress, and cooling rate significantly influence this orientation. A similar phenomenon occurs during casting, where solidification conditions and cooling rates dictate the crystallographic alignment of newly formed grains. For hcp metals, preferred orientation is closely linked to the c/a ratio; in the case of Zn, which has a c/a ratio greater than 1.633, the basal plane $[0002]$ tends to align parallel to the sample surface or mold wall [143].

4.3 Microstructural characterization of Zn

The surface morphology of both as-cast and SPS-processed Zn samples was examined using optical microscopy and SEM, as shown in Figure 4.3. The as-cast samples (Figure 4.3-(a,b)) reveal a heterogeneous microstructure with a noticeable presence of twins (highlighted by yellow arrows). Additionally, regions of fine grains embedded within larger grains (red arrows) suggest localized recrystallization. However, the SPS samples shown in Figure 4.3-(c,d) exhibit a well-consolidated microstructure free from visible defects such as pores or cracks at the observed magnification. This indicates that the SPS samples approached near-theoretical density ($\rho \approx 7.1 \text{ g/cm}^3$). The enhanced densification

achieved during SPS is attributed to the combined effects of pressure and temperature, which promote plastic deformation of powder particles. As noted by Chaim et al. [144], once the applied stress surpasses the yield strength, densification is facilitated through plastic deformation. Particle size plays a crucial role in this process, as larger particles undergo deformation under applied pressure, while smaller ones may locally melt or evaporate [145]. The resulting microstructure shows a relatively uniform arrangement of large equiaxed grains, with occasional finer grains and subgrain boundaries within them [146].

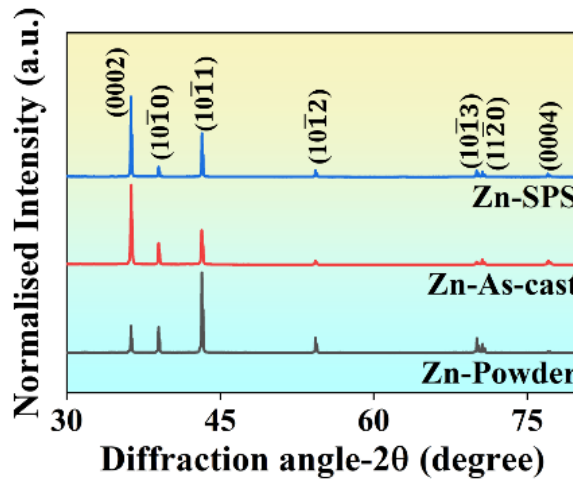


Figure 4.2. X-ray diffraction patterns for the as-received zinc (Zn) powder and the bulk Zn samples fabricated by casting and spark plasma sintering processes. Reproduced with permission from [120].

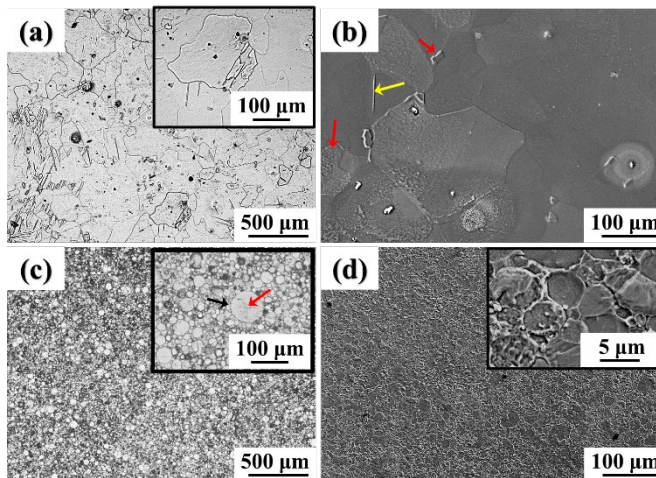


Figure 4.3. Microstructural comparison of zinc (Zn) samples fabricated by different processing routes (a,c) optical, and (b,d) scanning electron microscopy images of the Zn samples fabricated by (a,b) casting, and (c,d) spark plasma sintering processes. Reproduced with permission from [120].

To further investigate crystallographic orientation and grain boundary distribution, EBSD analysis was performed (Figure 4.4-(a-f)). The IPF maps confirm that most grains in SPS samples are red-colored, indicating that their c-axes are aligned nearly perpendicular to the sample surface, with basal planes {0001} lying parallel to the surface. The image quality (IQ) maps with superimposed grain boundaries (Figure 4.4-(b,e)) differentiate high-angle grain boundaries (HAGBs, $>15^\circ$, marked in blue) from LAGBs ($<15^\circ$, marked in red and green). The as-cast samples contain approximately 33% LAGBs, whereas SPS samples exhibit a reduced fraction of 15%, mainly confined to sub-grain structures within larger grains. Fine-grain regions in the SPS samples are dominated by HAGBs, likely due to strain accumulation. The SPS-processed Zn shows a refined grain size ($19\ \mu\text{m}$) compared to the as-cast material ($150\ \mu\text{m}$). The increase in HAGBs and the development of fine grains suggest dynamic recrystallization, promoted by the concurrent action of heat and applied pressure during SPS. This results in a bimodal grain structure composed of both coarse and fine grains. In contrast, the as-cast Zn retains predominantly coarse grains with extensive twinning. These observations highlight how the differences in processing routes, casting versus SPS, govern microstructural evolution. SPS enables grain refinement and recrystallization, while casting preserves a coarser microstructure with twinning features.

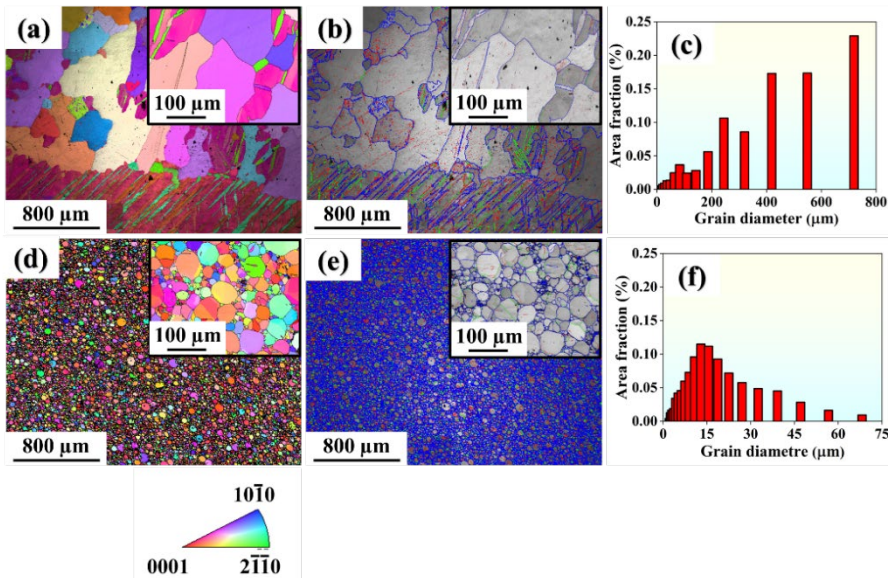


Figure 4.4. Electron backscattered maps of zinc processed by (a-c) casting, and (d-f) spark plasma sintering, showing the (a,d) inverse pole figure maps, (b,e) image quality maps, and (c,f) grain size distribution plot. Reproduced with permission from [120].

4.4 Mechanical behavior of Zn

Figure 4.5 presents the compressive stress-strain and strain-hardening responses of as-cast and SPS-processed Zn. The SPS samples exhibited a significantly higher yield strength (0.2% offset, $115\pm 4\ \text{MPa}$) compared to the as-cast samples ($60\pm 16\ \text{MPa}$). In contrast, the ultimate compressive strength (UCS) was higher for the as-cast Zn ($274\pm 37\ \text{MPa}$) than for SPS samples ($191\pm 6\ \text{MPa}$). The enhanced yield strength in SPS samples can be attributed

to grain refinement during sintering, where micron and submicron-sized grains are formed. This trend is consistent with the Hall-Petch relationship as shown in Eq. 4.1.

$$\sigma_y = \sigma_0 + kd^{-1/2} \quad (\text{Eq. 4.1})$$

$$\sigma_y \propto d^{-1/2}$$

where σ_y is the yield strength of the materials, σ_0 is the lattice friction stress, k is the Hall-Petch coefficient, and d is the average grain size of the material. Finer grains (19 μm in SPS Zn) increase grain boundary density, impeding dislocation motion and raising yield strength, while coarse grains (150 μm in as-cast Zn) allow easier dislocation glide, resulting in lower yield strength. However, the opposite trend was observed for UCS. The numerous grain boundaries in SPS Zn, while strengthening against yield, also act as potential crack initiation sites, limiting plastic deformation and lowering UCS. Conversely, as-cast Zn, with its coarse grains and strong basal texture, facilitates twinning as a major deformation mechanism [120]. Twinning accommodates additional strain at higher stresses, thereby enhancing UCS [147]. In SPS Zn, recrystallization suppresses twin activity due to the obstruction imposed by grain boundaries [148]. As a result, deformation is mainly carried by dislocation slip, producing higher yield strength but reduced strain hardening and ultimate strength. Macroscopically, SPS samples displayed uniform bulging after compression, whereas as-cast samples exhibited irregular deformation (Figure 4.5-(a) inset). Bulging corresponds to more homogeneous energy absorption with reduced twin activity. The strain-hardening plots (Figure 4.5-(b)) reveal that SPS samples show a rapid decline in hardening rate with strain, while as-cast Zn maintains a plateau, reflecting extended strain hardening capacity associated with its coarse-grained structure and active twinning.

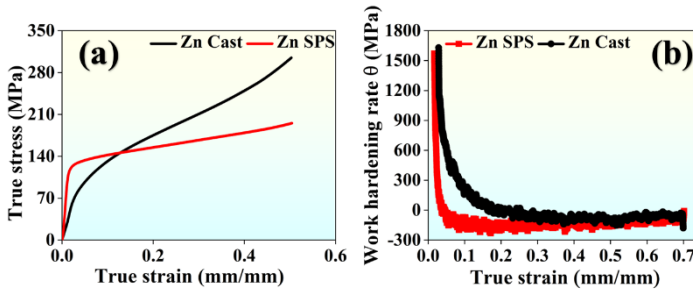


Figure 4.5. (a) True compressive stress-strain curves, and (b) corresponding strain hardening rate plot for zinc samples fabricated by casting and spark plasma sintering. Reproduced with permission from [120].

4.5 *In-vitro* biodegradation analysis of Zn

The *in-vitro* degradation response of the as-cast and SPS-processed Zn samples was evaluated following ASTM G31-72 standard. Polished samples were immersed in SBF under physiological conditions for 7, 14, and 21 days. In the first 7 days, the SPS Zn surface developed a thin and uniform whitish layer, which progressively thickened with time, accompanied by the uneven accumulation of corrosion products, as shown in Figure 4.6. After 7 days of immersion, SPS Zn exhibited a degradation rate of 0.1325 mm/year, which aligns with previously reported values [149]. At longer exposure periods of 14 and 21 days, the rates decreased to 0.0965 mm/year and 0.075 mm/year, respectively. This reduction in degradation rate is associated with the progressive growth

of a stable protective layer that limits ion exchange between the alloy surface and the surrounding medium. In the early stages, however, the initially fragile oxide layer was prone to localized breakdown, resulting in the formation of surface voids and promoting further degradation.

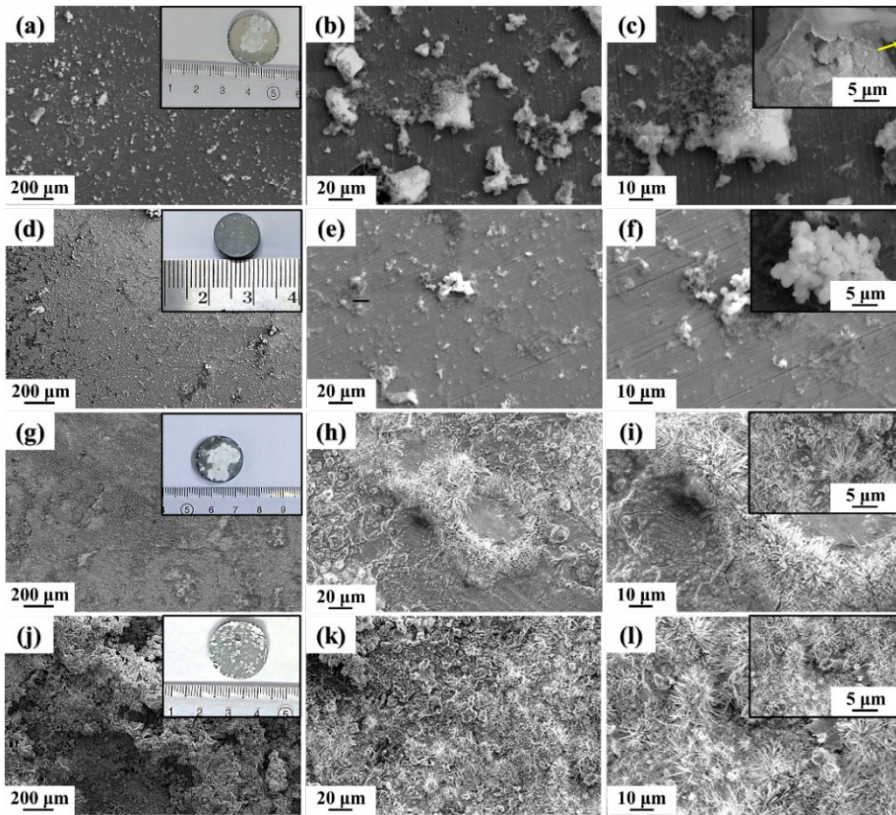


Figure 4.6. Scanning electron microscopy images of zinc samples after immersion in simulated body fluid for 7 and 21 days. (a-c) correspond to the as-cast samples after 7 days of immersion, while (g-i) represent the as-cast samples after 21 days, (d-f) correspond to the spark plasma sintered samples after 7 days, and (j-l) 21 days of immersion, respectively. Insets show macroscopic views of the immersed specimens along with localized high-magnification details of the corroded surface. Reproduced with permission from [120].

4.6 Electrochemical corrosion analysis of Zn

Figure 4.7 presents the PDP curves of the Zn samples. Corrosion parameters, including corrosion current density (I_{corr}) and corrosion potential (E_{corr}), were determined using the Tafel extrapolation method [150–152], and the results are summarized in Table 4.1. The E_{corr} values of the as-cast and SPS samples are comparable, though more negative than the open circuit potential (OCP) values. This difference arises because OCP reflects the equilibrium state without an external current, while Tafel measurements are recorded after the samples have been exposed to SBF, where Zn interacts with chloride ions, accelerating degradation and lowering the potential.

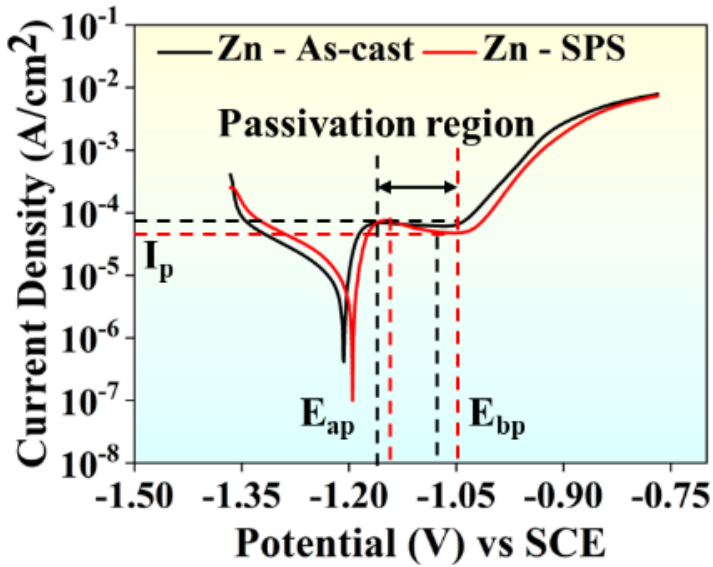


Figure 4.7. Potentiodynamic polarization curves of as-cast zinc, and spark plasma sintered samples obtained after immersion in simulated body fluid for 1 hour. Reproduced with permission from [120].

The anodic polarization behavior indicates an active-to-passive transition for both samples in SBF. Initially, Zn undergoes active dissolution, after which a passive film forms, stabilizing the current density within the passive region (Figure 4.7). Once the breakdown potential (E_{bp}) is reached, the current density rises sharply, signaling transpassive corrosion. From the Tafel curves, values of I_{corr} , E_{corr} , I_p (passivation current density), E_{pp} (passivation potential), and corrosion rate (CR) were extracted (Table 4.1). Both as-cast and SPS Zn samples displayed similar cathodic polarization behavior, with E_{corr} values of -1.21 and -1.20 V and I_{corr} values of 8.61 and 12.16 $\mu\text{A}/\text{cm}^2$, respectively. Upon increasing potential, a stable passive layer formed, with passivation potentials (E_{ap}) of -1.16 and -1.15 V and passivation current densities (I_p) of 62.0 and 52.9 $\mu\text{A}/\text{cm}^2$ for the as-cast and SPS samples, respectively. The lower I_p value for SPS Zn suggests improved corrosion resistance compared to the as-cast sample. At higher potentials, both samples exhibited a sharp rise in current density, with E_{bp} of -1.06 V for the as-cast Zn and -1.03 V for the SPS Zn, indicating passive film breakdown.

The observed variation in E_{corr} can be primarily attributed to differences in grain size. SPS Zn exhibited a finer grain size compared to the much coarser grains in the as-cast condition, resulting in a higher density of grain boundaries per unit volume. Since grain boundaries possess higher energy and often differ chemically from the bulk, they are more vulnerable to corrosion. The presence of finer grains also enhances hydrophilicity, accelerates diffusion, and promotes deeper electrolyte penetration, which can cause localized pitting, as seen in the SEM micrographs in Figure 4.8.

Table 4.1. Polarization data for the as-cast and spark plasma sintered zinc samples immersed in simulated body fluid [120].

Sample condition	E_{corr} (V) vs SCE	I_{corr} ($\mu\text{A}/\text{cm}^2$)	I_p ($\mu\text{A}/\text{cm}^2$)	E_{pp} (V) vs SCE	E_{bp} (V) vs SCE	CR (mm/year) $\times 10^{-4}$
As-cast	- 1.21 ± 0.02	8.61 ± 0.11 1	62.0 ± 3.1	- 1.16 ± 0.025	- 1.06 ± 0.17	0.60 ± 0.08
SPS	- 1.20 ± 0.035	12.16 ± 0.9 9	52.9 ± 1.2	- 1.15 ± 0.032	- 1.03 ± 0.23	0.88 ± 0.05

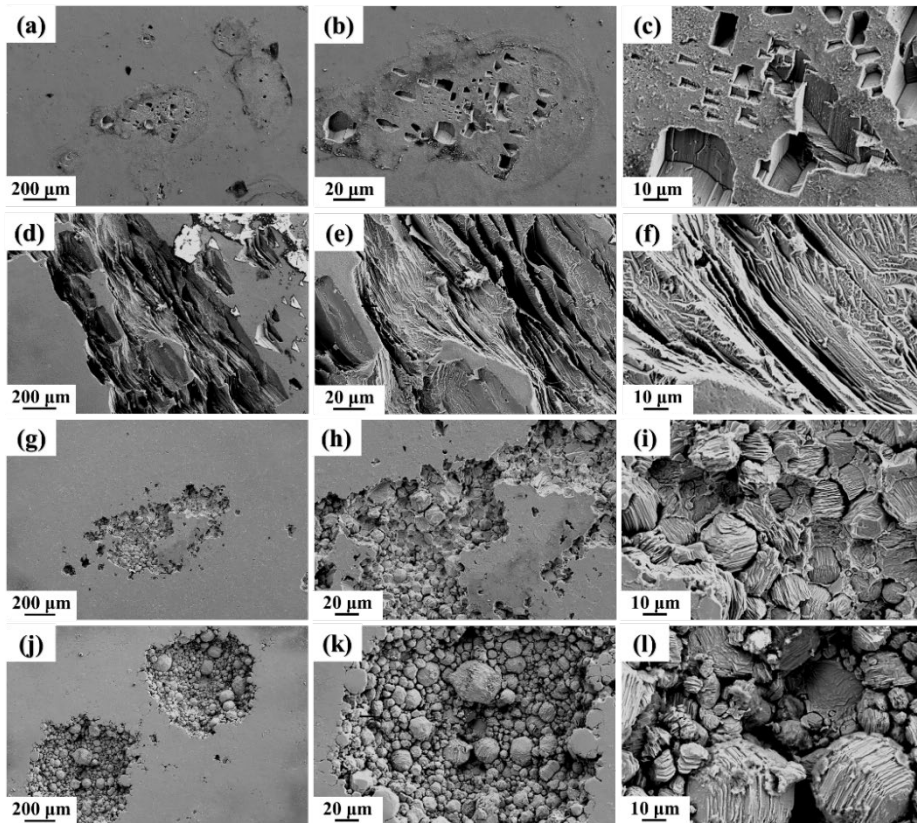


Figure 4.8. Scanning electron microscopy images after 1 and 24 hours of potentiodynamic polarization in simulated body fluid, (a-f) correspond to as-cast Zn after (a-c) 1 hour, and (d-f) 24 hours of immersion, while (g-l) correspond to spark plasma sintered Zn after (g-i) 1 hour, and (j-l) 24 hours of immersion. Reproduced with permission from [120].

In addition to grain size, crystallographic texture significantly affects corrosion performance. As shown in Figure 4.7, both as-cast and SPS Zn samples exhibit a stable passivation layer within the potential range of -1.15 V to -1.05 V. Beyond this range, passive film breakdown occurs, exposing the underlying material to the electrolyte and increasing corrosion susceptibility. While SPS Zn demonstrates improved passivation due

to fine grains, the higher density of grain boundaries also accelerates localized corrosion, leading to an overall higher corrosion rate compared to as-cast Zn.

Figure 4.8 and Figure 4.9 present the SEM and EDS, respectively, for corroded Zn samples after immersion in SBF for 1 h and 24 h. After 1 h of polarization, localized corrosion in the form of pits was observed on both samples. The as-cast Zn exhibited a higher density of pits with relatively uniform cross-sections concentrated in specific regions. In contrast, the SPS samples displayed a more widespread corrosion pattern characterized by deeper grooves within the pits (highlighted in the higher-magnification image of Figure 4.8), which can be attributed to the higher density of grain boundaries. The SEM images indicate that corrosion preferentially initiated along grain boundaries, likely due to their higher reactivity. These boundary regions act as micro-galvanic sites, enhancing electron transfer and making them more prone to localized attack. While both as-cast and SPS Zn showed similar electrochemical responses, their corrosion morphologies differed, reflecting variations in grain structure.

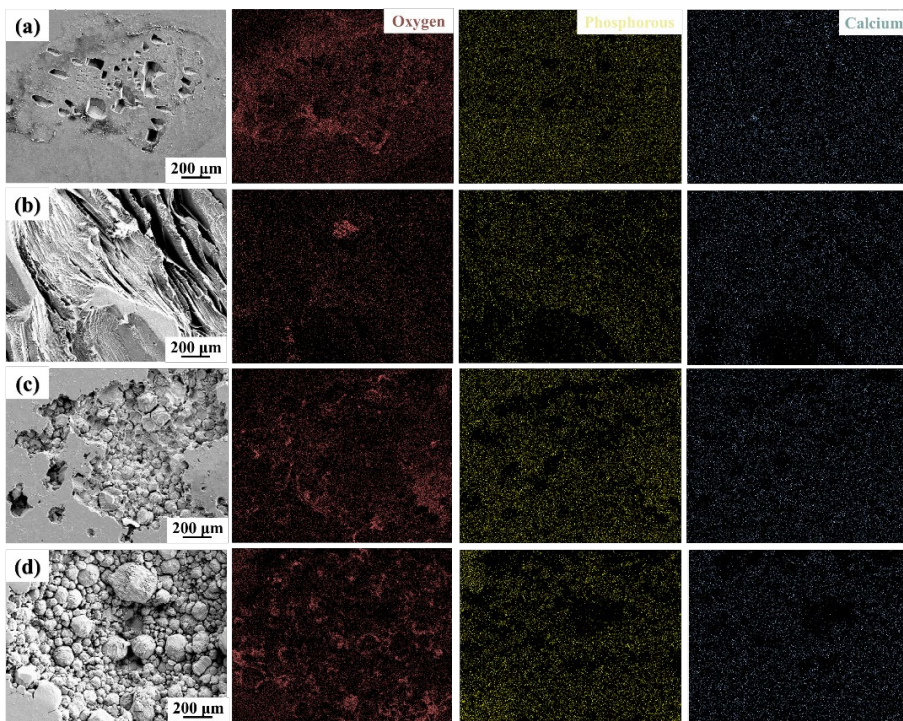


Figure 4.9. Energy-dispersive spectroscopy mapping of zinc (Zn) samples after potentiodynamic polarization, (a,b) corresponds to as-cast Zn, while (c,d) corresponds to spark plasma sintered Zn. Reproduced with permission from [120].

4.7 Cytocompatibility assessment of Zn

The cytocompatibility of the Zn samples was assessed using an indirect approach, in which cells were cultured in conditioned media containing the degradation products of the material. The cellular response of MC3T3-E1 pre-osteoblasts was quantified in terms of relative growth rate (RGR) after exposure to the conditioned medium for 1 day and 3 days, while cells maintained in fresh culture medium were used as the control. The

viability of cells cultured in undiluted (1x, 100%) and diluted (8x, 12.5%) conditioned media for both incubation periods is presented in Figure 4.10. Figure 4.10-(a) shows the proliferation behavior of cells exposed to 24 h and 72 h conditioned media after 1 day of incubation. Upon eightfold dilution, no cytotoxic effects were observed, and both samples exhibited comparable cell growth rates, consistent with previous findings [153]. In contrast, cells cultured in the undiluted 72 h conditioned medium showed reduced compatibility, whereas favourable cellular responses were maintained in the diluted extracts. Figure 4.10-(b) illustrates cell proliferation after 3 days of incubation. A marked reduction in RGR was observed for cells exposed to the undiluted conditioned media for both 24 h and 72 h extraction periods. However, no toxicity was detected in the eightfold diluted conditioned media, and the corresponding cell growth rates were comparable to those of the control for both extraction durations.

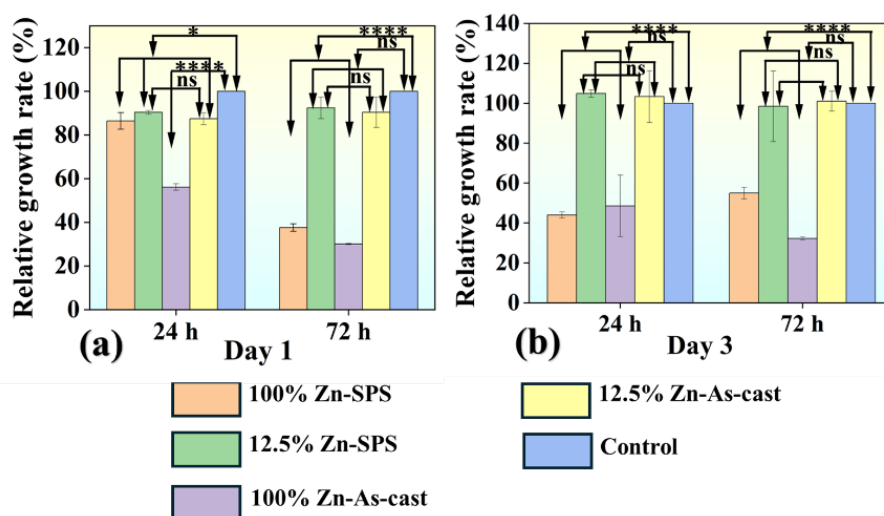


Figure 4.10. Relative growth rate measured by water-soluble tetrazolium assay for MC3T3-E1 cells cultured for 24 hours, and 72 hours conditioned media for (a) 1 day, and (b) 3 days. Cells in fresh medium were taken as the control for each day. The significance level is taken as $p=0.05$, i.e., $p<0.05$ (*), $p<0.01$ (**), $p<0.001$ (***) and $p<0.0001$ (****) and $p>0.05$, non-significant (ns), $n=4$. Reproduced with permission from [120].

A live-dead assay was conducted to further assess the cytotoxic effects induced by the leachates released from the samples. The results of the live-dead staining are presented in Figure 4.11, where viable cells are indicated by green fluorescence and non-viable cells by red fluorescence. For both samples, the eightfold diluted conditioned media exhibited only a small number of dead cells on both day 1 and day 3, indicating good cytocompatibility. In addition, a noticeable increase in cell number was observed on day 3 compared to day 1, demonstrating sustained cell proliferation. In contrast, when cells were exposed to undiluted (100%) conditioned media, a large fraction of cells detached following cell death, which is consistent with the observations from the WST assay.

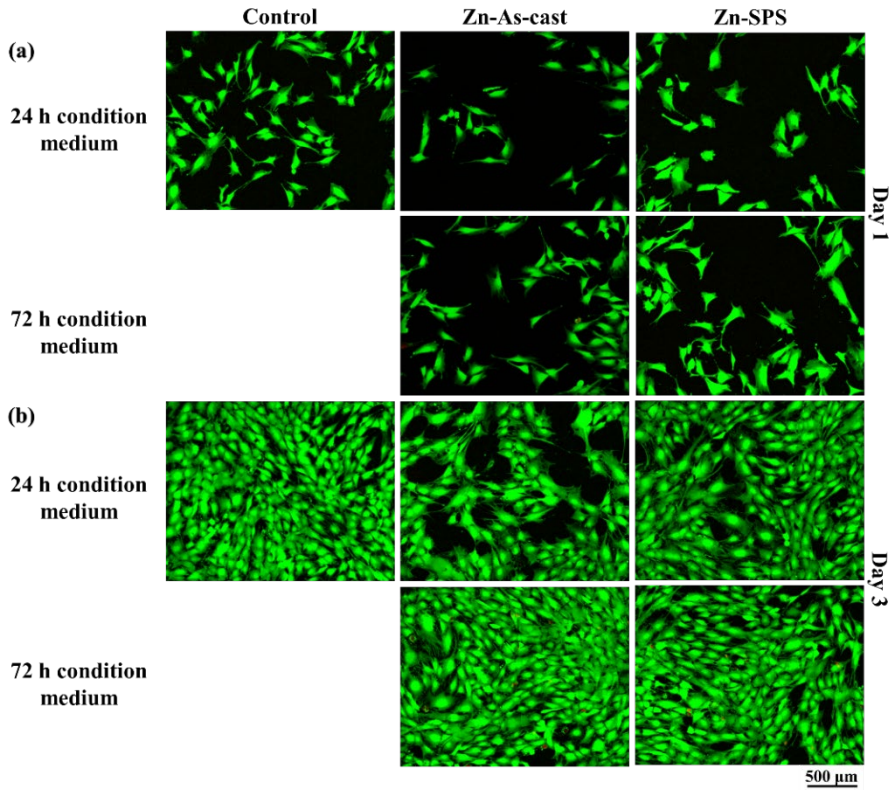


Figure 4.11. Live-dead stained images of MC3T3-E1 cells treated with conditioned medium (8x) of as-cast and spark plasma sintered samples after (a) 1, and (b) 3 days of incubation. Live cells are depicted in green, while dead cells are in red. Cells cultured in fresh complete media served as the control. Reproduced with permission from [120].

Cellular morphology was further examined using fluorescence microscopy, and representative images obtained after 1 and 3 days of incubation in conditioned media are shown in Figure 4.12. Cells cultured in the eightfold diluted conditioned media displayed well-developed morphology with uniformly distributed and organized actin filaments.

In both samples, the cells exhibited good spreading behavior comparable to that of the control group, further confirming the non-toxic nature of the eightfold dilution. However, cells exposed to the undiluted conditioned media in both cases showed stressed and compromised morphology. Based on these observations, it can be concluded that both SPS-processed and as-cast Zn samples demonstrate comparable and favourable cytocompatibility. At eightfold dilution, no cytotoxic effects were detected, with healthy cell proliferation and morphology similar to the control, whereas the undiluted extracts resulted in reduced cell viability and stressed cellular features. These results indicate that both SPS and as-cast Zn are suitable for potential biomedical applications when appropriately diluted.

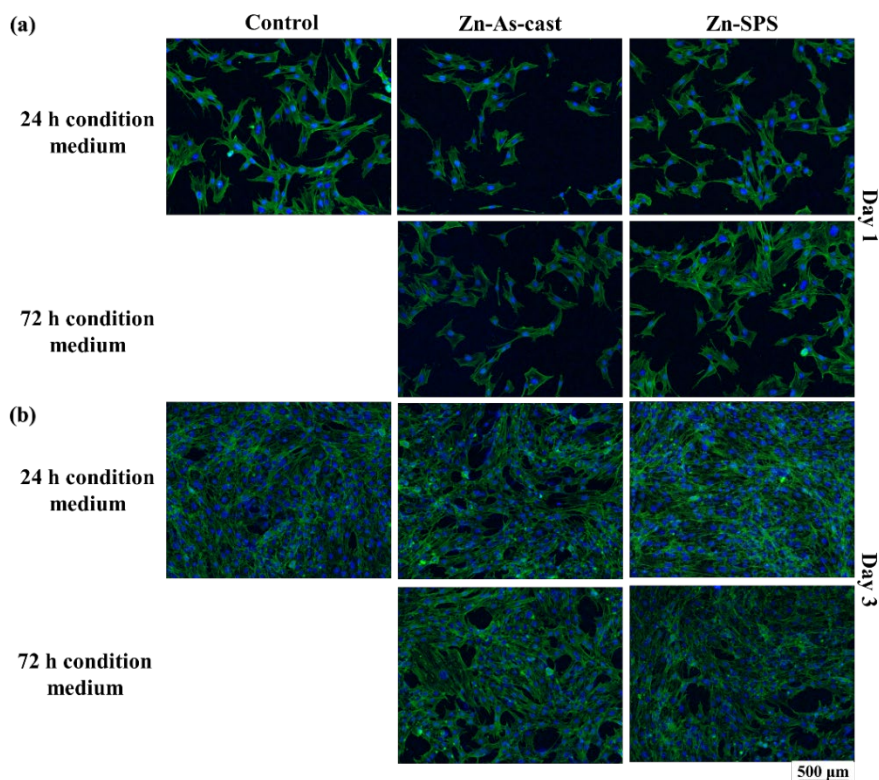


Figure 4.12. Fluorescent images of MC3T3 cells treated with conditioned media after (a) 1 and (b) 3 days of incubation, showing actin filaments (green) and nuclei (blue). The control represents cells treated with fresh complete medium. Reproduced with permission from [120].

4.8 Summary

The current chapter systematically compared SPS Zn with conventionally cast Zn in terms of microstructure, mechanical, corrosion, and biological behavior. SPS processing refined the grain size, reduced texture intensity, and significantly enhanced CYS, though the ultimate strength was lower than that of cast Zn. Corrosion analysis revealed that SPS Zn exhibited a stable and gradual degradation profile in SBF due to the formation of a protective corrosion layer, while cytocompatibility tests confirmed that both SPS and cast Zn supported cell viability and proliferation, especially at diluted extract concentrations.

Overall, the results demonstrate that SPS is an effective processing route for tailoring the microstructure and degradation characteristics of Zn, making it a promising biodegradable metallic material for implant and tissue engineering applications. However, while Zn offers controlled biodegradation, its relatively limited mechanical strength restricts its direct use in load-bearing implants. Therefore, combining Zn with a mechanically stable metallic framework offers a promising pathway to achieve both structural integrity and controlled biodegradation. In this context, the following chapter investigates the feasibility of hybrid manufacturing approaches for integrating different metallic material systems, establishing the foundation for developing multimaterial architectures through combined AM and PM routes.

5 Development of novel partially biodegradable Ti64-Zn MBMC by a hybrid manufacturing approach

This chapter focuses on the development of a novel Ti64-Zn MBMC system that combines the structural stability of Ti64 with the controlled biodegradability of Zn. Prior studies have demonstrated that hybrid manufacturing approaches integrating AM and PM can successfully produce metallic multimaterials using a variety of precursor systems [154]. Hexagonal lattices fabricated from Ti64 and 316L SS have been effectively infiltrated with secondary metallic phases like Mg, Al, Fe, Ni, and Cu. The resulting composite is structurally stable with well-defined phase distribution and minimal interfacial reactions [154].

Building on this framework, the present chapter introduces a strengthening strategy by integrating a Ti64 framework with Zn to fabricate a partially degradable Ti64-Zn MBMC. The design concept follows the principle of IPCs, where a Ti64 honeycomb lattice with continuous wall architecture was engineered to infiltrate Zn within its individual continuous network. The continuous wall architecture was chosen to maintain structural stability while effectively retaining Zn inside the composite. Inspired by natural honeycomb structures, this biomimetic geometry was adopted for its remarkable strength-to-weight ratio, excellent energy absorption capacity, and superior mechanical stability. The interconnected hexagonal arrangement enhances load distribution, improves impact resistance, and minimizes material consumption while maintaining high integrity. By combining the biocompatibility and mechanical robustness of Ti64 with the biodegradable nature of Zn, the developed MBMC aims to achieve a balance between mechanical reliability and controlled degradation, offering a promising pathway toward next-generation biodegradable metallic implants.

5.1 Phase and microstructural analysis of Ti64-Zn MBMC

Figure 5.1 displays the XRD patterns of SPS-processed Zn, SLM-processed Ti64 hexagonal structures, and the developed Ti64-Zn MBMC, along with their respective feedstock powders (Zn and Ti64). The diffraction peaks of both feedstock powders confirm a single-phase structure, with no evidence of impurities within the detectable limits of XRD. The SLM-fabricated Ti64 lattice exhibits α/α' martensitic phases, a typical outcome of the rapid cooling inherent to the SLM process [155,156]. For the SPS Zn samples, the patterns confirm a single-phase HCP structure without additional peaks, indicating the absence of oxidation or secondary phases during sintering. A shift in peak intensity between Zn powder and SPS Zn is noticeable, which can be attributed to preferred orientation effects, as reported in [120]. In the case of the Ti64-Zn MBMC, the diffraction pattern clearly reveals the coexistence of Zn (HCP) and α/α' Ti phases. The relatively lower peak intensity of Ti in the MBMC compared to the SLM Ti64 structure arises from its smaller volume fraction within the composite. Importantly, no extra peaks associated with intermetallic or secondary compounds are detected, confirming the absence of interfacial reactions and validating that the fabrication process preserved the structural integrity of both phases.

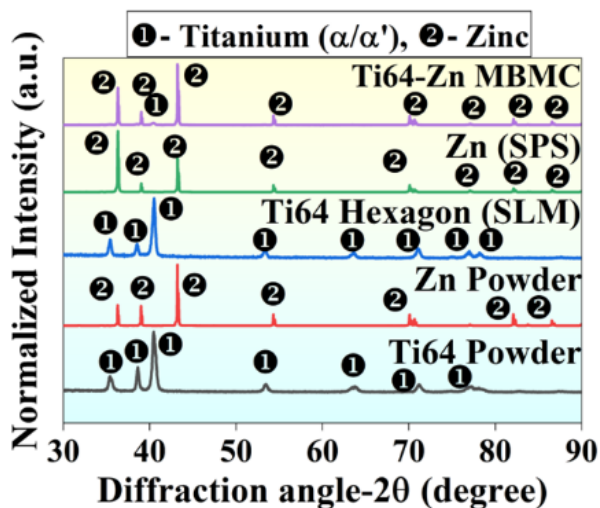


Figure 5.1. X-ray diffraction patterns for the as-received powders, spark plasma sintered zinc (Zn), selective laser melted Ti6Al4V (Ti64) hexagonal lattice, and the Ti64-Zn metallic bimetal composite. Reproduced with permission from [121].

The architecture and phase distribution of the Ti64-Zn MBMC were examined using three-dimensional X-ray tomography (micro-CT), as shown in Figure 5.2-(a,b). The Ti64 architecture, reconstructed by thresholding the Zn sub-volumes, reveals a honeycomb-like interconnected geometry that is consistent with the design intent, despite differences in composition. Quantitative tomography analysis indicated that the bioinspired hexagonal Ti64 phase occupies a volume fraction of $27 \pm 1.5\%$. Based on the rule of mixtures, the theoretical density of the composite was calculated as $6.42 \pm 0.05 \text{ g/cm}^3$, which is in close agreement with the experimentally measured density of $6.63 \pm 0.06 \text{ g/cm}^3$. Furthermore, the 3D reconstructions confirmed that Ti64 and Zn phases are uniformly distributed throughout the structure. These observations strongly validate the classification of the developed MBMC, accurately reflecting its distinctive structural and compositional features.

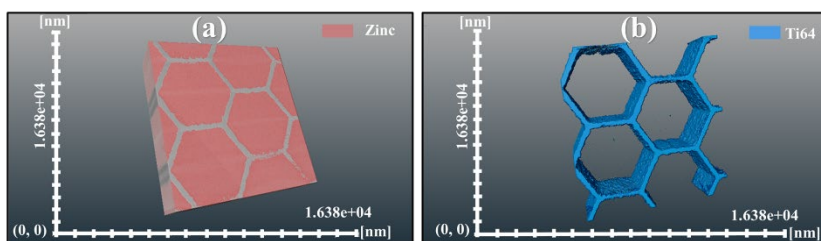


Figure 5.2. Micro computed tomography volume-rendered images of the Ti6Al4V-Zinc (Ti64-Zn) metallic bimetal composite showing (a) Zn distribution and (b) Ti64 hexagonal structure. Reproduced with permission from [121].

The surface morphology and microstructural characteristics of Zn and Ti64 within selected regions of the composite are presented in Figure 5.3 and Figure 5.4. Figure 5.3 shows that the hexagonal Ti64 lattice is uniformly distributed throughout the composite,

preserving its original architecture without notable distortions after SPS, indicating the suitability of the processing parameters for MBMC fabrication. SEM images at different magnifications (Figure 5.3-(a-c)) and EDS maps (Figure 5.3-(d)) reveal well-defined, crack-free and pore-free interfaces between Ti64 and Zn. EDS analysis further confirms the absence of interfacial reactions between the matrix (Zn) and reinforcement (Ti64), consistent with XRD results.

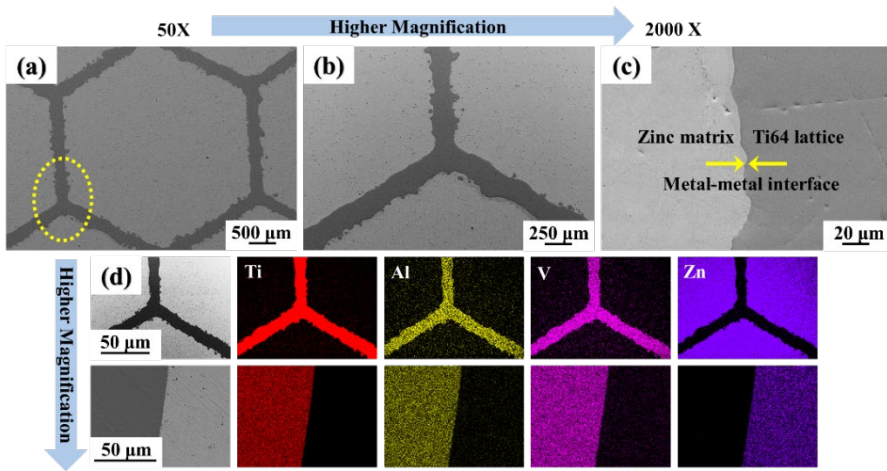


Figure 5.3. Scanning electron microscopy (SEM) images and energy-dispersive spectroscopy (EDS) maps of the Ti6Al4V-zinc (Ti64-Zn) metallic bimetal composite, (a-c) SEM images acquired at different magnifications showing, (a) overview of the composite highlighting different phases, (b) intermediate-magnification image of the triple-junction region, (c) high-magnification view of the metal-metal interface between the Zn matrix and Ti64 lattice, and (d) EDS maps obtained at two magnifications, illustrating the spatial distribution of elements. Reproduced with permission from [121].

EBSD analysis of the MBMC in Figure 5.4 shows that Zn exhibits a bimodal grain structure, comprising coarse circular grains with embedded finer grains, and sub-grain boundaries present within the larger grains. The IPF maps (Figure 5.4-(b,c)) indicate that most grains are red-colored, suggesting that their c-axes are oriented approximately parallel to the specimen normal, with basal planes {0001} nearly aligned with the surface. The Ti64 microstructure (Figure 5.4-(d)) displays a fine acicular α/α' martensitic structure, corroborating the XRD results similar to those reported in Chapter 3. The needle-like martensite forms due to rapid cooling during SLM, facilitating the transformation of prior β phase into α/α' laths following the Burgers orientation relationship [130,157,158]. IPF map in Figure 5.4-(e) shows that the α' laths are randomly oriented, likely a consequence of the rapid thermal gradients and heterogeneous nucleation during SLM [159]. KAM maps reveal higher local misorientations in the SLM Ti64 regions, especially near martensitic interfaces (Figure 5.4-(f)), reflecting increased dislocation density from rapid $\beta \rightarrow \alpha/\alpha'$ transformation [160,161]. In contrast, the SPS-processed Zn exhibits relatively uniform strain distribution within sub-grains (Figure 5.4-(a-c)), indicating that densification was dominated by diffusion and grain boundary sliding rather than dislocation-mediated plasticity. The low KAM values for Zn suggest minimal plastic strain, likely facilitated by the low processing temperature and the material's inherent softness. Quantitatively, SLM Ti64 shows a higher localized strain and dislocation density (KAM \approx

4.96) compared to SPS Zn (KAM \approx 3.1), highlighting the differences in microstructural evolution and strain accumulation between the two processing routes.

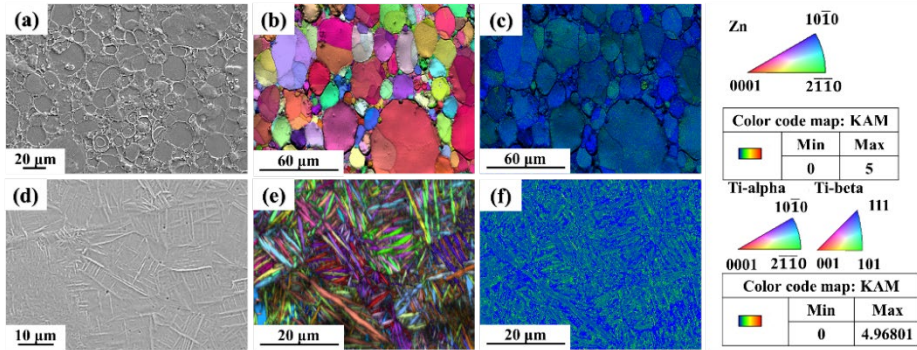


Figure 5.4. Scanning electron microscopy images, and electron backscatter diffraction maps of (a-c) zinc, and (d-f) Ti6Al4V struts. showing the (a,d) microstructure, (b,e) inverse pole figure maps, and (c,f) kernel average misorientation maps. Reproduced with permission from [121].

5.2 Mechanical behavior of Ti64-Zn MBMC

The mechanical behavior of the Ti64-Zn MBMC was assessed using Vickers microhardness and compression testing. Figure 5.5-(a-c) shows the Vickers indentations on Ti64 and Zn regions, along with the corresponding hardness profile and indentation map, highlighting the variation in hardness across different phases of the composite. The Ti-rich areas exhibit an average hardness of 440 ± 10 HV_{0.1}, whereas the Zn-rich regions show a substantially lower hardness of 44 ± 2 HV_{0.1}. The elevated hardness in Ti64 is attributed to the α' Ti martensitic microstructure formed due to rapid solidification during AM. Additionally, the unique spatial arrangement of Ti64 and Zn, coupled with their significant hardness contrast, produces a sinusoidal hardness profile (Figure 5.5-(d)), a distinctive feature of MBMCs fabricated via the combined SPS and SLM processing.

Figure 5.6 presents the compressive engineering stress-strain response of the Ti64-Zn MBMC, alongside SPS Zn and SLM Ti64 hexagonal lattices. Fractured samples are also shown as insets. The Ti64-Zn MBMC exhibits a CYS of 265 ± 25 MPa and an ultimate compressive strength (UCS) of 292 ± 25 MPa, values that are significantly higher than those of SPS Zn and SLM Ti64 lattice, as summarized in Table 5.1. Fractography indicates interfacial cracking between Ti64 and Zn phases, suggesting that crack propagation is influenced by phase partitioning and effective load distribution within the composite. Upon implantation, the biodegradable Zn phase is expected to degrade gradually, causing a progressive reduction in the composite's strength, while the bioinert Ti64 scaffold maintains structural stability. Simultaneously, the formation of pores due to Zn degradation will facilitate osseointegration and bone ingrowth, eventually resulting in a bone-Ti64 interpenetrating network that ensures long-term mechanical support and enhanced implant stability [103].

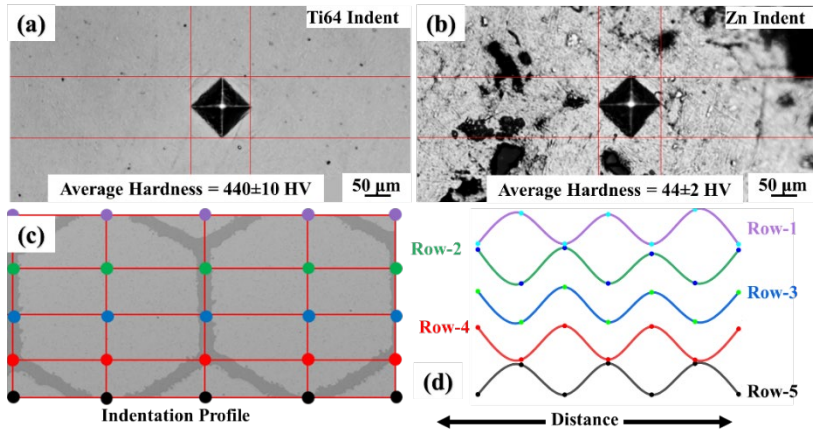


Figure 5.5. Hardness profile of Ti6Al4V-Zinc (Ti64-Zn) metallic bimetal composite, (a, b) representative indents on Ti64, and Zn surfaces at 0.1 kgf load, (c) microstructural region showing positions of indents, and (d) hardness profile map illustrating the variation of hardness across the composite surface. Reproduced with permission from [121].

Table 5.1. Comparison of compressive properties of the Ti6Al4V-Zinc (Ti64-Zn) metallic bimetal composite, spark plasma sintered Zn, and selective laser melted Ti64 hexagonal structures [121].

Sample composition	Compressive yield strength (MPa)	Ultimate compressive strength (MPa)
Ti64 Hexagon	165±2	182±13
Zn (SPS)	115±5	191±6
Ti64-Zn (MBMC)	265±25	292±25

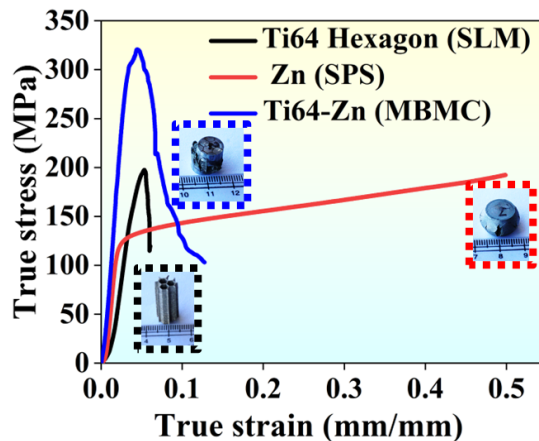


Figure 5.6. True compressive stress-strain curves of Ti6Al4V-Zinc (Ti64-Zn) metallic bimetal composite, selective laser melted Ti64 hexagonal lattice, and spark plasma sintered Zn. Inset images show representative fracture surfaces for each sample. Reproduced with permission from [121].

5.3 In-vitro biodegradation analysis of Ti64-Zn MBMC

The degradation behavior and rate of the Ti64-Zn MBMC were investigated by immersing the samples in SBF for varying durations, with periodic weight measurements taken every 7 days. For comparison, SPS Zn and bulk SLM Ti64 were also incubated under identical conditions. During the initial stages, a thin white layer uniformly formed on the MBMC surface. As immersion progressed, the layer thickened, and degradation products accumulated unevenly, as shown in Figure 5.7. After 7 days, the Ti64-Zn MBMC exhibited a degradation rate of 0.1577 mm/year, slightly higher than that of SPS Zn at 0.1325 mm/year, while bulk SLM Ti64 showed negligible weight loss due to its bioinert nature. The composite's degradation rate is lower than that of pure Mg and Mg-based composites [162,163], which is advantageous for biomedical applications. The elevated degradation in the composite is primarily attributed to galvanic coupling between Zn and Ti64, where the rate depends on the exposed surface areas of both constituents and their interaction with the electrolyte. During early immersion, the initially weak oxide layer on Zn undergoes continuous breakdown, forming surface voids and initiating progressive degradation. At extended immersion times of 14 and 21 days, the degradation rate of Ti64-Zn MBMC decreased to 0.0872 mm/year and 0.0845 mm/year, respectively. This reduction is ascribed to the formation of a thicker protective layer, limiting ion exchange between the composite and the surrounding medium. A similar trend was observed for SPS Zn, while bulk SLM Ti64 remained essentially unaffected, as summarized in Table 5.2.

SEM images of Ti64-Zn MBMC after 21 days of immersion at different locations and magnifications are presented in Figure 5.7-(a-f). Figure 5.7-(a) shows the overall surface, revealing a uniform oxide layer with accumulation of degradation products along the periphery. Higher magnification images at the center and near the Ti64-Zn interface (Figure 5.7-(b,c)) depict an oxide-rich surface layer.

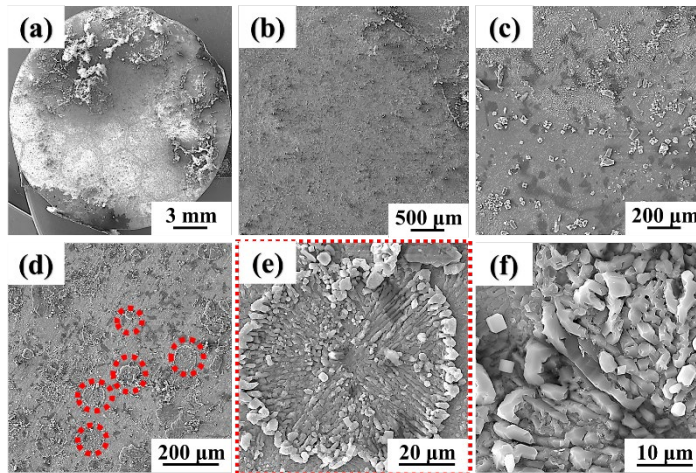


Figure 5.7. Scanning electron microscopy images of Ti6Al4V-Zinc metallic bimetal composite samples after immersion in simulated body fluid for 21 days, (a) overall surface image, (b), and (c) higher magnification images from the center and at the interfacial region respectively, (d) presence of circular patches on the surface, (e) magnified view of patches showing petal-like structures suggestive of an apatite layer formation, and (f) high-magnification image revealing rectangular and irregularly shaped crystals, possibly indicating the apatite crystallization. Reproduced with permission from [121].

Table 5.2. Degradation data in mm/year for Ti6Al4V-Zn metallic bimetal composite, spark plasma sintered Zn, and bulk selective laser melted Ti6Al4V after incubation in simulated body fluid as a function of varying time [121].

Samples	After 7 days	After 14 days	After 21 days
Ti64-Zn (MBMC)	0.1577±0.0100	0.0872±0.0100	0.0845±0.0300
SPS Zn	0.1325±0.0800	0.0965±0.1000	0.0858±0.0500
SLM bulk Ti64	0	0.0072±0.0100	0.0004±0.0100

Circular patches observed in certain regions (Figure 5.7-(d), highlighted in yellow) and the petal-like floral structures in Figure 5.7-(e) suggest the formation of apatite, a calcium phosphate layer resembling the formation of natural HAp ($\text{Ca}_{10}(\text{PO}_4)_6(\text{OH})_2$). The high-magnification image in Figure 5.7-(f) further reveals multiple rectangular and irregular crystals, reinforcing the likelihood of apatite layer formation. EDS elemental maps of a single hexagonal unit and the interface (Figure 5.8-(a,b)) confirm a uniform oxide layer and the presence of calcium (Ca) and phosphorus (P). Point EDS analysis of Figure .7-(f) indicates a Ca/P atomic ratio of 0.96, which is lower than the ideal HAp ratio of 1.67, but supports the formation of a calcium phosphate-based apatite layer. These observations indicate the bioactivity of Ti64-Zn MBMC under simulated physiological conditions.

Further insights into surface degradation were obtained by SEM imaging after removing the oxide layer and corrosion products (Figure 5.9-(a-f)). Figure 5.9-(a) provides an overview of a single hexagonal unit, showing uniform and controlled degradation across Zn-rich regions. Higher magnification (Figure 5.9-(b)) highlights widespread surface degradation, and Figure 5.9-(c) shows deep grooves within corrosion pits, indicating preferential dissolution along grain boundaries due to higher electrochemical activity and localized micro-galvanic effects.

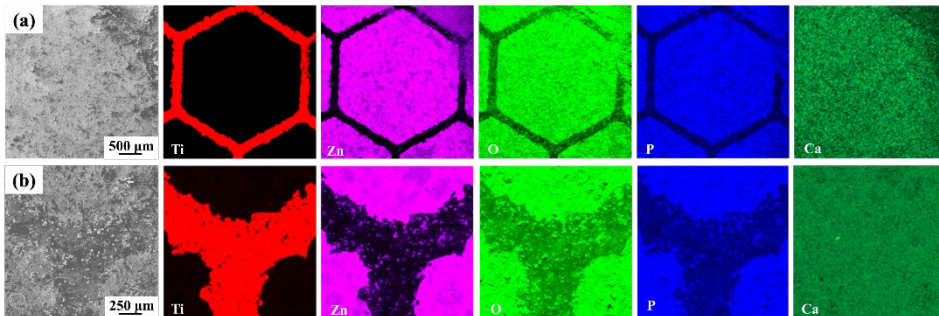


Figure 5.8. Energy dispersive spectroscopy mapping of the Ti6Al4V-Zn metallic bimetal composite surface after 21 days in simulated body fluid, (a) elemental distribution across a single hexagonal unit, and (b) at the interfacial region. Reproduced with permission from [121].

The interfacial region (Figure 5.9-(d-f)) exhibits uneven degradation, with widened gaps at the Ti64-Zn junction, signifying accelerated Zn degradation while Ti64 remains stable. This behavior is driven by enhanced ion exchange facilitated by galvanic coupling, consistent with observations in other dissimilar metallic systems such as Ti-Mg and Ti-Zn [164,165], supporting the proposed degradation mechanism in the present study.

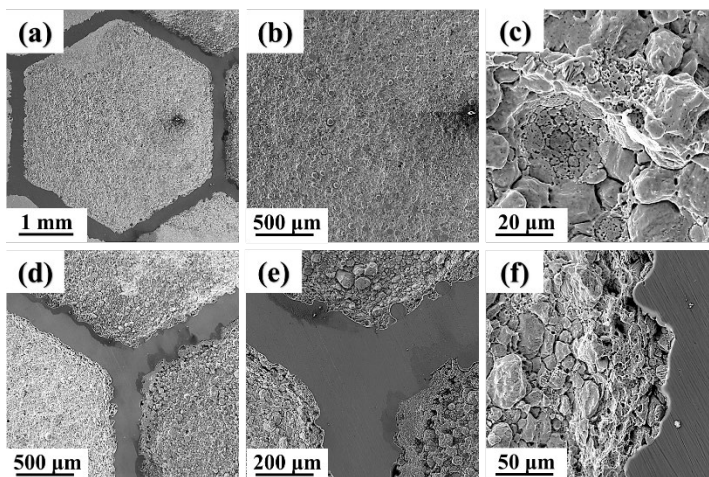


Figure 5.9. Scanning electron microscopy images of the Ti6Al4V-Zinc (Ti64-Zn) metallic bimetal composite (MBMC) after removal of the oxide layer and corrosion products, (a) overall view of a single hexagonal unit, (b) magnified Zn-rich region, (c) higher magnification highlighting deep grooves within corrosion pits, and (d-f) Ti64-Zn interfacial region at varying magnifications. Reproduced with permission from [121].

5.4 Electrochemical corrosion behavior of Ti64-Zn MBMC

To assess the corrosion response of the fabricated composite, PDP tests were performed in SBF to mimic physiological conditions. The electrochemical response of the Ti64-Zn MBMC was compared against SPS-processed Zn and bulk Ti64, which served as reference samples. The PDP curves of Ti64-Zn MBMC, SPS-processed Zn, and SLM-processed Ti64 are shown in Figure 5.10, providing a comparative evaluation of their electrochemical behavior. E_{corr} and I_{corr} were determined using the Tafel extrapolation method, and the corresponding values are summarized in Table 5.3. E_{corr} reflects the tendency of a material toward corrosion, where more negative values indicate higher susceptibility to electrochemical activity. In contrast, I_{corr} represents the degradation rate, with lower values corresponding to improved corrosion resistance and slower dissolution kinetics. The analysis mainly focuses on comparing pure Zn and the Ti64-Zn MBMC, as Ti64 is inherently bioinert and nondegradable; however, examining its electrochemical response remains important for implant-related applications [166].

The bulk SLM Ti64 sample exhibited an E_{corr} of -264 mV and an I_{corr} of $3.35 \mu\text{A}/\text{cm}^2$, values that align well with those typically reported for Ti64 alloys. Similar electrochemical response for additively manufactured Ti64 immersed in SBF was also observed by Chen et al. [167]. In comparison, Zn demonstrated an E_{corr} of -1180 mV and an I_{corr} of $0.045 \mu\text{A}/\text{cm}^2$. When the Ti64-Zn MBMC was exposed to the SBF environment, it displayed an E_{corr} of -1185 mV, slightly more negative than Zn, indicating comparable electrochemical activity. Interestingly, the I_{corr} for Ti64-Zn composite was $0.027 \mu\text{A}/\text{cm}^2$, which is lower than that of SPS Zn, suggesting that the composite undergoes a slower degradation process despite its more negative E_{corr} . To further investigate the corrosion mechanism, SEM analysis was carried out.

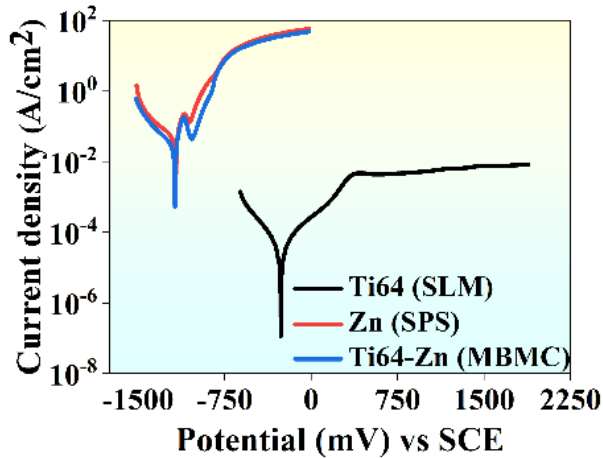


Figure 5.10. Potentiodynamic polarization curve of Ti6Al4V-Zinc (Ti64-Zn) metallic bimetal composite, selective laser melted Ti64, and spark plasma sintered Zn samples obtained after immersion in simulated body fluid for 1 hour. Reproduced with permission from [121].

Table 5.3. Polarization data of the Ti6Al4V-Zinc metallic bimetal composite in comparison to the spark plasma sintered Zn and selective laser melted Ti6Al4V bulk sample immersed in simulated body fluid for 1 hour [121].

Samples	E_{corr} (mV) vs SCE	I_{corr} ($\mu\text{A}/\text{cm}^2$)	I_p ($\mu\text{A}/\text{cm}^2$)	E_{pp} (mV) vs SCE
Ti64-Zn MBMC	-1185±60	0.027±0.010	7.50±1.01	-754±7
Zn (SPS)	-1180±48	0.046±0.010	6.66±0.89	-774±5
Ti64 bulk (SLM)	-264±10	3.355±0.600	4.68±0.24	429±7

SEM images of corroded SPS Zn and Ti64-Zn MBMC samples in SBF are shown in Figure 5.11. As demonstrated in Figure 5.11 and supported by previous studies, bulk SLM Ti64 exhibits superior corrosion resistance, primarily due to the formation of a protective TiO_2 passive layer that inhibits pitting and surface degradation [166,168]. In contrast, SPS Zn and Ti64-Zn MBMC exhibited localized corrosion, with noticeable differences in pit morphology (Figure 5.11). High-resolution SEM images of Zn-rich zones in the MBMC (Figure 5.11-(e,f)) revealed uniformly distributed corrosion pits, most likely due to the abundance of grain boundaries serving as preferential dissolution sites [120]. At the Ti64-Zn interface (Figure 5.11-(g)), active corrosion was evident, whereas the Ti64 surface remained intact, smooth, and pits-free, as confirmed in Figure 5.11-(i), supporting its passive and bioinert nature. The interface corrosion is primarily driven by galvanic coupling between Ti64 and Zn. The high electrochemical potential difference between Ti64 (-250 mV) acting as the cathode and Zn (-1200 mV) as the anode promotes accelerated dissolution of Zn [166].

Ti64's higher resistance to corrosion is attributed to the formation of a protective TiO_2 layer, which provides strong resistance against Cl^- ion attack in SBF [167]. In contrast, Zn and its alloys are more anodic, degrading more readily in chloride-rich media with the concurrent release of Zn^{2+} ions. Consequently, the Ti64-Zn MBMC exhibits a lower E_{corr} and higher passivation current (I_p). The distinct interfacial gap observed in Figure 5.11

likely results from enhanced ion transport during galvanic interactions between Ti64 and Zn. Importantly, the lower I_{corr} value for the composite highlights that its degradation remains controlled, supporting its suitability for biomedical implants where a moderate and predictable degradation rate is desired. These electrochemical findings are consistent with the *in-vitro* immersion studies discussed in the previous sections, collectively confirming the controlled degradation characteristics of the Ti64-Zn MBMC.

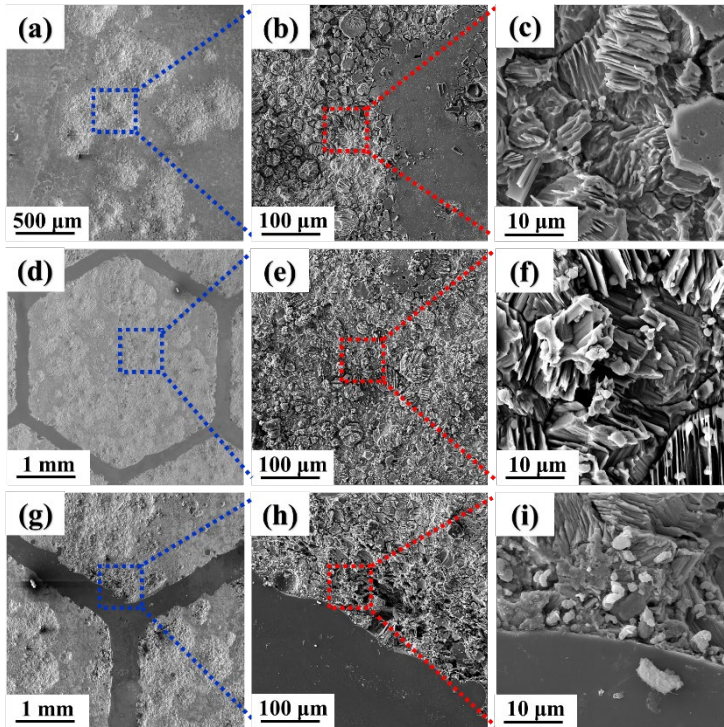


Figure 5.11. Scanning electron microscopy images after 1 hour of potentiodynamic polarization in simulated body fluid, (a-c) spark plasma sintered Zn surfaces at different magnifications, (d-f) Ti6Al4V-Zinc (Ti64-Zn) metallic bimetal composite (MBMC) surfaces depicting a complete hexagonal unit and localized corrosion within Zn-rich regions away from Ti64, and (g-i) Ti64-Zn MBMC at interfacial regions. Reproduced with permission from [121].

5.5 Cytocompatibility assessment of Ti64-Zn MBMC

The *in-vitro* biological performance of the composite was evaluated using an indirect approach, where the cellular response to the degradation products was studied. MC3T3-E1 pre-osteoblast cells were cultured in a conditioned medium prepared from the composite, following the method described in Section 2.4.4. Cell proliferation was quantified in terms of the RGR after 1 and 3 days of incubation, with fresh medium serving as the control. The RGR values of the composite were compared to those of SPS Zn and SLM Ti64 under identical conditions. As shown in Figure 5.12, cell viability in both 1x and 8x extracts (representing 100% and 12.5% dilutions of conditioned medium) was assessed after 24 h and 72 h. Cells exposed to the undiluted (1x) extract of the composite displayed reduced viability compared to SLM Ti64, while SPS Zn exhibited a similar

response, likely due to higher Zn ion concentrations in solution. In contrast, when the medium was diluted 8x, no cytotoxic effects were observed, and viability was comparable to Ti64 and Zn controls. A similar trend persisted for 72 h extracts, where 1x dilutions of both Ti64-Zn MBMC and SPS Zn led to reduced growth, whereas 8x dilutions supported healthy proliferation. Figure 5.12-(b) further confirms that after 3 days of incubation, cell proliferation in 8x extracts remained comparable to the control, with RGR exceeding 75%, meeting the noncytotoxic criteria outlined in cytotoxicity standards [169,170].

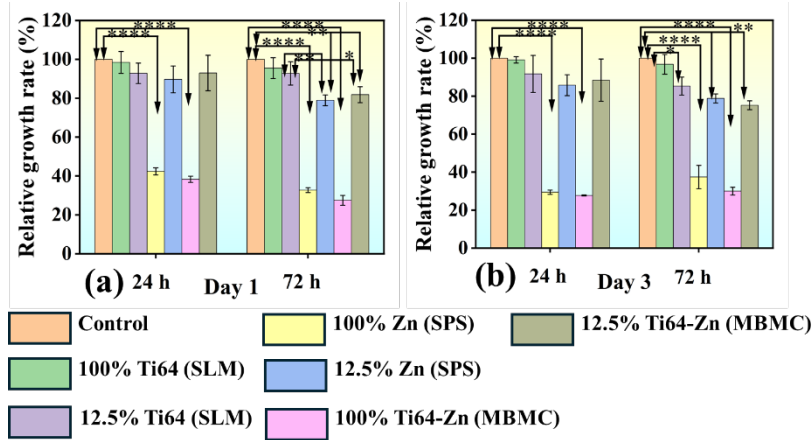


Figure 5.12. Relative growth rate measured by water-soluble tetrazolium assay for MC3T3-E1 cells cultured for 24 hours and 72 hours, conditioned medium for (a) 1 day, and (b) 3 days. Cells in fresh medium were taken as the control for each day. The significance level is taken as $p=0.05$, i.e., $p<0.05$ (*), $p<0.01$ (**), $p<0.001$ (***), $p<0.0001$ (****), and $p>0.05$, non-significant (ns), $n=3$. Reproduced with permission from [121].

To further validate cytocompatibility, live-dead staining was conducted as shown in Fig. 6.13. Green fluorescence (live cells) dominated in all groups after 1 and 3 days of incubation in 8x diluted extracts, with the presence of very few dead cells (red), similar to the control. Moreover, an increase in live cell density over time confirms active proliferation. However, in the case of 1x dilution, most cells detached after death, which aligns with the findings from the WST assay. Fluorescence microscopy (Figure 5.14) revealed well-spread cell morphology on MBMC surfaces in 8x extracts, comparable to SPS Zn, SLM Ti64, and the control medium. However, under 1x conditions, both the composite and SPS Zn showed stressed cell morphologies, consistent with elevated Zn^{2+} concentrations in the medium.

Overall, the Ti64-Zn MBMC demonstrated good cytocompatibility, particularly under 8x dilution, where healthy proliferation and normal cell morphology were maintained. These observations align with reports that low concentrations of Zn^{2+} ions stimulate cellular activity in human vascular cells [171,172] and play a role in immune regulation [173]. In contrast, exposure to 100% conditioned medium resulted in reduced cell viability and signs of cellular stress. These results confirm that the bioinspired partially biodegradable Ti64-Zn MBMC exhibits excellent biocompatibility at 8x dilution, making it a promising candidate for biomedical applications.

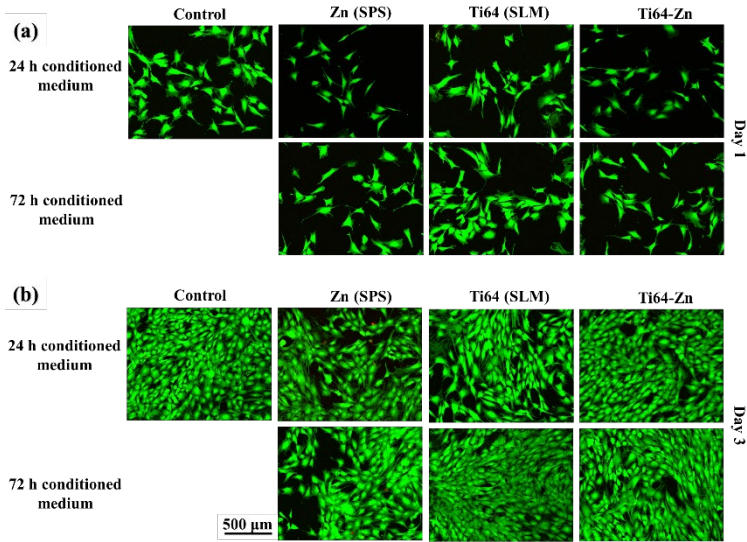


Figure 5.13. Live-dead stained images of MC3T3-E1 cells treated with conditioned medium (8x) of spark plasma sintered zinc (Zn), selective laser melted Ti6Al4V (Ti64), and Ti64-Zn metallic bimetal composites after (a) 1 day, and (b) 3 days of incubation. Live cells are depicted in green, while dead cells are in red. Cells cultured in fresh complete medium served as the control. Reproduced with permission from [121].

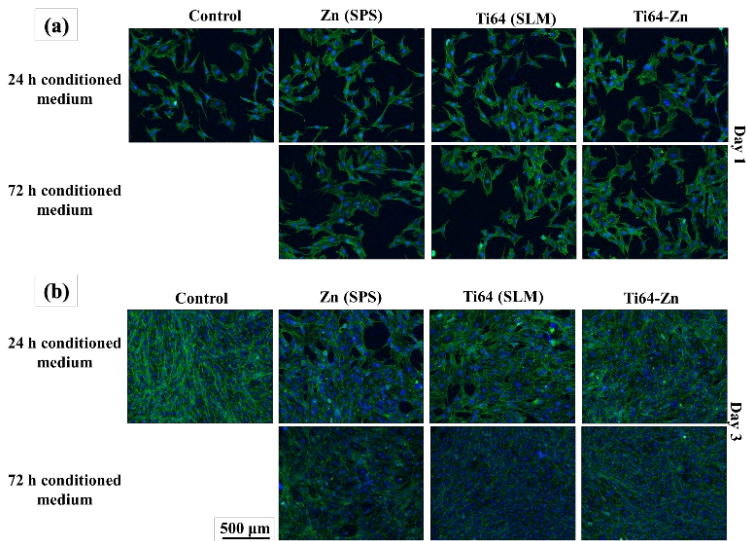


Figure 5.14. Fluorescence images of MC3T3-E1 cells treated with conditioned medium after (a) 1 and (b) 3 days of incubation, showing actin filaments (green) and nuclei (blue). The control represents cells treated with fresh complete medium. Reproduced with permission from [121].

5.6 Summary

This chapter focused on the development and comprehensive evaluation of a novel, partially biodegradable Ti64-Zn MBMC fabricated using a hybrid manufacturing approach that combines AM and PM. A bioinspired Ti64 honeycomb lattice, produced by SLM, served as the structural framework, while Zn was infiltrated and consolidated using SPS to form the MBMC. Detailed structural characterization confirmed the successful integration of both phases without interfacial reactions or secondary phase formation. Microstructural analysis revealed that Ti64 retained its acicular α' martensitic morphology, while Zn exhibited a bimodal grain structure, ensuring mechanical stability and controlled degradability.

Mechanical testing demonstrated that the Ti64-Zn MBMC exhibited superior compressive strength and hardness compared to pure Zn, with distinct sinusoidal hardness arising from the periodic distribution of Ti64 and Zn. Electrochemical studies indicated that the composite undergoes controlled corrosion, with Zn serving as the sacrificial phase while Ti64 maintained stability through passivation. Long-term immersion in SBF showed a gradual reduction in degradation rate due to the formation of protective layers, while surface analyses confirmed the development of calcium phosphate-based apatite, highlighting the bioactivity of the composite. *In-vitro* cytocompatibility assessments using MC3T3-E1 pre-osteoblasts demonstrated favorable cell viability and proliferation at diluted extract concentrations, with negligible cytotoxic effects under 8x dilution. Live-dead and fluorescence microscopy confirmed healthy cell morphology and spreading, reinforcing the biocompatibility of the MBMC. Overall, the chapter establishes the Ti64-Zn MBMC as a promising candidate for next-generation biomedical implants. By combining the mechanical robustness and structural integrity of Ti64 with the controlled biodegradability and bioactivity of Zn, the hybrid composite design effectively bridges the gap between permanent and fully resorbable implants, offering a pathway toward multifunctional, partially biodegradable biomaterials.

6 Conclusion and outlook of the thesis

6.1 Conclusion

In this work, a bioinspired Ti64-Zn MBMC was developed for partially biodegradable load-bearing implant applications using a hybrid manufacturing approach. A porous Ti64 framework was fabricated by SLM to provide structural support. The degradable Zn phase was incorporated into the Ti64 scaffold using spark plasma sintering. The hybrid SLM-SPS route enabled the feasibility of integrating dissimilar metals. The developed system was evaluated in terms of phase stability, microstructure, mechanical integrity, corrosion, and biodegradation behavior, and in-vitro cytocompatibility. The following conclusions can be drawn from this study:

- Comparative evaluation of Ti64 processed by SLM and SPS demonstrated that the fabrication route significantly influenced microstructure and performance. SLM produced a refined acicular α' martensitic structure with higher hardness and superior biological responses under physiological conditions.
- SPS processing of commercially pure Zn resulted in improved densification and microstructural refinement compared to the as-cast condition. Enhanced mechanical properties and a more controlled degradation response were observed, along with acceptable in-vitro cytocompatibility under physiological conditions.
- A Ti64-Zn MBMC was successfully fabricated with a bioinspired porous Ti64 scaffold acting as the reinforcement phase and Zn as the matrix phase. The structural integrity of the Ti64 framework was retained after SPS consolidation. Phase analysis of the composite confirmed the coexistence of Ti64 and Zn without the formation of detrimental intermetallic phases, indicating good metallurgical compatibility between the constituent materials. Mechanical evaluation revealed improved compressive strength compared to pure Zn and stable deformation behavior suitable for load-bearing conditions. Electrochemical and immersion studies demonstrated controlled degradation of the Zn phase. Surface apatite formation was observed, indicating bioactive behavior under physiological conditions. In-vitro cytocompatibility assessment confirmed a favourable cellular response, supporting the biological safety of the developed composite.

6.2 Outlook

Looking forward, several research directions can extend the impact of this work:

- Long-term animal studies are required to assess the composite's degradation kinetics, osseointegration, and biological safety under dynamic physiological conditions.
- Modifying the Ti64 lattice design and Zn infiltration strategy could further balance mechanical performance and degradation behavior.
- Applying bioactive coatings, alloying elements, or ion doping may regulate Zn ion release, accelerate apatite formation, and enhance osteogenesis.
- The hybrid approach could be extended to other material combinations (e.g., Ti-Mg, Ti-Fe, or other biocompatible systems) to design composites with tailored degradation rates and multifunctionality.
- Coupling lattice-based architecture with SLM offers opportunities to produce patient-specific implants with spatially graded degradation and mechanical properties.

References

- [1] M. Geetha, A.K. Singh, R. Asokamani, A.K. Gogia, Ti based biomaterials, the ultimate choice for orthopaedic implants – A review, *Progress in Materials Science* 54 (2009) 397–425. <https://doi.org/10.1016/j.pmatsci.2008.06.004>.
- [2] D.R. Sumner, T.M. Turner, R. Igloria, R.M. Urban, J.O. Galante, Functional adaptation and ingrowth of bone vary as a function of hip implant stiffness, *Journal of Biomechanics* 31 (1998) 909–917. [https://doi.org/10.1016/s0021-9290\(98\)00096-7](https://doi.org/10.1016/s0021-9290(98)00096-7).
- [3] N. Khan, A. Riccio, A systematic review of design for additive manufacturing of aerospace lattice structures: Current trends and future directions, *Progress in Aerospace Sciences* 149 (2024) 101021. <https://doi.org/10.1016/j.paerosci.2024.101021>.
- [4] N.T. Kirkland, N. Birbilis, M.P. Staiger, Assessing the corrosion of biodegradable magnesium implants: A critical review of current methodologies and their limitations, *Acta Biomaterialia* 8 (2012) 925–936. <https://doi.org/10.1016/j.actbio.2011.11.014>.
- [5] P.K. Bowen, E.R. Shearier, S. Zhao, R.J. Guillory, F. Zhao, J. Goldman, J.W. Drelich, Biodegradable metals for cardiovascular stents: from clinical concerns to recent Zn-Alloys, *Advanced Healthcare Materials* 5 (2016) 1121–1140. <https://doi.org/10.1002/adhm.201501019>.
- [6] K.G. Prashanth, Interpenetrating Composites: A Nomenclature Dilemma, *Materials* 18 (2025) 273. <https://doi.org/10.3390/ma18020273>.
- [7] A. Asar, W. Zaki, A comprehensive review of the mechanisms and structure of interpenetrating phase composites with emphasis on metal-metal and polymer-metal variants, *Composites Part B: Engineering* 275 (2024) 111314. <https://doi.org/10.1016/j.compositesb.2024.111314>.
- [8] M. Zhang, N. Zhao, Q. Yu, Z. Liu, R. Qu, J. Zhang, S. Li, D. Ren, F. Berto, Z. Zhang, R.O. Ritchie, On the damage tolerance of 3-D printed Mg-Ti interpenetrating-phase composites with bioinspired architectures, *Nature Communications* 13 (2022) 3247. <https://doi.org/10.1038/s41467-022-30873-9>.
- [9] R. Shukla, M.K. Yadav, L.Y.C. Madruga, J. Jayaraj, K. Popat, Z. Wang, L. Xi, K.G. Prashanth, A novel Ti-eggshell-based composite fabricated by combined additive manufacturing-powder metallurgical routes as bioimplants, *Ceramics International* 51 (2025) 6281–6291. <https://doi.org/10.1016/j.ceramint.2024.12.073>.
- [10] R.B. Martin, D.B. Burr, Structure, function and adaptation of compact bone, *Skeletal Radiology* 18 (1989) 506. <https://doi.org/10.1007/bf00351748>.
- [11] T.J. Webster, Nanophase ceramics: The future orthopedic and dental implant material, *Advances in Chemical Engineering* 27 (2001) 125–166. [https://doi.org/10.1016/s0065-2377\(01\)27005-7](https://doi.org/10.1016/s0065-2377(01)27005-7).
- [12] D. Wu, P. Isaksson, S.J. Ferguson, C. Persson, Young’s modulus of trabecular bone at the tissue level: A review, *Acta Biomaterialia* 78 (2018) 1–12. <https://doi.org/10.1016/j.actbio.2018.08.001>.

- [13] D. Lopes, C.M. Cruz, M.B. Oliveira, J.F. Mano, Bone physiology as inspiration for tissue regenerative therapies, *Biomaterials* 185 (2018) 240–275. <https://doi.org/10.1016/j.biomaterials.2018.09.028>.
- [14] I.S. Raja, D.R. Preeth, M. Vedhanayagam, S.H. Hyon, D. Lim, B. Kim, S. Rajalakshmi, D.W. Han, Polyphenols-loaded electrospun nanofibers in bone tissue engineering and regeneration, *Biomaterials Research* 25 (2021) 1–16. <https://doi.org/10.1186/s40824-021-00229-3>.
- [15] H.M. Frost, Bone's mechanostat: A 2003 update, *The Anatomical Record Part A* 275A (2003) 1081–1101. <https://doi.org/10.1002/ar.a.10119>.
- [16] P. Rowe, A. Koller, S. Sharma, *Physiology, Bone Remodeling, StatPearls* (2023) Bookshelf ID: NBK499863. <https://www.ncbi.nlm.nih.gov/books/nbk499863/>.
- [17] H.M. Frost, Skeletal structural adaptations to mechanical usage (SATMU): 1. Redefining Wolff's Law: The bone modeling problem, *The Anatomical Record* 226 (1990) 403–414. <https://doi.org/10.1002/ar.1092260402>.
- [18] M.J. Gardner, M.C.H.V. Meulen, D. Demetrakopoulos, T.M. Wright, E.R. Myers, M.P. Bostrom, In vivo cyclic axial compression affects bone healing in the mouse tibia, *Journal of Orthopaedic Research* 24 (2006) 1679–1686. <https://doi.org/10.1002/jor.20230>.
- [19] D. Zhao, F. Witte, F. Lu, J. Wang, J. Li, L. Qin, Current status on clinical applications of magnesium-based orthopaedic implants: A review from clinical translational perspective, *Biomaterials* 112 (2017) 287–302. <https://doi.org/10.1016/j.biomaterials.2016.10.017>.
- [20] S. Agarwal, J. Curtin, B. Duffy, S. Jaiswal, Biodegradable magnesium alloys for orthopaedic applications: A review on corrosion, biocompatibility and surface modifications, *Materials Science and Engineering: C* 68 (2016) 948–963. <https://doi.org/10.1016/j.msec.2016.06.020>.
- [21] C. Piconi, G. Maccauro, Zirconia as a ceramic biomaterial, *Biomaterials* 20 (1999) 1–25. [https://doi.org/10.1016/s0142-9612\(98\)00010-6](https://doi.org/10.1016/s0142-9612(98)00010-6).
- [22] M. Bohner, *Bioresorbable ceramics, Degradation Rate of Bioresorbable Materials: Prediction and Evaluation Elsevier* (2008) ISBN: 9781845693299. <https://doi.org/10.1533/9781845695033.2.95>.
- [23] M.K. Yadav, V. Pandey, K. Mohanta, V.K. Singh, A low-cost approach to develop silica doped tricalcium phosphate (TCP) scaffold by valorizing animal bone waste and rice husk for tissue engineering applications, *Ceramics International* 48 (2022) 25335–25345. <https://doi.org/10.1016/j.ceramint.2022.05.207>.
- [24] M.K. Yadav, R.H. Shukla, K.G. Prashanth, A comprehensive review on development of waste derived hydroxyapatite (HAp) for tissue engineering application, *Materials Today: Proceedings* In press (2023). <https://doi.org/10.1016/j.matpr.2023.04.669>.
- [25] H. Mehboob, S.H. Chang, Application of composites to orthopedic prostheses for effective bone healing: A review, *Composite Structures* 118 (2014) 328–341. <https://doi.org/10.1016/j.compstruct.2014.07.052>.

- [26] S. Sadeghzade, J. Liu, H. Wang, X. Li, J. Cao, H. Cao, B. Tang, H. Yuan, Recent advances on bioactive baghdadite ceramic for bone tissue engineering applications: 20 years of research and innovation (a review), *Materials Today Bio* 17 (2022) 100473. <https://doi.org/10.1016/j.mtbio.2022.100473>.
- [27] A.M.S. Ibrahim, P.G.L. Koolen, K. Kim, G.S. Perrone, D.L. Kaplan, S.J. Lin, Absorbable biologically based internal fixation, *Clinics in Podiatric Medicine and Surgery* 32 (2015) 61–72. <https://doi.org/10.1016/j.cpm.2014.09.009>.
- [28] S.C. Kim, D.W. Kim, Y.H. Shim, J.S. Bang, H.S. Oh, S.W. Kim, M.H. Seo, In vivo evaluation of polymeric micellar paclitaxel formulation: toxicity and efficacy, *Journal of Controlled Release* 72 (2001) 191–202. [https://doi.org/10.1016/s0168-3659\(01\)00275-9](https://doi.org/10.1016/s0168-3659(01)00275-9).
- [29] J. Lausmaa, B. Kasemo, H. Mattsson, H. Odelius, Multi-technique surface characterization of oxide films on electropolished and anodically oxidized titanium, *Applied Surface Science* 45 (1990) 189–200. [https://doi.org/10.1016/0169-4332\(90\)90002-h](https://doi.org/10.1016/0169-4332(90)90002-h).
- [30] X. Gu, Y. Zheng, Y. Cheng, S. Zhong, T. Xi, In vitro corrosion and biocompatibility of binary magnesium alloys, *Biomaterials* 30 (2009) 484–498. <https://doi.org/10.1016/j.biomaterials.2008.10.021>.
- [31] Y.J. Chen, Y.J. Li, J.C. Walmsley, S. Dumoulin, P.C. Skaret, H.J. Roven, Microstructure evolution of commercial pure titanium during equal channel angular pressing, *Materials Science and Engineering: A* 527 (2010) 789–796. <https://doi.org/10.1016/j.msea.2009.09.005>.
- [32] D.G. Barceloux, D. Barceloux, Chromium, *Journal of Toxicology: Clinical Toxicology* 37 (1999) 173–194. <https://doi.org/10.1081/clt-100102418>.
- [33] D.G. Barceloux, D. Barceloux, Nickel, *Journal of Toxicology: Clinical Toxicology* 37 (1999) 239–258. <https://doi.org/10.1081/clt-100102423>.
- [34] X. Li, P. Gao, P. Wan, Y. Pei, L. Shi, B. Fan, C. Shen, X. Xiao, K. Yang, Z. Guo, Novel bio-functional magnesium coating on porous Ti6Al4V orthopaedic implants: In vitro and In vivo study, *Scientific Reports* 7 (2017) 40755. <https://doi.org/10.1038/srep40755>.
- [35] M. He, L. Chen, M. Yin, S. Xu, Z. Liang, Review on magnesium and magnesium-based alloys as biomaterials for bone immobilization, *Journal of Materials Research and Technology* 23 (2023) 4396–4419. <https://doi.org/10.1016/j.jmrt.2023.02.037>.
- [36] F. Badkoobeh, H. Mostaan, M. Rafiei, H.R.B. Rad, S. Ramakrishna, X. Chen, Additive manufacturing of biodegradable magnesium-based materials: Design strategies, properties, and biomedical applications, *Journal of Magnesium and Alloys* 11 (2023) 801–839. <https://doi.org/10.1016/j.jma.2022.12.001>.
- [37] G.E.J. Poinern, S. Brundavanam, D. Fawcett, Biomedical magnesium alloys: A review of material properties, surface modifications and potential as a biodegradable orthopaedic implant, *American Journal of Biomedical Engineering* 2 (2012) 218–240. <https://doi.org/10.5923/j.ajbe.20120206.02>.

- [38] R. Murugan, S. Ramakrishna, Development of nanocomposites for bone grafting, *Composites Science and Technology* 65 (2005) 2385–2406. <https://doi.org/10.1016/j.compscitech.2005.07.022>.
- [39] Y. Zhao, G. Wu, J. Jiang, H.M. Wong, K.W.K. Yeung, P.K. Chu, Improved corrosion resistance and cytocompatibility of magnesium alloy by two-stage cooling in thermal treatment, *Corrosion Science* 59 (2012) 360–365. <https://doi.org/10.1016/j.corsci.2012.03.020>.
- [40] F. Witte, V. Kaese, H. Haferkamp, E. Switzer, A.M. Lindenberg, C.J. Wirth, H. Windhagen, In vivo corrosion of four magnesium alloys and the associated bone response, *Biomaterials* 26 (2005) 3557–3563. <https://doi.org/10.1016/j.biomaterials.2004.09.049>.
- [41] E. Ghali, Corrosion resistance of aluminum and magnesium alloys: Understanding, performance, and testing, Wiley (2010), ISBN:9780471715764. <https://doi.org/10.1002/9780470531778>.
- [42] M.K. Yadav, A. Yarlapati, Y.N. Aditya, P. Kesavan, V. Pandey, C.S. Perugu, A. Nain, K. Chatterjee, S. Suwas, J. Jayamani, K.G. Prashanth, Processing and development of porous titanium for biomedical applications: A comprehensive review, *Journal of Manufacturing and Materials Processing* 9 (2025) 401. <https://doi.org/10.3390/jmmp9120401>.
- [43] C. Leyens, M. Peters, Titanium and titanium alloys, Wiley (2003), ISBN: 9783527305346. <https://doi.org/10.1002/3527602119>.
- [44] D. Banerjee, J.C. Williams, Perspectives on titanium science and technology, *Acta Materialia* 61 (2013) 844–879. <https://doi.org/10.1016/j.actamat.2012.10.043>.
- [45] R. Singh, P.D. Lee, R.J. Dashwood, T.C. Lindley, Titanium foams for biomedical applications: A review, *Materials Technology* 25 (2010) 127–136. <https://doi.org/10.1179/175355510x12744412709403>.
- [46] M.R. Nikpour, S.M. Rabiee, M. Jahanshahi, Synthesis and characterization of hydroxyapatite/chitosan nanocomposite materials for medical engineering applications, *Composites Part B: Engineering* 43 (2012) 1881–1886. <https://doi.org/10.1016/j.compositesb.2012.01.056>.
- [47] P. Nasker, A. Samanta, S. Rudra, A. Sinha, A.K. Mukhopadhyay, M. Das, Effect of fluorine substitution on sintering behaviour, mechanical and bioactivity of hydroxyapatite, *Journal of Mechanical Behavior of Biomedical Materials* 95 (2019) 136–142. <https://doi.org/10.1016/j.jmbbm.2019.03.032>.
- [48] E. Kalantari, S.M. Naghib, N.J. Irvani, R. Esmaeili, M.R.N. Jamal, M. Mozafari, Biocomposites based on hydroxyapatite matrix reinforced with nanostructured monticellite (CaMgSiO₄) for biomedical application: Synthesis, characterization, and biological studies, *Materials Science and Engineering: C* 105 (2019) 109912. <https://doi.org/10.1016/j.msec.2019.109912>.
- [49] Y. Liu, Y. Zheng, X.H. Chen, J.A. Yang, H. Pan, D. Chen, L. Wang, J. Zhang, D. Zhu, S. Wu, K.W.K. Yeung, R.C. Zeng, Y. Han, S. Guan, Fundamental theory of biodegradable metals—definition, criteria, and design, *Advanced Functional Materials* 29 (2019) 1805402. <https://doi.org/10.1002/adfm.201805402>.

- [50] H. Hermawan, Updates on the research and development of absorbable metals for biomedical applications, *Progress in Biomaterials* 7 (2018) 93-110. <https://doi.org/10.1007/s40204-018-0091-4>.
- [51] H. Ibrahim, S.N. Esfahani, B. Poorganji, D. Dean, M. Elahinia, Resorbable bone fixation alloys, forming, and post-fabrication treatments, *Materials Science and Engineering: C* 70 (2017) 870–888. <https://doi.org/10.1016/j.msec.2016.09.069>.
- [52] Y. Liu, Y. Zheng, B. Hayes, Degradable, absorbable or resorbable—what is the best grammatical modifier for an implant that is eventually absorbed by the body?, *Science China Materials* 60 (2017) 377–391. <https://doi.org/10.1007/s40843-017-9023-9>.
- [53] F. Witte, The history of biodegradable magnesium implants: A review, *Acta Biomaterialia* 6 (2010) 1680–1692. <https://doi.org/10.1016/j.actbio.2010.02.028>.
- [54] M. Haude, H. Ince, A. Abizaid, R. Toelg, P.A. Lemos, C.V. Birgelen, E.H. Christiansen, W. Wijns, F.J. Neumann, C. Kaiser, E. Eeckhout, S.T. Lim, J. Escaned, H.M.G. Garcia, R. Waksman, Safety and performance of the second-generation drug-eluting absorbable metal scaffold in patients with de-novo coronary artery lesions (BIOSOLVE-II): 6 month results of a prospective, multicentre, non-randomised, first-in-man trial, *The Lancet* 387 (2016) 31–39. [https://doi.org/10.1016/s0140-6736\(15\)00447-x](https://doi.org/10.1016/s0140-6736(15)00447-x).
- [55] C. Plaass, C.V. Falck, S. Ettinger, L. Sonnow, F. Calderone, A. Weizbauer, J. Reifenrath, L. Claassen, H. Waizy, K. Daniilidis, C.S. Colman, H. Windhagen, Bioabsorbable magnesium versus standard titanium compression screws for fixation of distal metatarsal osteotomies – 3 year results of a randomized clinical trial, *Journal of Orthopaedic Science* 23 (2018) 321–327. <https://doi.org/10.1016/j.jos.2017.11.005>.
- [56] J.W. Lee, H.S. Han, K.J. Han, J. Park, H. Jeon, M.R. Ok, H.K. Seok, J.P. Ahn, K.E. Lee, D.H. Lee, S.J. Yang, S.Y. Cho, P.R. Cha, H. Kwon, T.H. Nam, J.H. Lo Han, H.J. Rho, K.S. Lee, Y.C. Kim, D. Mantovani, Long-term clinical study and multiscale analysis of in vivo biodegradation mechanism of Mg alloy, *Proceedings of the National Academy of Sciences* 113 (2016) 716–721. <https://doi.org/10.1073/pnas.1518238113>.
- [57] K.G. Prashanth, Z. Wang, Additive manufacturing: Alloy design and process innovations, *Materials* 13 (2020) 542. <https://doi.org/10.3390/ma13030542>.
- [58] K. Sivaprasad, N.R. Babu, K.G. Prashanth, Additive manufacturing and allied technologies, *Transactions of the Indian Institute of Metals* 76 (2023) 269. <https://doi.org/10.1007/s12666-023-02892-7>.
- [59] H.S. Maurya, R.J. Vikram, K. Kosiba, K. Juhani, F. Sergejev, S. Suwas, K.G. Prashanth, Additive manufacturing of CMCs with bimodal microstructure, *Journal of Alloys and Compounds* 938 (2023) 168416. <https://doi.org/10.1016/j.jallcom.2022.168416>.
- [60] H.S. Maurya, K. Kosiba, K. Juhani, F. Sergejev, K.G. Prashanth, Effect of powder bed preheating on the crack formation and microstructure in ceramic matrix composites fabricated by laser powder-bed fusion process, *Additive Manufacturing* 58 (2022) 103013. <https://doi.org/10.1016/j.addma.2022.103013>.

- [61] H.S. Maurya, J. Jayaraj, R.J. Vikram, K. Juhani, F. Sergejev, K.G. Prashanth, Additive manufacturing of TiC-based cermets: A detailed comparison with spark plasma sintered samples, *Journal of Alloys and Compounds* 960 (2023) 170436. <https://doi.org/10.1016/j.jallcom.2023.170436>.
- [62] H.S. Maurya, J. Marczyk, K. Juhani, F. Sergejev, R. Kumar, A. Hussain, F. Akhtar, M. Hebda, K.G. Prashanth, Binder jetting 3D printing of green TiC-FeCr based cermets- Effect of sintering temperature and systematic comparison study with Laser powder bed fusion fabricated parts, *Materials Today Advances* 25 (2025) 100562. <https://doi.org/10.1016/j.mtadv.2025.100562>.
- [63] K.G. Prashanth, S. Kolla, J. Eckert, Additive manufacturing processes: Selective laser melting, electron beam melting and binder jetting—selection guidelines, *Materials* 10 (2017) 672. <https://doi.org/10.3390/ma10060672>.
- [64] N. Singh, P. Hameed, R. Ummethala, G. Manivasagam, K.G. Prashanth, J. Eckert, Selective laser manufacturing of Ti-based alloys and composites: impact of process parameters, application trends, and future prospects, *Materials Today Advances* 8 (2020) 100097. <https://doi.org/10.1016/j.mtadv.2020.100097>.
- [65] D.G. Ahn, Directed energy deposition (DED) process: State of the art, *International Journal of Precision Engineering and Manufacturing - Green Technology* 8 (2021) 703–742. <https://doi.org/10.1007/s40684-020-00302-7>.
- [66] J. Ge, J. Huang, Y. Lei, P. O'Reilly, M. Ahmed, C. Zhang, X. Yan, S. Yin, Microstructural features and compressive properties of SLM Ti6Al4V lattice structures, *Surface and Coatings Technology* 403 (2020) 126419. <https://doi.org/10.1016/j.surfcoat.2020.126419>.
- [77] S. Scudino, C. Unterdörfer, K.G. Prashanth, H. Attar, N. Ellendt, V. Uhlenwinkel, J. Eckert, Additive manufacturing of Cu-10Sn bronze, *Materials Letters* 156 (2015) 202–204. <https://doi.org/10.1016/j.matlet.2015.05.076>.
- [68] J. Suryawanshi, K.G. Prashanth, U. Ramamurty, Mechanical behavior of selective laser melted 316L stainless steel, *Materials Science and Engineering: A* 696 (2017) 113–121. <https://doi.org/10.1016/j.msea.2017.04.058>.
- [69] J. Suryawanshi, K.G. Prashanth, S. Scudino, J. Eckert, O. Prakash, U. Ramamurty, Simultaneous enhancements of strength and toughness in an Al-12Si alloy synthesized using selective laser melting, *Acta Materialia* 115 (2016) 285–294. <https://doi.org/10.1016/j.actamat.2016.06.009>.
- [70] H.A. Zaharin, A.M.A. Rani, F.I. Azam, T.L. Ginta, N. Sallih, A. Ahmad, N.A. Yunus, T.Z.A. Zulkifli, Effect of unit cell type and pore size on porosity and mechanical behavior of additively manufactured Ti6Al4V scaffolds, *Materials* 11 (2018) 2402. <https://doi.org/10.3390/ma11122402>.
- [71] Z. Wang, M. Xie, Y. Li, W. Zhang, C. Yang, L. Kollo, J. Eckert, K.G. Prashanth, Premature failure of an additively manufactured material, *NPG Asia Materials* 12 (2020) 30. <https://doi.org/10.1038/s41427-020-0212-0>.
- [72] S. Arabnejad, B. Johnston, M. Tanzer, D. Pasini, Fully porous 3D printed titanium femoral stem to reduce stress-shielding following total hip arthroplasty, *Journal of Orthopaedic Research* 35 (2017) 1774–1783. <https://doi.org/10.1002/jor.23445>.

- [73] C. Fang, H. Cai, E. Kuong, E. Chui, Y.C. Siu, T. Ji, I. Drstvenšek, Surgical applications of three-dimensional printing in the pelvis and acetabulum: from models and tools to implants, *Der Unfallchirurg* 122 (2019) 278–285. <https://doi.org/10.1007/s00113-019-0626-8>.
- [74] Y. Zhu, A.B. Naseri, N.J. Dunbar, M.R.W. Brake, P. Zandiyeh, G. Li, A. Leardini, B. Spazzoli, B.J. Fregly, Finite element analysis of screw fixation durability under multiple boundary and loading conditions for a custom pelvic implant, *Medical Engineering & Physics* 111 (2023) 103930. <https://doi.org/10.1016/j.medengphy.2022.103930>.
- [75] K.C. Wong, S.M. Kumta, N.V.L. Gee, J. Demol, One-step reconstruction with a 3D-printed, biomechanically evaluated custom implant after complex pelvic tumor resection, *Computer Aided Surgery* 20 (2015) 14–23. <https://doi.org/10.3109/10929088.2015.1076039>.
- [76] D. Broekhuis, R. Boyle, S. Karunaratne, A. Chua, P. Stalley, Custom designed and 3D-printed titanium pelvic implants for acetabular reconstruction after tumour resection, *HIP International* 33 (2022) 905–915. <https://doi.org/10.1177/11207000221135068>.
- [77] D.A. Hollander, M.V. Walter, T. Wirtz, R. Sellei, B.S. Rohlfing, O. Paar, H.J. Erli, Structural, mechanical and in vitro characterization of individually structured Ti-6Al-4V produced by direct laser forming, *Biomaterials* 27 (2006) 955–963. <https://doi.org/10.1016/j.biomaterials.2005.07.041>.
- [78] C.Y. Lin, T. Wirtz, F. LaMarca, S.J. Hollister, Structural and mechanical evaluations of a topology optimized titanium interbody fusion cage fabricated by selective laser melting process, *Journal of Biomedical Materials Research Part A* 83A (2007) 272–279. <https://doi.org/10.1002/jbm.a.31231>.
- [79] L.E. Murr, Open-cellular metal implant design and fabrication for biomechanical compatibility with bone using electron beam melting, *Journal of Mechanical Behavior of Biomedical Materials* 76 (2017) 164–177. <https://doi.org/10.1016/j.jmbbm.2017.02.019>.
- [80] A. Mazzoli, M. Germani, R. Raffaelli, Direct fabrication through electron beam melting technology of custom cranial implants designed in a PHANToM-based haptic environment, *Materials & Design* 30 (2009) 3186–3192. <https://doi.org/10.1016/j.matdes.2008.11.013>.
- [81] R. Yan, D. Luo, H. Huang, R. Li, N. Yu, C. Liu, M. Hu, Q. Rong, Electron beam melting in the fabrication of three-dimensional mesh titanium mandibular prosthesis scaffold, *Scientific Reports* 8 (2018) 750. <https://doi.org/10.1038/s41598-017-15564-6>.
- [82] K. Moiduddin, S.H. Mian, U. Umer, N. Ahmed, H. Alkhalefah, W. Ameen, Reconstruction of complex zygomatic bone defects using mirroring coupled with EBM fabrication of titanium implant, *Metals* 9 (2019) 1250. <https://doi.org/10.3390/met9121250>.
- [83] A. Yáñez, A. Cuadrado, O. Martel, H. Afonso, D. Monopoli, Gyroid porous titanium structures: A versatile solution to be used as scaffolds in bone defect reconstruction, *Materials & Design* 140 (2018) 21–29. <https://doi.org/10.1016/j.matdes.2017.11.050>.

- [84] O.M. Ivasishin, D.G. Savvakina, The impact of diffusion on synthesis of high-strength titanium alloys from elemental powder blends, *Key Engineering Materials* 436 (2010) 113–121. <https://doi.org/10.4028/www.scientific.net/kem.436.113>.
- [85] Y.F. Yang, S.D. Luo, G.B. Schaffer, M. Qian, Sintering of Ti–10V–2Fe–3Al and mechanical properties, *Materials Science and Engineering: A* 528 (2011) 6719–6726. <https://doi.org/10.1016/j.msea.2011.05.041>.
- [86] V. Mamedov, Spark plasma sintering as advanced PM sintering method, *Powder Metallurgy* 45 (2002) 322–328. <https://doi.org/10.1179/003258902225007041>.
- [87] G. Xie, O. Ohashi, K. Chiba, N. Yamaguchi, M. Song, K. Furuya, T. Noda, Frequency effect on pulse electric current sintering process of pure aluminum powder, *Materials Science and Engineering: A* 359 (2003) 384–390. [https://doi.org/10.1016/s0921-5093\(03\)00393-9](https://doi.org/10.1016/s0921-5093(03)00393-9).
- [88] Y.F. Yang, M. Qian, Spark plasma sintering and hot pressing of titanium and titanium alloys, *Titanium Powder Metallurgy: Science, Technology and Applications*, Elsevier (2015), ISBN: 9780128000540. <https://doi.org/10.1016/b978-0-12-800054-0.00013-7>.
- [89] M. Omori, Sintering, consolidation, reaction and crystal growth by the spark plasma system (SPS), *Materials Science and Engineering: A* 287 (2000) 183–188. [https://doi.org/10.1016/s0921-5093\(00\)00773-5](https://doi.org/10.1016/s0921-5093(00)00773-5).
- [90] J.R. Groza, A. Zavaliangos, Sintering activation by external electrical field, *Materials Science and Engineering: A* 287 (2000) 171–177. [https://doi.org/10.1016/s0921-5093\(00\)00771-1](https://doi.org/10.1016/s0921-5093(00)00771-1).
- [91] M. Eriksson, Z. Shen, M. Nygren, Fast densification and deformation of titanium powder, *Powder Metallurgy* 48 (2005) 231–236. <https://doi.org/10.1179/174329005x71939>.
- [92] A. Ibrahim, F. Zhang, E. Otterstein, E. Burkel, Processing of porous Ti and Ti5Mn foams by spark plasma sintering, *Materials & Design* 32 (2011) 146–153. <https://doi.org/10.1016/j.matdes.2010.06.019>.
- [93] A. Kashimbetova, K. Slámecka, S.D.D.L. Torre, J.C.M. García, B.H. Morales, M.C.P. Barba, D. Hui, L. Celko, E.B. Montufar, Pressure-less spark plasma sintering of 3D-plotted titanium porous structures, *Journal of Materials Research and Technology* 22 (2023) 2147–2157. <https://doi.org/10.1016/j.jmrt.2022.12.072>.
- [94] F. Zhang, E. Otterstein, E. Burkel, Spark plasma sintering, microstructures, and mechanical properties of macroporous titanium foams, *Advanced Engineering Materials* 12 (2010) 863–872. <https://doi.org/10.1002/adem.201000106>.
- [95] R. Schmidt, S. Pilz, I. Lindemann, C. Damm, J. Hufenbach, A. Helth, D. Geissler, A. Henss, M. Rohnke, M. Calin, M. Zimmermann, J. Eckert, M.H. Lee, A. Gebert, Powder metallurgical processing of low modulus β -type Ti-45Nb to bulk and macro-porous compacts, *Powder Technology* 322 (2017) 393–401. <https://doi.org/10.1016/j.powtec.2017.09.015>.

- [96] M. Kon, L.M. Hirakata, K. Asaoka, Porous Ti-6Al-4V alloy fabricated by spark plasma sintering for biomimetic surface modification, *Journal of Biomedical Materials Research Part B Applied Biomaterials* 68B (2004) 88–93. <https://doi.org/10.1002/jbm.b.20004>.
- [97] O. Ertorer, T.D. Topping, Y. Li, W. Moss, E.J. Lavernia, Nanostructured Ti consolidated via spark plasma sintering, *Metallurgical and Materials Transactions A* 42 (2011) 964–973. <https://doi.org/10.1007/s11661-010-0499-5>.
- [98] M. Zadra, F. Casari, L. Girardini, A. Molinari, Microstructure and mechanical properties of cp-titanium produced by spark plasma sintering, *Powder Metallurgy* 51 (2008) 59–65. <https://doi.org/10.1179/174329008x277000>.
- [99] Y.J. Liu, H.L. Wang, S.J. Li, S.G. Wang, W.J. Wang, W.T. Hou, Y.L. Hao, R. Yang, L.C. Zhang, Compressive and fatigue behavior of beta-type titanium porous structures fabricated by electron beam melting, *Acta Materialia* 126 (2017) 58–66. <https://doi.org/10.1016/j.actamat.2016.12.052>.
- [100] A.A. Zadpoor, Mechanical performance of additively manufactured meta-biomaterials, *Acta Biomaterialia* 85 (2019) 41–59. <https://doi.org/10.1016/j.actbio.2018.12.038>.
- [101] Q. Ran, W. Yang, Y. Hu, X. Shen, Y. Yu, Y. Xiang, K. Cai, Osteogenesis of 3D printed porous Ti6Al4V implants with different pore sizes, *Journal of Mechanical Behavior of Biomedical Materials* 84 (2018) 1–11. <https://doi.org/10.1016/j.jmbbm.2018.04.010>.
- [102] S. Panzavolta, P. Torricelli, S. Amadori, A. Parrilli, K. Rubini, E.D. Bella, M. Fini, A. Bigi, 3D interconnected porous biomimetic scaffolds: In vitro cell response, *Journal of Biomedical Materials Research Part A* 101 (2013) 3560–3570. <https://doi.org/10.1002/jbm.a.34662>.
- [103] C. Dou, M. Zhang, D. Ren, H. Ji, Z. Yi, S. Wang, Z. Liu, Q. Wang, Y. Zheng, Z. Zhang, R. Yang, Bi-continuous Mg-Ti interpenetrating-phase composite as a partially degradable and bioactive implant material, *Journal of Materials Science and Technology* 146 (2023) 211–220. <https://doi.org/10.1016/j.jmst.2022.11.011>.
- [104] Z. Zhang, Z. Wang, Q. Zhao, K.G. Prashanth, Metal-metal interpenetrating phase composites: A review, *Journal of Alloys and Compounds* 1009 (2024) 176951. <https://doi.org/10.1016/j.jallcom.2024.176951>.
- [105] O.A. Ketan, R.K.A.A. Rub, R. Rowshan, Mechanical properties of a new type of architected interpenetrating phase composite materials, *Advanced Materials Technologies* 2 (2017) 1600235. <https://doi.org/10.1002/admt.201600235>.
- [106] U.G.K. Wegst, H. Bai, E. Saiz, A.P. Tomsia, R.O. Ritchie, Bioinspired structural materials, *Nature Materials* 14 (2015) 23–36. <https://doi.org/10.1038/nmat4089>.
- [107] D. Kokkinis, M. Schaffner, A.R. Studart, Multimaterial magnetically assisted 3D printing of composite materials, *Nature Communications* 6 (2015) 1–10. <https://doi.org/10.1038/ncomms9643>.
- [108] L.Y. Chen, S.X. Liang, Y. Liu, L.C. Zhang, Additive manufacturing of metallic lattice structures: Unconstrained design, accurate fabrication, fascinated performances, and challenges, *Materials Science and Engineering: R: Reports* 146 (2021) 100648. <https://doi.org/10.1016/j.mser.2021.100648>.

- [109] F. Liu, T. Li, Z. Jia, L. Wang, Combination of stiffness, strength, and toughness in 3D printed interlocking nacre-like composites, *Extreme Mechanics Letters* 35 (2020) 100621. <https://doi.org/10.1016/j.eml.2019.100621>.
- [110] E.E. de Obaldia, C. Jeong, L.K. Grunenfelder, D. Kisailus, P. Zavattieri, Analysis of the mechanical response of biomimetic materials with highly oriented microstructures through 3D printing, mechanical testing and modeling, *Journal of the Mechanical Behavior of Biomedical Materials* 48 (2015) 70–85. <https://doi.org/10.1016/j.jmbbm.2015.03.026>.
- [111] A.V. Hogan, J. Xu, M.A. Meyers, Additive manufacturing as a method to design and optimize bioinspired structures, *Advanced Materials* 30 (2018) 1800940. <https://doi.org/10.1002/adma.201800940>.
- [112] L. Bai, C. Gong, X. Chen, Y. Sun, J. Zhang, L. Cai, S. Zhu, S.Q. Xie, Additive manufacturing of customized metallic orthopedic implants: Materials, structures, and surface modifications, *Metals* 9 (2019) 1004. <https://doi.org/10.3390/met9091004>.
- [113] A.A. Raheem, P. Hameed, R. Whenish, R.S. Elsen, G. Aswin, A.K. Jaiswal, K.G. Prashanth, G. Manivasagam, A review on development of bio-inspired implants using 3d printing, *Biomimetics* 6 (2021) 65. <https://doi.org/10.3390/biomimetics6040065>.
- [114] P.A. Khan, A. Raheem, C. Kalirajan, K.G. Prashanth, G. Manivasagam, In vivo assessment of a triple periodic minimal surface based biomimetic gyroid as an implant material in a rabbit tibia model, *ACS Materials Au* 4 (2024) 479–488. <https://doi.org/10.1021/acsmaterialsau.4c00016>.
- [115] J.B. Jin, S. Zhou, H. Yang, J. Yang, Z. Zhang, B. Guo, L.C. Zhang, Breaking through the strength-ductility trade-off of LPBF-produced Ti-xNb alloys from mixed powders via ω -phase induced heterostructure, *International Journal of Extreme Manufacturing* 7 (2025) 065003. <https://doi.org/10.1088/2631-7990/aded4e>.
- [116] K. Li, J. Yang, Y. Yi, X. Liu, Y. Liu, L.C. Zhang, W. Zhang, W. Li, D. Chen, S. Zhou, Enhanced strength-ductility synergy and mechanisms of heterostructured Ti6Al4V-Cu alloys produced by laser powder bed fusion, *Acta Materialia* 256 (2023) 119112. <https://doi.org/10.1016/j.actamat.2023.119112>.
- [117] R. Rahmani, M. Antonov, L. Kollo, Y. Holovenko, K.G. Prashanth, Mechanical behavior of Ti6Al4V scaffolds filled with CaSiO₃ for implant applications, *Applied Sciences* 9 (2019) 3844. <https://doi.org/10.3390/app9183844>.
- [118] R. Rahmani, N. Kamboj, M. Brojan, M. Antonov, K.G. Prashanth, Hybrid metal-ceramic biomaterials fabricated through powder metallurgy for improved impact resistance of craniofacial implants, *Materialia* 24 (2022) 101465. <https://doi.org/10.1016/j.mtla.2022.101465>.
- [119] A.M. Birt, V.K. Champagne, R.D. Sisson, D. Apelian, Microstructural analysis of Ti–6Al–4V powder for cold gas dynamic spray applications, *Advanced Powder Technology* 26 (2015) 1335–1347. <https://doi.org/10.1016/j.apt.2015.07.008>.
- [120] M.K. Yadav, R. Shukla, P. Kesavan, S. Nilawar, C. Perugu, P. Sellamuthu, K. Chatterjee, S. Suwas, J. Jayamani, K.G. Prashanth, Microstructural, mechanical, corrosion, and biological behavior of spark plasma sintered commercially pure zinc for biomedical applications, *Materials Advances* 6 (2025) 3546–3560. <https://doi.org/10.1039/d5ma00092k>.

- [121] M.K. Yadav, K. Praveenkumar, R.H. Shukla, S. Nilawar, C.S. Perugu, K. Chatterjee, S. Suwas, J. Jayaraj, K.G. Prashanth, Novel partially biodegradable Ti-6Al-4V/Zn composites fabricated through hybrid additive manufacturing and powder metallurgy, *Advanced Light Materials* 1 (2026) 1–18. <https://doi.org/10.1016/j.almate.2026.03.001>.
- [122] Z. Zhang, Y. Yang, Y. Guo, Z. Xu, P. Sha, Z. Yu, L. Ren, The corrosion resistance and biomineralization of the DCPD-PCL coating on the surface of the additively manufactured NiTi alloy, *Surface and Coatings Technology* 466 (2023) 129653. <https://doi.org/10.1016/j.surfcoat.2023.129653>.
- [123] H. Galarraga, R.J. Warren, D.A. Lados, R.R. Dehoff, M.M. Kirka, P. Nandwana, Effects of heat treatments on microstructure and properties of Ti-6Al-4V ELI alloy fabricated by electron beam melting (EBM), *Materials Science and Engineering: A* 685 (2017) 417–428. <https://doi.org/10.1016/j.msea.2017.01.019>.
- [122] B. Wysocki, P. Maj, R. Sitek, J. Buhagiar, K.J. Kurzydłowski, W. Świeszkowski, Laser and electron beam additive manufacturing methods of fabricating titanium bone implants, *Applied Sciences* 7 (2017) 657. <https://doi.org/10.3390/app7070657>.
- [125] L. Thijs, F. Verhaeghe, T. Craeghs, J. Van Humbeeck, J.P. Kruth, A study of the microstructural evolution during selective laser melting of Ti-6Al-4V, *Acta Materialia* 58 (2010) 3303–3312. <https://doi.org/10.1016/j.actamat.2010.02.004>.
- [126] M. Simonelli, Y.Y. Tse, C. Tuck, On the texture formation of selective laser melted Ti-6Al-4V, *Metallurgical and Materials Transactions A* 45 (2014) 2863–2872. <https://doi.org/10.1007/s11661-014-2218-0>.
- [127] A.A. Antonysamy, J. Meyer, P.B. Prangnell, Effect of build geometry on the β -grain structure and texture in additive manufacture of Ti-6Al-4V by selective electron beam melting, *Materials Characterization* 84 (2013) 153–168. <https://doi.org/10.1016/j.matchar.2013.07.012>.
- [128] J. Yang, H. Yu, J. Yin, M. Gao, Z. Wang, X. Zeng, Formation and control of martensite in Ti-6Al-4V alloy produced by selective laser melting, *Materials & Design* 108 (2016) 308–318. <https://doi.org/10.1016/j.matdes.2016.06.117>.
- [129] X. Yuan, C. Yu, R. Li, J. Kang, P. Niu, D. Zheng, K. Gan, N. Kang, L. Ke, P. Xiao, K. Yang, Influence of stacking fault energy synergistic non-equilibrium solidification on dislocation substructures and mechanical properties of Ti alloys, *J. Alloys Compd.* 1039 (2025) 183134. <https://doi.org/10.1016/j.jallcom.2025.183134>.
- [130] S.K. Gupta, N. Shahidsha, S. Bahl, D. Kedaria, S. Singamneni, P.K.D.V. Yarlagadda, S. Suwas, K. Chatterjee, Enhanced biomechanical performance of additively manufactured Ti-6Al-4V bone plates, *Journal of Mechanical Behavior of Biomedical Materials* 119 (2021) 104552. <https://doi.org/10.1016/j.jmbbm.2021.104552>.
- [131] R. Sabban, S. Bahl, K. Chatterjee, S. Suwas, Globularization using heat treatment in additively manufactured Ti-6Al-4V for high strength and toughness, *Acta Materialia* 162 (2019) 239–254. <https://doi.org/10.1016/j.actamat.2018.09.064>.

- [132] S. Cao, R. Chu, X. Zhou, K. Yang, Q. Jia, C.V.S. Lim, A. Huang, X. Wu, Role of martensite decomposition in tensile properties of selective laser melted Ti-6Al-4V, *Journal of Alloys and Compounds* 744 (2018) 357–363. <https://doi.org/10.1016/j.jallcom.2018.02.111>.
- [133] P. Krakhmalev, G. Fredriksson, I. Yadroitsava, N. Kazantseva, A.D. Plessis, I. Yadroitsev, Deformation behavior and microstructure of Ti6Al4V manufactured by SLM, *Physics Procedia* 83 (2016) 778–788. <https://doi.org/10.1016/j.phpro.2016.08.080>.
- [134] ISO 10993-5:2009, Biological evaluation of medical devices — Part 5: Tests for in vitro cytotoxicity. <https://www.iso.org/standard/36406.html>.
- [135] A.E. Medvedev, A. Neumann, H.P. Ng, R. Lapovok, C. Kasper, T.C. Lowe, V.N. Anumalasetty, Y. Estrin, Combined effect of grain refinement and surface modification of pure titanium on the attachment of mesenchymal stem cells and osteoblast-like SaOS-2 cells, *Materials Science and Engineering: C* 71 (2017) 483–497. <https://doi.org/10.1016/j.msec.2016.10.035>.
- [136] X. Tong, Q. Sun, D. Zhang, K. Wang, Y. Dai, Z. Shi, Y. Li, M. Dargusch, S. Huang, J. Ma, C. Wen, J. Lin, Impact of scandium on mechanical properties, corrosion behavior, friction and wear performance, and cytotoxicity of a β -type Ti–24Nb–38Zr–2Mo alloy for orthopedic applications, *Acta Biomaterialia* 134 (2021) 791–803. <https://doi.org/10.1016/j.actbio.2021.07.061>.
- [137] M. Abedi, D.O. Moskovskikh, A.S. Rogachev, A.S. Mukasyan, Spark plasma sintering of titanium spherical particles, *Metallurgical and Materials Transactions B* 47 (2016) 2725–2731. <https://doi.org/10.1007/s11663-016-0732-8>.
- [138] C.S. Bonifacio, J.F. Rufner, T.B. Holland, K.V. Benthem, In situ transmission electron microscopy study of dielectric breakdown of surface oxides during electric field-assisted sintering of nickel nanoparticles, *Applied Physics Letters* 101 (2012) 093107. <https://doi.org/10.1063/1.4749284>.
- [139] M. Kermani, M. Razavi, M.R. Rahimpour, M. Zakeri, The effect of mechanical alloying on microstructure and mechanical properties of MoSi₂ prepared by spark plasma sintering, *Journal of Alloys and Compounds* 593 (2014) 242–249. <https://doi.org/10.1016/j.jallcom.2014.01.041>.
- [140] D. Kumar, G. Shankar, K.G. Prashanth, S. Suwas, Texture dependent strain hardening in additively manufactured stainless steel 316L, *Materials Science and Engineering: A* 820 (2021) 141483. <https://doi.org/10.1016/j.msea.2021.141483>.
- [141] D. Kumar, G. Shankar, K.G. Prashanth, S. Suwas, Control of texture and microstructure in additive manufacturing of stainless steel 316 L, *Journal of Alloys and Compounds* 976 (2024) 173040. <https://doi.org/10.1016/j.jallcom.2023.173040>.
- [142] R.J. Vikram, L. Kollo, K.G. Prashanth, S. Suwas, Investigating the structure, microstructure, and texture in selective laser-melted sterling silver 925, *Metallurgical and Materials Transactions A* 52 (2021) 5329–5341. <https://doi.org/10.1007/s11661-021-06471-7>.

- [143] B. Hutchinson, J. Komenda, S. Kada, M. Barnett, A. Oskarsson, Observations on remarkable texture in cast zinc, *Scripta Materialia* 166 (2019) 78–80. <https://doi.org/10.1016/j.scriptamat.2019.03.012>.
- [144] R. Chaim, Densification mechanisms in spark plasma sintering of nanocrystalline ceramics, *Materials Science and Engineering: A* 443 (2007) 25–32. <https://doi.org/10.1016/j.msea.2006.07.092>.
- [145] Y. Cheng, Z. Cui, L. Cheng, D. Gong, W. Wang, Effect of particle size on densification of pure magnesium during spark plasma sintering, *Advanced Powder Technology* 28 (2017) 1129–1135. <https://doi.org/10.1016/j.appt.2017.01.017>.
- [146] G. Dirras, J. Gubicza, H. Couque, A. Ouarem, P. Jenei, Mechanical behaviour and underlying deformation mechanisms in coarse- and ultrafine-grained Zn over a wide range of strain rates, *Materials Science and Engineering: A* 564 (2013) 273–283. <https://doi.org/10.1016/j.msea.2012.12.010>.
- [147] H. Li, Q.Q. Duan, X.W. Li, Z.F. Zhang, Compressive and fatigue damage behavior of commercially pure zinc, *Materials Science and Engineering: A* 466 (2007) 38–46. <https://doi.org/10.1016/j.msea.2007.02.062>.
- [148] Y. Xin, X. Zhou, L. Lv, Q. Liu, The influence of a secondary twin on the detwinning deformation of a primary twin in Mg–3Al–1Zn alloy, *Materials Science and Engineering: A* 606 (2014) 81–91. <https://doi.org/10.1016/j.msea.2014.03.068>.
- [149] S. Yu, H. Chi, P. Li, B. Guo, Z. Yu, Z. Xu, P. Liang, Z. Zhang, Y. Guo, L. Ren, Interpenetrating phases composites Ti6Al4V/Zn as partially degradable biomaterials to improve bone-implant properties, *Additive Manufacturing* 93 (2024) 104411. <https://doi.org/10.1016/j.addma.2024.104411>.
- [150] M.A. Amin, K.F. Khaled, S.A.F. Allah, Testing validity of the Tafel extrapolation method for monitoring corrosion of cold rolled steel in HCl solutions – Experimental and theoretical studies, *Corrosion Science* 52 (2010) 140–151. <https://doi.org/10.1016/j.corsci.2009.08.055>.
- [151] Z. Shi, M. Liu, A. Atrens, Measurement of the corrosion rate of magnesium alloys using Tafel extrapolation, *Corrosion Science* 52 (2010) 579–588. <https://doi.org/10.1016/j.corsci.2009.10.016>.
- [152] E. Poorqasemi, O. Abootalebi, M. Peikari, F. Haqdar, Investigating accuracy of the Tafel extrapolation method in HCl solutions, *Corrosion Science* 51 (2009) 1043–1054. <https://doi.org/10.1016/j.corsci.2009.03.001>.
- [153] L. Upadhayay, S. Nilawar, C. Kumar, K. Chatterjee, P. Kumar, Effect of processing Mg–6Zn–0.2Ce through high-pressure torsion on its use as a biomaterial, *Journal of Materials Science* 59 (2024) 5872–5890. <https://doi.org/10.1007/s10853-024-09460-4>.
- [154] M.K. Yadav, R.H. Shukla, L. Xi, Z. Wang, K.G. Prashanth, Metallic multimaterials fabricated by combining additive manufacturing and powder metallurgy, *Journal of Composites Science* 9 (2025) 80. <https://doi.org/10.3390/jcs9020080>.

- [155] J. Karimi, M. Antonov, L. Kollo, K.G. Prashanth, Role of laser remelting and heat treatment in mechanical and tribological properties of selective laser melted Ti6Al4V alloy, *Journal of Alloys and Compounds* 897 (2022) 163207. <https://doi.org/10.1016/j.jallcom.2021.163207>.
- [156] J. Karimi, C. Suryanarayana, I. Okulov, K.G. Prashanth, Selective laser melting of Ti6Al4V: Effect of laser re-melting, *Materials Science and Engineering: A* 805 (2021) 140558. <https://doi.org/10.1016/j.msea.2020.140558>.
- [157] J. Karimi, C. Zhao, K.G. Prashanth, Massive transformation in dual-laser powder bed fusion of Ti6Al4V alloys, *Journal of Manufacturing Processes* 119 (2024) 282–292. <https://doi.org/10.1016/j.jmapro.2024.03.083>.
- [158] S.C. Wang, M. Aindow, M.J. Starink, Effect of self-accommodation on α/α boundary populations in pure titanium, *Acta Materialia* 51 (2003) 2485–2503. [https://doi.org/10.1016/s1359-6454\(03\)00035-1](https://doi.org/10.1016/s1359-6454(03)00035-1).
- [159] C. Zhao, Z. Wang, D. Li, L. Kollo, Z. Luo, W. Zhang, K.G. Prashanth, Cu–Ni–Sn alloy fabricated by melt spinning and selective laser melting: a comparative study on the microstructure and formation kinetics, *Journal of Materials Research and Technology* 9 (2020) 13097–13105. <https://doi.org/10.1016/j.jmrt.2020.09.047>.
- [160] C. Tan, Y. Chew, F. Weng, S. Sui, Z. Du, F.L. Ng, G. Bi, Superior strength–ductility in laser aided additive manufactured high-strength steel by combination of intrinsic tempering and heat treatment, *Virtual and Physical Prototyping* 16 (2021) 460–480. <https://doi.org/10.1080/17452759.2021.1964268>.
- [161] J. Su, X. Ji, J. Liu, J. Teng, F. Jiang, D. Fu, H. Zhang, Revealing the decomposition mechanisms of dislocations and metastable α' phase and their effects on mechanical properties in a Ti–6Al–4V alloy, *Journal of Materials Science & Technology* 107 (2022) 136–148. <https://doi.org/10.1016/j.jmst.2021.07.048>.
- [162] M.Q. Cheng, T. Wahafu, G.F. Jiang, W. Liu, Y.Q. Qiao, X.C. Peng, T. Cheng, X.L. Zhang, G. He, X.Y. Liu, A novel open-porous magnesium scaffold with controllable microstructures and properties for bone regeneration, *Scientific Reports* 6 (2016) 24134. <https://doi.org/10.1038/srep24134>.
- [163] Y. Xin, T. Hu, P.K. Chu, Degradation behaviour of pure magnesium in simulated body fluids with different concentrations of HCO_3^- , *Corrosion Science* 53 (2011) 1522–1528. <https://doi.org/10.1016/j.corsci.2011.01.015>.
- [164] X. Yang, W. Huang, D. Zhan, D. Ren, H. Ji, Z. Liu, Q. Wang, N. Zhang, Z. Zhang, Biodegradability and cytocompatibility of 3D-printed Mg–Ti interpenetrating phase composites, *Frontiers in Bioengineering and Biotechnology* 10 (2022) 891632. <https://doi.org/10.3389/fbioe.2022.891632>.
- [165] X. Han, L. Zhou, Z. Liu, S. Zhang, Q. Wang, X. Lu, M.R.I. Abueida, Q. Wang, Z. Zhang, D. Zhang, Degradation behavior of biomedical partially degradable Ti–Mg composite fabricated by 3D printing and pressureless infiltration, *Journal of Materials Research and Technology* 29 (2024) 3192–3204. <https://doi.org/10.1016/j.jmrt.2024.02.059>.
- [166] A.N. Aufa, M.Z. Hassan, Z. Ismail, Recent advances in Ti–6Al–4V additively manufactured by selective laser melting for biomedical implants: Prospect development, *Journal of Alloys and Compounds* 896 (2022) 163072. <https://doi.org/10.1016/j.jallcom.2021.163072>.

- [167] X. Chen, Q. Liao, M. Gong, Q. Fu, Corrosion performances of selective laser melting Ti6Al4V alloy in different solutions, *Metals* 13 (2023) 192. <https://doi.org/10.3390/met13020192>.
- [168] A. Sharma, M.C. Oh, J.T. Kim, A.K. Srivastava, B. Ahn, Investigation of electrochemical corrosion behavior of additive manufactured Ti–6Al–4V alloy for medical implants in different electrolytes, *Journal of Alloys and Compounds* 830 (2020) 154620. <https://doi.org/10.1016/j.jallcom.2020.154620>.
- [169] R. Liu, K. Memarzadeh, B. Chang, Y. Zhang, Z. Ma, R.P. Allaker, L. Ren, K. Yang, Antibacterial effect of copper-bearing titanium alloy (Ti–Cu) against *Streptococcus mutans* and *Porphyromonas gingivalis*, *Scientific Reports* 6 (2016) 29985. <https://doi.org/10.1038/srep29985>.
- [170] J. Luo, S. Guo, Y. Lu, X. Xu, C. Zhao, S. Wu, J. Lin, Cytocompatibility of Cu-bearing Ti6Al4V alloys manufactured by selective laser melting, *Materials Characterization* 143 (2018) 127–136. <https://doi.org/10.1016/j.matchar.2017.12.003>.
- [171] J. Ma, N. Zhao, D. Zhu, Endothelial cellular responses to biodegradable metal zinc, *ACS Biomaterials Science & Engineering* 1 (2015) 1174–1182. <https://doi.org/10.1021/acsbiomaterials.5b00319>.
- [172] E.R. Shearier, P.K. Bowen, W. He, A. Drelich, J. Drelich, J. Goldman, F. Zhao, In vitro cytotoxicity, adhesion, and proliferation of human vascular cells exposed to zinc, *ACS Biomaterials Science & Engineering* 2 (2016) 634–642. <https://doi.org/10.1021/acsbiomaterials.6b00035>.
- [173] N.Z. Gammoh, L. Rink, Zinc in infection and inflammation, *Nutrients* 9 (2017) 624. <https://doi.org/10.3390/nu9060624>.

Acknowledgements

I would like to express my deepest gratitude to my supervisor, Prof. K. G. Prashanth, for his invaluable guidance, constant encouragement, and unwavering support throughout the course of my doctoral research. His vision, expertise, and mentorship have played a pivotal role in shaping this work and in my growth as a researcher. I am equally grateful to my co-supervisor, Dr. J. Jayaraj, for his constructive insights, technical guidance, and continuous motivation at every stage of the project.

I gratefully acknowledge the financial support provided by the Estonian Research Council under Project ID ETAG21021, which played a crucial role in enabling the successful completion of my doctoral research. I also extend my sincere thanks to the Erasmus+ Mobility Programme for supporting my international research stay, which significantly enriched the scientific outcomes of this work and contributed to my academic growth.

I extend my heartfelt thanks to Prof. Satyam Suwas and Prof. Kaushik Chatterjee for providing me with the opportunity to carry out part of my research work at IISc Bengaluru. I also sincerely thank Dr. Prabhu Kumar Sellamuthu for his scientific support, guidance, and for facilitating access to research facilities that enriched my work and broadened my learning experience.

My sincere appreciation goes to my senior colleagues, Dr. Chandrasekhar Perugu and Dr. K. Praveenkumar, for their invaluable scientific discussions, continuous encouragement, and support throughout my Ph.D. journey. I am also grateful to my colleagues and friends at TalTech, Dr. Riddhi Shukla, Shangavi Subramaniam, and Lokesh Raj, as well as to my friends at IISc, Vamsi Krishna, Gautham V., Y. Akshay, Prasadinee Maharana, and Saurav Ranjan, for their friendship, collaborative spirit, and support that made this journey both productive and memorable.

I acknowledge the technical and non-technical staff at TalTech and IISc Bengaluru for their assistance, timely help, and for ensuring a smooth workflow in the laboratory and research facilities.

Finally, I would like to express my profound gratitude to my family for their unconditional love, patience, and belief in me. Their constant emotional support has been my greatest strength throughout this journey.

Abstract

Design and Development of Novel Partially Biodegradable Composite by Hybrid Manufacturing

The development of biomaterials that closely replicate the structural, mechanical, and biological functions of natural bone remains a critical challenge in orthopedic and tissue engineering applications. Conventional metallic implants such as Ti64, SS, and Co-Cr alloys provide excellent mechanical strength but suffer from stress shielding and long-term incompatibility due to their nondegradable nature. Conversely, biodegradable metals like Mg, Zn, and Fe offer controlled resorption and reduced long-term complications, yet their mechanical limitations restrict their use in load-bearing environments. This thesis addresses these challenges by systematically investigating Ti64 and Zn as potential candidates for developing next-generation partially biodegradable metallic systems through advanced manufacturing approaches.

The work begins with a detailed evaluation of Ti64 fabricated using SPS and SLM. SLM-processed Ti64 exhibited a fine α' martensitic microstructure, superior hardness, enhanced mechanical strength, and improved cytocompatibility response compared to SPS-Ti64. Similarly, SPS-processed Zn demonstrated refined grain morphology, controlled degradation behavior, and favorable biological response, outperforming conventionally cast Zn. These findings established Ti64 and Zn as structurally and biologically complementary materials.

The central contribution of this work is the development of a novel Ti64-Zn MBMC. A bioinspired Ti64 hexagonal lattice fabricated via SLM served as the structural scaffold, into which Zn was infiltrated using SPS. The resulting composite exhibited a continuous architecture, suitable mechanical properties, predictable degradation behavior, and excellent cytocompatibility at diluted ion concentrations. Importantly, the Ti64 scaffold maintained mechanical integrity as Zn gradually degraded, demonstrating the potential for controlled load transfer and enhanced bone regeneration.

Overall, this thesis presents a comprehensive pathway for designing partially biodegradable metallic composites using hybrid AM-PM approaches and establishes Ti64-Zn MBMC as a promising candidate for next-generation biomedical implants.

Lühikokkuvõte

Uue Osaliselt Biolaguneva Komposiidi Projekteerimine ja Väljatootamine Hübriidtootmise Teel

Biomaterjalide väljatootamine, mis jälgendavad täpselt loodusliku luu struktuurilisi, mehaanilisi ja bioloogilisi funktsioone, on ortopeedilistes ja koetehnoloogia rakendustes endiselt kriitilise tähtsusega väljakutse. Tavapärased metallimplantaadid, nagu Ti64, roostevaba teras ja Co-Cr sulamid, pakuvad suurepäraselt mehaanilist tugevust, kuid kannatavad pingekaitse ja pikaajalise kokkusobimatuse all oma mittelaguneva olemuse tõttu. Seevastu biolagunevad metallid, nagu Mg, Zn ja Fe, pakuvad kontrollitud resorptsiooni ja vähendavad pikaajalisi tüsistusi, kuid nende mehaanilised piirangud piiravad nende kasutamist koormust kandvates keskkondades. See väitekiri käsitleb neid väljakutseid, uurides süstemaatiliselt Ti64 ja Zn kui potentsiaalseid kandidaate järgmise põlvkonna osaliselt biolagunevate metallsüsteemide arendamiseks täiustatud tootmismeetodite abil.

Töö algab SLM-i ja SPS-i abil valmistatud Ti64 detailse hindamisega. SLM-töödeldud Ti64-l oli SPS-Ti64-ga võrreldes peen α' martensiitne mikrostruktuur, parem kõvadus, suurem mehaaniline tugevus ning parem . Samamoodi näitas SPS-töödeldud Zn rafineeritud teramorfoloogiat, kontrollitud lagunemiskäitumist ja soodsat bioloogilist reaktsiooni, edestades tavapäraselt valatud Zn-i. Need leiud kinnitasid, et Ti64 ja Zn on struktuurilt ja bioloogiliselt teineteist täiendavad materjalid.

Selle töö keskseks panuseks on uude Ti64-Zn MBMC väljatootamine. Struktuurkarkassina toimis SLM abil valmistatud bioloogiliselt inspireeritud Ti64 kuusnurkne võre, millesse SPS-i abil infiltreeriti Zn. Saadud komposiidil oli pidev läbipõimuv arhitektuur, kohandatud mehaanilised omadused, prognoositav lagunemiskäitumine ja suurepärase tsütosobivus lahjendatud ionkontsentratsioonide korral. Oluline on see, et Ti64 karkass säilitas mehaanilise terviklikkuse Zn järkjärgulise lagunemise ajal, mis näitab potentsiaali kontrollitud koormuse ülekandmiseks ja luu regeneratsiooni paranemiseks.

Kokkuvõttes esitab see väitekiri tervikliku tee osaliselt biolagunevate metallkomposiitide kujundamiseks hübriidsete AM-PM meetodite abil ning seab Ti64-Zn MBMC-d paljulubavateks kandidaatideks järgmise põlvkonna biomeditsiiniliste implantaatide jaoks.

Appendix

Publication I

M.K. Yadav, A. Yarlapati, Y.N. Aditya, K. Praveenkumar, V. Pandey, C.S. Perugu, A. Nain, K. Chatterjee, S. Suwas, J. Jayaraj, K.G. Prashanth, Processing and development of porous titanium for biomedical applications: a comprehensive review, *Journal of Manufacturing and Materials Processing* 9 (2025) 401. <https://doi.org/10.3390/jmmp9120401>.



Review

Processing and Development of Porous Titanium for Biomedical Applications: A Comprehensive Review

Mayank Kumar Yadav ¹, Akshay Yarlapati ², Yarlapati Naga Aditya ³, Praveenkumar Kesavan ⁴, Vaibhav Pandey ⁵, Chandra Shekhar Perugu ⁶, Amit Nain ⁷, Kaushik Chatterjee ², Satyam Suwas ², Jayamani Jayaraj ^{8,9} and Konda Gokuldoss Prashanth ^{1,10,11,*}

- ¹ Department of Mechanical and Industrial Engineering, Tallinn University of Technology, 19086 Tallinn, Estonia
- ² Department of Materials Engineering, Indian Institute of Science, Bengaluru 560012, India
- ³ Department of Mechanical and Mechatronics Engineering, University of Waterloo, 200 University, Avenue West, Waterloo, ON N2L 3G1, Canada
- ⁴ Faculty of Materials Science and Technology, VSB-Technical University of Ostrava, 17. listopadu 2172/15, 70 800 Ostrava, Czech Republic
- ⁵ Department of Ceramic Engineering, Indian Institute of Technology (BHU), Varanasi 221005, India
- ⁶ Emerging Nanoscience Research Institute (EnRI), Nanyang Technological University, 50 Nanyang Avenue, Singapore 639798, Singapore
- ⁷ Department of Applied Mechanics and Biomedical Engineering, Indian Institute of Technology-Madras, Chennai 600036, India
- ⁸ Materials Technology, School of Information and Engineering, Dalarna University, 79188 Falun, Sweden
- ⁹ Department of Mechanical and Materials Engineering, Karlstad University, 65188 Karlstad, Sweden
- ¹⁰ Centre for Biomaterials, Cellular and Molecular Theranostics (CBCMT), School of Engineering, Vellore Institute of Technology, Vellore 632014, India
- ¹¹ National Engineering Research Center of Near-Net-Shape Forming for Metallic Materials, South China University of Technology, Guangzhou 510640, China
- * Correspondence: kgprashanth@gmail.com

Abstract

Titanium (Ti) and its alloys are widely used in orthopedic applications, including total hip and knee replacements, bone plates, and dental implants, because of their superior biocompatibility, bioactivity, corrosion resistance, and mechanical robustness. These alloys effectively overcome several limitations of conventional metallic implants, such as 316L stainless steel and Co-Cr alloys, particularly with respect to corrosion, fatigue performance, and biological response. However, dense Ti alloys possess a relatively high elastic modulus, which can cause stress shielding in load-bearing applications. This challenge has motivated significant research toward engineered porous Ti structures that exhibit a reduced and bone-matched modulus while preserving adequate mechanical integrity. This review provides a comprehensive examination of powder metallurgy and additive manufacturing approaches used to fabricate porous Ti and Ti-alloy scaffolds, including additive manufacturing and different powder metallurgy techniques. Processing routes are compared in terms of achievable porosity, pore size distribution, microstructural evolution, mechanical properties, and biological outcomes, with emphasis on the relationship between processing parameters, pore architecture, and functional performance. The reported findings indicate that optimized powder-metallurgy techniques can generate interconnected pores in the 100–500 μm range suitable for osseointegration while maintaining compressive strengths of 50–300 MPa, whereas additive manufacturing enables the precise control of hierarchical architectures but requires careful post-processing to remove adhered powder, stabilize microstructures, and ensure corrosion and wear resistance. In addition, this review integrates fundamental aspects of bone biology and bone implant interaction to contextualize the functional requirements of porous Ti scaffolds.



Academic Editor: Shuo Yin

Received: 31 October 2025

Revised: 22 November 2025

Accepted: 1 December 2025

Published: 4 December 2025

Citation: Yadav, M.K.; Yarlapati, A.; Aditya, Y.N.; Kesavan, P.; Pandey, V.; Perugu, C.S.; Nain, A.; Chatterjee, K.; Suwas, S.; Jayaraj, J.; et al. Processing and Development of Porous Titanium for Biomedical Applications: A Comprehensive Review. *J. Manuf. Mater. Process.* **2025**, *9*, 401. <https://doi.org/10.3390/jmmp9120401>

Copyright: © 2025 by the authors. Licensee MDPI, Basel, Switzerland. This article is an open access article distributed under the terms and conditions of the Creative Commons Attribution (CC BY) license (<https://creativecommons.org/licenses/by/4.0/>).

Keywords: titanium; porous material; powder metallurgy; biomaterial; tissue engineering

1. Introduction

The demand for orthopedic implants is experiencing an unprecedented surge, primarily due to the increased prevalence of conditions such as osteoporosis, which weakens bones, and osteoarthritis, which causes joint inflammation [1]. Human bone joints are most likely to be affected by degenerative and inflammatory diseases [1]. Degenerative diseases impair the mechanical strength of bones either through excessive stress or due to a lack of the body's natural healing mechanisms. Studies suggest that nearly 90% of individuals above the age of 40 are affected to some extent by degenerative joint disorders [2]. The replacement of diseased joint surfaces using metallic, ceramic, or polymeric material through arthroplasty surgery is the ultimate solution to this problem [3]. Arthroplasty is a surgical procedure where damaged natural joint surfaces are replaced with specialized implant materials to alleviate pain and improve mobility by creating a new prosthetic joint. Bones comprise four cell populations crucial for growth and resorption: osteoblasts, osteoclasts, osteogenic cells, and osteocytes, all originating from bone marrow. Although bones possess the capacity for physiological remodeling and self-repair, they are unable to effectively cope with severe injuries such as critical-sized defects (CSDs) [4]. CSDs are defects that will not heal on their own during the natural lifespan of the individual [5], and typically, defects in the range of 2 cm to 5 cm are considered critical in humans [6,7]. The standard approaches for treating CSDs include autograft (bone harvested from the same patients), allograft (bone harvested from other patients), and xenograft (bone sourced from other species) [8,9]. While these approaches often yield positive results, they come with specific limitations.

The application of autograft is not suitable for large-sized defects such as spinal arthrodesis [10], while allograft poses risks of immunologic rejection, donor dependency, poor osteogenesis, and a higher resorption rate [11]. Although xenografts present a promising solution to organ shortages, their clinical use is restricted by immune barriers, zoonotic infection risks, ethical concerns, and physiological challenges [12–14]. Such challenges and constraints drive researchers to actively explore and create dependable bone substitutes that closely mimic the characteristics of natural human bone. The field of biomaterials research began with the inaugural biomaterial conference held at Clemson University in South Carolina in 1969 [15]. Extensive research has led to the development of various metallic [16], ceramic [17,18], and polymeric [19] materials suitable for mimicking the properties of a healthy human bone. These materials belong to different classes, each possessing distinct physical, mechanical, chemical, and biological properties. For instance, metallic alloys, known for their robust mechanical properties, are commonly used in load-bearing joint prostheses [20–23]. Ceramic materials, renowned for their wear resistance and bioactive properties, are often used to coat metallic implants [24–29]. Polymers, being biodegradable and harmless to the body, are utilized in bone repair applications [30].

Scientists attribute the primary cause of failure in metallic implants to the 'stress shielding effect' [31–33]. This effect occurs due to the mismatch in mechanical properties like Young's modulus, yield strength, ultimate tensile strength, fracture toughness, fatigue strength, and ductility (including elongation and toughness under cyclic loading) between natural bone and metallic alloys under *in vivo* conditions, leading to the resorption of bone tissues surrounding the implant material [34]. Moreover, metallic implants are limited by issues such as poor wear and corrosion resistance, as well as insufficient biocompatibility [35–40]. Traditional metallic implants, such as 316L stainless steel and

Co-Cr alloys, particularly suffer from localized corrosion, ion release, and inadequate long-term biological compatibility. Although titanium (Ti) and its alloys are also metallic materials, they offer significantly improved corrosion resistance, superior biocompatibility, and better mechanical performance compared to these earlier metallic systems. Owing to their high durability and excellent biological response, Ti-based materials have become the focus of implant development; however, they still present challenges such as a relatively high elastic modulus in dense form, which must be addressed through alloy design and porosity engineering. The commercial production of titanium began with the invention of the Kroll process in 1946 [41], followed shortly by the introduction of titanium alloy-based implants within a year [42]. Since its inception, titanium and its alloys have found extensive use in biomedical applications such as spinal fusion, skeletal repair, and dental implants [15,43–47]. Titanium and its alloys have demonstrated superiority over medical-grade stainless steel, cobalt–chromium, and magnesium-based alloys concerning biocompatibility, mechanical strength, and corrosion resistance. However, their higher Young’s modulus (~110 GPa) initially limited their biomedical applications. The development of second-generation titanium alloys, specifically β alloys, aimed to reduce this modulus. Titanium alloys with a low elastic modulus, such as Ti-Nb-Zr-T, have been specifically developed to closely align with the modulus of different types of human bone [48–52].

The concept of porous biomaterials for osseointegration was introduced by Weber and White in 1972 [53], leading to extensive research on porous implant materials using various processing methods [54–57]. Porous scaffolds, characterized by a lower effective Young’s modulus than conventional titanium implants, offer several advantages. These materials enhance biological fixation by encouraging bone tissue to grow into the implant’s porous structure, enabling even stress distribution between the implant and surrounding bone. Moreover, porous scaffolds enhance colonization and subsequent substitution by biological cells [58,59]. Numerous manufacturing methods have been developed to produce porous structures for implant applications. Palka et al. [60] reviewed porous titanium implants, emphasizing various types of porosity in their structure, while Koju et al. [61] examined porous Ti6Al4V bone implants produced by additive manufacturing. However, a systematic review encompassing all production methods to fabricate porous implants is still not available. Hence, the primary aim of this review is to survey all existing methods to fabricate porous titanium through powder metallurgy and to provide a comprehensive overview of the research status of titanium and its alloys targeted for orthopedic applications. This article is divided into nine sections with several sub-sections, focusing primarily on the various techniques employed to develop porous titanium scaffolds for orthopedic applications using powder metallurgy.

2. Material Characteristics Critical to Implant Functionality

“As defined by Williams in 1987, biomaterials are non-living materials designed for use in medical devices that interact with biological systems”. Biomaterials are artificial or natural materials that restore the integrity and functionality of damaged or diseased biological structures. For an implant to achieve longevity and high compatibility with the body, the biomaterial must possess certain properties suitable for biomedical applications. These properties include biocompatibility, osseointegration, mechanical strength, wear resistance, and corrosion resistance. Figure 1 outlines the fundamental requirements that must be considered in the design and development of implants.

2.1. Mechanical Properties

The primary function of bone is to provide structural support under mechanical loading and protect vital organs. In cases of trauma or diseased biological structures,

implants often replace the function of the affected organ. Currently, most implants used in orthopedic traumas and arthroplasty are of metallic composition due to their excellent mechanical strength [62]; therefore, the mechanical analysis of metallic implants is of prime concern. Essential properties include Young’s modulus, fracture toughness, hardness, yield strength, ultimate tensile strength, stiffness, ductility, time-dependent deformation, and creep. Wolff’s law of bone remodeling (1892) states that mechanical load can affect bone architecture [63] and hence promote bone remodeling and fracture healing [64,65]. Fatigue strength is also critical, as it affects material performance under cyclic loads, influencing the long-term success of implants [15]. Young’s modulus is crucial for the success of implants. A significant mismatch between the modulus of bone and the implant material can negatively impact load transfer from the implant to the bone and within the bone, leading to bone resorption and implant loosening. This biomechanical incompatibility is the stress-shielding effect [15,66,67]. Table 1 lists the mechanical properties of materials used for orthopedic implant applications and human bone.

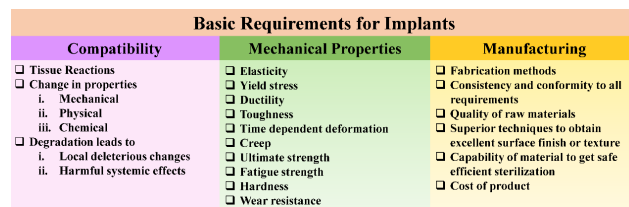


Figure 1. Diagram showing the basic requirements for implant materials regarding compatibility, mechanical properties, and manufacturing.

Table 1. Physical and mechanical properties of metallic, ceramic, and polymeric biomaterials (ρ —density in g/cm³; E—Young’s modulus in GPa; YS—yield strength in MPa; UTS—ultimate tensile strength in MPa; UCS—Ultimate compressive strength in MPa; and FS—fatigue strength in MPa, 10⁷ cycles).

Material	ρ	E	YS	UTS	UCS	FS	Ref.
Natural Bone							
Cortical bone	1.8–2.0	7–30	-	164–240	100–230	27–35	[68]
Cancellous bone	1.0–1.4	0.01–3.0	-	-	2–12	-	
Metals and Alloys							
Ti-6Al-4V (cast)	4.43	114	760–880	895–930	-	600–700	[68]
Ti-6Al-4V (wrought)	4.43	114	827–1103	860–965	896–1172	500–800	
Ti-6Al-7Nb	4.52	105	880	900	-	-	[15]
SS316L	8.0	193	170–310	540–1000	480–620	240–480	[68]
Fe ₂₀ Mn	7.73	207	420	700	-	-	[69]
Zn-Al-Cu	5.79	90	171	210	-	-	
Co-Cr-Mo	8.3	240	500–1500	900–1540	-	500–900	
CoCr20Ni15Mo7	7.8	195–230	240–450	450–960	-	-	
Pure Mg (cast)	1.74	41	21	87	40	-	[34]
Pure Mg (wrought)	1.74	41	100	180	100–140	-	
AZ31 (Mg-based alloy)	1.78	45	185	263	-	-	
AZ91 (Mg-based alloy)	1.81	45	160	150	-	-	

Table 1. *Cont.*

Material	ρ	E	YS	UTS	UCS	FS	Ref.
Ceramics							
Alumina Ceramics	4	260–410	-	400–580	-	-	[34]
Synthetic hydroxyapatite	3.15	6–102	-	-	0.22–4.1	-	[18,70]
Zirconia	3.98	210	-	800–1500	1990	-	[71]
Polymers							
PLGA	1.2–1.3	1.69	3.8–26.6	13.9–16.7	-	-	
PCL	1.15	281–686	8.37–14.66	68–103	-	-	[34]
PLA	1.8	3750	70	59	-	-	

2.2. Corrosion and Wear Resistance

Corrosion and wear are inevitable problems associated with orthopedic implants [72]. When a metallic implant is introduced into the body, it encounters biological fluid containing various cations and anions, leading to electrochemical corrosion on the implant surface. Four types of corrosion are typically observed in orthopedic implants: galvanic, pitting crevice, and fretting corrosion. Galvanic corrosion occurs due to the electrochemical potential difference between two different or the same metal surfaces when introduced in a biological fluid [73–75]. Studies showed that when Ti-based and Co-based alloys are coupled, the corrosion rate was observed to be as low as 0.02 $\mu\text{A}/\text{cm}^2$, and no instances of corrosion were found on the metallic interface [76]. Pitting corrosion is a localized form of corrosion that creates cavities in the material [77–79]. In the case of metallic implants, chloride ion breakdowns and the protective passive oxide films result in the formation of pits at the site [80,81]. Crevice corrosion is like pitting corrosion in terms of propagation mechanism but differs in the initiation mechanism [82–84]. Crevice corrosion generally occurs in confined spaces with low oxygen tension and high chloride concentration, destroying the passivation layer [85]. The mechanism of fretting corrosion differs from other types of corrosion. In fretting corrosion, the passivation layer is disrupted due to micro-motion between parts of an implant [86–88]. Continuous relative motion between two surfaces under load generates wear debris around the implant-bone interface. Research indicates that inadequate wear resistance can result in implant loosening, while the accumulation of these wear particles may provoke negative tissue responses [89]. In natural joints, synovial fluid functions as an effective lubricant, providing boundary and mixed lubrication regimes that significantly reduce wear [90]. However, the stability of this lubricant film depends strongly on surface chemistry, roughness, and pore geometry, which regulate protein adsorption and fluid retention. Poorly designed surface features or trapped debris can disrupt the synovial film and accelerate third-body abrasion. Therefore, implant materials and surface designs must ensure adequate corrosion and wear resistance while also supporting stable synovial lubrication to prevent premature mechanical failure.

Corrosion in metallic implants is an electrochemical degradation process that occurs when the metal interacts with physiological fluids. As described in the review article by Eliaz et al. [91], the human body behaves as an electrolyte containing chloride ions, proteins, and dissolved oxygen, which facilitates metal dissolution through anodic and cathodic reactions. The breakdown of the passive oxide film, especially under mechanical loading or fretting conditions, results in the release of metallic ions and particulate debris into surrounding tissues. This degradation can lead to local inflammatory responses, hypersensitivity, cytotoxic effects, and ultimately implant loosening or failure. The article emphasizes that corrosion is strongly influenced by alloy composition, microstructure,

mechanical wear, and the stability of the protective oxide layer on the implant surface. Therefore, selecting materials with high corrosion resistance, such as titanium and its alloys, and optimizing surface treatments are essential for minimizing clinical complications associated with corrosion-induced degradation in biomedical implants [91].

The corrosion mechanism inside the human body can be easily understood by taking the example of Fe and Ti in biological environments. In physiological (aqueous) environments, the corrosion of metallic implants is propelled by coupled electrochemical half-reactions: metal dissolution (anodic) and reduction (cathodic) at the metal/electrolyte interface. For titanium alloys (e.g., Ti-6Al-4V), corrosion begins with the oxidation of titanium atoms, producing Ti^{4+} ions that hydrolyze to form a stable titanium dioxide (TiO_2) passive film. This passivation layer strongly inhibits further metal dissolution under steady-state conditions, but local disruption (due to mechanical stress, chloride, or reactive oxygen species) can lead to breakdown and renewed dissolution. Studies show that inflammation (e.g., H_2O_2) and cathodic activation can degrade the oxide film and drive selective dissolution of phases, particularly the β -phase in Ti-6Al-4V. The relevant electrochemical reactions can be expressed as follows:

For titanium alloys, we have the following:

Anodic Reactions (Oxidation)

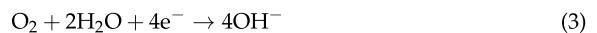


Passive Film Formation



This is consistent with the mechanism of oxide-film stabilization seen in studies of Ti-6Al-4V [92].

Cathodic Reaction (Reduction)



This is the dominant cathodic process in neutral, oxygenated physiological solutions [93].

For Fe-based alloys, corrosion typically proceeds via continuous dissolution due to the relatively less stable protective films in chloride-rich physiological environments.

The primary anodic reactions are as follows:



Meanwhile, the cathodic reaction is generally the same oxygen-reduction process:



These equations and their relevance to in vivo degradation have been documented in the context of biodegradable metal implants [93,94].

2.3. Porosity Effect

Porosity is crucial in developing effective implants for bone tissue engineering. The key factors include pore interconnectivity, porosity volume, and pore sizes. The porous structure must have interconnected pores of appropriate size [95,96]. Interconnected pores are vital as they facilitate cell infiltration, in vivo vascular formation, osteogenesis, cell proliferation, oxygen and nutrient flow, and waste removal [97,98]. It is also reviewed that

interconnectivity provides a way for the ingrowth of blood vessels to facilitate multiple vessel formation [99]. Earlier studies suggest that a minimum interconnection size of over 50 μm is suitable for bone ingrowth [100]. The porosity of the implant enhances bone integration because the porous surface provides an interlocking medium to the surrounding tissue and implant, resulting in good biomechanical compatibility and high resistance to fatigue loading [101,102]. It has been reported that pore sizes ranging between 100 μm and 200 μm are suitable for osseointegration [15].

It is important to note that any increase in the implant's porosity content decreases the mechanical properties of the system [103]. Therefore, without compromising the mechanical properties, the porosity of the system should be optimized, and the pore size should be strictly controlled. Different techniques for adding space holder materials of defined size, densification of the green compacts, sintering conditions, etc., can be employed to incorporate pores in the final structure [104]. A detailed discussion of the production of porous structures using different techniques will be discussed in subsequent sections.

2.4. Surface Wettability and Its Role in Implant Performance

Surface wettability is a critical design parameter for metallic implants, directly influencing both their biological and tribological performance. Wettability governs the interaction of synovial fluid, proteins, and cells with the implant surface, thereby affecting lubrication, friction, wear, and early-stage osseointegration. Hydrophilic surfaces generally facilitate more favorable biological interactions compared to hydrophobic surfaces, largely because wettability affects the first biomolecular events at the implant interface. Surface wettability is known to regulate four major aspects of host response: (i) adsorption and conformation of proteins and macromolecules that form the initial conditioning layer; (ii) adhesion, spreading, and differentiation of hard and soft tissue cells; (iii) bacterial adhesion and biofilm formation; and (iv) the overall rate and quality of *in vivo* osseointegration [105]. These interactions begin within milliseconds of implantation and significantly depend on the hydrophilic or hydrophobic nature of Ti surfaces.

Recent works have demonstrated that micro- and nano-scale surface textures strongly influence the spreading characteristics and retention of lubricants and biological fluids on Ti alloys. Several studies [106,107] highlight that multiscale fractal roughness enhances dynamic wetting, fluid transport, and boundary lubrication, thereby reducing wear at articulating implant interfaces. These findings emphasize that wettability is not only important for osseointegration but also for the flow behavior of synovial fluid, which plays a major role in limiting wear during joint articulation. Insights from Gittens et al. [108–110] further confirm that hydrophilic surfaces support improved protein adsorption in favorable conformations, enhance osteoblast maturation, and promote faster bone–implant contact compared to hydrophobic surfaces. Hydrophilic and superhydrophilic surfaces also reduce hydrocarbon contamination and strengthen the biochemical environment for cell attachment, proliferation, and differentiation [111]. Conversely, hydrophobic surfaces may denature adsorbed proteins, inhibit cell adhesion, and alter the biological cascade leading to integration. Overall, incorporating appropriate surface wettability, often achieved through micro/nano-texturing, plasma modification, chemical treatments, or photocatalytic activation, provides a significant advantage for titanium implants [112]. It enhances lubrication and wear performance in load-bearing joints and concurrently improves osseointegration, offering a dual benefit highly relevant to porous titanium structures discussed in this review.

2.5. Biocompatibility

The biocompatibility of any material is the basis of understanding the host response to implants and is defined diversely by different researchers and regulatory bodies. According to the US Food and Drug Administration, biocompatibility is defined as the effect that the materials induce no measurable harm to the host [113]. It is observed that improper biocompatibility leads to dysesthesia (loss of sense), discomfort, pain, infection, resorption of bone [114], etc. The ions released from the metallic implant may induce hypersensitivity and lead to implant failure [115]. Williams (1987) [116] defines biocompatibility as a material's capacity to generate a suitable response from the host in a given medical application. This implies that a biocompatible material must exhibit both bioactivity and bifunctionality.

The biocompatibility of any material can be defined as the 'ability of a material to perform with an appropriate host response in a specific application', which means that a biocompatible material should be bioactive and bifunctional. Similarly, Retner et al. [117] defined that no material can be biocompatible if it leaches cytotoxic substances when implanted. The success of biomaterials largely depends on the body's reaction to the implant, which measures the material's biocompatibility. In other words, an implant material is considered biocompatible if it elicits a positive response when exposed to a biological environment [118]. Biocompatibility is primarily determined by two key factors: the biological response the material triggers in the host and the extent to which the material degrades within the bodily environment [15]. Therefore, to achieve good biocompatibility, non-toxic alloying elements with excellent corrosion and wear resistance should be chosen during the design and development of metallic implants.

As discussed in Section 2.2, corrosion can directly affect the overall success rate of the implant, as biocompatibility and corrosion are intrinsically linked. As the degradation of metallic implants *in vivo* directly influences the host response. A biocompatible material must not trigger thrombosis, toxic or allergic reactions, adverse immune responses, or destruction of cellular components, and it should maintain its structural integrity without releasing harmful ions into surrounding tissues [91]. However, corrosion alters the implant surface chemistry and accelerates metal-ion release, which can destabilize local biological equilibrium and initiate inflammation or hypersensitivity. As corrosion progresses, ions such as Ni, Cr, Co, or V can accumulate and provoke cytotoxic or allergenic responses, sometimes even at low corrosion rates that do not compromise mechanical performance [91].

Body fluid composition further governs this relationship. Chloride ions promote passive-film breakdown, fluctuating pH during inflammation (as low as 4.0) increases localized corrosion, and reduced dissolved oxygen levels hinder repassivation, collectively intensifying degradation and influencing biocompatibility outcomes [119]. Proteins and macromolecules in extracellular fluids can bind metal ions and transport them away from the surface, destabilizing the electrical double layer, or alternatively form an adsorbed barrier that slows corrosion; thus, protein–metal interactions directly affect degradation rates and biological responses. Cells adhering to implant surfaces may either protect the metal by forming a physical barrier or enhance corrosion through secretion of reactive oxygen species such as O_2^- and H_2O_2 , which accelerate metal dissolution and negatively impact surrounding tissue [91].

2.6. Osseointegration

According to the American Academy of Implant Dentistry (1986), osseointegration refers to the direct contact between normal remodeled bone and an implant without any intervening non-bone tissue, ensuring sustained load transfer and distribution from the implant to and within the bone tissue. Clinically, osseointegration can be defined as the process by which a clinically asymptomatic, rigid fixation of alloplastic materials is

achieved and maintained in bone under functional loading [120]. Factors such as design, surface chemistry, roughness, chemical composition, and loading conditions should be considered before developing an implant for optimal osseointegration [121]. Figure 2 shows a schematic diagram illustrating the timeline of osseointegration of a metallic implant with respect to cellular events for 28 days [122].

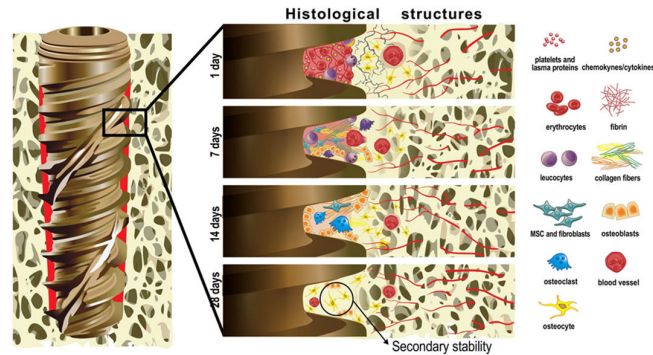


Figure 2. A schematic diagram illustrating the timeline of osseointegration of a metallic implant with respect to cellular events for a duration of 28 days. Reproduced with permission from [122].

3. Bone Metabolism

Bone is a rigid, living tissue that provides support during mechanical loading and protects vital organs inside the body [123]. When a baby is born, their body contains approximately 300 soft bones. These bones are primarily made of cartilage, which allows for flexibility and growth. As the baby matures, bones gradually fuse and harden through ossification. By adulthood, this fusion reduces the total number of bones to 206, providing a more rigid and supportive skeletal structure. To understand bone metabolism, it is necessary to grasp bone physiology and mechanical properties. The different structural levels of bone are shown in Figure 3, illustrating that the bone tissue comprises collagen fibers at the nanoscale.

3.1. Bone Physiology

At the microscopic level, bone structure can be classified into two types based on the arrangement of fibers: woven bone and lamellar bone [124]. The following sections will explore these two types in detail.

3.1.1. Woven Bone

Woven bone, considered an immature type of bone tissue, typically has a mineral grain size ranging from 10 to 15 nanometers. It is commonly located in the metaphyseal region and at sites of fracture healing, such as the callus [125]. These are coarse-fibred and collagen fibers and are randomly oriented throughout the structure. It can also be inferred that the direction-independent mechanical behavior of woven bone results from nonuniform collagen [126].

3.1.2. Lamellar Bone

Lamellar bone is another structure of bone that can be distinguished at the microscopic level. Unlike woven bone, it consists of a mineralized matrix known as hydroxyapatite, with the chemical formula $\text{Ca}_{10}(\text{PO}_4)_6(\text{OH})_2$. In the human femur, hydroxyapatite crystals typically measure between 20 and 80 nm in length and from 2 to 5 nm in thickness [125]. As

implied by their name, lamellar bones are structured in layers and feature collagen fibers aligned with stress directions, contributing to their anisotropic mechanical behavior [126].

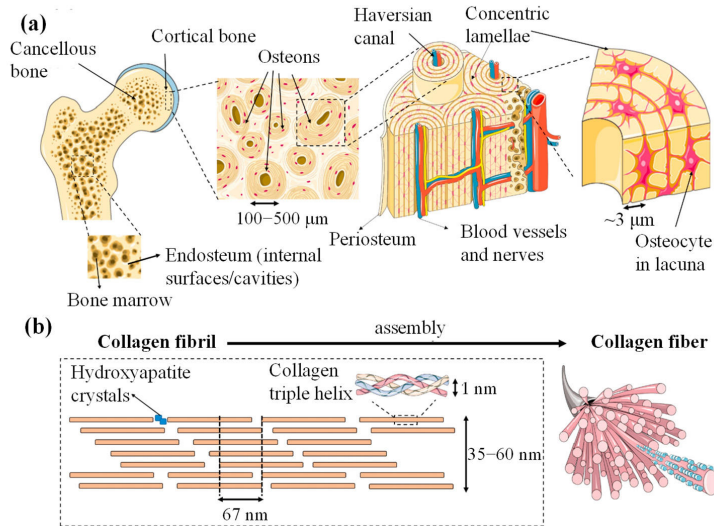


Figure 3. (a) Macro-to-microscopic picture of cancellous and cortical bones. The endosteum structure lines the spaces of cancellous bone, where bone marrow is stored. The periosteum barrier protects the cortical tissue that is tightly packed within osteons. Haversian canals, which comprise blood vessels and nerve tissue, surround concentric lamellae with thicknesses of around 3 μm to create osteons. Osteocytes live in the osteon’s lacuna structures. (b) At the nanometric scale, bone tissue comprises collagen fibers with 67 nm periodic spacing and 40 nm gaps for mineral components. Reproduced with permissions from [127].

Further, based on structural organization, woven and lamellar bones are organized into trabecular and cortical bones [125,128]. Trabecular bone is highly porous, having 50 to 90% porosity and large pores up to several millimeters in diameter. Therefore, these bones are also known as spongy bones or cancellous bones. The trabecular bone bears compressive forces under physiological loading conditions [126]. These bones are typically located in the metaphyseal and epiphyseal regions of both long and cuboidal bones. The distal end radius is an example of a trabecular bone. Similarly, cortical bones are less porous and possess small pores of size up to 1 mm in diameter. Therefore, it is also known as compact bone, contributing to 80% of the weight of the human skeleton. It is harder, stronger, and stiffer than trabecular bone due to less porosity. The humerus and femur are examples of cortical bone.

3.2. Chemical Composition of Bone

Bone is primarily composed of approximately 70% inorganic material, 20% organic content, and 10% water. The inorganic portion mainly consists of crystalline hydroxyapatite (HAp) $\text{Ca}_{10}(\text{PO}_4)_6(\text{OH})_2$, while around 90% of the organic component is made up of Type I collagen. The remaining 10% includes non-collagenous proteins, lipids, and various other macromolecules [125,126]. HAp is the principal inorganic component of natural bone and has been widely studied for orthopedic and dental applications because of its exceptional biocompatibility and bioactivity. Its crystal structure is hexagonal, and its Ca/P molar ratio of 1.67 closely matches that of biological apatite, enabling strong chemical affinity with native bone tissue [17,18]. Synthetic HAp exhibits the ability to directly bond with bone through the formation of a biologically active apatite layer, which stimulates osteoblast

adhesion, proliferation, and mineralization. In addition to its osteoconductive behavior, HAp provides good compressive strength and structural stability, although it remains brittle and exhibits relatively low fracture toughness, which limits its role as a standalone load-bearing material. Consequently, HAp is frequently used as a coating material to enhance osseointegration and improve the biological interface. Its thermal stability, ionic substitution capability (e.g., carbonate, magnesium, zinc), and similarity to natural bone mineral make HAp an essential material for engineered bone scaffolds and composite implant systems. Boskey and Coleman [129] suggested that the mineral component of bone changes with age. Various changes in bone mineral composition, which occur with age, are listed below [123]:

- An increase in overall mineral content;
- Greater carbonate substitution within the mineral structure;
- A reduction in acid phosphate substitution;
- Higher hydroxyl content;
- An elevated calcium-to-phosphorus (Ca/P) molar ratio;
- Growth in crystal size and improved crystallinity.

3.3. Types of Cells in the Bone

Bones comprise four types of cells: osteoblasts, osteoclasts, osteocytes, and osteogenic cells. Figure 4 provides a schematic diagram of these cell types [130].

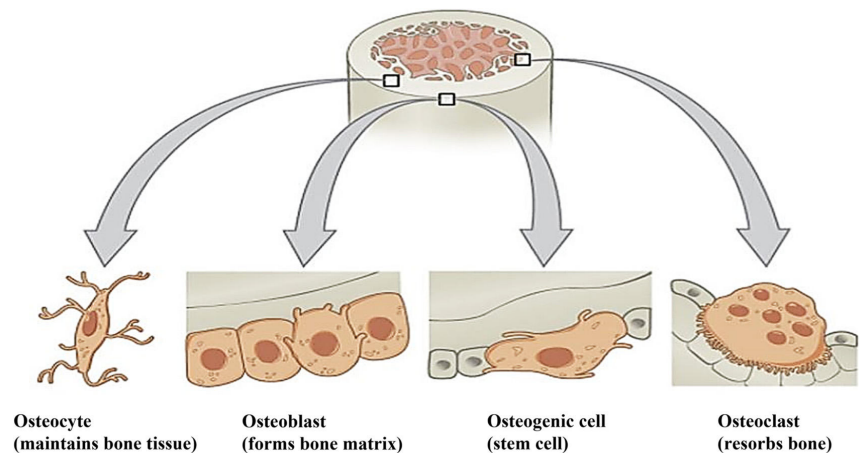


Figure 4. Schematic diagram illustrates the classification of the four types of bone tissue cells. Reproduced with permissions from [130].

3.3.1. Osteoblasts

These cells are also known as bone-forming cells because they synthesize new bones. Osteoid (a protein mixture secreted by osteoblasts) plays an important role in this process, as it mineralizes to form bone [130].

3.3.2. Osteocytes

Osteocytes are fully differentiated bone cells derived from osteoblasts. The primary distinction between these two cell types lies in their position within the bone structure: osteoblasts reside along the periosteal and endosteal surfaces, while osteocytes are embedded within the bone matrix, organized in concentric rings around the central canal of an osteon and situated between lamellae [130].

3.3.3. Osteoclast

Osteoclast cells are responsible for bone tissue breakdown and essential for maintaining, remodeling, and repairing the vertebral skeleton's bones. The osteoclast secretes acid and collagenase through bone resorption, which molecularly breaks down and digests the mixture of hydrated proteins and minerals. This mechanism similarly regulates the blood calcium level. A bone with a physiological grain size of less than 100 nm in diameter is generally termed a healthy bone. A healthy bone is continuously remodeled throughout the life span by a process that involves the formation of a bone modeling unit and activating bone cells. Osteoclasts perform the phenomenon of bone resorption. The osteoclast is derived from pluripotent cells of the bone marrow. Pluripotent cells tend to discriminate against different cells, including monocytes and macrophages. These pluripotent cells resorb bone by forming disordered cell membrane edges and thus increase the surface area of attachment on the bone surface. The carbonic anhydrase system produces hydrogen ions, which decreases the pH of the local environment, and due to this, the solubility of hydroxyapatite (a major inorganic component of bone) increases. After this process, proteolytic digestion takes place to remove an organic component, and the removal of organic and inorganic components results in the formation of resorption pits [131].

3.3.4. Osteogenic Cells

Osteoprogenitor cells, also known as osteogenic cells, are stem cells found in bone tissue that play a vital role in bone formation and regeneration. Located within the bone marrow, they serve as precursors to more specialized bone cells, including osteoblasts and osteocytes. From immature mesenchymal cells, osteoprogenitor cells develop into spindle cells on the surface of adult bones. They are more common in growing bones, triggering multifunctional phases that reshape them. As we age, our body's capacity to produce or use more osteoprogenitor cells declines [132].

4. Materials Used for Orthopedic Implant Applications: Advantages and Disadvantages

Materials such as metals, polymers, and ceramics are commonly used for implants. This review article focuses on an in-depth study of the development of Ti-based porous materials. Still, it also includes a brief section on other materials like ceramics and polymers used in implant applications. The selection of material depends on the application area. Table 2 briefly describes the advantages, disadvantages, and applications of various materials used as implants. Ceramics are inorganic oxides of non-metals known for their excellent corrosion resistance, biocompatibility, and bioactivity. They are primarily composed of ionic bonds with some covalent character, making them brittle with low fracture toughness and a high elastic modulus. There are two main types of bioceramics: bio-inert ceramics and bioresorbable ceramics. Bio-inert ceramics, such as zirconia and alumina, exhibit high chemical inertness, making them suitable for biological applications [133–135]. Bioresorbable ceramics, like hydroxyapatite and β -tricalcium phosphate, are designed to gradually dissolve and be replaced by natural bone [136–138]. However, due to their poor mechanical properties, pure ceramics are not ideal for weight-bearing prostheses in long bones, as they tend to fail under load-bearing conditions. However, ceramics are successfully used in bone filling and dentistry applications [139]. Similarly, polymers are organic non-metal oxides; they can be used as an implant material in low-load-bearing fracture sites. Polymers have emerged as promising materials for orthopedic use due to their mechanical properties, which are comparable to those of trabecular bone, and their biodegradability has further heightened interest in their application [140]. Polymer-like ultra-high-molecular-weight polyethylene (UHMWPE) has properties like high impact

strength, low friction coefficient, and low density. These properties have made UHMWPE a popular choice for joint replacement. However, the application of UHMWPE is limited due to long-term radicals in the bulk resulting from the ionizing radiation employed in the sterilization process [141]. Natural polysaccharide polymers like starch, cellulose, and alginate are also used in biomedical applications [139,140]. The main problem associated with the use of polymers in orthopedic applications is the overproduction of wear debris, which leads to inflammatory reactions between adjacent tissue and implant. This adverse tissue reaction causes osteolysis, bone resorption, and implant failure [142].

Metals and their alloys are preferred over ceramics and polymers for implant applications due to their excellent mechanical properties and biocompatibility [143]. Commonly used metals include titanium and its alloys, medical-grade stainless steel, cobalt–chromium, and magnesium alloys. These metals may contain elements such as Co, Cr, Al, Cu, V, and Ni, classified as allergic. Additionally, elements like Cd, Be, Pb, Ba, and Th are classified as toxic [144,145]. These considerations are crucial in ensuring the safety and efficacy of implants in medical applications. Elements like Ni, Co, and Cr are released from 316L stainless steel and Co-Cr alloy due to corrosion in the body environment [146,147]. The toxicity of Ni causes skin-related diseases like dermatitis, and the release of Co causes carcinogenicity [15]. Young’s modulus of 316L SS and Co-Cr alloy is much higher than that of natural bone, causing nonuniform load transfer between bone and implant and leading to bone resorption and implant loosening. Also, 316L SS steel has poor fatigue strength and wear resistance, limiting its application in orthopedics. 316L exhibits acceptable bulk corrosion resistance but is susceptible to localized pitting and crevice corrosion in chloride-rich physiological fluids and may release Ni/Cr ions under certain conditions, leading to allergic responses.

However, due to the low cost of 316L SS compared to all other metallic alloys, 316L SS has maintained its demand in fixation devices like bone plates, bone screws, etc. Magnesium, zinc, and their alloys, due to their biodegradability and potential for preventing revision surgery, have increased the attention of the general orthopedic community for surgical fixation of injured musculoskeletal tissue [148–151]. It is believed that when a Mg-based alloy is introduced in a saline environment, it degrades to magnesium chloride, oxide, sulfate, or phosphate, and these ions do not cause any adverse effect on local tissues [152,153]. Despite many advantages, there are certain limitations to using Mg-based alloys. The high corrosion rate of Mg-based alloys is one of the major problems [154]. Corrosion causes the evolution of hydrogen gas, which creates the balloon effect in vivo [155]. Due to the high corrosion rate, the pH value of the surrounding surface also increases [156].

Table 2. Table shows a comprehensive list of biomaterials, along with their advantages, disadvantages, and applications [15,17,157].

Material	Advantages	Disadvantages	Applications
SS 316L	Widely available and cost-effective, excellent mechanical properties, biocompatible	High elastic modulus, inadequate resistance to corrosion, low wear resistance, potential to trigger allergic reactions in surrounding tissues, and stress shielding, which can lead to bone resorption	Bone plates, bone screws, pins, wires, etc.
Co-Cr alloys	Excellent resistance to corrosion, fatigue, and wear. High mechanical strength. Sustained biocompatibility over the long term	High cost, limited machinability, induction of stress shielding, potential biological toxicity from the release of cobalt (Co), chromium (Cr), and nickel (Ni) ions	Shorter-term implants, bone plates and wires, total hip replacements (THR), and stem or hard-on-hard bearing system

Table 2. *Cont.*

Material	Advantages	Disadvantages	Applications
Mg alloy	Biocompatible, biodegradable, bioresorbable, similar density, Young’s modulus is that of natural bone, less stress-shielding effect, and lightweight	Hydrogen evolution during degradation and less corrosion resistance	Bone screws, bone plates, bone pins, etc.
Ti alloy	Excellent resistance, lower modulus, stronger than stainless steel, lightweight, and biocompatible	Poor wear resistance, poor bending ductility, and expensive	Fracture fixation devices such as plates, nails, rods, screws, fasteners, and wires; femoral hip stems; total joint replacement (TJR) systems; and arthroplasty procedures, particularly for hip and knee joints
Alumina (Al ₂ O ₃)	Biocompatibility and bio-inert behavior, elevated hardness, strength, resistance to abrasion, minimal formation of fibrous tissue at the implant–tissue interface	Low fracture toughness, brittleness, limited ductility, and radiopacity	Porous coatings for femoral stems, femoral head, bone screws and plates, and knee prosthesis
Zirconia (Zr ₂ O ₃)	Excellent fracture toughness; high flexural strength; low Young’s modulus; closely matching that of bone; bio-inert nature; good biocompatibility; and non-toxic behavior within the biological environment	Phase transformation, brittleness, and low toughness	Femoral head, artificial knee, bone screws, and plates
Bioglass	Biocompatibility, bioactivity, promoting integration with surrounding tissue, non-toxicity, and brittleness, which may limit load-bearing applications	Brittleness, low tensile strength, and poor fatigue resistance	Artificial bone and dental implants
Hydroxyapatite (HAp)	Bio-resorbable, bioactive, biocompatible, similar composition to bone, and good osteoconductive properties	Brittleness, low tensile strength, and poor fatigue resistance	Femoral knee, femoral hips, tibial components, and acetabular cup

5. Titanium and Its Alloys: Material of Ultimate Choice for Implant Application

Titanium (Ti) is the ninth most abundant element in the lithosphere, as it is a constituent of practically all crystalline rock. Reverend William Gregor discovered it in 1798 [114]. Thorough explanations of titanium’s science, technology, and applications may be found in recent investigations. During the last 30 years, titanium and its alloy manufacturing techniques have advanced at a faster rate than any other structural material in metallurgical history. To enhance the performance and dependability of Ti and its alloys and prevent unanticipated failures, there has been an exceptionally high focus on removing manufacturing errors, from extraction and melting procedures to machining and joining. We observe that the primary impediment to an even wider variety of Ti and its alloy applications remains costly. The need to convert Ti oxides or chlorides to their metallic state accounts for a significant portion of the material’s cost. The industrial reduction technique is a batch operation that requires a lot of energy. It was developed many years ago by Kroll. Several initiatives are underway to co-reduce mixed chlorides using various reduction techniques to create metallic or alloyed Ti. Several of these techniques have proven workable in the lab, but scaling up to manufacturing volumes is proving more difficult than anticipated.

Ti is a transition metal with atomic number 22 with an incomplete valence shell. It can form a substitutional solid solution (SSS) with an element having a size factor of $\pm 20\%$. The melting point of Ti is $\sim 1678^\circ\text{C}$, and the crystal structure of Ti is a hexagonally close-packed (hcp) α -Ti structure up to the beta transus temperature (882.5°C), transforming to a body-centered cubic β -Ti structure (bcc) above this temperature (Figure 5) [158,159]. The nature of the alloying element determines the microstructure (alpha (α) to beta (β) transformation temperature) of the Ti-based alloy. Elements like Al, O, N, etc., are commonly known as α -stabilizers because they tend to stabilize the α phase, as adding these elements increases the β transus temperature. Similarly, elements like V, Mo, Nb, Fe, Cr, etc., stabilize the β transus temperature and are known as β stabilizers. The addition of this element depresses the β transus temperature.

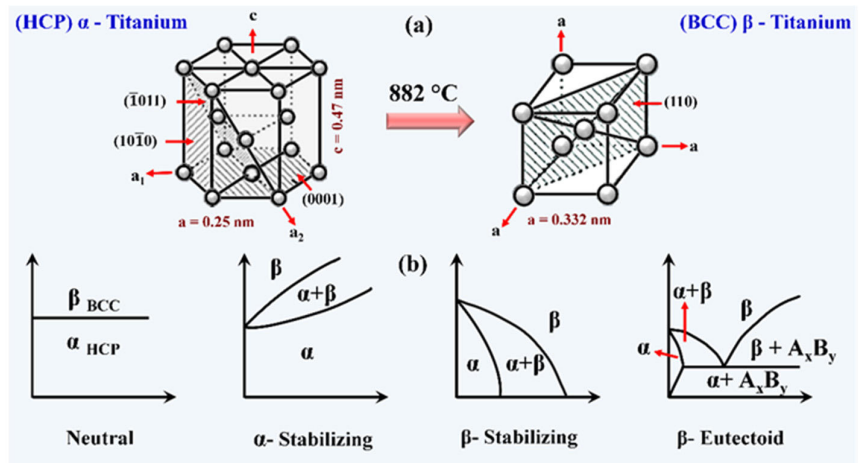


Figure 5. Schematic representations illustrating the following: (a) the allotropic forms of titanium—hexagonal close-packed (HCP) α -Ti, which is stable up to 882°C , and body-centered cubic (BCC) β -Ti, stable at temperatures above this point; and (b) the formation of various phases and corresponding phase diagrams resulting from the addition of different alloying elements to titanium. Reproduced with permissions from [159].

Titanium alloys are generally classified based on alpha (α) and beta (β) phases. They are classified as α , near- α , ($\alpha + \beta$), and metastable β -alloy. The α alloy consists of only α phase (with or without the help of α stabilizers, i.e., Al, O, N, etc.). Near α alloys are a special class of α alloys comprising 1–2% of β stabilizers and about 5–10% of the β phase. Similarly, $\alpha + \beta$ alloys contain 10–30% of the β phase, and alloys with higher β stabilizers where the β phase is formed by fast cooling are known as metastable β alloys. Generally, $\alpha + \beta$ or metastable β alloys are employed in biomedical applications. Among all these alloys, α and ($\alpha + \beta$) alloys are considered first-generation Ti alloys and possess a high Young’s modulus value (110 GPa). The development of a second-generation Ti-based alloy, i.e., β alloy, was established in 1990 [160]. Due to their ability to possess a lower Young’s modulus value (55–90 GPa), β alloys are the material of choice for orthopedic applications. The different Ti alloys and the mechanical properties used for biomedical applications are mentioned in Table 3. Figure 6 highlights the various biomedical applications where Ti and its alloys are used.

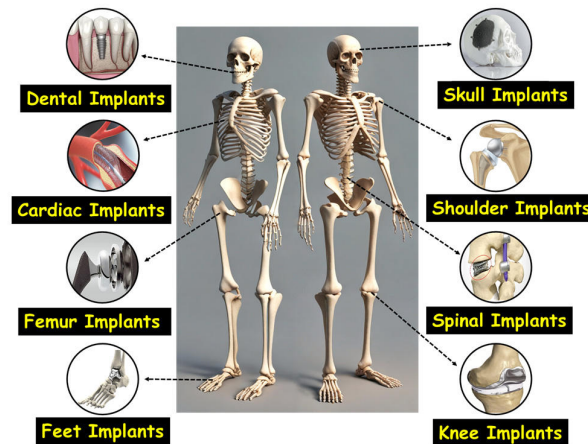


Figure 6. Graphical representation illustrating different Ti-based implants in the human body for biomedical applications.

Table 3. List showing the mechanical properties of titanium and its alloys (E—modulus in GPa; UTS—ultimate tensile strength in MPa) [15].

Material	Standard	E	UTS	Alloy Composition
First-generation biomaterials (1950–1990)				
Commercially pure Ti (CP grade 1–4)	ASTM F1341	100	240–550	α
Ti–6Al–4V ELI wrought	ASTM F136	110	860–965	$\alpha + \beta$
Ti–6Al–4V ELI standard grade	ASTM F1472	112	895–930	$\alpha + \beta$
Ti–6Al–7Nb wrought	ASTM F1295	110	900–1050	$\alpha + \beta$
Ti–5Al–2.5Fe	-	110	1020	$\alpha + \beta$
Second-generation biomaterials (1990–to date)				
Ti–13Nb–13Zr wrought	ASTM F1713	79–84	973–1037	Metastable β
Ti–12Mo–6Zr–2Fe (TMZF)	ASTM F1813	74–85	1060–1100	β
Ti–35Nb–7Zr–5Ta (TNZT)	-	55	596	β
Ti–29Nb–13Ta–4.6Zr	-	65	911	β
Ti–35Nb–5Ta–7Zr–0.40 (TNZTO)	-	66	1010	β
Ti–15Mo–5Zr–3Al	-	22	-	β
Ti–Mo	ASTM F2066	-	-	β

6. Fabrication of Porous Titanium Using Various Powder Metallurgical Techniques

Ti-based materials have low thermal conductivity and high reactivity with the surrounding environment. Due to this, their machining, melting, and casting are difficult. Therefore, Ti-based components are generally machined from forged Ti blanks at a low speed; in this procedure, ~95% of the raw materials are lost as scrap, and recycling this scrap is still a challenge [161]. Also, dense Ti-based alloys tend to have a stress-shielding effect due to their high modulus. Incorporating pores is a promising solution to reduce the stress-shielding effect in Ti-based implants, but manufacturing porous Ti-based structures is not technically easy. Various manufacturing methods have been established to produce porous titanium structures. Figure 7 presents a graphical comparison of porosity levels and pore size distributions achieved through these different fabrication techniques [160]. The use of porous material in artificial joint replacement is an attractive field of research as it

includes different methods and materials that can be used to reduce stiffness mismatch with bone. In the present study, different methods for the synthesis of porous Ti scaffolds are described. Figure 8 shows the classification of various techniques that can be used to fabricate porous Ti structures. However, the following sections will focus exclusively on a few processes that can fabricate porous Ti-based structures.

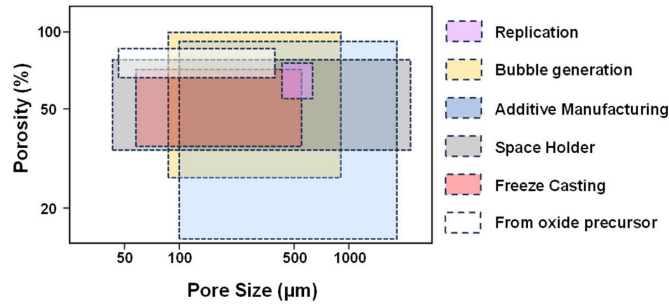


Figure 7. Porosity and pore size observed in porous titanium structures fabricated using different manufacturing techniques. Reproduced with permissions from [160].

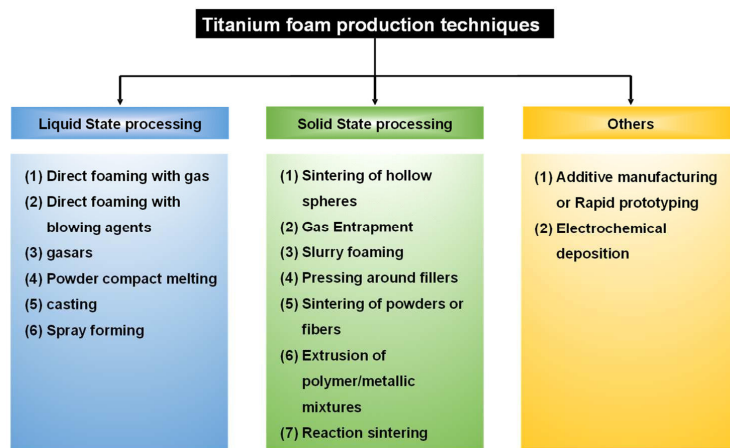


Figure 8. Classification of various processing techniques employed to fabricate porous Ti structures.

6.1. Space Holder Technique

The space holder technique is one of the important powder metallurgical techniques that can control the size and shape of the pores, amount of porosity, etc. Because these parameters depend on the size of space-holder particles. The basic requirement of this process is that the particle size of the metal powder should be less than the particle size of the space holder. This method involves the addition of space holder particles with the metal powder, followed by mixing them uniformly throughout. Then, the mixture is compacted uniaxially to form a green compact. The green sample is pre-sintered at an optimized temperature (low temperature) so that the complete removal of space holder particles can occur. This also leads to the initial sintering of metal powders. Finally, the pre-sintered samples are sintered at an elevated temperature in an inert atmosphere to avoid contamination (including metal oxidation). The schematic representation of the process for preparing porous Ti via the space holder technique is shown in Figure 9. Several materials have been used as space holders, including bio-wastes, metals like Mg granules, urea, ammonium hydro carbonate, water-soluble materials (like sucrose, potassium chloride,

and sodium chloride), paraformaldehyde, etc. Before selecting the space holder, the factors to be considered are its affinity with Ti, the amount of left-out residue after burning, and ease of processing. Complete removal of space holder material from the substrate is the main problem associated with the space holder technique because the presence of any residue may impart detrimental effects, which may influence biocompatibility. Materials like NaCl and sucrose are suggested as they can be removed completely when treated with water [162].

Kim et al. [163] used sacrificial Mg granules as space holder particles since Mg ions are directly involved in numerous biological mechanisms in our body, such as the channelizing of ions, DNA stabilization, enzyme activation, and stimulation of cell growth and proliferation. So, the problems associated with space holders, like partial removal of space holder particles, are completely mitigated. Mg particles of size 20 mesh to 100 mesh with 0.5 wt.% ethanol as a binder were used. The mixture of Ti and Mg was compacted uniaxially, followed by removing space holder particles by dipping them in HCl and ethanol for 24 h. Sintering the green samples at an elevated temperature of 1300 °C for 2 h in high vacuum results in controlling the porosity within 50–71% and pore size within 132–262 μm. The mechanical testing of the samples reveals that the compressive and rupture strengths are 59–280 MPa and 85 MPa, respectively. Esen and Bor [164] processed Ti foam using Mg as a space holder particle; the porosity content was observed to vary between 45 and 70%; the pore size was found to be 525 μm; Young’s modulus ranged between 0.42 GPa and 8.8 GPa.

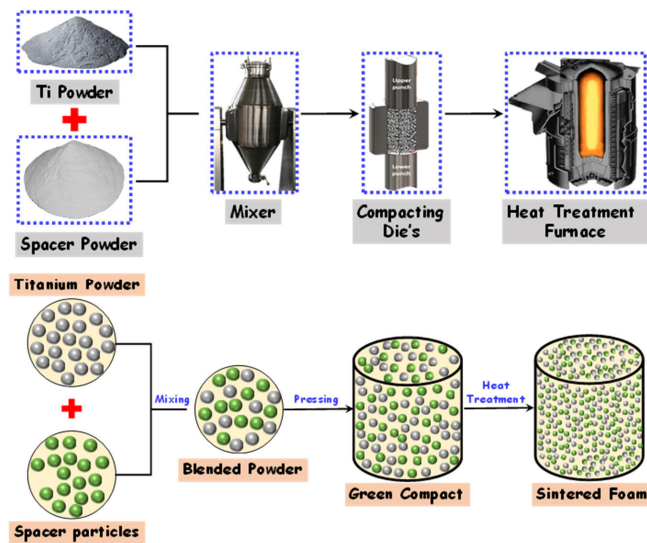


Figure 9. Schematic diagram illustrates the process of fabricating porous titanium using space holder technique.

Bio-waste, like rice husk, is a rich source of silica, and its low-temperature combustion property can be utilized for space-holder applications. Due to the amorphous nature of silica and its high relative reactivity along with carbon for thermal reduction, rice husk can be a favorable candidate for synthesizing low-temperature porous material [165,166]. Apart from the above space holders, researchers have used many other materials to produce porous titanium scaffolds. Dabrowski et al. [3] employed paraformaldehyde, with an average particle size of 500 μm, as a space holder in the fabrication of porous titanium implants due to its ability to fully decompose at relatively low temperatures. The resulting porosity can vary between 60% and 70%, and Young’s modulus can vary between 1 GPa

and 8 GPa, which is very close to that of cancellous bone. Xiao Jian et al. [167] studied the porous Ti structures produced with varied spacer contents (Figure 10).

Reports suggest that urea is an effective space-holder material that tends to decompose at low temperatures, resulting in the formation of a pore. Vasconcellos et al. [168] synthesized porous Ti with 3D interconnected pores with a size of ~480 μm and a total porosity of 36%. Wenjuan et al. [169] used urea of size 200–600 μm as a space holder and polyethylene glycol as a binder to synthesize a porous Ti scaffold with porosity varying between 55 and 75% and pore size varying between 200 μm and 500 μm. The porous scaffold reveals Young’s modulus in the range of 3–6.4 GPa, which is close to that of natural bone. It has also been noticed that the rapid decomposition of urea at low temperatures causes rough control over porosity. The needle-like shape of urea particles provides sharp corners and notches in the pore, which lead to stress concentration, deteriorating their mechanical properties. It is also found that the remaining urea in pores makes the implant unfit for medical use [170].

Xiang et al. [171] prepared porous Ti with a porosity between 44 and 77% by using ammonium acid carbonate as a space holder. The fabricated porous Ti scaffolds have pore sizes between 200 μm and 500 μm, with Young’s modulus and compressive strength values ranging between 2.1 GPa and 3.4 GPa and 60 MPa and 140 MPa, respectively. In addition to the space holders, other materials can serve as pore formers, meeting essential criteria such as complete residue removal through dissolution in water and being economically viable. In this class, sucrose and NaCl are the best-suited materials that can be used as a pore former. Torres et al. [172] reported excellent adhesion and proliferation of cells when NaCl is used as a space holder. Also, any left-out residue in the scaffold will not affect the in vivo performance of the Ti alloy.

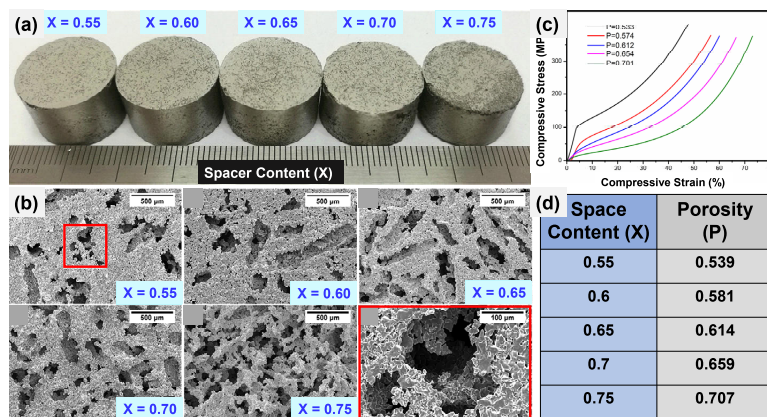


Figure 10. (a) Images of the porous titanium structures produced with varying spacer content (X = 0.55, 0.6, 0.65, 0.7, and 0.75, respectively). (b) Microstructure of the porous titanium structures with varied spacer content. (c) Compression behavior of the porous structures with varied porosity content and (d) tabular representation of the porosity content with varying spacer content. Reproduced with permissions from [167].

Chen et al. [173] introduced a novel space holder material that offers excellent biocompatibility for fabricating porous titanium structures with open and interconnected pore networks. Spherical sugar pellets were used to synthesize porous Ti with 20 to 54% porosity and a pore size ranging from 212 μm to 500 μm. The Young’s modulus of the scaffold is found between 12.1 GPa and 18.5 GPa, which is very close to that of natural bone. Polymethyl methacrylate (PMMA) is also used as a space holder material to fabricate porous scaffolds. Li et al. [174] used PMMA to produce macro pores of size 200–400 μm

and porosity 10–65%. The green compact was heated between 250 and 450 °C to completely remove the space holder particles. The compressive strength and elastic modulus were observed to be between 32 MPa and 530 MPa and 0.7 GPa and 23.3 GPa, respectively. Table 4 summarizes the mechanical properties of different porous materials.

Table 4. Mechanical properties of titanium scaffolds prepared by different space holders (P—porosity in %; PS—pore size (µm); E—Young’s modulus in GPa; YS—Yield strength in MPa; UTS—ultimate tensile strength in MPa; UCS—ultimate compressive strength in MPa).

Space Holder Material	P	PS	E	YS	UTS	UCS	Ref.
Mo Wire	32–47	-	23–62	76–192	-	-	[175]
Mg	45–70	525	0.42–8.8	15–116	-	-	[164]
Mg	50–71	262–132	-	-	-	59–280	[163]
Mg	30–50	-	15–44	117–222	-	-	[176]
Ti Fibers	35–84	150–600	2–4	-	200–600	-	[177]
Rice Husk	50–60	100–550	-	-	-	17–70	[165]
Rice Husk	25–36	-	-	-	-	440–938	[166]
Rice Husk	15–34	-	6–15	-	-	116–396	[16]
Sucrose	20–54	212–500	12–50	-	-	-	[173]
Urea	36	480	-	-	-	-	[168]
Urea	55–75	200–500	3–6	-	10–35	-	[169]

6.2. Replication Method

The synthesis of porous Ti with the help of replicating polymeric sponges followed by high-temperature sintering is a unique technique. This process offers the fabrication of scaffolds with a high degree of porosity and highly interconnected microspores with identical shapes and sizes. The porous structure produced via this method has a pore shape and size like cancellous bone [178–181]. In this method, the precise regulation of the rapid drying process of the coated slurry is essential for achieving the desired structural characteristics. Cachinho et al. [182] described a unique method of preparing a porous Ti scaffold in which the scaffold was prepared by replication of a sponge followed by reactive sintering. The main advantage of this method is the easy production of complex shapes at a low cost. The use of a sacrificial polymeric sponge results in scaffolds with interconnected pores, a critical feature for promoting bone ingrowth and vascularization in newly formed tissue [183]. Such porous architectures are commonly applied in dental implants, permanent osteosynthesis plates, and intervertebral disc replacements [184]. Cachinho et al. [182] reported using 45 vol.% TiH₂ powder with a mean particle size of 15.6 µm and a specific surface area of 0.5336 m²/g. The polymeric sponge blocks were dipped into the slurry and infiltrated. After the removal of excess slurry, the samples are dried at room temperature for a period of 24 h. The sintering of samples at a low heating rate of 1 °C/min with dwelling at 500 °C for 2 h and 1000 °C for 4 h results in the formation of a highly porous Ti scaffold with a porosity of 75% and a pore size ranging between 100 µm and 600 µm. The porosity range of 100 µm and 600 µm is appropriate for the growth of new bone tissues and the transport of body fluids. Further, to improve biological properties, the porous Ti is coated with hydroxyapatite and heat-treated at 700 °C. Li et al. [185] synthesized a porous Ti-6Al-4V alloy by replicating 70 wt.% of Ti-6Al-4V powder in water and ammonia solutions. The high-temperature sintering of samples results in open-cell porous Ti struts with a porosity of 88% and a compressive strength of 10 MPa. It should be noticed that the second deposition of powder slurry on the previously sintered scaffold, followed by re-sintering, increases density and compressive strength to 36 MPa. Wang et al. [186], in his study, proposed an improved sponge replication method. A novel solvent consisting of ethanol and water was used to maintain a fast-drying rate and appropriate viscosity of Ti slurry. This slurry was used for multiple Ti coatings, and the Ti scaffold prepared possesses a compressive strength of ~84 MPa with a porosity of ~66%.

Wang et al. [186] explored an enhanced polymeric sponge replication method to fabricate biomedical porous titanium scaffolds. By optimizing key processing parameters, they achieved scaffolds with open and interconnected pore architectures. In their approach, titanium slurries were prepared using a mixture of ethanol and water as the liquid phase. Figure 11a,b display the asymmetrical titanium particles and the open, interconnected structure of the polyurethane (PU) foam used as the sacrificial template. Figure 11c outlines the process flowchart for fabricating porous titanium via this improved replication technique. Notably, three modifications distinguished this method from conventional approaches: (1) Ethanol–water mixtures replaced water alone to improve slurry formulation; (2) excess slurry was removed through centrifugation rather than squeezing, preventing the formation of closed pores; (3) variations in slurry viscosity were introduced for more uniform coating. SEM images in Figure 11d,e illustrate the resulting microstructures, showing that scaffolds fabricated with ethanol exhibited a denser titanium coating compared to those produced using only water. This densification, attributed to ethanol’s anti-foaming properties, resulted in enhanced compressive strength. Furthermore, *in vitro* studies demonstrated that the scaffolds supported the adhesion, proliferation, and growth of mesenchymal stem cells (MSCs), confirming their suitability for biomedical applications.

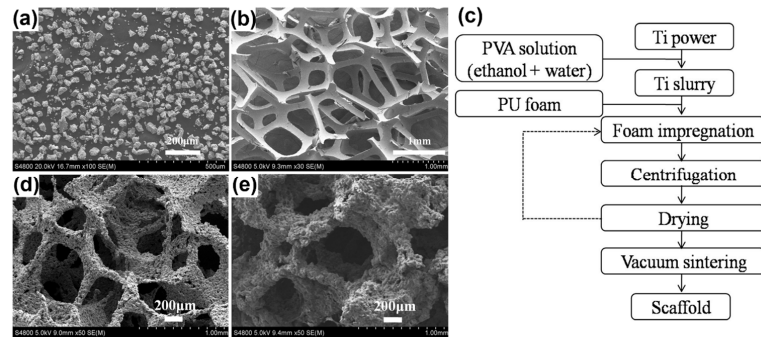


Figure 11. (a) Secondary electron image of Ti-powder, (b) secondary electron image of PU foam, (c) flowchart describing the process of porous Ti fabrication via enhanced polymeric sponge replication method, (d) secondary electron image of the porous Ti produced without ethanol in the solvent, and (e) secondary electron image of porous Ti produced with ethanol in the solvent. Reproduced with permissions from [186].

6.3. Entangled Metal Wire Technique

Porous Ti implants fabricated via conventional methods exhibit low toughness and tensile strength. The major drawback of these conventional techniques is the difficulty in avoiding contamination and impurities in Ti that arise during processing. Sometimes, undesirable cracks and metallographic defects in sintered Ti struts make them brittle, and thus, they fail to bear tensile load [187]. Also, the porous Ti fabricated by powder metallurgical techniques using a space holder and plasma spray technique has low ductility that may break in the body’s environment when subjected to uncertain overloading and accidents [188]. The entangled metal wire technique (EMWT) is a novel technique that improves these mechanical properties. In this technique, a Ti wire of a diameter of ~0.08 mm to 0.27 mm is used as raw material, and this wire is coiled around a 1.5 mm-diameter rod to form a coiled spring-like structure. The coiled structure is stretched equably such that the distance between two spirals (screw pitch) reaches the external diameter of the coil. This stretched coil is now entangled around a 1 mm diameter rod to form a pre-compacted sample. Finally, this pre-compacted sample is compacted with the help of a piston in a cylindrical die [189].

The mechanism of fabrication and sample porous titanium scaffold prepared by the entangled metal wire technique is shown in Figure 12. Several researchers have fabricated porous titanium scaffolds using EWMT. Zou et al. in 2008 [177] prepared open-cell porous titanium with porosity of 35 to 84% by sintering titanium fibers of 200 μm diameter in a vacuum. The titanium fibers were curved into a helix with the help of a screw, and then, this helix was arranged in a cylindrical form, followed by compaction and vacuum sintering at 1250 °C for 2 h. The resulting porous scaffold has a pore size of 150–600 μm. Young’s modulus was in the range of 3.5–4.2 GPa, and compressive strength was 100–200 MPa. Liu et al. [190] fabricated entangled titanium wire material through different procedures: one with normal wire and another with coiled wire; its compressive and pseudo-elastic hysteresis behavior was investigated. The details of the properties obtained are discussed in Table 5. Jiang et al. [191] fabricated an entangled porous titanium composite filled with biodegradable magnesium melted at 700 °C under the protective environment of SF₆ and CO₂ to improve the fixation bonding between the implant and host bone. Bisphenol A glycidyl methacrylate (BisGMA) is suggested as a bonding material to provide strong bonding strength and help in fixing the free nodes of the entangled structure [192]. Wang et al. in 2017 [175] proposed a novel technique for the fabrication of a three-dimensional porous titanium scaffold. This method combined two methods: An entangled Molybdenum wire was used as a space holder, and titanium liquid was cast in a vacuum environment, followed by etching off SH particles in an aqua regia solution. The resulting porous scaffold has three-dimensional interconnected pores with porosity in the range of 32–47% and exhibits elastic modulus in the range of 23–62 GPa and yield strength in the range of 76–192 MPa, as shown in Table 5.

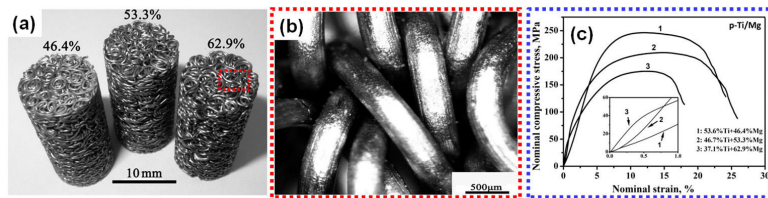


Figure 12. (a) Porous titanium samples prepared by the entangled metal wire technique; (b) magnified image of the marked region in Figure 12. (a,c) Compressive behavior of the porous titanium structures produced by the entangled metal wire technique. Reproduced with permissions from [191].

Table 5. Mechanical properties of porous titanium prepared by entangled metal wire technique (P—porosity in %; PS—pore size (μm); E—Young’s modulus in GPa; YS—yield strength in MPa; UTS—ultimate tensile strength in MPa; UCS—ultimate compressive strength in MPa; FS—flexural strength in MPa; NR—not reported).

Method	Material Used	P	PS	E	YS	UTS	UCS	FS	Ref.
EWMT	Entangled Mo Wire	32–47	0.4	23–62	76–192	-	-	-	[175]
EWMT	Ti Wire	35–84	150–600	2–4.2	-	200–600	-	-	[177]
EWMT	Entangled Ti Wires	44–81	NR	0.03–2.25	-	-	-	9–325	[193]
EWMT	Entangled Ti Wire	53–55	NR	0.03–1	3–3.5	-	-	-	[188]
EWMT	Entangled Ti Wire	37–54	NR	22–47	-	-	175–246	-	[191]
EWMT	Entangled Ti Wire	40–55	100–400	0.4–1.4	12.9–52.5	-	-	-	[192]
EWMT	Entangled Ti Wire	45–58	50–200	1.05–0.33	75–124	48–108	-	-	[187]
EMWT	Normally entangled Ti Wire	48–73	-	0.13–0.82	2–31	-	-	-	[190]
	Coiled entangled Ti Wire	48–78	-	0.04–0.62	1–19	-	-	-	

6.4. Spark Plasma Sintering (SPS) and Hot Pressing (HP)

The conventional sintering or pressureless sintering process involves heating Ti and its alloys at an elevated temperature of 1200 °C to 1400 °C (but below the melting point of the material) and a high vacuum of the order of 4×10^{-4} Pa to 6×10^{-6} Pa for a long time period of about 24 h to 48 h [194] for densification and homogenization [195,196]. Even after this lengthy procedure, achieving a pore-free homogeneous microstructure is challenging [196]. SPS is an advanced consolidation technique that uses pressure-assisted pulsed current to sinter and can produce porous samples. In this process, the powder is loaded in an electrically conducting die that acts as a heating source when subjected to a pulsed direct current. Thus, the powdered samples will be heated from both sides under uniaxial pressure [197–200], and due to this fast heating, enhanced mass transfer and rapid powder consolidation will occur [201]. Two theories explain the consolidation mechanism of commercially pure (CP) Ti. According to the first hypothesis, the surface of the powder particles is cleaned and activated by spark discharges generated between metallic powdered particles, thus promoting mass transport for sintering [202,203]. Another hypothesis suggests that the densification of powder is due to particle deformation because, as the temperature increases, the yield strength of the powder particles decreases [204]. Spark plasma sintering (SPS) is also referred to by several alternative names, including field-assisted consolidation, electrical field-activated sintering, plasma-activated sintering, and electrical discharge compaction [203,205–207]. SPS is also known by other names, such as field-assisted consolidation technique [205], electrical field-activated sintering [203], plasma-activated sintering [206], and electrical discharge compaction [207]. These methods enable the rapid sintering of metallic powders by applying electrical discharge in combination with swift heating and concurrent pressure. Similarly, in HP, the metallic powder is sintered with the help of electrical resistance in a closed die under uniaxial pressure. Different heating methods, such as induction heating and electric conduction/convection/radiation heating, can be used in HP [208,209]. Ibrahim et al. [210] synthesized porous Ti and its alloy using a cost-effective SPS technique. In this process, porous Ti with different porosities was successfully synthesized by the powder metallurgy technique using NH_4HCO_3 as a space holder and TiH_2 as a foaming agent. SPS is used to consolidate powder at 16 MPa under pressureless conditions. The experimental results showed that pure titanium samples achieved full relative density at a relatively low temperature of 750 °C and a pressure of 16 MPa. The porosity of 53% and Young's modulus of 40 GPa were achieved in the case of pressureless sintering at a temperature of 1000 °C.

Kashimbetova et al. [211] investigated the fabrication of porous titanium structures using pressure-less spark plasma sintering (PL-SPS). Their study focused on examining how different sintering temperatures influence the microstructural features and mechanical performance of porous Ti. Figure 13a,d,g display the porous strands formed at 1400 °C, where bonding occurred primarily at contact points between adjacent Ti particles in the early sintering stage. At 1500 °C, more developed sintering necks between particles were observed, as shown in Figure 13b,e,h, indicating enhanced densification with limited grain growth. Further sintering at 1600 °C brought the structures into the mid-stage of sintering, marked by significant pore shrinkage, though overall porosity was maintained (Figure 13c,f,i). Increased densification at higher temperatures had a direct effect on compressive yield strength (Figure 13j). At 1400 °C, the weakly bonded particles resulted in a low yield strength of 4.7 MPa. This increased to 26.7 MPa at 1500 °C due to the growth of sintering necks and reached 52.6 MPa at 1600 °C because of further densification. The samples sintered at 1500 °C and 1600 °C exhibited elastic deformation followed by strain hardening during compression. In contrast, the structure sintered at 1400 °C reached peak stress shortly after yielding and then gradually fractured, as shown in Figure 13k. The

compressed sample sintered at 1600 °C maintained its pore geometry, particularly in the printing plane (Figure 13). The findings suggest that intra-strand porosity significantly influences mechanical strength when inter-strand porosity is kept constant. A comparison of the properties of porous titanium synthesized using SPS and hot pressing (HP) from various studies is presented in Table 6.

6.5. Microwave Sintering

Electromagnetic waves with a frequency in the range of 300 MHz to 300 GHz are referred to as microwaves. The most used microwaves for material processing have frequencies between 2.45 GHz and 915 MHz [212]. When materials interact with microwaves, they convert electromagnetic energy into heat energy within the material. The main advantage of microwave sintering is the complete sintering of the material without forming impurities (like oxides). This technique is applicable for sintering ceramics, metals, and composites, offering advantages such as reduced processing time and energy consumption, cost-effectiveness, and environmental sustainability [213]. In powder metallurgy-based manufacturing routes, particularly after pressing and sintering, incompletely bonded or loosely attached particles may remain on the surface of porous titanium structures, and their release into the body can trigger inflammatory responses, macrophage activation, and osteolysis, ultimately jeopardizing implant stability [214]. Preventing such complications requires ensuring adequate particle bonding through optimized sintering conditions and robust neck formation, followed by thorough post-processing steps such as ultrasonic cleaning, chemical/acid etching, abrasive or mechanical removal of weakly attached particles, and thermal treatments to consolidate surface layers. Complementary quality-control procedures, including micro-CT analysis, surface morphology inspection, and mechanical integrity assessments, are also essential to verify the absence of detachable particles. A comprehensive discussion of surface post-treatments for bio-implants is presented in Section 6.6 of this review article. Table 6 demonstrates the processing conditions and physical and mechanical properties obtained using SPS, HP, and microwave sintering.

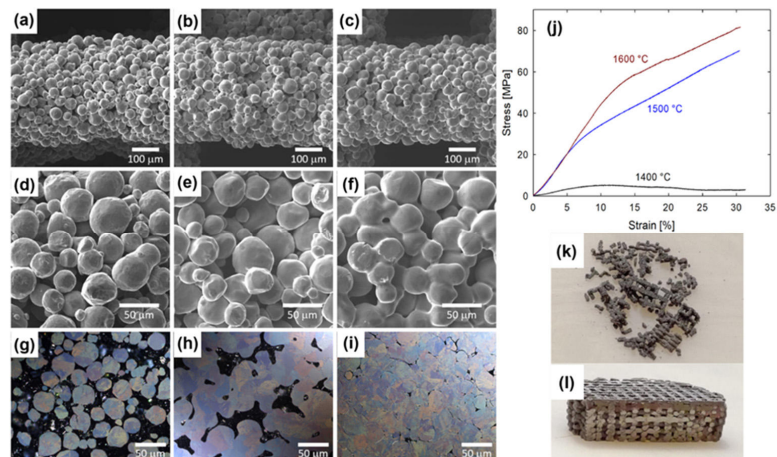


Figure 13. Images depicting porous titanium fabricated using pressureless spark plasma sintering as a function of varying sintering temperatures: (a,d,g) 1400 °C, (b,e,h) 1500 °C, and (c,f,i) 1600 °C. (j) Compressive stress–strain curves of porous titanium as a function of different sintering temperatures. Images of the (k) fractured sample sintered at 1400 °C and (l) compressed sample (sintered at 1600 °C). Reproduced with permission from [211].

Table 6. Processing conditions and mechanical properties of porous titanium prepared by spark plasma sintering, hot pressing, and microwave sintering (ST—sintering temperature in °C; TP—time and pressure; P—porosity in %; PS—pore size (µm); E—Young’s modulus (MPa); YS—yield strength in MPa; UCS—ultimate compressive strength in MPa; UTS—ultimate tensile strength in MPa).

p	ST	TP	P	PS	E	YS	UCS	UTS	Ref.
Spark plasma sintering									
Pure Ti	750	16 MPa	Fully dense	-	~125	-	-	-	
Pure Ti	1000	Pressureless	53	-	40	-	-	-	[210]
Ti5Mn alloy	950	Pressureless	56	-	35	-	-	-	
Ti5Mn alloy	1100	Pressureless	21	-	52	-	-	-	
Pure Ti	700	-	30–70	125–800	6–36	27–94	-	-	[215]
β-alloy Ti-45Nb (gas-atomized)	1000	10 min, 30 MPa	0.5 ± 0.1	-	72 ± 1	550	-	-	[216]
β-alloy Ti-45Nb (milled)	1000	10 min, 30 MPa	4.0 ± 0.2	-	72 ± 1	867	-	-	[216]
Ti-6Al-4V	700	3 min, 30 MPa	32 ± 0.2	-	-	-	125	-	[217]
Pure Ti	600	3 min, 30 MPa	32 ± 0.4	-	-	-	113	-	[217]
CP Ti (Grade 1) Powder	900	5 min, 60 MPa	-	-	-	340	-	445	
Cryomilled nanocrystalline CP Ti (Grade 2) powder	850	-	-	-	-	770	-	840	[218,219]
CP Ti (Grade 3) powder	900	5 min, 60 MPa	-	-	-	595	-	720	
Wrought titanium grade 4	-	3 min, 80 MPa	-	-	-	480–635	-	655–690	
Hot pressing									
Ti-45Nb (gas-atomized)	600	30 min, 700 MPa	0.7 ± 0.2	-	70 ± 1	447	-	-	[216]
Ti-45Nb (milled)	600	30 min, 700 MPa	3.7 ± 0.1	-	70 ± 1	940	-	-	[216]
Microwave sintering									
Ti6Al4V/MWCNTi powder	1620	-	25	-	11 ± 3	145	270	-	[213]

6.6. Additive Manufacturing (AM) or Rapid Prototyping (RP)

Additive manufacturing (AM), also known as rapid prototyping (RP), is a computer-assisted advanced fabrication technique that utilizes computer-aided design (CAD) and computer-aided manufacturing (CAM) models to construct predefined microstructures, macrostructures, and precisely controlled hierarchical architectures [220,221]. As the demand of the manufacturing sector is more focused on precision and specific design, the AM technique has emerged as a strong tool for mitigating problems associated with conventional powder metallurgy techniques like material loss during post-processing (like machining, drilling, etc.), large production time, difficulty in producing complex shapes, etc. [222–225]. AM has been extensively utilized in the medical field by creating patient-specific components based on patients’ medical imaging [226]. The major advantage of this technology is the control over scaffold pore structure, including pore size, shape, volume, and interconnectivity [227]. It is a layer-by-layer fabrication process in which the selected part is built in a CAD file [228–230]. The file is sliced along the Z-axis in a virtual environment, and a machine-specific tool path is generated for each slice.

AM offers specific advantages like site-specific deposition with higher cooling rates and can easily produce intricate shapes [231]. The interconnectivity of the porous structures is a key issue in porous metallic structures. As mentioned above, this issue cannot be perfectly controlled by other conventional manufacturing techniques. In contrast, the final structure of the AM-fabricated components relies on the initial design with interconnected

structures through AM. The porous Ti can be easily fabricated without design restrictions. Additive manufacturing (AM) techniques can be categorized based on the energy–powder interaction and consolidation mechanism, including methods such as electron beam melting (EBM), selective laser melting (SLM)—also referred to as laser powder bed fusion (LPBF)—laser-engineered net shaping (LENS), and binder jetting (BJG) [232,233]. Though there are several AM processes, only a few techniques, including SLM/LPBF and EBM, are widely used and can fabricate a wide variety of materials. Other AM processes like directed energy deposition (DED) are widely used for higher deposition rates and large-scale manufacturing [234].

Apart from fabricating intricate shapes, the AM structures also exhibit improved properties because of hierarchical microstructures resulting from higher cooling rates observed during the process [235–237]. Moreover, AM produces a unique microstructure and texture compared to conventional processing, which helps to improve the strength by maintaining the same porosity [238]. As mentioned in Section 5, Ti shows allotropy. Moreover, Ti6Al4V exhibits the coexistence of α and β microstructures, providing versatility in the Ti-based alloys. Since SLM/LPBF offers high cooling rates, a fine α' martensite or α' martensite-based microstructure is observed in these samples [239–241]. The α' martensite appears as an acicular or needle-shaped microstructure, which has an hcp crystal structure like the α phase. Like ferrous martensite, Ti-based martensite also helps improve its strength at the cost of ductility. Hence, AM-fabricated structures may require post-processing, such as heat treatment, to tune their properties according to the requirements [242,243]. Sabban et al. [244] introduced a novel heat treatment approach that successfully transformed martensitic laths into a bimodal globularized microstructure in the AM Ti64 alloy, resulting in an 80% enhancement of ductility and a 66% improvement in toughness. In subsequent research by the same group, Gupta et al. [245] fabricated a Ti64-based bone plate using the AM technique. They employed a specially designed process of repeated cyclic heating and cooling, as previously described, to transform the microstructure from acicular to bimodal without the need for plastic deformation before heat treatment. Moreover, the in situ dissolution of α' is also possible by changing the processing parameters and providing double or triple laser scanning in selective laser manufacturing [246–248].

AM-fabricated porous Ti alloys exhibit relatively better mechanical properties due to interconnected structures [35,249]. The good interconnectivity of the porous implants enables uniform load distribution among the structures, while poorly connected porous structures typically fail prematurely at the joints. Ample evidence in the literature suggests premature failure for porous metallic implants [250,251]. Given the advantages, there are also some drawbacks, including surface defects, which usually tend to deteriorate the build's properties. One can understand the importance of AM for biomedical applications, as illustrated in Figures 14–18. Biomedical implant dimensions and requirements vary from patient to patient, making other routes challenging. Porous Ti implants are usually used for orthopedic implants owing to their outstanding mechanical and biological properties. The elastic modulus of bone ranges between 10 and 20 GPa and is mostly composed of inner cancellous and outer cortical bone [252]. Meanwhile, dense Ti alloys have an elastic modulus of around 110 GPa. However, it is worth mentioning that metallic alloys fabricated via AM tend to possess a lower elastic modulus than regular Ti-based alloys, making them comparable to bone [32]. In addition, porous Ti also possesses high rigidity and good fatigue properties, making it a suitable candidate for biomedical implants.

Figure 14 shows the Ti femoral implant and the hip ball-and-socket joints [253–255]. Pelvic injury is prevalent in trauma patients, caused by impact, rolling, steep falls, and other injuries. Recently, AM has often been employed for preoperative examination and simulated surgery treating pelvic fractures. Investigations demonstrate the possibility

of employing AM-fabricated Ti alloys for pelvic implants [256,257]. Wong et al. [258] manufactured pelvic-specific implants from Ti alloy and evaluated their performance. Broekhuis et al. [259] used AM to customize and create metallic pelvic prostheses for acetabular repair following tumor resections.

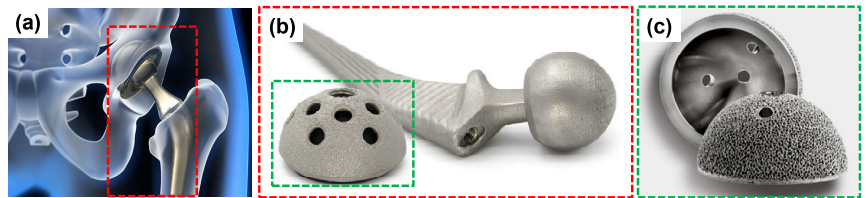


Figure 14. (a) Medical titanium alloy for anti-corrosive properties in femoral implant [253]; (b) 3D-printed titanium hip ball-and-socket implant: image credit: Jabil [254]; (c) first trabecular titanium hip cup produced by Lima Corporate, San Daniele del Friuli, Italy and Arcam Mölndal, Sweden (now a GE Additive company) in the year 2007 [255].

The spinal column is composed of interconnecting bones called vertebrae, which begin at the base of the head and finish at the tailbone in the lower back. The vertebral column is formed by stacking one bony vertebra on top of the next. The intervertebral discs are cushions that sit between each of the vertebral bodies. These discs act as shock absorbers, connecting the vertebrae (Figure 15). These discs also allow for the spine's bending and twisting action, assisted by facet joints. The spinal column protects the spinal cord, which links the brain's nerves to other body parts. In 2017, the United States FDA (Food and Drug Administration) authorized two alloys of Ti spinal implants made by AM. One example of an additively manufactured vertebral implant is the HAWKEYE Ti, while another is the NEXXT MATRIX 3D-printed spinal implant. Hollander et al. [260,261] employed AM technology to fabricate spinal implants with tailored porosity and demonstrated that their surface characteristics supported the adhesion and proliferation of human osteoblasts. Lin et al. [261] utilized the SLM/LPBF method to achieve a porosity of approximately 55%, resulting in an elastic modulus close to that of natural human bone (~3 GPa). This structure also exhibited superior bone regeneration capabilities compared to conventional PEEK cages.

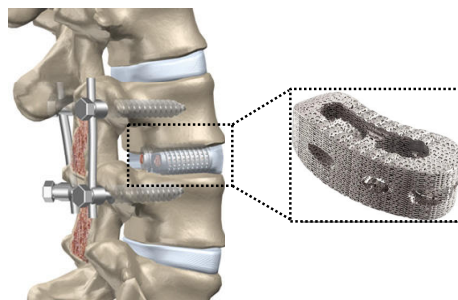


Figure 15. Human spinal column with the insert in black illustrating ATEC's IdentiTi posterior curved porous titanium interbody implants [262].

In certain cases, implants can act as bone replacements without being subjected to considerable and constant bearing or additional stress. Figure 16 is the cranial implant developed by Novax DMA [263] for a patient requiring a large metallic implant. In the case of a skull implant, external variables, particularly the implant itself, should be promoted rather than hindering the healing process. Most significantly, the implant should fit as

perfectly as feasible, as offered by AM. The manufacturing technique, which uses a laser for building up a material (Ti) layer by layer, allows for maximum customization in terms of form and size. Because of the large hole in the patient’s bone structure, integrating biological activities and minimizing heat loss into the brain tissue were given high priority. A Ti construction may also be impermeable to brain tissue fluid. Only permeable construction may satisfy the requirements.

A lattice-structured implant with skull-integrated, screw-in fasteners allows fluids to pass through and combine with the skull’s bone. Furthermore, such a construction would provide insulation, reducing heat transfer entering the cranial cavity. The pore spaces are around 1 mm, whereas the cell links are about 0.2 mm thick. Murr et al. [264] described a reticular skull implant developed through EBM. Mazzoli et al. [265] used CT imaging, computer modeling, and AM to produce a biocompatible Ti skull implant. Zhao et al. [266] observed that personalized Ti-based skull prosthetics made via AM offered higher impact resistance while efficiently repairing skull deformities and protecting intracranial brain tissue. Yan et al. [267] employed EBM to create a mandibular prosthetic implant that had a 3D mesh and a porosity of 81.3%, which fits the parameters for implantation in the human body (Figure 17). Figure 17a illustrates the 3D anatomic model of the human mandible developed using a CT imaging technique. Figure 17b shows the 3D structure developed in CAD software (Unigraphics NX 8.0, EDS) by providing internal 3D meshing for porous structures. Meanwhile, Figure 17c,d demonstrate the mandibular prosthetic implant produced by EBM. Moiduddin et al. [268] utilized a Ti-based alloy to fabricate cheekbones.

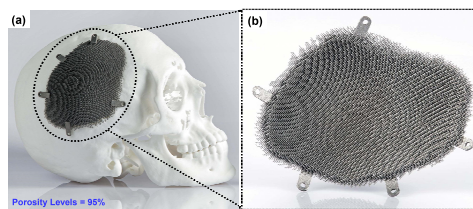


Figure 16. (a) Skull implants developed by Novax DMA. (b) Magnified image of the porous titanium cranial implants with porosity levels of 95% [263].

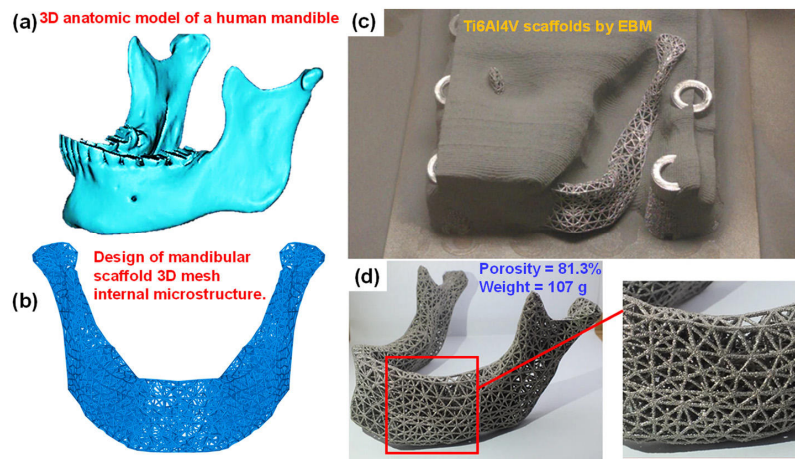


Figure 17. (a) Three-dimensional anatomic model of a human mandible prosthetic. (b) Design of mandibular scaffold 3D mesh internal microstructure. (c,d) Titanium alloy scaffolds produced by EBM with porosity levels of 81.3% and a weight of 107 g. Reproduced with permissions from [267].

Yanez et al. [269] studied the gyroid porous Ti structures, where triply periodic minimum surfaces (TPMS) have been recognized as an effective approach for developing porous biomaterials. They developed a variety of porous Ti structures with varying degrees of porosities using EBM to investigate mechanical characteristics under compression and torsion loads, as illustrated in Figure 18. Compression testing indicated that deformed gyroid structures possess significant strength and stiffness when subjected to axial loading, particularly when a reinforcing shell is incorporated. In torsional loading, however, conventional gyroids outperformed deformed gyroids with high CAD-defined porosity (90%) in terms of both torsional strength and stiffness. Notably, deformed gyroids exhibited superior mechanical behavior under compressive loads compared to their regular counterparts. Conversely, regular gyroids demonstrated better adaptability to non-axial and torsional loading conditions [269].

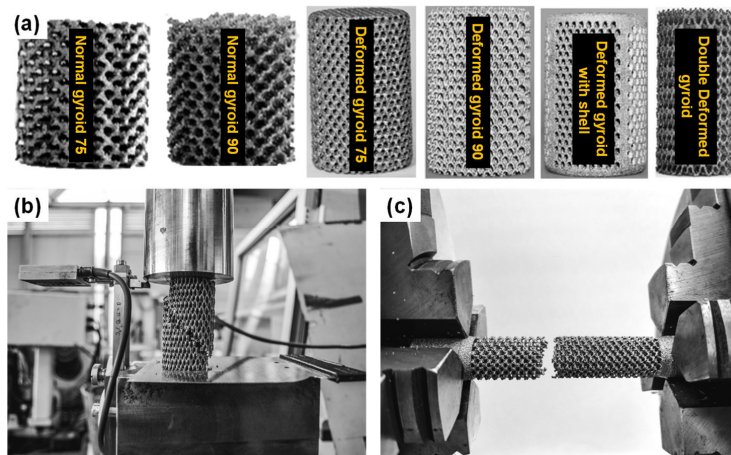


Figure 18. (a) Six variations of gyroid-structured porous titanium: normal gyroid 75, normal gyroid 90, deformed gyroid 75, deformed gyroid 90, deformed gyroid with shell reinforcement, and double deformed gyroid. (b) Visual depiction of compressive testing performed on the gyroid porous titanium structures. (c) Image capturing the torsional testing of one of the porous titanium configurations. Reproduced with permissions from [269].

Figure 19 depicts the many surface flaws that arise during bio-implant manufacturing. AM-processed bio-implants are often not ready for use due to surface defects such as powder adhesions, semi-welds, surface casing, porosity, balling effect, etc., highlighting the need for post-processing. The nature of the designs, prior processing software, and processing equipment all influence post-processing requirements. Post-processing includes removing unwanted material, improving the texture of the surface, aesthetic enhancements, component separation, rebinding and sintering, machining, surface finishing, non-thermal performance enhancement, heat treatment, and quality assurance. It is critical to enhance the surface finish by employing suitable surface quality techniques for AM-built biomedical implants to compete alongside widely recognized traditionally fabricated bio-implants [270–272].

Conventional processes involve employing multipoint or single-point instruments for cutting directly over the surface that is being finished or polished. These include robot-based finishing, rigid tool-based finishing, and computer numerical control-based finishing. Conventional processes are more difficult and time-consuming as they tend to induce residual stress on the surface. Cutting speed, feed, and other factors impact the machining characteristics and efficacy of difficult-to-cut minerals or metals, particularly Ti. The right choice of cutting and finishing parameters is critical for increased production

and widespread use in industries. Because of the increased use of implant finishing and existing issues with traditional machining, innovative methods are necessary to improve the machining properties of metallic implants [273]. The finishing procedure comprises polishing, but only for the outside cylindrical sections; it cannot complete the inside cylinders or intricate geometrical forms of the implants. Similarly, the grinding method of finishing does not allow access to the implants' deep holes and may leave markings on the final surface. Lapping is a laborious finishing method that is not suitable for intricate geometrical designs of implants. The burnishing procedure causes the completed surface to harden, making it unsuitable for thin-walled surfaces [274]. All limitations of conventional procedures have necessitated the development of improved finishing methods for bioimplants. Figure 20 illustrates the categories of surface post-treatments that may improve the surface characteristics of traditional or additively made bio-implants.

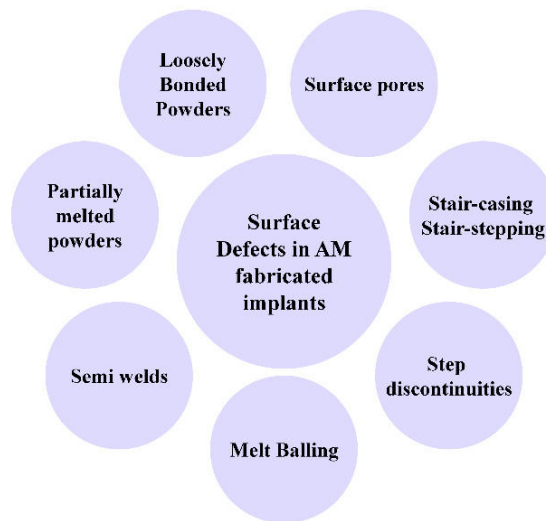


Figure 19. Surface defects occurring during AM-fabricated implants (reproduced with permission from [272]).

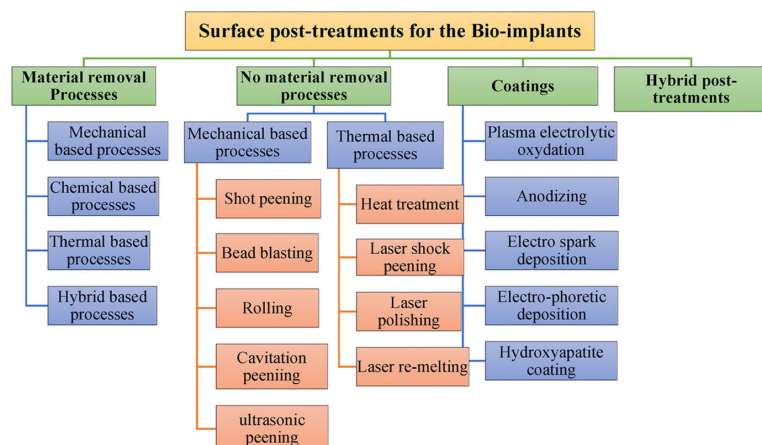


Figure 20. Classification of surface post-treatment for titanium implant materials for enhanced surface properties. Reproduced with permission from [270–272].

Srijan et al. [275] utilized surface mechanical attrition treatment (SMAT), a severe plastic deformation technique, to enhance the surface-dependent and functional properties of β -Ti alloy. The increased defect density resulting from SMAT led to a reduced corrosion rate through the formation of a stronger oxide layer and an improvement in wear resistance. Srijan et al. reviewed and classified recent advancements in surface modification, focusing on the induction of nano-crystallization on metallic biomaterials through various surface modification techniques [276].

6.7. Recent Trends in the Development of Porous Ti Scaffold: Titanium-Based Interpenetrating Phase Composites

As discussed in the previous sections, the major causes of implant failure, like stress shielding, implant loosening, etc., can be mitigated by reducing Young's modulus by making them porous using different fabrication techniques. However, these modifications invariably reduce the strength and fatigue resistance as compared to their dense counterpart [31,277–280]. To enhance the mechanical and biological properties of Ti-based scaffolds, researchers explore various techniques to integrate a secondary bioactive phase into the 3D-printed porous framework [281]. Magnesium, zinc, calcium, and iron [44,282–285], or their alloys, are commonly utilized metallic biomaterials. At the same time, hydroxyapatite (HAp), wollastonite (CaSiO_3) [28], etc., are common ceramic materials that can serve as filler material. The logic behind adding all these materials inside the metallic porous network is to provide mechanical and biological support during the initial implantation period. Since these filler materials are either biodegradable or bioresorbable, they naturally degrade within the human body over time [286]. Zhang et al. [287] developed a Mg-Ti composite via the pressureless infiltration of Mg into an AM-fabricated Ti6Al4V scaffold. Since the constituents of the composite were continuous and mutually interpenetrated in the 3-D space, the composite was termed an interpenetrating phase composite. These porous structures were designed to mimic the bioinspired architecture (Figure 21). The composite shows effective stress transfer, delocalized damage, and arrest cracking. Similarly, Dou et al. [281] fabricated partially degradable interpenetrating phase composites by first creating a pure titanium-based dodecahedral cellular structure with pore sizes ranging from 400 to 500 μm using selective laser melting (SLM), followed by pressureless infiltration of pure magnesium into the porous framework. The developed composite possesses a higher strength (yield strength of ~ 64 MPa and ultimate compressive strength of ~ 275 MPa) and lower modulus (~ 47.3 GPa) than cast pure Mg and Ti. Also, the degradation of the Mg supports the ingrowth of bone tissue and biological fixation between the host and implant. In vitro and in vivo studies of these composites revealed that the composite exhibits accelerated corrosion compared to pure Mg. Still, it remains non-cytotoxic and does not induce obvious adverse reactions following implantation.

In a similar approach, Rahmani et al. [28] reported the addition of three different types of wollastonite (CaSiO_3)-based bio-ceramic via SPS in an AM Ti6Al4V lattice, as shown in Figure 22. The produced composite exhibited higher wear resistance, damage tolerance, and mechanical properties, which can improve the durability of the bones. In addition to Ti6Al4V, TiNi, and Ti22Al25Nb, porous samples infiltrated with wollastonite showed that TiNi has a higher damping capacity, while Ti22Al25Nb induces a higher portion of elastic deformation. In another study, Rahmani et al. [28] reported improved impact and osteoinductivity by manufacturing hybrid wollastonite and Ti6Al4V for craniofacial implants.

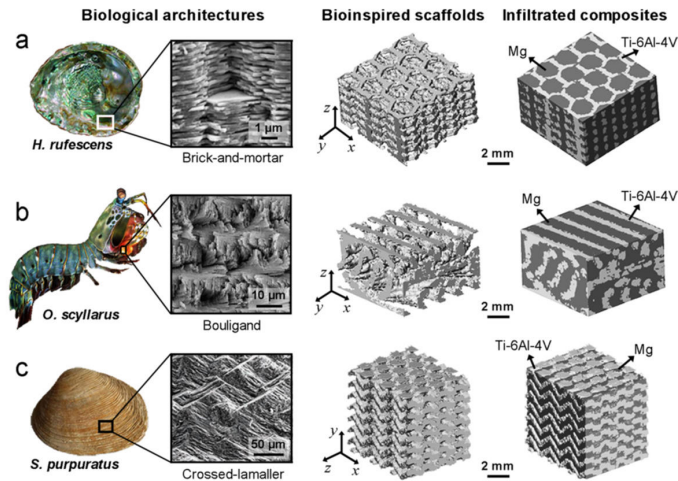


Figure 21. Bioinspired architecture comprises additively manufactured Ti6Al4V and pressureless infiltrated Mg. The developed Mg-Ti composite resembles bioinspired architecture showing (a) brick-and-mortar structure, (b) Bouligand structure and (c) crossed-lamellar structure. Reproduced with permission from [287].

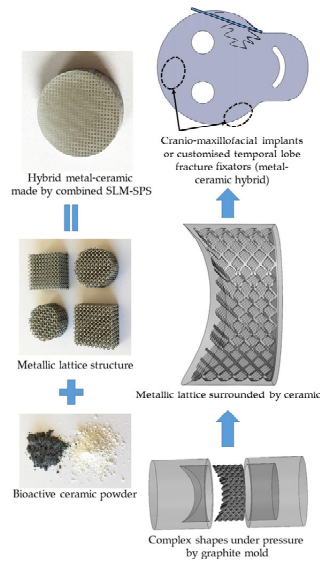


Figure 22. Processing step for designing cranio-maxillofacial implant by infiltrating wollastonite and hydroxyapatite-based nanoscale bioceramics inside titanium alloys with arbitrary lattice structures. Reproduced with permissions from [27].

7. Current Challenges for Porous Titanium

Porous Ti has the potential to be suited for biomedical applications due to its high strength, lower elastic modulus, longer fatigue life, and good wear and corrosion resistance. In addition to the abovementioned mechanical properties, porous Ti exhibits excellent biocompatibility and helps pass fluids through the porous structures. Nevertheless, challenges are associated with the fabrication and processing of porous Ti implants:

- (1) Porous Ti implants are difficult to manufacture, and optimally controlling pores and maintaining the uniformity of pores are challenging tasks.
- (2) The interconnectivity of the pores is essential in determining the mechanical properties of the implants. It is paramount to maintain a tradeoff between the strength and porosity of porous Ti implants.
- (3) As implants undergo repeated cycles of loading and unloading during daily activities, the porous structures generally exhibit lower fatigue resistance compared to their dense counterpart. The pores serve as potential initiation points for fatigue cracks, which can gradually propagate and ultimately result in premature implant failure.
- (4) There must be a balance between patient-specific implants and large-scale production of implants, i.e., customization and production, since developing porous structures and meshing is time-consuming.
- (5) The implant cost should also be considered, as porous Ti implants are usually costlier than fully dense implants. Higher costs of implants reduce the demand in the market.
- (6) Implementing thorough checking to minimize defect concentration is important to obtain high-quality implants with better mechanical properties and biocompatibility.
- (7) Especially in the case of AM, thermal gradients can lead to variations in pore sizes and porosity levels.
- (8) The post-processing of the porous structures is also very difficult and time-consuming. It must be carried out carefully, as small disruptions can damage the interconnected structures, leading to defective implants.

8. Future Scope of Titanium-Based Porous Implants

Porous Ti has been proven to be the best-suited candidate, especially for orthopedic implants and prosthetics. It has taken the field of biomaterials, specifically implants, by storm and is expected to be the future of biomedical implants, especially orthopedic implants. However, in short, a few porous Ti challenges must be resolved to make it irreplaceable in the market:

- (1) AM has been gaining momentum in producing porous Ti structures. However, more efforts must be taken to fabricate porous structures with good pore interconnectivity, which will, in turn, pave the way for better mechanical properties and biocompatibility.
- (2) A biocompatible coating can be applied to enhance the osseointegration of the implant with body fluids.
- (3) Porous Ti structures can be used as multifunctional implants by integrating them with drug delivery systems or sensors.
- (4) Efforts should be made to make the porous Ti implants more accessible at an affordable price, which is possible through process optimization to achieve higher productivity at a lower cost.
- (5) Investigations of biocompatible joining strategies should be carried out for integrating porous Ti into various biomaterials or metallic implant structures.
- (6) The development of interpenetrating phase composites is limited to the Ti-Mg system since the developed composite has the potential to be utilized as an implant; therefore, a composite system comprising Ti-Zn/Ca/Fe and SS-Mg/Zn/Ca/Fe should be explored.

9. Conclusions

The present review focused on exploring the development of Ti-based porous biomaterial for orthopedic applications. Different characteristics and requirements of biomaterials, like mechanical, physical, and biological properties, are comprehensively reviewed. A section of the review was dedicated to the structure of bone and its physiology for the

basic understanding of bone metabolism, which should be considered while designing and synthesizing next-generation orthopedic and dental implants. Considering the importance of porous Ti-based implants for orthopedic applications, this review presents different processing techniques, particularly based on powder metallurgy processes, and the properties of the developed porous implants are compared. Given the importance of the powder metallurgical route for synthesizing porous implants, a detailed study of various powder processing techniques was carried out. Finally, this review concludes by discussing the current challenges and future potential of porous Ti-based alloys for biomaterial implant application.

Author Contributions: Conceptualization, M.K.Y., P.K., J.J. and P.K.G.; methodology, M.K.Y., A.Y., Y.N.A., P.K. and V.P.; validation, C.S.P., A.N., K.C., S.S., J.J. and P.K.G.; formal analysis, M.K.Y. and A.Y.; investigation, M.K.Y., A.Y., P.K., V.P. and C.S.P.; resources, S.S., K.C. and P.K.G.; data curation, M.K.Y., A.Y. and P.K.; writing—original draft preparation, M.K.Y., A.Y., Y.N.A. and P.K.; writing—review and editing, V.P., C.S.P., A.N., K.C., S.S., J.J. and P.K.G.; supervision, P.K.G.; project administration, P.K.G. All authors have read and agreed to the published version of the manuscript.

Funding: This work was supported by the European Union through the REFRESH—Research Excellence for Region Sustainability and High-tech Industries—project (Project No. CZ.10.03.01/00/22_003/0000048), funded under the Operational Programme Just Transition.

Data Availability Statement: No new data were created or analyzed in this study. Data sharing is not applicable to this article.

Conflicts of Interest: The authors declare no conflicts of interest.

References

1. Cui, Y.W.; Wang, L.; Zhang, L.C. Towards Load-Bearing Biomedical Titanium-Based Alloys: From Essential Requirements to Future Developments. *Prog. Mater. Sci.* **2024**, *144*, 101277. [[CrossRef](#)]
2. Banhart, J. Manufacture, Characterisation and Application of Cellular Metals and Metal Foams. *Prog. Mater. Sci.* **2001**, *46*, 559–632. [[CrossRef](#)]
3. Dabrowski, B.; Swieszkowski, W.; Godlinski, D.; Kurzydowski, K.J. Highly Porous Titanium Scaffolds for Orthopaedic Applications. *J. Biomed. Mater. Res. B Appl. Biomater.* **2010**, *95*, 53–61. [[CrossRef](#)] [[PubMed](#)]
4. Nabyouni, M.; Brückner, T.; Zhou, H.; Gbureck, U.; Bhaduri, S.B. Magnesium-Based Bioceramics in Orthopedic Applications. *Acta Biomater.* **2018**, *66*, 23–43. [[CrossRef](#)]
5. Kim, T.; See, C.W.; Li, X.; Zhu, D. Orthopedic Implants and Devices for Bone Fractures and Defects: Past, Present and Perspective. *Eng. Regen.* **2020**, *1*, 6–18. [[CrossRef](#)]
6. Spicer, P.P.; Kretlow, J.D.; Young, S.; Jansen, J.A.; Kasper, F.K.; Mikos, A.G. Evaluation of Bone Regeneration Using the Rat Critical Size Calvarial Defect. *Nat. Protoc.* **2012**, *7*, 1918–1929. [[CrossRef](#)]
7. Oryan, A.; Alidadi, S.; Moshiri, A.; Maffulli, N. Bone Regenerative Medicine: Classic Options, Novel Strategies, and Future Directions. *J. Orthop. Surg. Res.* **2014**, *9*, 18. [[CrossRef](#)]
8. Zhou, H.; Lawrence, J.G.; Bhaduri, S.B. Fabrication Aspects of PLA-CaP/PLGA-CaP Composites for Orthopedic Applications: A Review. *Acta Biomater.* **2012**, *8*, 1999–2016. [[CrossRef](#)]
9. Stevens, M.M. Biomaterials for Bone Tissue Engineering. *Mater. Today* **2008**, *11*, 18–25. [[CrossRef](#)]
10. Keating, J.F.; McQueen, M.M. Substitutes for autologous bone graft in orthopaedic trauma. *J. Bone Jt. Surg. Br. Vol.* **2001**, *83*, 3–8. [[CrossRef](#)]
11. Damien, C.J.; Parsons, J.R. Bone Graft and Bone Graft Substitutes: A Review of Current Technology and Applications. *J. Appl. Biomater.* **1991**, *2*, 187–208. [[CrossRef](#)] [[PubMed](#)]
12. Hering, B.J.; Walawalkar, N. Pig-to-Nonhuman Primate Islet Xenotransplantation. *Transpl. Immunol.* **2009**, *21*, 81–86. [[CrossRef](#)] [[PubMed](#)]
13. Fishman, J.A.; Patience, C. Xenotransplantation: Infectious Risk Revisited. *Am. J. Transplant.* **2004**, *4*, 1383–1390. [[CrossRef](#)] [[PubMed](#)]
14. Cooper, D.K.C.; Ezzelarab, M.B.; Hara, H.; Iwase, H.; Lee, W.; Wijkstrom, M.; Bottino, R. The Pathobiology of Pig-to-Primate Xenotransplantation: A Historical Review. *Xenotransplantation* **2016**, *23*, 83–105. [[CrossRef](#)]

15. Geetha, M.; Singh, A.K.; Asokamani, R.; Gogia, A.K. Ti Based Biomaterials, the Ultimate Choice for Orthopaedic Implants—A Review. *Prog. Mater. Sci.* **2009**, *54*, 397–425. [[CrossRef](#)]
16. Yadav, M.K.; Pandey, V.; Jyoti, Kumar, A.; Mohanta, K.; Singh, V.K. Mechanical and Biological Behaviour of Porous Ti–SiO₂ Scaffold for Tissue Engineering Application. *Ceram. Int.* **2021**, *47*, 22191–22200. [[CrossRef](#)]
17. Kumar Yadav, M.; Hiren Shukla, R.; Prashanth, K.G. A Comprehensive Review on Development of Waste Derived Hydroxyapatite (HAp) for Tissue Engineering Application. *Mater. Today Proc.* **2023**. [[CrossRef](#)]
18. Yadav, M.K.; Pandey, V.; Mohanta, K.; Singh, V.K. A Low-Cost Approach to Develop Silica Doped Tricalcium Phosphate (TCP) Scaffold by Valorizing Animal Bone Waste and Rice Husk for Tissue Engineering Applications. *Ceram. Int.* **2022**, *48*, 25335–25345. [[CrossRef](#)]
19. Ershad-Langroudi, A.; Babazadeh, N.; Alizadegan, F.; Mehdi Mousaei, S.; Moradi, G. Polymers for Implantable Devices. *J. Ind. Eng. Chem.* **2024**, *137*, 61–86. [[CrossRef](#)]
20. Singh, N.; Srikanth, K.P.; Gopal, V.; Rajput, M.; Manivasagam, G.; Prashanth, K.G.; Chatterjee, K.; Suwas, S. In Situ Production of Low-Modulus Ti–Nb Alloys by Selective Laser Melting and Their Functional Assessment toward Orthopedic Applications. *J. Mater. Chem. B* **2024**, *12*, 5982–5993. [[CrossRef](#)]
21. Ummethala, R.; Karamched, P.S.; Rathinavelu, S.; Singh, N.; Aggarwal, A.; Sun, K.; Ivanov, E.; Kollo, L.; Okulov, I.; Eckert, J.; et al. Selective Laser Melting of High-Strength, Low-Modulus Ti–35Nb–7Zr–5Ta Alloy. *Materialia* **2020**, *14*, 100941. [[CrossRef](#)]
22. Hameed, P.; Liu, C.F.; Ummethala, R.; Singh, N.; Huang, H.H.; Manivasagam, G.; Prashanth, K.G. Biomorphic Porous Ti6Al4V Gyroid Scaffolds for Bone Implant Applications Fabricated by Selective Laser Melting. *Prog. Addit. Manuf.* **2021**, *6*, 455–469. [[CrossRef](#)]
23. Khan, P.A.; Raheem, A.; Kalirajan, C.; Prashanth, K.G.; Manivasagam, G. In Vivo Assessment of a Triple Periodic Minimal Surface Based Biomimetic Gyroid as an Implant Material in a Rabbit Tibia Model. *ACS Mater. Au* **2024**, *4*, 479–488. [[CrossRef](#)] [[PubMed](#)]
24. Neto, J.V.C.; Teixeira, A.B.V.; Cândido dos Reis, A. Hydroxyapatite Coatings versus Osseointegration in Dental Implants: A Systematic Review. *J. Prosthet. Dent.* **2023**, *134*, 92–99. [[CrossRef](#)] [[PubMed](#)]
25. Salahinejad, E.; Vahedifard, R. Deposition of Nanodiopside Coatings on Metallic Biomaterials to Stimulate Apatite-Forming Ability. *Mater. Des.* **2017**, *123*, 120–127. [[CrossRef](#)]
26. Rahmani, R.; Lopes, S.I.; Prashanth, K.G. Selective Laser Melting and Spark Plasma Sintering: A Perspective on Functional Biomaterials. *J. Funct. Biomater.* **2023**, *14*, 521. [[CrossRef](#)]
27. Rahmani, R.; Kamboj, N.; Brojan, M.; Antonov, M.; Prashanth, K.G. Hybrid Metal–Ceramic Biomaterials Fabricated through Powder Bed Fusion and Powder Metallurgy for Improved Impact Resistance of Craniofacial Implants. *Materialia* **2022**, *24*, 101465. [[CrossRef](#)]
28. Rahmani, R.; Antonov, M.; Kollo, L.; Holovenko, Y.; Prashanth, K.G. Mechanical Behavior of Ti6Al4V Scaffolds Filled with CaSiO₃ for Implant Applications. *Appl. Sci.* **2019**, *9*, 3844. [[CrossRef](#)]
29. Kamboj, N.; Rodríguez, M.A.; Rahmani, R.; Prashanth, K.G.; Hussainova, I. Bioceramic Scaffolds by Additive Manufacturing for Controlled Delivery of the Antibiotic Vancomycin. *Proc. Est. Acad. Sci.* **2019**, *68*, 185–190. [[CrossRef](#)]
30. Al-Shalawi, F.D.; Azmah Hanim, M.A.; Ariffin, M.K.A.; Looi Seng Kim, C.; Brabazon, D.; Calin, R.; Al-Osaimi, M.O. Biodegradable Synthetic Polymer in Orthopaedic Application: A Review. *Mater. Today Proc.* **2023**, *74*, 540–546. [[CrossRef](#)]
31. Praveenkumar, K.; Manivasagam, G.; Swaroop, S. Effect of Laser Peening on the Residual Stress Distribution and Wettability Characteristics of Ti-6Al-4V Alloy for Biomedical Applications. *Trends Biomater. Artif. Organs* **2022**, *36*, 18–25.
32. Arabnejad, S.; Johnston, B.; Tanzer, M.; Pasini, D. Fully Porous 3D Printed Titanium Femoral Stem to Reduce Stress-Shielding Following Total Hip Arthroplasty. *J. Orthop. Res.* **2017**, *35*, 1774–1783. [[CrossRef](#)] [[PubMed](#)]
33. Engler, I.D.; Hart, P.A.; Swanson, D.P.; Kirsch, J.M.; Murphy, J.P.; Wright, M.A.; Murthi, A.; Jawa, A. High Prevalence of Early Stress Shielding in Stemless Shoulder Arthroplasty. *Semin. Arthroplast. JSES* **2022**, *32*, 751–756. [[CrossRef](#)]
34. Nagels, J.; Stokdijk, M.; Rozing, P.M. Stress Shielding and Bone Resorption in Shoulder Arthroplasty. *J. Shoulder Elb. Surg.* **2003**, *12*, 35–39. [[CrossRef](#)]
35. Praveenkumar, K.; Vishnu, J.; Samuel S., C.; Gopal, V.; Arivarasu, M.; Lackner, J.M.; Meier, B.; Karthik, D.; Suwas, S.; Swaroop, S.; et al. High Temperature Dry Sliding Wear Behaviour of Selective Laser Melted Ti-6Al-4V Alloy Surfaces. *J. Mater. Process. Technol.* **2024**, *329*, 118439. [[CrossRef](#)]
36. Praveenkumar, K.; Swaroop, S.; Manivasagam, G. Effect of Multiple Laser Shock Peening without Coating on Residual Stress Distribution and High Temperature Dry Sliding Wear Behaviour of Ti-6Al-4 V Alloy. *Opt. Laser Technol.* **2023**, *164*, 109398. [[CrossRef](#)]
37. Praveenkumar, K.; Mylavarapu, P.; Sarkar, A.; Isaac Samuel, E.; Nagesha, A.; Swaroop, S. Residual Stress Distribution and Elevated Temperature Fatigue Behaviour of Laser Peened Ti-6Al-4V with a Curved Surface. *Int. J. Fatigue* **2022**, *156*, 106641. [[CrossRef](#)]

38. Praveenkumar, K.; Vishnu, J.; Raheem, A.; Gopal, V.; Swaroop, S.; Suwas, S.; Shankar, B.; Manivasagam, G. In-Vitro Fretting Tribocorrosion and Biocompatibility Aspects of Laser Shock Peened Ti-6Al-4V Surfaces. *Appl. Surf. Sci.* **2024**, *665*, 160334. [[CrossRef](#)]
39. Bandyopadhyay, A.; Mitra, I.; Goodman, S.B.; Kumar, M.; Bose, S. Improving Biocompatibility for next Generation of Metallic Implants. *Prog. Mater. Sci.* **2023**, *133*, 101053. [[CrossRef](#)]
40. Bai, L.; Gong, C.; Chen, X.; Sun, Y.; Zhang, J.; Cai, L.; Zhu, S.; Xie, S.Q. Additive Manufacturing of Customized Metallic Orthopedic Implants: Materials, Structures, and Surface Modifications. *Metals* **2019**, *9*, 1004. [[CrossRef](#)]
41. Donachie, M.J. *Titanium: A Technical Guide*; ASM International: Almere, The Netherlands, 2000. [[CrossRef](#)]
42. Sanan, A.; Haines, S.J. Repairing Holes in the Head: A History of Cranioplasty. *Neurosurgery* **1997**, *40*, 588–603. [[CrossRef](#)] [[PubMed](#)]
43. Praveenkumar, K.; Mylavarapu, P.; Swaroop, S. Surface Oxidation and Subsurface Deformation in a Laser-Peened Ti-6Al-4V. *J. Mater. Eng. Perform.* **2023**, *32*, 7348–7362. [[CrossRef](#)]
44. Vishnu, J.; Praveenkumar, K.; Kumar, A.A.; Nair, A.; Arjun, R.; Pillai, V.G.; Shankar, B.; Shankar, K.V. Multifunctional Zinc Oxide Loaded Stearic Acid Surfaces on Biodegradable Magnesium WE43 Alloy with Hydrophobic, Self-Cleaning and Biocompatible Attributes. *Appl. Surf. Sci.* **2025**, *680*, 161455. [[CrossRef](#)]
45. Spoerke, E.D.; Murray, N.G.; Li, H.; Brinson, L.C.; Dunand, D.C.; Stupp, S.I. A Bioactive Titanium Foam Scaffold for Bone Repair. *Acta Biomater.* **2005**, *1*, 523–533. [[CrossRef](#)]
46. Müller, U.; Imwinkelried, T.; Horst, M.; Sievers, M.; Graf-Hausner, U. Do Human Osteoblasts Grow into Open-Porous Titanium? *Cell Mater* **2006**, *11*, 8–15. [[CrossRef](#)]
47. Pohler, O.E.M. Unalloyed Titanium for Implants in Bone Surgery. *Injury* **2000**, *31*, D7–D13. [[CrossRef](#)]
48. Yang, S.; Leong, K.F.; Du, Z.; Chua, C.K. The Design of Scaffolds for Use in Tissue Engineering. Part I. Traditional Factors. *Tissue Eng.* **2001**, *7*, 679–689. [[CrossRef](#)]
49. Maity, T.; Balci, Ö.; Gammer, C.; Ivanov, E.; Eckert, J.; Prashanth, K.G. High Pressure Torsion Induced Lowering of Young’s Modulus in High Strength TNZT Alloy for Bio-Implant Applications. *J. Mech. Behav. Biomed. Mater.* **2020**, *108*, 103839. [[CrossRef](#)]
50. Nag, S.; Samuel, S.; Puthucode, A.; Banerjee, R. Characterization of Novel Borides in Ti-Nb-Zr-Ta + 2B Metal-Matrix Composites. *Mater. Charact.* **2009**, *60*, 106–113. [[CrossRef](#)]
51. Luo, J.P.; Huang, Y.J.; Xu, J.Y.; Sun, J.F.; Dargusch, M.S.; Hou, C.H.; Ren, L.; Wang, R.Z.; Ebel, T.; Yan, M. Additively Manufactured Biomedical Ti-Nb-Ta-Zr Lattices with Tunable Young’s Modulus: Mechanical Property, Biocompatibility, and Proteomics Analysis. *Mater. Sci. Eng. C* **2020**, *114*, 110903. [[CrossRef](#)]
52. Sahay, S.; Kesavan, P.; Yadav, M.K.; Nilawar, S.; Manivasagam, G.; Chatterjee, K. High-Pressure Torsion Affects Mechanical Properties, Electrochemical Behavior, and Cellular Response to a Biomedical Ti-Nb-Zr-Ta Alloy. *Mater. Trans.* **2025**, *66*, 490–500. [[CrossRef](#)]
53. Weber, J.N.; White, E.W. Carbon-Metal Graded Composites for Permanent Osseous Attachment of Non-Porous Metals. *Mater. Res. Bull.* **1972**, *7*, 1005–1016. [[CrossRef](#)]
54. Prashanth, K.; Zhuravleva, K.; Okulov, I.; Calin, M.; Eckert, J.; Gebert, A. Mechanical and Corrosion Behavior of New Generation Ti-45Nb Porous Alloys Implant Devices. *Technologies* **2016**, *4*, 33. [[CrossRef](#)]
55. Zhang, L.; He, Z.Y.; Tan, J.; Calin, M.; Prashanth, K.G.; Sarac, B.; Völker, B.; Jiang, Y.H.; Zhou, R.; Eckert, J. Designing a Multifunctional Ti-2Cu-4Ca Porous Biomaterial with Favorable Mechanical Properties and High Bioactivity. *J. Alloys Compd.* **2017**, *727*, 338–345. [[CrossRef](#)]
56. Attar, H.; Löber, L.; Funk, A.; Calin, M.; Zhang, L.C.; Prashanth, K.G.; Scudino, S.; Zhang, Y.S.; Eckert, J. Mechanical Behavior of Porous Commercially Pure Ti and Ti-TiB Composite Materials Manufactured by Selective Laser Melting. *Mater. Sci. Eng. A* **2015**, *625*, 350–356. [[CrossRef](#)]
57. Zhuravleva, K.; Bönisch, M.; Prashanth, K.G.; Hempel, U.; Helth, A.; Gemming, T.; Calin, M.; Scudino, S.; Schultz, L.; Eckert, J.; et al. Production of Porous β -Type Ti-40Nb Alloy for Biomedical Applications: Comparison of Selective Laser Melting and Hot Pressing. *Materials* **2013**, *6*, 5700–5712. [[CrossRef](#)]
58. Fisher, J.P.; Mikos, A.G.; Bronzino, J.D. Tissue Engineering. *Science* **1993**, *260*, 1–583. [[CrossRef](#)]
59. Hutmacher, D.W. Scaffolds in Tissue Engineering Bone and Cartilage. *Biomaterials* **2000**, *21*, 2529–2543. [[CrossRef](#)]
60. Palka, K.; Pokrowiecki, R. Porous Titanium Implants: A Review. *Adv. Eng. Mater.* **2018**, *20*, 1700648. [[CrossRef](#)]
61. Koju, N.; Niraula, S.; Fotovvati, B. Additively Manufactured Porous Ti6Al4V for Bone Implants: A Review. *Metals* **2022**, *12*, 687. [[CrossRef](#)]
62. Niinomi, M.; Nakai, M.; Hieda, J. Development of New Metallic Alloys for Biomedical Applications. *Acta Biomater.* **2012**, *8*, 3888–3903. [[CrossRef](#)] [[PubMed](#)]
63. Frost, H.M. Bone’s Mechanostat: A 2003 Update. *Anat. Rec. Part A Discov. Mol. Cell. Evol. Biol.* **2003**, *275*, 1081–1101. [[CrossRef](#)] [[PubMed](#)]

64. Gardner, M.J.; Van Der Meulen, M.C.H.; Demetrakopoulos, D.; Wright, T.M.; Myers, E.R.; Bostrom, M.P. In Vivo Cyclic Axial Compression Affects Bone Healing in the Mouse Tibia. *J. Orthop. Res.* **2006**, *24*, 1679–1686. [[CrossRef](#)] [[PubMed](#)]
65. Bozec, L.; Horton, M.A. Skeletal Tissues as Nanomaterials. *J. Mater. Sci. Mater. Med.* **2006**, *17*, 1043–1048. [[CrossRef](#)]
66. Long, M.; Rack, H.J. Titanium Alloys in Total Joint Replacement—A Materials Science Perspective. *Biomaterials* **1998**, *19*, 1621–1639. [[CrossRef](#)]
67. Sumner, D.R.; Turner, T.M.; Igloria, R.; Urban, R.M.; Galante, J.O. Functional Adaptation and Ingrowth of Bone Vary as a Function of Hip Implant Stiffness. *J. Biomech.* **1998**, *31*, 909–917. [[CrossRef](#)]
68. Zhao, D.; Witte, F.; Lu, F.; Wang, J.; Li, J.; Qin, L. Current Status on Clinical Applications of Magnesium-Based Orthopaedic Implants: A Review from Clinical Translational Perspective. *Biomaterials* **2017**, *112*, 287–302. [[CrossRef](#)]
69. Agarwal, S.; Curtin, J.; Duffy, B.; Jaiswal, S. Biodegradable Magnesium Alloys for Orthopaedic Applications: A Review on Corrosion, Biocompatibility and Surface Modifications. *Mater. Sci. Eng. C* **2016**, *68*, 948–963. [[CrossRef](#)]
70. Osuchukwu, O.A.; Salihi, A.; Abdullahi, I.; Obada, D.O.; Abolade, S.A.; Akande, A.; Csaki, S.; Dodoo-Arhin, D. Datasets on the Elastic and Mechanical Properties of Hydroxyapatite: A First Principle Investigation, Experiments, and Pedagogical Perspective. *Data Brief* **2023**, *48*, 109075. [[CrossRef](#)]
71. Piconi, C.; Maccauro, G. Zirconia as a Ceramic Biomaterial. *Biomaterials* **1999**, *20*, 1–25. [[CrossRef](#)]
72. Attar, H.; Prashanth, K.G.; Chaubey, A.K.; Calin, M.; Zhang, L.C.; Scudino, S.; Eckert, J. Comparison of Wear Properties of Commercially Pure Titanium Prepared by Selective Laser Melting and Casting Processes. *Mater. Lett.* **2015**, *142*, 38–41. [[CrossRef](#)]
73. Yan, Q.; Hou, L.; Sun, J.; Li, D.; Song, J.; Liu, X.; Wang, Q.; Wei, Y. Regulating the Localized Corrosion of Grain Boundary and Galvanic Corrosion by Adding the Electronegative Element in Magnesium Alloy. *Corros. Sci.* **2025**, *244*, 112667. [[CrossRef](#)]
74. Zhang, T.; Wang, Z.; Qiu, Y.; Iftikhar, T.; Liu, H. “Electrons-Siphoning” of Sulfate Reducing Bacteria Biofilm Induced Sharp Depletion of Al-Zn-In-Mg-Si Sacrificial Anode in the Galvanic Corrosion Coupled with Carbon Steel. *Corros. Sci.* **2023**, *216*, 111103. [[CrossRef](#)]
75. Nomura, K.; Sakairi, M.; Fushimi, K. Ion-Selectivity of Galvanic Corrosion Products Formed in Multi-Material Gaps under Atmospheric Corrosion Conditions with Anti-Freezing Salts. *Corros. Sci.* **2024**, *237*, 112305. [[CrossRef](#)]
76. Lucas, L.C.; Buchanan, R.A.; Lemons, J.E. Investigations on the Galvanic Corrosion of Multialloy Total Hip Prostheses. *J. Biomed. Mater. Res.* **1981**, *15*, 731–747. [[CrossRef](#)] [[PubMed](#)]
77. Szklarska-Smialowska, Z. Pitting Corrosion of Aluminum. *Corros. Sci.* **1999**, *41*, 1743–1767. [[CrossRef](#)]
78. Loto, R.T. Pitting Corrosion Resistance and Inhibition of Lean Austenitic Stainless Steel Alloys. *Austenitic Stainl. Steels New Asp.* **2017**, 147–170. [[CrossRef](#)]
79. Zhao, K.; Liu, J.H.; Yu, M.; Li, S.M. Through-Thickness Inhomogeneity of Precipitate Distribution and Pitting Corrosion Behavior of Al–Li Alloy Thick Plate. *Trans. Nonferrous Met. Soc. China* **2019**, *29*, 1793–1802. [[CrossRef](#)]
80. McCafferty, E. *Introduction to Corrosion Science*; Springer: Berlin/Heidelberg, Germany, 2010; ISBN 9781441904546.
81. Prashanth, K.G.; Debalina, B.; Wang, Z.; Gostin, P.F.; Gebert, A.; Calin, M.; Kühn, U.; Kamaraj, M.; Scudino, S.; Eckert, J. Tribological and Corrosion Properties of Al-12Si Produced by Selective Laser Melting. *J. Mater. Res.* **2014**, *29*, 2044–2054. [[CrossRef](#)]
82. Aoyama, T.; Kato, C. Introduction of Cu²⁺ to the inside of the Crevice by Chelation and Its Effect on Crevice Corrosion of Type 316L Stainless Steel. *Corros. Sci.* **2023**, *210*, 110850. [[CrossRef](#)]
83. Zhao, M.; Wang, J.; Ma, Y.; Xu, Y.; Zhang, X.; Li, Z.; Xu, D.; Wang, F. Electroactive Shewanella Algae Accelerates the Crevice Corrosion of X70 Pipeline Steel in Marine Environment. *Corros. Sci.* **2024**, *235*, 112226. [[CrossRef](#)]
84. Liu, H.; Wang, Z.; Qiao, L.; Su, Y.; Yan, Y. Role of Protein in Crevice Corrosion of CoCrMo Alloy: An Investigation Using Wire Beam Electrodes. *Corros. Sci.* **2023**, *215*, 111028. [[CrossRef](#)]
85. Levine, D.L.; Staehle, R.W. Crevice Corrosion in Orthopedic Implant Metals. *J. Biomed. Mater. Res.* **1977**, *11*, 553–561. [[CrossRef](#)] [[PubMed](#)]
86. Uva Narayanan, C.; Daniel, A.; Praveenkumar, K.; Manivasagam, G.; Suwas, S.; Prashanth, K.G.; Suya Prem Anand, P. Effect of Scanning Speed on Mechanical, Corrosion, and Fretting-Tribocorrosion Behavior of Austenitic 316L Stainless Steel Produced by Laser Powder Bed Fusion Process. *J. Manuf. Process* **2024**, *131*, 1582–1593. [[CrossRef](#)]
87. Kang, L.Z.; Lu, Y.H.; Bian, W.W.; Yu, P.J.; Wang, Y.B.; Xin, L.; Han, Y.M. Fretting Corrosion Behavior and Microstructure Evolution of Hydrided Zirconium Alloy under Gross Slip Regime in High Temperature High Pressure Water Environment. *Corros. Sci.* **2025**, *242*, 112582. [[CrossRef](#)]
88. Bian, W.W.; Lu, Y.H.; Zhang, X.F.; Han, Y.M.; Wang, F.; Shoji, T. Effect of Fretting Wear Regimes on Stress Corrosion Cracking of Alloy 690TT in High-Temperature Pressurized Water. *Corros. Sci.* **2024**, *237*, 112320. [[CrossRef](#)]
89. Sargeant, A.; Goswami, T. Hip Implants: Paper V. Physiological Effects. *Mater. Des.* **2006**, *27*, 287–307. [[CrossRef](#)]
90. Ghosh, S.; Choudhury, D.; Roy, T.; Moradi, A.; Masjuki, H.H.; Pinguan-Murphy, B. Tribological Performance of the Biological Components of Synovial Fluid in Artificial Joint Implants. *Sci. Technol. Adv. Mater.* **2015**, *16*, 045002. [[CrossRef](#)]
91. Eliaz, N. Corrosion of Metallic Biomaterials: A Review. *Materials* **2019**, *12*, 407. [[CrossRef](#)]

92. Seo, E.; Lee, Y.N.; Shin, W.Y.; Kim, K.H.; Jung, S.H.; Kang, H.G.; Kim, R.; Sung, H.; Jung, I.D.; Park, J.W. Structural Influence on Titanium Ion Dissolution in 3D-Printed Ti6Al4V Orthopedic Implants. *Sci. Rep.* **2025**, *15*, 1–18. [[CrossRef](#)]
93. Hermawan, H.; Razavi, M. *Absorbable Metals for Biomedical Applications*; MDPI-Multidisciplinary Digital Publishing Institute: Basel, Switzerland, 2021; ISBN 9783036517643.
94. Nair, M.M.; Swaroop, S. Impact of the Oxide Layer and Subsurface Micromechanical Properties of Laser Peened 31L Stainless Steel on Biocorrosion Resistance in Simulated Body Fluid. *Surf. Interfaces* **2025**, *56*, 105672. [[CrossRef](#)]
95. Prashanth, K.G. Interpenetrating Composites: A Nomenclature Dilemma. *Materials* **2025**, *18*, 273. [[CrossRef](#)] [[PubMed](#)]
96. Zhang, Z.; Wang, Z.; Zhao, Q.; Prashanth, K.G. Metal-Metal Interpenetrating Phase Composites: A Review. *J. Alloys Compd.* **2024**, *1009*, 176951. [[CrossRef](#)]
97. Abbasi, N.; Hamlet, S.; Love, R.M.; Nguyen, N.T. Porous Scaffolds for Bone Regeneration. *J. Sci. Adv. Mater. Devices* **2020**, *5*, 1–9. [[CrossRef](#)]
98. Kuboki, Y.; Takita, H.; Kobayashi, D.; Tsuruga, E.; Inoue, M.; Murata, M.; Nagai, N.; Dohi, Y.; Ohgushi, H. BMP-Induced Osteogenesis on the Surface of Hydroxyapatite with Geometrically Feasible and Nonfeasible Structures: Topology of Osteogenesis. *J. Biomed. Mater. Res.* **1998**, *39*, 190–199. [[CrossRef](#)]
99. Bai, F.; Wang, Z.; Lu, J.; Liu, J.; Chen, G.; Lv, R.; Wang, J.; Lin, K.; Zhang, J.; Huang, X. The Correlation between the Internal Structure and Vascularization of Controllable Porous Bioceramic Materials in Vivo: A Quantitative Study. *Tissue Eng. Part A* **2010**, *16*, 3791–3803. [[CrossRef](#)]
100. Lu, J.X.; Flautre, B.; Anselme, K.; Hardouin, P.; Gallur, A.; Descamps, M.; Thierry, B. Role of Interconnections in Porous Bioceramics on Bone Recolonization in Vitro and in Vivo. *J. Mater. Sci. Mater. Med.* **1999**, *10*, 111–120. [[CrossRef](#)]
101. Abdel-Hady Gepreel, M.; Niinomi, M. Biocompatibility of Ti-Alloys for Long-Term Implantation. *J. Mech. Behav. Biomed. Mater.* **2013**, *20*, 407–415. [[CrossRef](#)]
102. Sauer, B.W.; Weinstein, A.M.; Klawitter, J.J.; Hulbert, S.F.; Leonard, R.B.; Bagwell, J.G. The Role of Porous Polymeric Materials in Prosthesis Attachment. *J. Biomed. Mater. Res.* **1974**, *8*, 145–153. [[CrossRef](#)]
103. Dewidar, M.M.; Lim, J.K. Properties of Solid Core and Porous Surface Ti–6Al–4V Implants Manufactured by Powder Metallurgy. *J. Alloys Compd.* **2008**, *454*, 442–446. [[CrossRef](#)]
104. Laptev, A.; Vyal, O.; Bram, M.; Buchkremer, H.P.; Stöver, D. Green Strength of Powder Compacts Provided Production of Highly Porous Titanium Parts. *Powder Metall.* **2005**, *48*, 358–364. [[CrossRef](#)]
105. Gittens, R.A.; Scheideler, L.; Rupp, F.; Hyzy, S.L.; Geis-Gerstorfer, J.; Schwartz, Z.; Boyan, B.D. A Review on the Wettability of Dental Implant Surfaces II: Biological and Clinical Aspects. *Acta Biomater.* **2014**, *10*, 2907–2918. [[CrossRef](#)] [[PubMed](#)]
106. Peta, K.; Kubiak, K.J.; Sfravara, F.; Brown, C.A. Dynamic Wettability of Complex Fractal Isotropic Surfaces—Multiscale Correlations. *Tribol. Int.* **2026**, *214*, 111145. [[CrossRef](#)]
107. Peta, K.; Bartkowiak, T.; Rybicki, M.; Galek, P.; Mendak, M.; Wieczorowski, M.; Brown, C.A. Scale-Dependent Wetting Behavior of Bioinspired Lubricants on Electrical Discharge Machined Ti6Al4V Surfaces. *Tribol. Int.* **2024**, *194*, 109562. [[CrossRef](#)]
108. Gittens, R.A.; Olivares-Navarrete, R.; Cheng, A.; Anderson, D.M.; McLachlan, T.; Stephan, I.; Geis-Gerstorfer, J.; Sandhage, K.H.; Fedorov, A.G.; Rupp, F.; et al. The Roles of Titanium Surface Micro/Nanotopography and Wettability on the Differential Response of Human Osteoblast Lineage Cells. *Acta Biomater.* **2013**, *9*, 6268–6277. [[CrossRef](#)]
109. Gittens, R.A.; Olivares-Navarrete, R.; McLachlan, T.; Cai, Y.; Hyzy, S.L.; Schneider, J.M.; Schwartz, Z.; Sandhage, K.H.; Boyan, B.D. Differential Responses of Osteoblast Lineage Cells to Nanotopographically-Modified, Microroughened Titanium–Aluminum–Vanadium Alloy Surfaces. *Biomaterials* **2012**, *33*, 8986–8994. [[CrossRef](#)]
110. Gittens, R.A.; McLachlan, T.; Olivares-Navarrete, R.; Cai, Y.; Berner, S.; Tannenbaum, R.; Schwartz, Z.; Sandhage, K.H.; Boyan, B.D. The Effects of Combined Micron-/Submicron-Scale Surface Roughness and Nanoscale Features on Cell Proliferation and Differentiation. *Biomaterials* **2011**, *32*, 3395–3403. [[CrossRef](#)]
111. Huang, Q.; Lin, L.; Yang, Y.; Hu, R.; Vogler, E.A.; Lin, C. Role of Trapped Air in the Formation of Cell-and-Protein Micropatterns on Superhydrophobic/Superhydrophilic Microtemplated Surfaces. *Biomaterials* **2012**, *33*, 8213–8220. [[CrossRef](#)]
112. Park, J.H.; Schwartz, Z.; Olivares-Navarrete, R.; Boyan, B.D.; Tannenbaum, R. Enhancement of Surface Wettability via the Modification of Microtextured Titanium Implant Surfaces with Polyelectrolytes. *Langmuir* **2011**, *27*, 5976–5985. [[CrossRef](#)]
113. Viceconti, M.; Muccini, R.; Bernakiewicz, M.; Baleani, M.; Cristofolini, L. Large-sliding contact elements accurately predict levels of bone–implant micromotion relevant to osseointegration. *J. Biomech.* **2000**, *33*, 1611–1618. [[CrossRef](#)]
114. Van Noort, R. Titanium: The Implant Material of Today. *J. Mater. Sci.* **1987**, *22*, 3801–3811. [[CrossRef](#)]
115. Hallab, N.J.; Anderson, S.; Stafford, T.; Glant, T.; Jacobs, J.J. Lymphocyte Responses in Patients with Total Hip Arthroplasty. *J. Orthop. Res.* **2005**, *23*, 384391. [[CrossRef](#)] [[PubMed](#)]
116. Donaruma, L.G. Definitions in Biomaterials, D.F. Williams, Ed., Elsevier, Amsterdam, 1987, 72 pp. *J. Polym. Sci. Part C Polym. Lett.* **1988**, *26*, 414. [[CrossRef](#)]
117. Ratner, B.D. *The Biocompatibility of Implant Materials*; Elsevier: Amsterdam, The Netherlands, 2015; ISBN 9780128005002.
118. Williams, D.F. On the Mechanisms of Biocompatibility. *Biomaterials* **2008**, *29*, 2941–2953. [[CrossRef](#)]

119. Manivasagam, G.; Dhinasekaran, D.; Rajamanickam, A. Biomedical Implants: Corrosion and Its Prevention—A Review. *Recent Pat. Corros. Science* **2010**, *2*, 40–54. [[CrossRef](#)]
120. Zidrou, C.; Kapetanou, A.; Rizou, S. The Effect of Drugs on Implant Osseointegration—A Narrative Review. *Injury* **2023**, *54*, 110888. [[CrossRef](#)]
121. Jin, W.; Chu, P.K. Orthopedic Implants. *Encycl. Biomed. Eng.* **2019**, *1*, 425–439. [[CrossRef](#)]
122. Mello-Machado, R.C.; Sartoretto, S.C.; Granjeiro, J.M.; Calasans-Maia, J.d.A.; de Uzeda, M.J.P.G.; Mourão, C.F.d.A.B.; Ghiraldini, B.; Bezerra, F.J.B.; Senna, P.M.; Calasans-Maia, M.D. Osseodensification Enables Bone Healing Chambers with Improved Low-Density Bone Site Primary Stability: An in Vivo Study. *Sci. Rep.* **2021**, *11*, 15436. [[CrossRef](#)]
123. Martin, R.B.; Burr, D.B. Structure, Function and Adaptation of Compact Bone. *Skelet. Radiol.* **1989**, *18*, 506. [[CrossRef](#)]
124. Siddiqui, S.A.; Srikanth, S.P.; Wu, Y.S.; Kalita, T.; Ambartsumov, T.G.; Tseng, W.; Kumar, A.P.; Ahmad, A.; Michalek, J.E. Different Types of Algae Beneficial for Bone Health in Animals and in Humans—A Review. *Algal. Res.* **2024**, *82*, 103593. [[CrossRef](#)]
125. Lakes, R.S.; Park, J. *Biomaterials. An Introduction*, 2nd ed.; Springer: Berlin/Heidelberg, Germany, 1993; ISBN 0-306-43992-1.
126. Fung, Y.-C. *Biomechanics*; Springer: Berlin/Heidelberg, Germany, 1993. [[CrossRef](#)]
127. Lopes, D.; Martins-Cruz, C.; Oliveira, M.B.; Mano, J.F. Bone Physiology as Inspiration for Tissue Regenerative Therapies. *Biomaterials* **2018**, *185*, 240–275. [[CrossRef](#)] [[PubMed](#)]
128. Kaplan, F.S.; Hayes, W.C.; Keaveny, T.M.; Boskey, A.; Einhorn, T.A.; Iannotti, J.P. Form and Function of Bone. *Orthop. Basic Sci.* **1994**, *4*, 127–185.
129. Boskey, A.L.; Coleman, R. Aging and Bone. *J. Dent. Res.* **2015**, *89*, 1333–1348. [[CrossRef](#)] [[PubMed](#)]
130. Raja, I.S.; Preeth, D.R.; Vedhanayagam, M.; Hyon, S.H.; Lim, D.; Kim, B.; Rajalakshmi, S.; Han, D.W. Polyphenols-Loaded Electrospun Nanofibers in Bone Tissue Engineering and Regeneration. *Biomater. Res.* **2021**, *25*, 29. [[CrossRef](#)]
131. Webster, T.J. Nanophase Ceramics: The Future Orthopedic and Dental Implant Material. *Adv. Chem. Eng.* **2001**, *27*, 125–166. [[CrossRef](#)]
132. Friedenstein, A.J.; Chailakhyan, R.K.; Gerasimov, U.V. Bone Marrow Osteogenic Stem Cells: In Vitro Cultivation and Transplantation in Diffusion Chambers. *Cell Prolif.* **1987**, *20*, 263–272. [[CrossRef](#)]
133. Liu, J.; Liu, D.; Li, S.; Deng, Z.; Pan, Z.; Li, C.; Chen, T. The Effects of Graphene Oxide Doping on the Friction and Wear Properties of TiN Bioinert Ceramic Coatings Prepared Using Wide-Band Laser Cladding. *Surf. Coat. Technol.* **2023**, *458*, 129354. [[CrossRef](#)]
134. Desante, G.; Labude, N.; Rütten, S.; Römer, S.; Kaufmann, R.; Zybala, R.; Jagiello, J.; Lipińska, L.; Chlanda, A.; Telle, R.; et al. Graphene Oxide Nanofilm to Functionalize Bioinert High Strength Ceramics. *Appl. Surf. Sci.* **2021**, *566*, 150670. [[CrossRef](#)]
135. Chen, T.; Deng, Z.; Liu, D.; Zhu, X.; Xiong, Y. Bioinert TiC Ceramic Coating Prepared by Laser Cladding: Microstructures, Wear Resistance, and Cytocompatibility of the Coating. *Surf. Coat. Technol.* **2021**, *423*, 127635. [[CrossRef](#)]
136. Bohner, M. Bioresorbable Ceramics. In *Degradation Rate of Bioresorbable Materials: Prediction and Evaluation*; CRC Press: Boca Raton, FL, USA, 2008; pp. 95–114. [[CrossRef](#)]
137. Tian, X.; Raina, D.B.; Oberländer, J.T.; Liu, Y.; Goronzy, J.; Apolle, R.; Vater, C.; Richter, R.F.; Tägil, M.; Lidgren, L.; et al. Comparison of Immediate Anchoring Effectiveness of Two Different Techniques of Bioresorbable Ceramic Application for Pedicle Screw Augmentation. *Ceram. Int.* **2024**, *50*, 12877–12889. [[CrossRef](#)]
138. Wang, X.; Aziz, A.; Sheng, X.; Wang, L.; Yin, L. Bioresorbable Neural Interfaces for Bioelectronic Medicine. *Curr. Opin. Biomed. Eng.* **2024**, *32*, 100565. [[CrossRef](#)]
139. Mehboob, H.; Chang, S.H. Application of Composites to Orthopedic Prostheses for Effective Bone Healing: A Review. *Compos. Struct.* **2014**, *118*, 328–341. [[CrossRef](#)]
140. Ibrahim, A.M.S.; Koolen, P.G.L.; Kim, K.; Perrone, G.S.; Kaplan, D.L.; Lin, S.J. Absorbable Biologically Based Internal Fixation. *Clin. Podiatr. Med. Surg.* **2015**, *32*, 61–72. [[CrossRef](#)] [[PubMed](#)]
141. Lee, H.; Zeng, F.; Dunne, M.; Allen, C. Methoxy Poly(Ethylene Glycol)-Block-Poly(δ -Valerolactone) Copolymer Micelles for Formulation of Hydrophobic Drugs. *Biomacromolecules* **2005**, *6*, 3119–3128. [[CrossRef](#)]
142. Kim, S.C.; Kim, D.W.; Shim, Y.H.; Bang, J.S.; Oh, H.S.; Kim, S.W.; Seo, M.H. In Vivo Evaluation of Polymeric Micellar Paclitaxel Formulation: Toxicity and Efficacy. *J. Control. Release* **2001**, *72*, 191–202. [[CrossRef](#)]
143. Lausmaa, J.; Kasemo, B.; Mattsson, H.; Odellius, H. Multi-Technique Surface Characterization of Oxide Films on Electropolished and Anodically Oxidized Titanium. *Appl. Surf. Sci.* **1990**, *45*, 189–200. [[CrossRef](#)]
144. Gu, X.; Zheng, Y.; Cheng, Y.; Zhong, S.; Xi, T. In Vitro Corrosion and Biocompatibility of Binary Magnesium Alloys. *Biomaterials* **2009**, *30*, 484–498. [[CrossRef](#)]
145. Chen, Y.J.; Li, Y.J.; Walmsley, J.C.; Dumoulin, S.; Skaret, P.C.; Roven, H.J. Microstructure Evolution of Commercial Pure Titanium during Equal Channel Angular Pressing. *Mater. Sci. Eng. A* **2010**, *527*, 789–796. [[CrossRef](#)]
146. Barceloux, D.G.; Barceloux, D. Chromium. *J. Toxicol. Clin. Toxicol.* **1999**, *37*, 173–194. [[CrossRef](#)]
147. Barceloux, D.G.; Barceloux, D. Nickel. *J. Toxicol. Clin. Toxicol.* **1999**, *37*, 239–258. [[CrossRef](#)]
148. Li, X.; Gao, P.; Wan, P.; Pei, Y.; Shi, L.; Fan, B.; Shen, C.; Xiao, X.; Yang, K.; Guo, Z. Novel Bio-Functional Magnesium Coating on Porous Ti6Al4V Orthopaedic Implants: In Vitro and In Vivo Study. *Sci. Rep.* **2017**, *7*, 1–11. [[CrossRef](#)] [[PubMed](#)]

149. He, M.; Chen, L.; Yin, M.; Xu, S.; Liang, Z. Review on Magnesium and Magnesium-Based Alloys as Biomaterials for Bone Immobilization. *J. Mater. Res. Technol.* **2023**, *23*, 4396–4419. [[CrossRef](#)]
150. Badkoobeh, F.; Mostaan, H.; Rafiei, M.; Bakhsheshi-Rad, H.R.; RamaKrishna, S.; Chen, X. Additive Manufacturing of Biodegradable Magnesium-Based Materials: Design Strategies, Properties, and Biomedical Applications. *J. Magnes. Alloys* **2023**, *11*, 801–839. [[CrossRef](#)]
151. Yadav, M.; Shukla, R.; Kesavan, P.; Nilawar, S.; Perugu, C.; Sellamuthu, P.; Chatterjee, K.; Suwas, S.; Jayamani, J.; Prashanth, K. Microstructural, Mechanical, Corrosion, and Biological Behavior of Spark Plasma Sintered Commercially Pure Zinc for Biomedical Applications. *Mater. Adv.* **2025**, *6*, 3546–3560. [[CrossRef](#)]
152. Eddy Jai Poinern, G.; Brundavanam, S.; Fawcett, D. Biomedical Magnesium Alloys: A Review of Material Properties, Surface Modifications and Potential as a Biodegradable Orthopaedic Implant. *Am. J. Biomed. Eng.* **2013**, *2*, 218–240. [[CrossRef](#)]
153. Murugan, R.; Ramakrishna, S. Development of Nanocomposites for Bone Grafting. *Compos. Sci. Technol.* **2005**, *65*, 2385–2406. [[CrossRef](#)]
154. Zhao, Y.; Wu, G.; Jiang, J.; Wong, H.M.; Yeung, K.W.K.; Chu, P.K. Improved Corrosion Resistance and Cytocompatibility of Magnesium Alloy by Two-Stage Cooling in Thermal Treatment. *Corros. Sci.* **2012**, *59*, 360–365. [[CrossRef](#)]
155. Witte, F.; Kaese, V.; Haferkamp, H.; Switzer, E.; Meyer-Lindenberg, A.; Wirth, C.J.; Windhagen, H. In Vivo Corrosion of Four Magnesium Alloys and the Associated Bone Response. *Biomaterials* **2005**, *26*, 3557–3563. [[CrossRef](#)]
156. Ghali, E. Corrosion Resistance of Aluminum and Magnesium Alloys: Understanding, Performance, and Testing. In *Corrosion Resistance of Aluminum and Magnesium Alloys: Understanding, Performance, and Testing*; John Wiley & Sons: Hoboken, NJ, USA, 2010. [[CrossRef](#)]
157. Radha, R.; Sreekanth, D. Insight of Magnesium Alloys and Composites for Orthopedic Implant Applications—A Review. *J. Magnes. Alloys* **2017**, *5*, 286–312. [[CrossRef](#)]
158. Leyens, C.; Peters, M. *Titanium and Titanium Alloys: Fundamentals and Applications*; Wiley-VCH: Weinheim, Germany, 2003. [[CrossRef](#)]
159. Banerjee, D.; Williams, J.C. Perspectives on Titanium Science and Technology. *Acta Mater.* **2013**, *61*, 844–879. [[CrossRef](#)]
160. Singh, R.; Lee, P.D.; Dashwood, R.J.; Lindley, T.C. Titanium Foams for Biomedical Applications: A Review. *Mater. Technol.* **2010**, *25*, 127–136. [[CrossRef](#)]
161. Qian, M.; Xu, W.; Brandt, M.; Tang, H.P. Additive Manufacturing and Postprocessing of Ti-6Al-4V for Superior Mechanical Properties. *MRS Bull.* **2016**, *41*, 775–783. [[CrossRef](#)]
162. Patnaik, P. *Handbook of Inorganic Chemicals*; McGraw-Hill: New York, NY, USA, 2003; ISBN 0070494398.
163. Kim, S.W.; Jung, H.D.; Kang, M.H.; Kim, H.E.; Koh, Y.H.; Estrin, Y. Fabrication of Porous Titanium Scaffold with Controlled Porous Structure and Net-Shape Using Magnesium as Spacer. *Mater. Sci. Eng. C* **2013**, *33*, 2808–2815. [[CrossRef](#)]
164. Esen, Z.; Bor, Ş. Processing of Titanium Foams Using Magnesium Spacer Particles. *Scr. Mater.* **2007**, *56*, 341–344. [[CrossRef](#)]
165. Wang, X.; Lu, Z.; Jia, L.; Li, F. Preparation and Properties of Low Cost Porous Titanium by Using Rice Husk as Hold Space. *Prog. Nat. Sci. Mater. Int.* **2017**, *27*, 344–349. [[CrossRef](#)]
166. Wang, X.S.; Lu, Z.L.; Jia, L.; Chen, J.X. Preparation of Porous Titanium Materials by Powder Sintering Process and Use of Space Holder Technique. *J. Iron Steel Res. Int.* **2017**, *24*, 97–102. [[CrossRef](#)]
167. Jian, X.; Yongning, L.; Yong, L.; Guibao, Q.; Jinming, L. The Application of Model Equation Method in Preparation of Titanium Foams. *J. Mater. Res. Technol.* **2021**, *13*, 121–127. [[CrossRef](#)]
168. Vasconcellos, L.M.R.D.; Oliveira, M.V.D.; Graça, M.L.D.A.; Vasconcellos, L.G.O.D.; Carvalho, Y.R.; Cairo, C.A.A. Porous Titanium Scaffolds Produced by Powder Metallurgy for Biomedical Applications. *Mater. Res.* **2008**, *11*, 275–280. [[CrossRef](#)]
169. Niu, W.; Bai, C.; Qiu, G.B.; Wang, Q. Processing and Properties of Porous Titanium Using Space Holder Technique. *Mater. Sci. Eng. A* **2009**, *506*, 148–151. [[CrossRef](#)]
170. Li, D.S.; Zhang, Y.P.; Ma, X.; Zhang, X.P. Space-Holder Engineered Porous NiTi Shape Memory Alloys with Improved Pore Characteristics and Mechanical Properties. *J. Alloys Compd.* **2009**, *474*, L1. [[CrossRef](#)]
171. Xiang, C.; Zhang, Y.; Li, Z.; Zhang, H.; Huang, Y.; Tang, H. Preparation and Compressive Behavior of Porous Titanium Prepared by Space Holder Sintering Process. *Procedia Eng.* **2012**, *27*, 768–774. [[CrossRef](#)]
172. Torres, Y.; Pavón, J.J.; Rodríguez, J.A. Processing and Characterization of Porous Titanium for Implants by Using NaCl as Space Holder. *J. Mater. Process. Technol.* **2012**, *212*, 1061–1069. [[CrossRef](#)]
173. Chen, Y.; Kent, D.; Bermingham, M.; Dehghan-Manshadi, A.; Dargusch, M. Manufacturing of Biocompatible Porous Titanium Scaffolds Using a Novel Spherical Sugar Pellet Space Holder. *Mater. Lett.* **2017**, *195*, 92–95. [[CrossRef](#)]
174. Li, B.Q.; Wang, C.Y.; Lu, X. Effect of Pore Structure on the Compressive Property of Porous Ti Produced by Powder Metallurgy Technique. *Mater. Des.* **2013**, *50*, 613–619. [[CrossRef](#)]
175. Wang, D.; Li, Q.; Xu, M.; Jiang, G.; Zhang, Y.; He, G. A Novel Approach to Fabrication of Three-Dimensional Porous Titanium with Controllable Structure. *Mater. Sci. Eng. C* **2017**, *71*, 1046–1051. [[CrossRef](#)]

176. Chen, Y.; Frith, J.E.; Dehghan-Manshadi, A.; Attar, H.; Kent, D.; Soro, N.D.M.; Bermingham, M.J.; Dargusch, M.S. Mechanical Properties and Biocompatibility of Porous Titanium Scaffolds for Bone Tissue Engineering. *J. Mech. Behav. Biomed. Mater.* **2017**, *75*, 169–174. [[CrossRef](#)]
177. Zou, C.; Zhang, E.; Li, M.; Zeng, S. Preparation, Microstructure and Mechanical Properties of Porous Titanium Sintered by Ti Fibres. *J. Mater. Sci. Mater. Med.* **2008**, *19*, 401–405. [[CrossRef](#)]
178. Wolf, F.I.; Trapani, V. Cell (Patho)Physiology of Magnesium. *Clin. Sci.* **2008**, *114*, 27–35. [[CrossRef](#)]
179. Maguire, M.E.; Cowan, J.A. Magnesium Chemistry and Biochemistry. *BioMetals* **2002**, *15*, 203–210. [[CrossRef](#)]
180. Vormann, J. Magnesium: Nutrition and Metabolism. *Mol. Aspects Med.* **2003**, *24*, 27–37. [[CrossRef](#)]
181. Flatman, P.W. Magnesium Transport across Cell Membranes. *J. Membr. Biol.* **1984**, *80*, 1–14. [[CrossRef](#)] [[PubMed](#)]
182. Cachinho, S.C.P.; Correia, R.N. Titanium Scaffolds for Osteointegration: Mechanical, in Vitro and Corrosion Behaviour. *J. Mater. Sci. Mater. Med.* **2008**, *19*, 451–457. [[CrossRef](#)]
183. Karageorgiou, V.; Kaplan, D. Porosity of 3D Biomaterial Scaffolds and Osteogenesis. *Biomaterials* **2005**, *26*, 5474–5491. [[CrossRef](#)] [[PubMed](#)]
184. Barrabés, M.; Sevilla, P.; Planell, J.A.; Gil, F.J. Mechanical Properties of Nickel–Titanium Foams for Reconstructive Orthopaedics. *Mater. Sci. Eng. C* **2008**, *28*, 23–27. [[CrossRef](#)]
185. Li, J.P.; Li, S.H.; De Groot, K.; Layrolle, P. Preparation and Characterization of Porous Titanium. *Key Eng. Mater.* **2002**, *218*, 51–54. [[CrossRef](#)]
186. Wang, C.; Chen, H.; Zhu, X.; Xiao, Z.; Zhang, K.; Zhang, X. An Improved Polymeric Sponge Replication Method for Biomedical Porous Titanium Scaffolds. *Mater. Sci. Eng. C* **2017**, *70*, 1192–1199. [[CrossRef](#)]
187. He, G.; Liu, P.; Tan, Q. Porous Titanium Materials with Entangled Wire Structure for Load-Bearing Biomedical Applications. *J. Mech. Behav. Biomed. Mater.* **2012**, *5*, 16–31. [[CrossRef](#)]
188. Jiang, G.; He, G. Enhancement of the Porous Titanium with Entangled Wire Structure for Load-Bearing Biomedical Applications. *Mater. Des.* **2014**, *56*, 241–244. [[CrossRef](#)]
189. Tan, Q.; Liu, P.; Du, C.; Wu, L.; He, G. Mechanical Behaviors of Quasi-Ordered Entangled Aluminum Alloy Wire Material. *Mater. Sci. Eng. A* **2009**, *527*, 38–44. [[CrossRef](#)]
190. Liu, P.; Tan, Q.; Wu, L.; He, G. Compressive and Pseudo-Elastic Hysteresis Behavior of Entangled Titanium Wire Materials. *Mater. Sci. Eng. A* **2010**, *527*, 3301–3309. [[CrossRef](#)]
191. Jiang, G.; Wang, C.; Li, Q.; Dong, J.; He, G. Porous Titanium with Entangled Structure Filled with Biodegradable Magnesium for Potential Biomedical Applications. *Mater. Sci. Eng. C* **2015**, *47*, 142–149. [[CrossRef](#)] [[PubMed](#)]
192. Liu, Y.; Jiang, G.; He, G. Enhancement of Entangled Porous Titanium by BisGMA for Load-Bearing Biomedical Applications. *Mater. Sci. Eng. C* **2016**, *61*, 37–41. [[CrossRef](#)] [[PubMed](#)]
193. He, G.; Liu, P.; Tan, Q.; Jiang, G. Flexural and Compressive Mechanical Behaviors of the Porous Titanium Materials with Entangled Wire Structure at Different Sintering Conditions for Load-Bearing Biomedical Applications. *J. Mech. Behav. Biomed. Mater.* **2013**, *28*, 309–319. [[CrossRef](#)] [[PubMed](#)]
194. Asaoka, K.; Kuwayama, N.; Okuno, O.; Miura, I. Mechanical Properties and Biomechanical Compatibility of Porous Titanium for Dental Implants. *J. Biomed. Mater. Res.* **1985**, *19*, 699–713. [[CrossRef](#)]
195. Ivasishin, O.M.; Savvakina, D.G. The Impact of Diffusion on Synthesis of High-Strength Titanium Alloys from Elemental Powder Blends. *Key Eng. Mater.* **2010**, *436*, 113–121. [[CrossRef](#)]
196. Yang, Y.F.; Luo, S.D.; Schaffer, G.B.; Qian, M. Sintering of Ti–10V–2Fe–3Al and Mechanical Properties. *Mater. Sci. Eng. A* **2011**, *528*, 6719–6726. [[CrossRef](#)]
197. Mamedov, V. Spark Plasma Sintering as Advanced PM Sintering Method. *Powder Metall.* **2002**, *45*, 322–328. [[CrossRef](#)]
198. Xie, G.; Ohashi, O.; Chiba, K.; Yamaguchi, N.; Song, M.; Furuya, K.; Noda, T. Frequency Effect on Pulse Electric Current Sintering Process of Pure Aluminum Powder. *Mater. Sci. Eng. A* **2003**, *359*, 384–390. [[CrossRef](#)]
199. Xie, G.; Ohashi, O.; Wada, K.; Ogawa, T.; Song, M.; Furuya, K. Interface Microstructure of Aluminum Die-Casting Alloy Joints Bonded by Pulse Electric-Current Bonding Process. *Mater. Sci. Eng. A* **2006**, *428*, 12–17. [[CrossRef](#)]
200. Wang, S.W.; Chen, L.D.; Kang, Y.S.; Niino, M.; Hirai, T. Effect of Plasma Activated Sintering (PAS) Parameters on Densification of Copper Powder. *Mater. Res. Bull.* **2000**, *35*, 619–628. [[CrossRef](#)]
201. Yang, Y.F.; Qian, M. Spark Plasma Sintering and Hot Pressing of Titanium and Titanium Alloys. In *Titanium Powder Metallurgy: Science, Technology and Applications*; Butterworth-Heinemann: Oxford, UK, 2015; pp. 219–235. [[CrossRef](#)]
202. Omori, M. Sintering, Consolidation, Reaction and Crystal Growth by the Spark Plasma System (SPS). *Mater. Sci. Eng. A* **2000**, *287*, 183–188. [[CrossRef](#)]
203. Groza, J.R.; Zavaliangos, A. Sintering Activation by External Electrical Field. *Mater. Sci. Eng. A* **2000**, *287*, 171–177. [[CrossRef](#)]
204. Eriksson, M.; Shen, Z.; Nygren, M. Fast Densification and Deformation of Titanium Powder. *Powder Metall.* **2013**, *48*, 231–236. [[CrossRef](#)]

205. Zou, X.; Li, H.; Bünger, M.; Egund, N.; Lind, M.; Bünger, C. Bone Ingrowth Characteristics of Porous Tantalum and Carbon Fiber Interbody Devices: An Experimental Study in Pigs. *Spine J.* **2004**, *4*, 99–105. [[CrossRef](#)]
206. Jones, G.; Groza, J.R.; Yamazaki, K.; Shoda, K. Plasma Activated Sintering (PAS) of Tungsten Powders. *Mater. Manuf. Process* **1994**, *9*, 1105–1114. [[CrossRef](#)]
207. Lifland, M.I.; Okazaki, K. Properties of Titanium Dental Implants Produced by Electro-Discharge Compaction. *Clin. Mater.* **1994**, *17*, 203–209. [[CrossRef](#)]
208. Fambri, L. Book Review: Biomaterials. An Introduction, Second Edition Edited by J. B. Park and R. S. Lakes Plenum Press, New York, 1992 ISBN 0-306-43992-1, 394 pp. *J. Bioact. Compat. Polym.* **1993**, *8*, 289–290. [[CrossRef](#)]
209. Ganesan, D.; Sellamuthu, P.; Prashanth, K.G. Vacuum Hot Pressing of Oxide Dispersion Strengthened Ferritic Stainless Steels: Effect of Al Addition on the Microstructure and Properties. *J. Manuf. Mater. Process.* **2020**, *4*, 93. [[CrossRef](#)]
210. Ibrahim, A.; Zhang, F.; Otterstein, E.; Burkel, E. Processing of Porous Ti and Ti5Mn Foams by Spark Plasma Sintering. *Mater. Des.* **2011**, *32*, 146–153. [[CrossRef](#)]
211. Kashimbetova, A.; Slámecka, K.; Díaz-De-La-Torre, S.; Méndez-García, J.C.; Hernández-Morales, B.; Piña-Barba, M.C.; Hui, D.; Celko, L.; Montufar, E.B. Pressure-Less Spark Plasma Sintering of 3D-Plotted Titanium Porous Structures. *J. Mater. Res. Technol.* **2023**, *22*, 2147–2157. [[CrossRef](#)]
212. Luo, S.D.; Qian, M.; Ashraf Imam, M. Microwave Sintering of Titanium and Titanium Alloys. In *Titanium Powder Metallurgy: Science, Technology and Applications*; Butterworth-Heinemann: Oxford, UK, 2015; pp. 237–251. [[CrossRef](#)]
213. Tang, C.Y.; Wong, C.T.; Zhang, L.N.; Choy, M.T.; Chow, T.W.; Chan, K.C.; Yue, T.M.; Chen, Q. In Situ Formation of Ti Alloy/TiC Porous Composites by Rapid Microwave Sintering of Ti6Al4V/MWCNTs Powder. *J. Alloys Compd.* **2013**, *557*, 67–72. [[CrossRef](#)]
214. Delgado-Ruiz, R.; Romanos, G. Potential Causes of Titanium Particle and Ion Release in Implant Dentistry: A Systematic Review. *Int. J. Mol. Sci.* **2018**, *19*, 3585. [[CrossRef](#)] [[PubMed](#)]
215. Zhang, F.; Otterstein, E.; Burkel, E. Spark Plasma Sintering, Microstructures, and Mechanical Properties of Macroporous Titanium Foams. *Adv. Eng. Mater.* **2010**, *12*, 863–872. [[CrossRef](#)]
216. Schmidt, R.; Pilz, S.; Lindemann, I.; Damm, C.; Hufenbach, J.; Helth, A.; Geissler, D.; Henss, A.; Rohnke, M.; Calin, M.; et al. Powder Metallurgical Processing of Low Modulus β -Type Ti-45Nb to Bulk and Macro-Porous Compacts. *Powder Technol.* **2017**, *322*, 393–401. [[CrossRef](#)]
217. Kon, M.; Hirakata, L.M.; Asaoka, K. Porous Ti-6Al-4V Alloy Fabricated by Spark Plasma Sintering for Biomimetic Surface Modification. *J. Biomed. Mater. Res. B Appl. Biomater.* **2004**, *68*, 88–93. [[CrossRef](#)]
218. Ertorer, O.; Topping, T.D.; Li, Y.; Moss, W.; Lavernia, E.J. Nanostructured Ti Consolidated via Spark Plasma Sintering. *Metall. Mater. Trans. A Phys. Metall. Mater. Sci.* **2011**, *42*, 964–973. [[CrossRef](#)]
219. Zadra, M.; Casari, F.; Girardini, L.; Molinari, A. Microstructure and Mechanical Properties of Cp-Titanium Produced by Spark Plasma Sintering. *Powder Metall.* **2008**, *51*, 59–65. [[CrossRef](#)]
220. Prashanth, K.G.; Wang, Z. Additive Manufacturing: Alloy Design and Process Innovations. *Materials* **2020**, *13*, 542. [[CrossRef](#)]
221. Sivaprasad, K.; Babu, N.R.; Prashanth, K.G. Additive Manufacturing and Allied Technologies. *Trans. Indian Inst. Met.* **2023**, *76*, 269. [[CrossRef](#)]
222. Maurya, H.S.; Vikram, R.J.; Kosiba, K.; Juhani, K.; Sergejev, F.; Suwas, S.; Prashanth, K.G. Additive Manufacturing of CMCs with Bimodal Microstructure. *J. Alloys Compd.* **2022**, *938*, 168416. [[CrossRef](#)]
223. Maurya, H.S.; Kosiba, K.; Juhani, K.; Sergejev, F.; Prashanth, K.G. Effect of Powder Bed Preheating on the Crack Formation and Microstructure in Ceramic Matrix Composites Fabricated by Laser Powder-Bed Fusion Process. *Addit. Manuf.* **2022**, *58*, 103013. [[CrossRef](#)]
224. Maurya, H.S.; Jayaraj, J.; Vikram, R.J.; Juhani, K.; Sergejev, F.; Prashanth, K.G. Additive Manufacturing of TiC-Based Cermets: A Detailed Comparison with Spark Plasma Sintered Samples. *J. Alloys Compd.* **2023**, *960*, 170436. [[CrossRef](#)]
225. Maurya, H.S.; Marczyk, J.; Juhani, K.; Sergejev, F.; Kumar, R.; Hussain, A.; Akhtar, F.; Hebda, M.; Prashanth, K.G. Binder Jetting 3D Printing of Green TiC-FeCr Based Cermets—Effect of Sintering Temperature and Systematic Comparison Study with Laser Powder Bed Fusion Fabricated Parts. *Mater. Today Adv.* **2025**, *25*, 100562. [[CrossRef](#)]
226. Horn, T.J.; Harrysson, O.L. Overview of Current Additive Manufacturing Technologies and Selected Applications. *Sci. Prog.* **2012**, *95*, 255–282. [[CrossRef](#)]
227. Kurtz, S.; Ong, K.; Lau, E.; Mowat, F.; Halpern, M. Projections of Primary and Revision Hip and Knee Arthroplasty in the United States from 2005 to 2030. *J. Bone Jt. Surg. Am.* **2007**, *89*, 780–785. [[CrossRef](#)]
228. Prashanth, K.; Löber, L.; Klauss, H.-J.; Kühn, U.; Eckert, J. Characterization of 316L Steel Cellular Dodecahedron Structures Produced by Selective Laser Melting. *Technologies* **2016**, *4*, 34. [[CrossRef](#)]
229. Baskaran, J.; Muthukannan, D.; Shukla, R.; Konda Gokuldoss, P. Manufacturability and Deformation Studies on a Novel Metallic Lattice Structure Fabricated by Selective Laser Melting. *Vacuum* **2024**, *222*, 113065. [[CrossRef](#)]
230. Jagadeesh, B.; Duraiselvam, M.; Prashanth, K.G. Deformation Behavior of Metallic Lattice Structures with Symmetrical Gradients of Porosity Manufactured by Metal Additive Manufacturing. *Vacuum* **2023**, *211*, 111955. [[CrossRef](#)]

231. Ge, J.; Huang, J.; Lei, Y.; O'Reilly, P.; Ahmed, M.; Zhang, C.; Yan, X.; Yin, S. Microstructural Features and Compressive Properties of SLM Ti6Al4V Lattice Structures. *Surf. Coat. Technol.* **2020**, *403*, 126419. [CrossRef]
232. Gokuldoss, P.K.; Kolla, S.; Eckert, J. Additive Manufacturing Processes: Selective Laser Melting, Electron Beam Melting and Binder Jetting—Selection Guidelines. *Materials* **2017**, *10*, 672. [CrossRef]
233. Singh, N.; Hameed, P.; Ummethala, R.; Manivasagam, G.; Prashanth, K.G.; Eckert, J. Selective Laser Manufacturing of Ti-Based Alloys and Composites: Impact of Process Parameters, Application Trends, and Future Prospects. *Mater. Today Adv.* **2020**, *8*, 100097. [CrossRef]
234. Ahn, D.G. Directed Energy Deposition (DED) Process: State of the Art. *Int. J. Precis. Eng. Manuf. Green Technol.* **2021**, *8*, 703–742. [CrossRef]
235. Scudino, S.; Unterdörfer, C.; Prashanth, K.G.; Attar, H.; Ellendt, N.; Uhlenwinkel, V.; Eckert, J. Additive Manufacturing of Cu-10Sn Bronze. *Mater. Lett.* **2015**, *156*, 202–204. [CrossRef]
236. Suryawanshi, J.; Prashanth, K.G.; Ramamurty, U. Mechanical Behavior of Selective Laser Melted 316L Stainless Steel. *Mater. Sci. Eng. A* **2017**, *696*, 113–121. [CrossRef]
237. Suryawanshi, J.; Prashanth, K.G.; Scudino, S.; Eckert, J.; Prakash, O.; Ramamurty, U. Simultaneous Enhancements of Strength and Toughness in an Al-12Si Alloy Synthesized Using Selective Laser Melting. *Acta Mater.* **2016**, *115*, 285–294. [CrossRef]
238. DebRoy, T.; Wei, H.L.; Zuback, J.S.; Mukherjee, T.; Elmer, J.W.; Milewski, J.O.; Beese, A.M.; Wilson-Heid, A.; De, A.; Zhang, W. Additive Manufacturing of Metallic Components—Process, Structure and Properties. *Prog. Mater. Sci.* **2018**, *92*, 112–224. [CrossRef]
239. Karimi, J.; Zhao, C.; Prashanth, K.G. Massive Transformation in Dual-Laser Powder Bed Fusion of Ti6Al4V Alloys. *J. Manuf. Process* **2024**, *119*, 282–292. [CrossRef]
240. Karimi, J.; Antonov, M.; Kollo, L.; Prashanth, K.G. Role of Laser Remelting and Heat Treatment in Mechanical and Tribological Properties of Selective Laser Melted Ti6Al4V Alloy. *J. Alloys Compd.* **2022**, *897*, 163207. [CrossRef]
241. Yu, S.; Chi, H.; Li, P.; Guo, B.; Yu, Z.; Xu, Z.; Liang, P.; Zhang, Z.; Guo, Y.; Ren, L. Interpenetrating Phases Composites Ti6Al4V/Zn as Partially Degradable Biomaterials to Improve Bone-Implant Properties. *Addit. Manuf.* **2024**, *93*, 104411. [CrossRef]
242. Liu, S.; Shin, Y.C. Additive Manufacturing of Ti6Al4V Alloy: A Review. *Mater. Des.* **2019**, *164*, 107552. [CrossRef]
243. Wysocki, B.; Maj, P.; Sitek, R.; Buhagiar, J.; Kurzydowski, K.J.; Świeszkowski, W. Laser and Electron Beam Additive Manufacturing Methods of Fabricating Titanium Bone Implants. *Appl. Sci.* **2017**, *7*, 657. [CrossRef]
244. Sabban, R.; Bahl, S.; Chatterjee, K.; Suwas, S. Globularization Using Heat Treatment in Additively Manufactured Ti-6Al-4V for High Strength and Toughness. *Acta Mater.* **2019**, *162*, 239–254. [CrossRef]
245. Gupta, S.K.; Shahidsha, N.; Bahl, S.; Kedaria, D.; Singamneni, S.; Yarlagadda, P.K.D.V.; Suwas, S.; Chatterjee, K. Enhanced Biomechanical Performance of Additively Manufactured Ti-6Al-4V Bone Plates. *J. Mech. Behav. Biomed. Mater.* **2021**, *119*, 104552. [CrossRef] [PubMed]
246. Karimi, J.; Suryanarayana, C.; Okulov, I.; Prashanth, K.G. Selective Laser Melting of Ti6Al4V: Effect of Laser Re-Melting. *Mater. Sci. Eng. A* **2021**, *805*, 140558. [CrossRef]
247. Sridharan, N.; Chaudhary, A.; Nandwana, P.; Babu, S.S. Texture Evolution During Laser Direct Metal Deposition of Ti-6Al-4V. *Jom* **2016**, *68*, 772–777. [CrossRef]
248. Xu, W.; Brandt, M.; Sun, S.; Elambasseril, J.; Liu, Q.; Latham, K.; Xia, K.; Qian, M. Additive Manufacturing of Strong and Ductile Ti-6Al-4V by Selective Laser Melting via in Situ Martensite Decomposition. *Acta Mater.* **2015**, *85*, 74–84. [CrossRef]
249. Subramanian, S.; Yadav, M.K.; Jayaraj, J.; Yangyang, F.; Xi, L.; Prashanth, K.G. Microstructural Homogenization through Laser Remelting in an Additively Manufactured Ti-40Nb Sample from Elemental Feedstock Powders. *J. Mater. Res. Technol.* **2025**, *38*, 4305–4320. [CrossRef]
250. Zaharin, H.A.; Rani, A.M.A.; Azam, F.I.; Ginta, T.L.; Sallih, N.; Ahmad, A.; Yunus, N.A.; Zulkifli, T.Z.A. Effect of Unit Cell Type and Pore Size on Porosity and Mechanical Behavior of Additively Manufactured Ti6Al4V Scaffolds. *Materials* **2018**, *11*, 2402. [CrossRef]
251. Wang, Z.; Xie, M.; Li, Y.; Zhang, W.; Yang, C.; Kollo, L.; Eckert, J.; Prashanth, K.G. Premature Failure of an Additively Manufactured Material. *NPG Asia Mater.* **2020**, *12*, 30. [CrossRef]
252. Zhang, X.Y.; Fang, G.; Zhou, J. Additively Manufactured Scaffolds for Bone Tissue Engineering and the Prediction of Their Mechanical Behavior: A Review. *Materials* **2017**, *10*, 50. [CrossRef]
253. Shanghai Cooyer New Material Co., L. *Medical Titanium Alloy Anticorrosive Material*. Available online: <https://www.openpr.com/news/1188745/hip-replacement-implants-market-opportunity-2018-2025-by-top-key-players-zimmer-biomet-depuy-synthes-styker-smith-and-nephew-b-braun-melsungen-ag-corin-arthrex-inc-evolutis.html> (accessed on 30 November 2025).
254. Technology Predictions 2022; 3D Printing in Healthcare. Available online: <https://futuredirections.ieee.org/2022/01/27/technology-predictions-2022-3d-printing-in-healthcare/> (accessed on 30 November 2025).
255. Metal AM, F.M. 3D Printing/A.M. Celebrating Ten Years of Metal Additively Manufactured Hip Cups. Available online: <https://www.metal-am.com/celebrating-ten-years-of-metal-additively-manufactured-hip-cups/> (accessed on 30 November 2025).
256. Fang, C.; Cai, H.; Kuong, E.; Chui, E.; Siu, Y.C.; Ji, T.; Drstvenšek, I. Surgical Applications of Three-Dimensional Printing in the Pelvis and Acetabulum: From Models and Tools to Implants. *Unfallchirurg* **2019**, *122*, 278–285. [CrossRef] [PubMed]

257. Zhu, Y.; Babazadeh-Naseri, A.; Dunbar, N.J.; Brake, M.R.W.; Zandiyeh, P.; Li, G.; Leardini, A.; Spazzoli, B.; Fregly, B.J. Finite Element Analysis of Screw Fixation Durability under Multiple Boundary and Loading Conditions for a Custom Pelvic Implant. *Med. Eng. Phys.* **2023**, *111*, 103930. [CrossRef] [PubMed]
258. Wong, K.C.; Kumta, S.M.; Gee, N.V.L.; Demol, J. One-Step Reconstruction with a 3D-Printed, Biomechanically Evaluated Custom Implant after Complex Pelvic Tumor Resection. *Comput. Aided Surg.* **2015**, *20*, 14–23. [CrossRef] [PubMed]
259. Broekhuis, D.; Boyle, R.; Karunaratne, S.; Chua, A.; Stalley, P. Custom Designed and 3D-Printed Titanium Pelvic Implants for Acetabular Reconstruction after Tumour Resection. *HIP Int.* **2023**, *33*, 905–915. [CrossRef]
260. Hollander, D.A.; Von Walter, M.; Wirtz, T.; Sellei, R.; Schmidt-Rohlfing, B.; Paar, O.; Erli, H.J. Structural, Mechanical and in Vitro Characterization of Individually Structured Ti-6Al-4V Produced by Direct Laser Forming. *Biomaterials* **2006**, *27*, 955–963. [CrossRef]
261. Lin, C.Y.; Wirtz, T.; LaMarca, F.; Hollister, S.J. Structural and Mechanical Evaluations of a Topology Optimized Titanium Interbody Fusion Cage Fabricated by Selective Laser Melting Process. *J. Biomed. Mater. Res. A* **2007**, *83*, 272–279. [CrossRef]
262. ATEC's IdentiTi™-PC ATEC's IdentiTi Posterior Curved Porous Ti Interbody Implants. Available online: <https://www.londonspine.com/instrumented-lumbar-fusion-for-degenerative-spondylolisthesis/> (accessed on 30 November 2025).
263. Laura Griffiths Stroke Patient Gets Life Back with 3D Printed Cranial Implant from EOS. Available online: <https://www.protolabs.com/en-gb/resources/blog/3d-printing-and-customised-medical-implants/> (accessed on 30 November 2025).
264. Murr, L.E. Open-Cellular Metal Implant Design and Fabrication for Biomechanical Compatibility with Bone Using Electron Beam Melting. *J. Mech. Behav. Biomed. Mater.* **2017**, *76*, 164–177. [CrossRef]
265. Mazzoli, A.; Germani, M.; Raffaelli, R. Direct Fabrication through Electron Beam Melting Technology of Custom Cranial Implants Designed in a PHANToM-Based Haptic Environment. *Mater. Des.* **2009**, *30*, 3186–3192. [CrossRef]
266. Zhao, X.; Li, K.; Bai, X. Research on Impact Resistance of 3D Printing Titanium Alloy Personalized Cranial Prosthesis. *J. Integr. Technol.* **2022**, *11*, 48–56. [CrossRef]
267. Yan, R.; Luo, D.; Huang, H.; Li, R.; Yu, N.; Liu, C.; Hu, M.; Rong, Q. Electron Beam Melting in the Fabrication of Three-Dimensional Mesh Titanium Mandibular Prosthesis Scaffold. *Sci. Rep.* **2018**, *8*, 750. [CrossRef]
268. Moiduddin, K.; Mian, S.H.; Umer, U.; Ahmed, N.; Alkhalefah, H.; Ameen, W. Reconstruction of Complex Zygomatic Bone Defects Using Mirroring Coupled with EBM Fabrication of Titanium Implant. *Metals* **2019**, *9*, 1250. [CrossRef]
269. Yáñez, A.; Cuadrado, A.; Martel, O.; Afonso, H.; Monopoli, D. Gyroid Porous Titanium Structures: A Versatile Solution to Be Used as Scaffolds in Bone Defect Reconstruction. *Mater. Des.* **2018**, *140*, 21–29. [CrossRef]
270. Hashmi, A.W.; Mali, H.S.; Meena, A.; Saxena, K.K.; Ahmad, S.; Agrawal, M.K.; Sagbas, B.; Valerga Puerta, A.P.; Khan, M.I. A Comprehensive Review on Surface Post-Treatments for Freeform Surfaces of Bio-Implants. *J. Mater. Res. Technol.* **2023**, *23*, 4866–4908. [CrossRef]
271. Maleki, E.; Bagherifard, S.; Bandini, M.; Guagliano, M. Surface Post-Treatments for Metal Additive Manufacturing: Progress, Challenges, and Opportunities. *Addit. Manuf.* **2021**, *37*, 101619. [CrossRef]
272. Hashmi, A.W.; Mali, H.S.; Meena, A. A Comprehensive Review on Surface Quality Improvement Methods for Additively Manufactured Parts. *Rapid. Prototyp. J.* **2023**, *29*, 504–557. [CrossRef]
273. Mruthunjaya, M.; Yogesha, K.B. A Review on Conventional and Thermal Assisted Machining of Titanium Based Alloy. *Mater. Today Proc.* **2021**, *46*, 8466–8472. [CrossRef]
274. Das, S.; Kibria, G.; Doloi, B.; Bhattacharyya Editors, B. *Materials Forming, Machining and Tribology Advances in Abrasive Based Machining and Finishing Processes*; Springer: Berlin/Heidelberg, Germany, 2020.
275. Acharya, S.; Panicker, A.G.; Gopal, V.; Dabas, S.S.; Manivasagam, G.; Suwas, S.; Chatterjee, K. Surface Mechanical Attrition Treatment of Low Modulus Ti-Nb-Ta-O Alloy for Orthopedic Applications. *Mater. Sci. Eng. C* **2020**, *110*, 110729. [CrossRef]
276. Acharya, S.; Suwas, S.; Chatterjee, K. Review of Recent Developments in Surface Nanocrystallization of Metallic Biomaterials. *Nanoscale* **2021**, *13*, 2286–2301. [CrossRef]
277. Liu, Y.J.; Wang, H.L.; Li, S.J.; Wang, S.G.; Wang, W.J.; Hou, W.T.; Hao, Y.L.; Yang, R.; Zhang, L.C. Compressive and Fatigue Behavior of Beta-Type Titanium Porous Structures Fabricated by Electron Beam Melting. *Acta Mater.* **2017**, *126*, 58–66. [CrossRef]
278. Zadpoor, A.A. Mechanical Performance of Additively Manufactured Meta-Biomaterials. *Acta Biomater.* **2019**, *85*, 41–59. [CrossRef]
279. Ran, Q.; Yang, W.; Hu, Y.; Shen, X.; Yu, Y.; Xiang, Y.; Cai, K. Osteogenesis of 3D Printed Porous Ti6Al4V Implants with Different Pore Sizes. *J. Mech. Behav. Biomed. Mater.* **2018**, *84*, 1–11. [CrossRef] [PubMed]
280. Panzavolta, S.; Torricelli, P.; Amadori, S.; Parrilli, A.; Rubini, K.; Della Bella, E.; Fini, M.; Bigi, A. 3D Interconnected Porous Biomimetic Scaffolds: In Vitro Cell Response. *J. Biomed. Mater. Res. A* **2013**, *101*, 3560–3570. [CrossRef] [PubMed]
281. Dou, C.; Zhang, M.; Ren, D.; Ji, H.; Yi, Z.; Wang, S.; Liu, Z.; Wang, Q.; Zheng, Y.; Zhang, Z.; et al. Bi-Continuous Mg-Ti Interpenetrating-Phase Composite as a Partially Degradable and Bioactive Implant Material. *J. Mater. Sci. Technol.* **2023**, *146*, 211–220. [CrossRef]
282. Li, Y.; Jahr, H.; Lietaert, K.; Pavanram, P.; Yilmaz, A.; Fockaert, L.I.; Leeftang, M.A.; Poursan, B.; Gonzalez-Garcia, Y.; Weinans, H.; et al. Additively Manufactured Biodegradable Porous Iron. *Acta Biomater.* **2018**, *77*, 380–393. [CrossRef]

283. Shi, Z.Z.; Yu, J.; Liu, X.F.; Zhang, H.J.; Zhang, D.W.; Yin, Y.X.; Wang, L.N. Effects of Ag, Cu or Ca Addition on Microstructure and Comprehensive Properties of Biodegradable Zn-0.8Mn Alloy. *Mater. Sci. Eng. C* **2019**, *99*, 969–978. [[CrossRef](#)]
284. Rad, H.R.B.; Idris, M.H.; Kadir, M.R.A.; Farahany, S. Microstructure Analysis and Corrosion Behavior of Biodegradable Mg–Ca Implant Alloys. *Mater. Des.* **2012**, *33*, 88–97. [[CrossRef](#)]
285. Yadav, M.K.; Shukla, R.; Xi, L.; Wang, Z.; Prashanth, K.G. Metallic Multimaterials Fabricated by Combining Additive Manufacturing and Powder Metallurgy. *J. Compos. Sci.* **2025**, *9*, 80. [[CrossRef](#)]
286. Shukla, R.; Yadav, M.K.; Madruga, L.Y.C.; Jayaraj, J.; Papat, K.; Wang, Z.; Xi, L.; Prashanth, K.G. A Novel Ti-Eggshell-Based Composite Fabricated by Combined Additive Manufacturing–Powder Metallurgical Routes as Bioimplants. *Ceram. Int.* **2025**, *51*, 6281–6291. [[CrossRef](#)]
287. Zhang, M.; Zhao, N.; Yu, Q.; Liu, Z.; Qu, R.; Zhang, J.; Li, S.; Ren, D.; Berto, F.; Zhang, Z.; et al. On the Damage Tolerance of 3-D Printed Mg-Ti Interpenetrating-Phase Composites with Bioinspired Architectures. *Nat. Commun.* **2022**, *13*, 3247. [[CrossRef](#)]

Disclaimer/Publisher’s Note: The statements, opinions and data contained in all publications are solely those of the individual author(s) and contributor(s) and not of MDPI and/or the editor(s). MDPI and/or the editor(s) disclaim responsibility for any injury to people or property resulting from any ideas, methods, instructions or products referred to in the content.

Publication II

M.K. Yadav, R.H. Shukla, K.G. Prashanth, A comprehensive review on development of waste derived hydroxyapatite (HAp) for tissue engineering application, Materials Today: Proceedings In press (2023). <https://doi.org/10.1016/j.matpr.2023.04.669>.



Contents lists available at ScienceDirect

Materials Today: Proceedings

journal homepage: www.elsevier.com/locate/matpr

A comprehensive review on development of waste derived hydroxyapatite (HAp) for tissue engineering application

Mayank Kumar Yadav^{a,*}, Riddhi Hiren Shukla^a, K.G. Prashanth^{a,b,c,*}

^aDepartment of Mechanical and Industrial Engineering, Tallinn University of Technology, Ehitajate tee 5, 19086 Tallinn, Estonia

^bErich Schmid Institute of Materials Science, Austrian Academy of Sciences, Jahnstrasse 12, 8700 Leoben, Austria

^cCBCMT, School of Mechanical Engineering, Vellore Institute of Technology, Vellore 630014, Tamil Nadu, India

ARTICLE INFO

Article history:
Available online xxxxx

Keywords:
Waste Bone
Waste management
Hydroxyapatite
Tricalcium phosphate
Biomaterials

ABSTRACT

The present review article is a comprehensive study on the development and utilization of materials derived from biological wastes like animal waste bone, eggshells, fish scale, etc. These waste materials are calcium rich and can act as a precursor for the development of highly bioactive hydroxyapatite (HAp), tri-calcium phosphate (TCP), and calcium. The developed HAp and TCP can be utilized in the field of bone tissue engineering. The concept of valorization of these wastes into bioactive materials is a promising solution for waste management and an approach towards sustainable development.

Copyright © 2023 Elsevier Ltd. All rights reserved.

Selection and peer-review under responsibility of the scientific committee of the International Conference on Materials and Manufacturing for Sustainable Developments – 2022.

1. Introduction

It has been estimated that around 4.89 billion livestock population is present globally [1] which produces 16–20 Million Metric Tons/Year of animal waste worldwide through different sources like slaughterhouse, restaurants, etc [2,3]. Bones, horns, seashells, fish scales, eggshells, etc are some of the major parts which are generally discarded. As the demand for industrial and agricultural products is increasing the amount of organic waste produced is also increasing. The vast amount of biological waste produced is left unattended or disposed of in landfills, which can spread infectious diseases through the emission of foul smell and the tendency of pollutants to leach into the environment [4,5]. The fertility of the agricultural land is also affected by these wastes [6]. To mitigate the problem associated with these types of waste proper waste management practices are required which involves additional cost. In other words, the disposal of this biological waste is a challenge for the scientific community as it creates a hindrance to environmental protection and sustainable development. If these waste materials are processed and recycled efficiently, they have the potential to be a source of extra revenue and will directly impact the economy of the country. Researchers throughout the world

are working vigorously to obtain a sustainable solution for valorizing these waste materials. Many researchers have reported the application of these waste materials in different fields like Trans-esterification of biodiesel, Tissue Engineering applications, Drug delivery, etc. In different research findings it is concluded that if these waste materials are treated specifically, they have the potential to be converted into a source of calcium phosphate [7,8].

Hydroxyapatite (HAp) with chemical formula $\text{Ca}_{10}(\text{PO}_4)_6(\text{OH})_2$, a member of the calcium phosphate family is considered one of the most suitable bioceramics materials due to its biocompatibility, non-toxicity, osteointegration, and osteoconduction properties [9,10]. The chemical and structural properties of HAp are similar to that of natural bone and therefore it can promote bone regeneration and biological fixation with the host tissue without any supplements [11]. When HAp is introduced in biological fluid, they release Ca^{2+} and PO_4^{4-} ions upon dissolution which helps in cell proliferation and bone metabolism [12,13]. Synthetic HAp produced through different chemical methods like mechanochemical reaction, wet chemical precipitation, hydrothermal conversion emulsion, and solgel methods is considered superior [14] with respect to those derived from natural sources as mentioned above. But most of these above-mentioned methods are costly and lack some beneficial trace elements [15–17]. HAp derived from xenogeneic (derived from different species) bone sources like bovine bone is always considered a good option with respect to that of allogeneic bone (derived from the same species) [18–22] because of ease of

* Corresponding authors at: Department of Mechanical and Industrial Engineering, Tallinn University of Technology, Ehitajate tee 5, 19086 Tallinn, Estonia.

E-mail addresses: mayada@taltech.ee (M. Kumar Yadav), kgprashanth@gmail.com (K.G. Prashanth).

<https://doi.org/10.1016/j.matpr.2023.04.669>

2214-7853/Copyright © 2023 Elsevier Ltd. All rights reserved.

Selection and peer-review under responsibility of the scientific committee of the International Conference on Materials and Manufacturing for Sustainable Developments – 2022.

availability and improvement in biological constituent and structure due to thermal and mechanical processing [22-24]. Table 1 lists different methods utilized to develop HAp using different animals' wastes bone, scale, and shells. The extent of the global research activity in the field of development of natural source bio-material especially by utilizing animal waste bones has created a scope for developing HAp. Considering the potential advantages of waste-derived HAp, the present review article is an approach to review the synthesis methods of HAp through different waste sources and its application in tissue engineering.

2. Animal bone waste: A source of natural hydroxyapatite (HAp)

Bio wastes like left-out bones of bovine, lamb, goat, pig, fish bone and scale, etc generally consist of proteins, lipids, collagens and polysaccharides as organic, and calcium phosphate (CaP) as inorganic constituents. These waste materials are widely used for the synthesis of HAp [22,30]. The synthesis of HAp from these wastes generally involves the removal of moisture and organic contents via different techniques. Thermal treatment, subcritical water treatment, and alkaline heat hydrolysis are some of the methods which are practiced for the development of HAp from bio-wastes. In the alkaline hydrolysis method, microbial biodegradation of keratin takes place through hydrolysis of isolated thermoactinomycete strains [31]. Since keratin and collagen are similar proteins due to their fibrous structure, Barakat et al. [25] performed alkaline hydrolysis of collagen and other organic content of bovine bones. In this method, grounded bone was mixed with 25 wt% of sodium hydroxide solution with a solid-to-liquid weight ratio of 1:40 followed by heating at 250 °C for 5 h. The SEM and TEM results revealed the formation of pure HAp nanoparticles at lower temperatures. In subcritical water treatment method pressurized hot water is employed which changes the solvent polarity, surface tension, and viscosity [32]. As the temperature increases the dielectric constant of water reduces resulting in a reduction in polarity and thus many organic compounds like collagen, protein, etc can be extracted [33]. This method is also known as the pressurized low-polarity water method. Apart from the above-mentioned two methods, there is another conventional method that is most widely used and commonly known as the thermal treatment method. Ofudje et al. synthesized waste-derived HAp by simple heat treatment of pig bone in the temper-

ature range of 600 to 1000 °C [29]. C.Y. Ooi et al. [22] examined the properties of HAp derived from bovine bone sintered at different temperatures between 400 and 1200 °C. The XRD results show that as the sintering temperature increases above 700 °C the crystallinity of the HAp phase enhances. At higher sintering temperatures i.e., 1100 °C and 1200 °C a phenomenon of phase transformation HAp to β -tricalcium phosphate (TCP) was observed [22]. The effect of calcination on the microstructural behavior of HAp derived from human and animal bone was studied by Figueiredo et al. and a similarity are drawn between allograft and xenograft samples [34]. Piccirillo et al. [35] for the first time utilised different parts of the same fish to synthesize HAp and chloroapatite by using fish bone and scale respectively. It is also important to note that the sintered bones form a mixture of HAp and β -TCP and as the temperature increases the content of β -TCP also increases [35]. The mechanism of phase transformation from HAp to TCP was explained by Shih et al. [36]. During high-temperature sintering phenomenon of decomposition and dehydroxylation takes place resulting in the formation of TCP (α and β) [36]. Thus, from the above observations and findings through different research work it can be concluded that waste bone obtained from different animal sources can be utilized for the development of HAp and TCP based materials suitable for biomedical applications.

3. Calcium derived from eggshell and other anthropogenic waste sources

An eggshell (ES) is basically a composite of calcite crystals that is surrounded by a protein framework [37]. Along with ES various mollusk shells like mussels, cuttlebone, oysters, snail shells, etc are mainly composed of calcium carbonate (CaCO_3), according to Soares et al. [38] ES contains about 88 g of CaCO_3 per 100 g of air-dried eggshells. This CaCO_3 can be easily converted to another form of Ca which can be used to synthesize HAp [39]. Calcium Phosphate (CaP) derived from ES shows in vitro biocompatibility and the scaffolds fabricated using CaP shows osteoinductive properties which are favourable for bone tissue engineering applications [40]. The fabrication of HAp using ES involves an essential reaction with Phosphorus precursor. There are two different methods based on the processing of raw precursor i.e., CaCO_3 . The first method is direct synthesis in which ES is directly treated with

Table 1
List of different animal waste and method for the development of HAp.

Waste Material	Method	Application	Major Conclusion	Ref.
Bovine bone	Thermal Decomposition	Production of pure HAp	65% average yield of HAp	[28]
Bovine bone	Subcritical water process	Production of pure HAp	Very small amount of nanoparticle HAp produced	[28]
Bovine bone	Alkaline Hydrothermal process	Production of pure HAp	Very small amount of nanoparticle HAp produced	[28]
Chicken bone	Simple calcination process	Guided bone regeneration	Chicken bone derived HAp can be used as an osteogenic filler to augments and can change the biological behaviour of chitosan membrane.	[26]
Lates HAp powder derived by	Calcarifer fish bone sintering fish bone at 1200 °C non-cytotoxic behaviour	Simple calcination process [27]	Biomedical application	
Fish Bone	Thermal treatment at 800–1050 °C for HAp preparation and polymeric sponge method for scaffold preparation	Highly porous 3D scaffold for tissue engineering application	Porosity of the scaffold was $85 \pm 0.4\%$ and compressive and bending strength was 0.13 ± 0.007 MPa and 1.72 ± 0.02 MPa respectively.	[37]
Pig Bone	Bone powder were calcined at different temperatures i.e., 600 °C, 800 °C and 1000 °C	Tissue engineering application	Development of HAp based scaffold with 65% porosity suitable for tissue engineering application	[22]
Fish Scale	By calcining fish scale between 200 °C and 1200 °C	Biomedical application	Crystallite size of fish scale derived HAp increases with the increase in temperature.	[25]

phosphorus-based reagents [41,42]. Another method also known as indirect synthesis involves the conversion of CaCO_3 into different calcium-based products like calcium oxide, calcium hydroxide, calcium chloride, etc. CaCO_3 can be converted into calcium-based products by direct heat treatment at different temperatures, by dissolving CaCO_3 in acids [43–47]. Wu. Et al. [41] prepared HAp by ball milling dicalcium phosphate dihydrate along with ES powder for 1 h followed by high temperature sintering at 1200 °C for 1 h. Prabakaran et al. [44] successfully synthesized nano-HAp by hydrothermal method using a cationic surfactant as a regulator of nucleation and grain growth. The microstructure of the developed HAp crystals depends on the processing route. Different shapes of HAp like rods, needles, flower-like shapes, etc are reported in different research work [45]. The effect of sintering time and temperature on the morphology of HAp crystal is shown in Fig. 1.

4. Production of HAp by valorizing fish bone and fish scale waste

The production of fish is increasing due to exponential growth in its demand. It is estimated that annually 91 million tons of fish are caught worldwide out of which 50–60% of it is consumed by humans and the remaining by-products are treated as waste which creates environmental-related issues as discussed earlier in the

introduction section. Considering this fact number of research studies are focused on the conversion of fish bone and scale waste into HAp [49]. There are different methods of synthesis of HAp by using fish waste, in general, this method involves washing of waste in running water and boiling followed by chemical treatment to remove protein [50]. Deb et al. [51] observed that HAp produced by acid-treated fish waste posse's smaller crystallite size with the interconnected porous network with respect to alkaline and acid alkaline-treated fish waste. Further, the chemically treated wastes are calcined at different temperatures to get different crystallite sizes and morphology of HAp powders. Barramundi, catfish, croaker, cod, salmon, sardine, tuna, yellowtail, etc are some of the common fish species whose waste parts are used for HAp synthesis [52]. Goto et al. [53] studied the effect of the presence of different trace elements like sodium, potassium, and magnesium on the thermal stability of HAp derived from different fish bone. The amount of Magnesium for different fish bone was in the order of: hoarse mackerel (0.21 mmol g^{-1}) > greater amberjack (0.15 mmol g^{-1}) > tuna = yellowtail (0.13 mmol g^{-1}). Tuna fish sintered at temperature above than 800 °C produces highly crystalline HAp with have higher value of Ca/P ratio and low magnesium content [53]. In another study conducted by Pujie Shi and co-workers reports the presence of carbonate ion (CO_3^{2-}) in all the fish bone i.e., rainbow trout, salmon except cod fish bone [54]. Huang et al. stud-

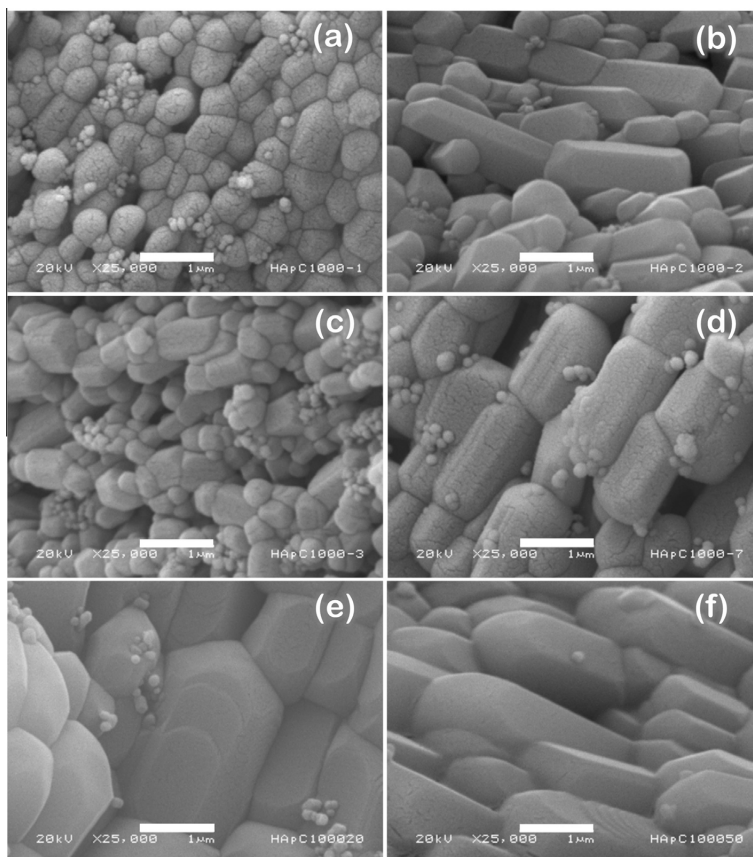


Fig. 1. SEM micrographs representing morphological transformation of samples calcined at 1000 °C for 1, 2, 3, 7, 20, and 50 h [48].

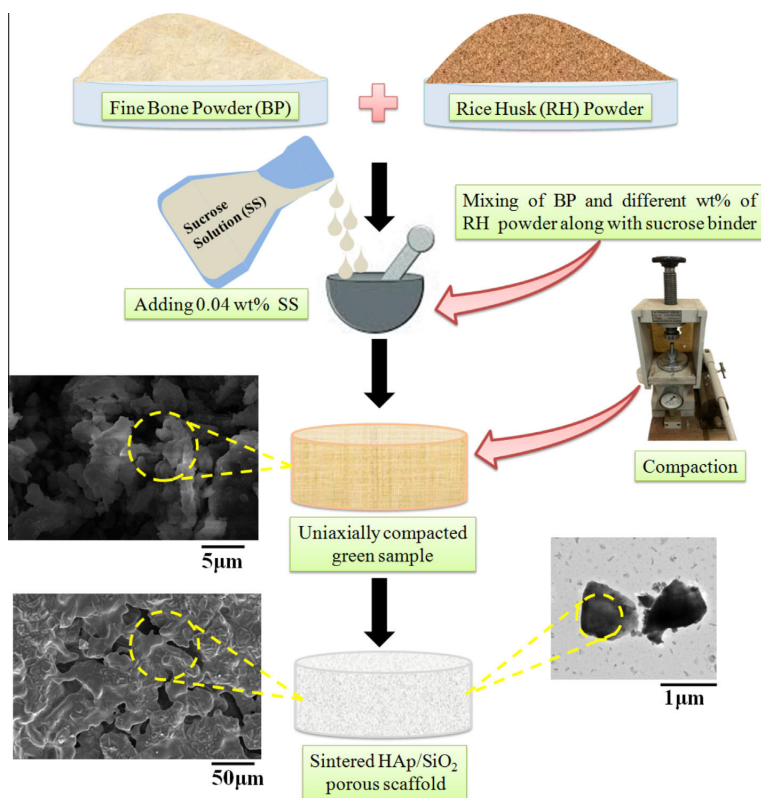


Fig. 2. Schematic diagram of the process involved in the development of HAP based scaffolds [3].

Table 2

Property comparison of 3D scaffold synthesized using different animal waste bone with respect to that of human cortical bone [3].

Type of bone	Space holder used	Binder used	Processing condition	Porosity (%)	Compressive Strength (MPa)	Ref.
Human cortical bone	NA	NA	NA	5–10	80–120	[55,56]
Bovine bone	Commercial sugar	NA	900 °C	76.7 ± 0.6	1.3 ± 0.09	[57]
Fish bone	High-density polyethylene sponge	PVA	Initial Sintering at 600 °C Final Sintering 1200 °C	85 ± 0.4	0.13 ± 0.007 MPa	[58]
Fish scale	Sponge replication	Starch	1000–1400 °C, 2hr	35	800 MPa	[38]
Pig bone	Ammonium bicarbonate	NA	600–1000 °C	65	NA	[22]
Fish bone	solvent casting particulate leaching technique/ NaCl (SH)	Ethanol (as solvent)	1200 °C, 3 hr	75 ± 0.8	7.26 ± 0.45	[39]
Bovine one	3D Printing	Glycerine (solvent)	900 °C	NA	3.22 ± 0.13 to 5.71 ± 0.43	[40]
Mixed bone waste	Rice Husk	Sucrose Solution	1000–1400 °C, 2 hr	34–61	0.22–4.1	[3]

ied the behaviour of HAP derived through enzymatic hydrolysis with Ca/P ratio of 1.76 through thermal treatment at 800 °C for 4 h.

5. Utilization of waste derived HAP for the development of 3D scaffold for tissue engineering application

Bone graft surgeries like autograft, allograft, xenograft, etc which involve the replacement of degenerated natural surfaces with the help of tissue, or organs of a donor of the same species or of different species are increasing. To reconstruct these damaged

tissues, bone tissue engineering can act as a substitute for conventional medical practices. In bone tissue engineering scaffolds are designed with the aim to proliferate bone tissues. Scaffold acts as a temporary extracellular matrix that promotes cell migration, proliferation, and differentiation [57,61] Biocompatibility, high porosity with interconnected pore structures, bioresorbability, osteoinduction, osteoconduction, and osteointegration are some of the important features of bio-scaffolds [62–65]. Since the structural and chemical resemblance of HAP is like that of natural bone, therefore the application of HAP has gained attention in the field of

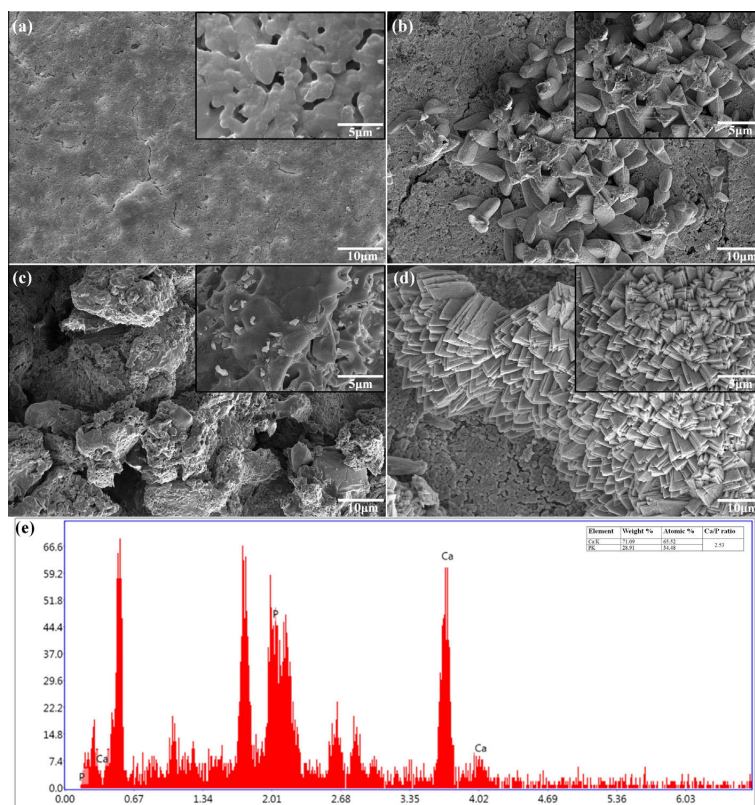


Fig. 3. SEM and EDS image of HAp based scaffold sintered at elevated temperature and immersed in simulated body fluid for different time periods [3].

bone tissue engineering. The elemental composition of HAp derived from different animal bone varies for example HAp derived from bovine bone contains 52.25 wt% CaO and 38.37 wt% P₂O₅ whereas HAp derived from Tenggiri fish bones contains 49.84 wt % Cao and 26.195 wt% P₂O₅ [20,66,67]. The calcination temperature of porous waste bone plays a major role in the osteoconductive property of the scaffold. A study conducted by Rhee et al. [68] concludes that HAp derived at 600 °C shows better osteoconductivity with respect to that of samples sintered at 1000 °C, the main reason behind this phenomenon is the depletion of carbonate ion and increase in crystallinity of HAp synthesized at 1000 °C. The above research finding is also supported by several other studies highlighting the role of carbonate ions and particle size in osteoblast activity [69,70]. Synthesis of porous 3D scaffolds for bone tissue engineering using different materials is reported by different researchers. In our recent research work [3] we fabricated a porous HAp-SiO₂ 3D scaffold using waste bone obtained from different sources like restaurants, slaughterhouses, etc. Along with the use of rice husk powder as a space holder material as shown in Fig. 2. The scaffold posse's porosity of 34–61% based on sintering temperature and weight percent of rice husk. The compressive strength of the developed scaffold was up to 4.1 MPa. The obtained properties of the developed scaffold are comparable to that of natural bone and hence can be used for tissue engineering applications. Table 2 lists the comparative analysis of porosity and mechanical properties of Hap-based 3D scaffold fabricated using different animal bone waste with that of human cortical bone. Similarly, Naga et al.

[28] fabricated a highly porous ceramic scaffold using thermally treated fishbone by polymeric sponge method. The overall process involves three stages starting with the extraction of pure HAp of average particle size 50–80 nm from the fishbone skeleton, followed by the formation of a highly porous HAp scaffold using a polymeric sponge and heat treatment at 900 °C. Mechanical and structural characterization revealed that the scaffold posse's porosity is in the range of 85 ± 0.4% with a pore diameter in the range of 1–3 µm along with bending and compressive strength of 1.72 ± 0.02 Mpa and 0.13 ± 0.007 MPa respectively. Weeraphat et al. [50] studied the physicochemical, bioactivity, and biological properties of HAp which is derived from fish scale, and compared it with that of chemically synthesized HAp. It was concluded that fish scale-derived HAp consists of flat plate nanocrystals with sizes of 15–20 nm whereas chemically derived HAp has crystals in the range of 100 nm. Biocompatibility and bioactivity studies also suggest that fish scale-derived HAp has the potential to be used as an alternate for bone scaffold or regenerative materials (see Fig. 3).

6. Conclusion and future perspective

Animal bone waste derived from different sources contains valuable precursors which can be utilized for the development of HAp-based materials as they are rich in calcium. In this review, different methods of development of HAp using different types of animal waste like bones, shells, scales, etc are discussed. Generally, HAp can be derived from calcium phosphate and calcium sources

thermal decomposition, subcritical water process, and alkaline hydrothermal process. The properties of 3D scaffold developed from waste-derived HAp possess mechanical and biological properties like that of natural bone and thus can be utilized for the development of biomaterials. The concept of valorization of animal waste by synthesizing HAp is an idea to reduce the cost of HAp-based biomaterials and also a strategy for effective waste management. It is beneficial to conduct future research in the field of bone regeneration using animal waste bone as a scaffold. It is important to investigate the biodegradation properties of the scaffold, as well as conduct an in-depth analysis of degradation products. Comprehensive studies on properties such as porosity and compressive strength of the scaffold, along with in-vitro and in-vivo analysis, are important.

Data availability

Data will be made available on request.

Declaration of Competing Interest

The authors declare that they have no known competing financial interests or personal relationships that could have appeared to influence the work reported in this paper.

Acknowledgments

The authors acknowledge financial support from the Baltic Research Programme project no. EEA-RESEARCH-85 "Waste-to-resource: eggshells as a source for next generation biomaterials for bone regeneration (EGGSHELL)" under the EEA Grant of Iceland, Liechtenstein, and Norway no. EEZ/BPP/VIAA/2021/1.

References

- [1] Advances in biomaterial production from animal derived waste _ Enhanced Reader, (n.d.).
- [2] Y. Liu, J. Chen, Phosphorus Cycle, Encyclopedia of Ecology. (2014) 181–191. Doi: 10.1016/B978-0-12-409548-9.09043-6.
- [3] M.K. Yadav, V. Pandey, K. Mohanta, V.K. Singh, A low-cost approach to develop silica doped Tricalcium Phosphate (TCP) scaffold by valorizing animal bone waste and rice husk for tissue engineering applications, *Ceram Int.* (2022), <https://doi.org/10.1016/j.ceramint.2022.05.207>.
- [4] M.J. Quina, M.A.R. Soares, R. Quinta-Ferreira, Applications of industrial eggshell as a valuable anthropogenic resource, *Resour Conserv Recycl.* 123 (2017) 176–186, <https://doi.org/10.1016/j.resconrec.2016.09.027>.
- [5] H. Yamamura, V.H.P. da Silva, P.L.M. Ruiz, V. Ussui, D.R.R. Lazar, A.C.M. Renno, D.A. Ribeiro, Physico-chemical characterization and biocompatibility of hydroxyapatite derived from fish waste, *J Mech Behav Biomed Mater.* 80 (2018) 137–142, <https://doi.org/10.1016/j.jmbm.2018.01.035>.
- [6] M. Boutinguiza, J. Pou, R. Comesaña, F. Lusquinos, A. de Carlos, B. León, Biological hydroxyapatite obtained from fish bones, *Materials Science and Engineering: C* 32 (2012) 478–486, <https://doi.org/10.1016/j.msec.2011.11.021>.
- [7] K. Fukui, N. Arimitsu, S. Kidoguchi, T. Yamamoto, H. Yoshida, Synthesis of calcium phosphate hydrogel from waste incineration fly ash and bone powder, *J Hazard Mater.* 163 (2009) 391–395, <https://doi.org/10.1016/j.jhazmat.2008.06.103>.
- [8] G.S. Kumar, E.K. Giriya, M. Venkatesh, G. Karunakaran, E. Kolesnikov, D. Kuznetsov, One step method to synthesize flower-like hydroxyapatite architecture using mussel shell bio-waste as a calcium source, *Ceram Int.* 43 (2017) 3457–3461, <https://doi.org/10.1016/j.ceramint.2016.11.163>.
- [9] M.R. Nikpour, S.M. Rabiee, M. Jahanshahi, Synthesis and characterization of hydroxyapatite/chitosan nanocomposite materials for medical engineering applications, *Compos B Eng.* 43 (2012) 1881–1886, <https://doi.org/10.1016/j.compositesb.2012.01.056>.
- [10] P. Nasker, A. Samanta, S. Rudra, A. Sinha, A.K. Mukhopadhyay, M. Das, Effect of fluorine substitution on sintering behaviour, mechanical and bioactivity of hydroxyapatite, *J Mech Behav Biomed Mater.* 95 (2019) 136–142, <https://doi.org/10.1016/j.jmbm.2019.03.032>.
- [11] G. Turnbull, J. Clarke, F. Picard, P. Riches, L. Jia, F. Han, B. Li, W. Shu, 3D bioactive composite scaffolds for bone tissue engineering, *Bioact Mater.* 3 (2018) 278–314, <https://doi.org/10.1016/j.bioactmat.2017.10.001>.
- [12] M. Sepantafar, H. Mohammadi, R. Maheronnaghs, L. Tayebi, H. Baharvand, Single phased silicate-containing calcium phosphate bioceramics: Promising biomaterials for periodontal repair, *Ceram Int.* 44 (2018) 11003–11012, <https://doi.org/10.1016/j.ceramint.2018.03.050>.
- [13] A. Hoppe, N.S. Güldal, A.R. Boccacini, A review of the biological response to ionic dissolution products from bioactive glasses and glass-ceramics, *Biomaterials.* 32 (2011) 2757–2774, <https://doi.org/10.1016/j.biomaterials.2011.01.004>.
- [14] Synthetic materials used for the substitution of bone defects: Critical review, *Annals of Oral & Maxillofacial Surgery*, (n.d.), <https://www.oapublishinglondon.com/article/398> (accessed July 31, 2022).
- [15] D.K. Pattanayak, R. Dash, R.C. Prasad, B.T. Rao, T.R. Rama Mohan, Synthesis and sintered properties evaluation of calcium phosphate ceramics, *Materials Science and Engineering C* 27 (2007) 684–690, <https://doi.org/10.1016/j.msec.2006.06.021>.
- [16] S. Koutsopoulos, Synthesis and characterization of hydroxyapatite crystals: A review study on the analytical methods, 2002.
- [17] M. Akram, A. Rashid, A. Imran, S. Wan, A. Wan, I. Rafoqat Hussain, Extracting hydroxyapatite and its precursors from natural resources, (n.d.). Doi: 10.1007/s10853-013-7864-x.
- [18] S. Joschek, B. Nies, R. Krotz, A. Göpferich, Chemical and physicochemical characterization of porous hydroxyapatite ceramics made of natural bone, *Biomaterials.* 21 (2000) 1645–1658, [https://doi.org/10.1016/S0142-9612\(00\)00036-3](https://doi.org/10.1016/S0142-9612(00)00036-3).
- [19] R. Murugan, S. Ramakrishna, K. Panduranga Rao, Nanoporous hydroxy-carbonate apatite scaffold made of natural bone, *Mater Lett.* 60 (2006) 2844–2847, <https://doi.org/10.1016/j.matlet.2006.01.104>.
- [20] K. Haberko, M.M. Bučko, J. Brzezińska-Miecznik, M. Haberko, W. Moggawa, T. Panz, A. Pyda, J. Zarebski, Natural hydroxyapatite—its behaviour during heat treatment, *J Eur Ceram Soc.* 26 (2006) 537–542, <https://doi.org/10.1016/j.jeurceramsoc.2005.07.033>.
- [21] R. Murugan, P. Rao, T.S.S. Kumar, Heat-deproteinated xenogeneic bone from slaughterhouse waste: Physico-chemical properties, 2003.
- [22] C.Y. Ooi, M. Hamdi, S. Ramesh, Properties of hydroxyapatite produced by annealing of bovine bone, *Ceram Int.* 33 (2007) 1171–1177, <https://doi.org/10.1016/j.ceramint.2006.04.001>.
- [23] S.A. Essien Etok Eugenia Valsami-Jones AE Timothy J Wess AE Jennifer C Hiller AE Clark A Maxwell AE Keith D Rogers AE David A C Manning AE Margaret L White AE Elisa Lopez-Capel AE Matthew J Collins AE Mike Buckley AE Kirsty E H Penkman AE Stephen L Woodgate, Structural and chemical changes of thermally treated bone apatite, (n.d.). Doi: 10.1007/s10853-007-1993-z.
- [24] J.C. Hiller, T.J.U. Thompson, M.P. Evison, A.T. Chamberlain, T.J. Wess, Bone mineral change during experimental heating: An X-ray scattering investigation, *Biomaterials.* 24 (2003) 5091–5097, [https://doi.org/10.1016/S0142-9612\(03\)00427-7](https://doi.org/10.1016/S0142-9612(03)00427-7).
- [25] N.A.M. Barakat, M.S. Khil, A.M. Omran, F.A. Sheikh, H.Y. Kim, Extraction of pure natural hydroxyapatite from the bovine bones bio waste by three different methods, *J Mater Process Technol.* 209 (2009) 3408–3415, <https://doi.org/10.1016/j.jmatprotec.2008.07.040>.
- [26] S.L. Bee, Z.A.A. Hamid, Characterization of chicken bone waste-derived hydroxyapatite and its functionality on chitosan membrane for guided bone regeneration, *Compos B Eng.* 163 (2019) 562–573, <https://doi.org/10.1016/j.compositesb.2019.01.036>.
- [27] A. Pal, S. Paul, A.R. Choudhury, V.K. Balla, M. Das, A. Sinha, Synthesis of hydroxyapatite from Lates calcarifer fish bone for biomedical applications, *Mater Lett.* 203 (2017) 89–92, <https://doi.org/10.1016/j.matlet.2017.05.103>.
- [28] S.M. Naga, H.F. El-Maghraby, E.M. Mahmoud, M.S. Talaat, A.M. Ibrahim, Preparation and characterization of highly porous ceramic scaffolds based on thermally treated fish bone, *Ceram Int.* 41 (2015) 15010–15016, <https://doi.org/10.1016/j.ceramint.2015.08.057>.
- [29] E.A. Ofudje, A. Rajendran, A.I. Adeogun, M.A. Idowu, S.O. Kareem, D.K. Pattanayak, Synthesis of organic derived hydroxyapatite scaffold from pig bone waste for tissue engineering applications, *Advanced Powder Technology.* 29 (2018) 1–8, <https://doi.org/10.1016/j.apt.2017.09.008>.
- [30] S. Paul, A. Pal, A.R. Choudhury, S. Bodhak, V.K. Balla, A. Sinha, M. Das, Effect of trace elements on the sintering effect of fish scale derived hydroxyapatite and its bioactivity, *Ceram Int.* 43 (2017) 15678–15684, <https://doi.org/10.1016/j.ceramint.2017.08.127>.
- [31] A. Gousterova, D. Braikova, I. Goshev, P. Christov, K. Tishinov, E. Vasileva-Tonkova, T. Haertel, P. Nedkov, Degradation of keratin and collagen containing wastes by newly isolated thermoactinomycetes or by alkaline hydrolysis, *Lett Appl Microbiol.* 40 (2005) 335–340, <https://doi.org/10.1111/j.1472-765X.2005.01692.X>.
- [32] Y. Yang, M. Belghazi, A. Lagadec, D.J. Miller, S.B. Hawthorne, Elution of organic solutes from different polarity sorbents using subcritical water, *J Chromatogr A* 810 (1998) 149–159, [https://doi.org/10.1016/S0021-9673\(98\)00222-2](https://doi.org/10.1016/S0021-9673(98)00222-2).
- [33] Y. Han, S. Li, X. Wang, L. Jia, J. He, Preparation of hydroxyapatite rod-like crystals by protein precursor method, *Mater Res Bull.* 42 (2007) 1169–1177, <https://doi.org/10.1016/j.materresbull.2006.09.003>.
- [34] M. Figueiredo, A. Fernando, G. Martins, J. Freitas, F. Judas, H. Figueiredo, Effect of the calcination temperature on the composition and microstructure of hydroxyapatite derived from human and animal bone, *Ceram Int.* 36 (2010) 2383–2393, <https://doi.org/10.1016/j.ceramint.2010.07.016>.
- [35] C. Piccirillo, R.C. Pullar, D.M. Tobaldi, P.M.L. Castro, M.M.E. Pintado, Hydroxyapatite and chlorapatite derived from sardine by-products, *Ceram Int.* 40 (2014) 13231–13240, <https://doi.org/10.1016/j.ceramint.2014.05.030>.

- [36] S.F. Ou, S.Y. Chiou, K.L. Ou, Phase transformation on hydroxyapatite decomposition, *Ceram Int.* 39 (2013) 3809–3816, <https://doi.org/10.1016/j.ceramint.2012.10.221>.
- [37] S. Meski, S. Ziani, H. Khireddine, F. Yataghane, N. Ferguene, Elaboration of the hydroxyapatite with different precursors and application for the retention of the lead, *Water Science and Technology.* 63 (2011) 2087–2096, <https://doi.org/10.2166/wst.2011.210>.
- [38] M.A.R. Soares, M.J. Quina, R.M. Quinta-Ferreira, Immobilisation of lead and zinc in contaminated soil using compost derived from industrial eggshell, *J Environ Manage.* 164 (2015) 137–145, <https://doi.org/10.1016/j.jenvman.2015.08.042>.
- [39] Y. Hou, A. Shavandi, A. Carne, A.A. Bekhit, T.B. Ng, R.C.F. Cheung, A.E. din A. Bekhit, Marine shells: Potential opportunities for extraction of functional and health-promoting materials, <http://dx.doi.org/10.1080/10643389.2016.1202669>, 46 (2016) 1047–1116. Doi: 10.1080/10643389.2016.1202669.
- [40] M.F.M.A. Zamri, R. Bahru, R. Amin, M.U. Aslam Khan, S.I.A. Razak, S.A. Hassan, M.R.A. Kadir, N.H.M. Nayan, Waste to health: A review of waste derived materials for tissue engineering, *J Clean Prod.* 290 (2021), <https://doi.org/10.1016/j.jclepro.2021.125792>.
- [41] S.C. Wu, H.C. Hsu, S.K. Hsu, Y.C. Chang, W.F. Ho, Effects of heat treatment on the synthesis of hydroxyapatite from eggshell powders, *Ceram Int.* 41 (2015) 10718–10724, <https://doi.org/10.1016/j.ceramint.2015.05.006>.
- [42] S.C. Wu, H.C. Hsu, Y.N. Wu, W.F. Ho, Hydroxyapatite synthesized from oyster shell powders by ball milling and heat treatment, *Mater Charact.* 62 (2011) 1180–1187, <https://doi.org/10.1016/j.matchar.2011.09.009>.
- [43] B. Chaudhuri, B. Mondal, D.K. Modak, K. Pramanik, B.K. Chaudhuri, Preparation and characterization of nanocrystalline hydroxyapatite from egg shell and K₂HPO₄ solution, *Mater Lett.* 97 (2013) 148–150, <https://doi.org/10.1016/j.matlet.2013.01.082>.
- [44] K. Prabakaran, S. Rajeswari, Spectroscopic investigations on the synthesis of nano-hydroxyapatite from calcined eggshell by hydrothermal method using cationic surfactant as template, *Spectrochim Acta A Mol Biomol Spectrosc.* 74 (2009) 1127–1134, <https://doi.org/10.1016/j.saa.2009.09.021>.
- [45] N.K. Nga, N.T. Thuy Chau, P.H. Viet, Facile synthesis of hydroxyapatite nanoparticles mimicking biological apatite from eggshells for bone-tissue engineering, *Colloids Surf B Biointerfaces.* 172 (2018) 769–778, <https://doi.org/10.1016/j.colsurfb.2018.09.039>.
- [46] S. Lahrich, M. Abderrahim, E. Mhammedi, A. Siddharthan, S. Kumar, S.K. Seshadri, Synthesis and characterization of nanocrystalline apatites from eggshells at different Ca/P ratios, *Biomedical Materials.* 4 (2009), <https://doi.org/10.1088/1748-6041/4/4/045010>.
- [47] G.S. Kumar, A. Thamizhavel, E.K. Giriya, Microwave conversion of eggshells into flower-like hydroxyapatite nanostructure for biomedical applications, *Mater Lett.* 76 (2012) 198–200, <https://doi.org/10.1016/j.matlet.2012.02.106>.
- [48] C.F. Ramirez-Gutierrez, S.M. Londoño-Restrepo, A. del Real, M.A. Mondragón, M.E. Rodríguez-García, Effect of the temperature and sintering time on the thermal, structural, morphological, and vibrational properties of hydroxyapatite derived from pig bone, *Ceram Int.* 43 (2017) 7552–7559, <https://doi.org/10.1016/j.ceramint.2017.03.046>.
- [49] J.A. da Cruz, W.R. Weinand, A.M. Neto, R.S. Palácios, P. Palácios, A.J.M. Sales, P. R. Prezas, M.M. Costa, M.P.F. Graç, Advanced manufacturing for biomaterials and biological materials low-cost hydroxyapatite powders from tilapia fish, *JOM.* 72 (n.d.). Doi: 10.1007/s11837-019-03998-4.
- [50] W. Pon-On, P. Suntornsaratoon, N. Charoengphandhu, J. Thongbunchoo, N. Krishnamra, I.M. Tang, Hydroxyapatite from fish scale for potential use as bone scaffold or regenerative material, *Materials Science and Engineering: C.* 62 (2016) 183–189, <https://doi.org/10.1016/j.msec.2016.01.051>.
- [51] P. Deb, A.B. Deoghare, Effect of pretreatment processes on physicochemical properties of hydroxyapatite synthesized from *Puntius conchionius* fish scales, *Bulletin of Materials Science.* 42 (2019), <https://doi.org/10.1007/s12034-018-1684-1>.
- [52] P. Terzioğlu, H. Öğüt, A. Kalemtaş, Natural calcium phosphates from fish bones and their potential biomedical applications, *Materials Science and Engineering: C.* 91 (2018) 899–911, <https://doi.org/10.1016/j.msec.2018.06.010>.
- [53] T. Goto, K. Sasaki, Effects of trace elements in fish bones on crystal characteristics of hydroxyapatite obtained by calcination, *Ceram Int.* 40 (2014) 10777–10785, <https://doi.org/10.1016/j.ceramint.2014.03.067>.
- [54] P. Shi, M. Liu, F. Fan, C. Yu, W. Lu, M. Du, Characterization of natural hydroxyapatite originated from fish bone and its biocompatibility with osteoblasts, *Materials Science and Engineering: C.* 90 (2018) 706–712, <https://doi.org/10.1016/j.msec.2018.04.026>.
- [55] S.C.P. Cachinho, R.N. Correia, Titanium scaffolds for osteointegration: Mechanical, in vitro and corrosion behaviour, *J Mater Sci Mater Med.* 19 (2008) 451–457, <https://doi.org/10.1007/s10856-006-0052-7/TABLES/3>.
- [56] A. Mukherjee, *Biomimetics Learning from Nature, Biomimetics Learning from Nature.* (2010), <https://doi.org/10.5772/198>.
- [57] G. Krishnamurthy, M.R. Murali, M. Hamdi, A.A. Abbas, H.B. Raghavendran, T. Kamarul, Characterization of bovine-derived porous hydroxyapatite scaffold and its potential to support osteogenic differentiation of human bone marrow derived mesenchymal stem cells, *Ceram Int.* 40 (2014) 771–777, <https://doi.org/10.1016/j.ceramint.2013.06.067>.
- [58] B. Mondal, S. Mondal, A. Mondal, M. Mandal, Fish scale derived hydroxyapatite scaffold for bone tissue engineering, *Mater Charact.* 121 (2016) 112–124, <https://doi.org/10.1016/j.matchar.2016.09.034>.
- [61] A. Olad, F. Farshi Azhar, The synergetic effect of bioactive ceramic and nanoclay on the properties of chitosan-gelatin/nanohydroxyapatite-montmorillonite scaffold for bone tissue engineering, *Ceram Int.* 40 (2014) 10061–10072, <https://doi.org/10.1016/j.ceramint.2014.04.010>.
- [62] X. yun Zhang, Y. ping Chen, J. Han, J. Mo, P. feng Dong, Y. hong Zhuo, Y. Feng, Biocompatible silk fibroin/carboxymethyl chitosan/strontium substituted hydroxyapatite/cellulose nanocrystal composite scaffolds for bone tissue engineering, *Int J Biol Macromol.* 136 (2019) 1247–1257. Doi: 10.1016/j.ijbiomac.2019.06.172.
- [63] W. Xiao, B. Sonny Bal, M.N. Rahaman, Preparation of resorbable carbonate-substituted hollow hydroxyapatite microspheres and their evaluation in osseous defects in vivo, *Materials Science and Engineering C.* 60 (2016) 324–332, <https://doi.org/10.1016/j.msec.2015.11.039>.
- [64] A. Szcześ, L. Hołysz, E. Chibowski, Synthesis of hydroxyapatite for biomedical applications, *Adv Colloid Interface Sci.* 249 (2017) 321–330, <https://doi.org/10.1016/j.cis.2017.04.007>.
- [65] Y. Tang, K. Zhao, L. Hu, Z. Wu, Two-step freeze casting fabrication of hydroxyapatite porous scaffolds with bionic bone graded structure, *Ceram Int.* 39 (2013) 9703–9707, <https://doi.org/10.1016/j.ceramint.2013.04.038>.
- [66] T. Jia, F. Zhou, H. Ma, Y. Zhang, A highly stable waste animal bone-based catalyst for selective nitriles production from biomass via catalytic fast pyrolysis in NH₃, *J Anal Appl Pyrolysis.* 157 (2021), <https://doi.org/10.1016/j.jaap.2021.105217>.
- [67] A. Buasri, T. Inkaew, L. Kodephun, W. Yenying, V. Loryuenyong, Natural Hydroxyapatite (NHAp) Derived from Pork Bone as a Renewable Catalyst for Biodiesel Production via Microwave Irradiation, *Key Eng Mater.* 659 (2015) 216–220, <https://doi.org/10.4028/www.scientific.net/KEM.659.216>.
- [68] S.H. Rhee, H.N. Park, Y.J. Seol, C.P. Chung, S.H. Han, Effect of heat-treatment temperature on the osteoconductivity of the apatite derived from bovine bone, *Key Eng Mater.* 309–311 (2006) 41–44, <https://doi.org/10.4028/0-87849-992-X.41>.
- [69] A.S. Stanislavov, L.F. Sukhodub, L.B. Sukhodub, V.N. Kuznetsov, K.L. Bychkov, M.I. Kravchenko, Structural features of hydroxyapatite and carbonated apatite formed under the influence of ultrasound and microwave radiation and their effect on the bioactivity of the nanomaterials, *Ultrason Sonochem.* 42 (2018) 84–96, <https://doi.org/10.1016/j.ultsonch.2017.11.011>.
- [70] Z. Shi, X. Huang, Y. Cai, R. Tang, D. Yang, Size effect of hydroxyapatite nanoparticles on proliferation and apoptosis of osteoblast-like cells, *Acta Biomater.* 5 (2009) 338–345, <https://doi.org/10.1016/j.actbio.2008.07.023>.

Further reading

- [59] P. Deb, E. Barua, A.B. Deoghare, S. das Lala, Development of bone scaffold using *Puntius conchionius* fish scale derived hydroxyapatite: Physico-mechanical and biotivity evaluations, *Ceram Int.* 45 (2019) 10004–10012, <https://doi.org/10.1016/j.ceramint.2019.02.044>.
- [60] J. Triyono, R. Alfiansyah, H. Sukanto, D. Ariawan, Y. Nugroho, Fabrication and characterization of porous bone scaffold of bovine hydroxyapatite-glycerin by 3D printing technology, *Bioprinting.* 18 (2020) e00078.



Publication III

M.K. Yadav, R.H. Shukla, K. Praveenkumar, S. Nilawar, C.S. Perugu, P. Sellamuthu, K. Chatterjee, S. Suwas, J. Jayaraj, K.G. Prashanth, Microstructural, mechanical, corrosion, and biological behavior of spark plasma sintered commercially pure zinc for biomedical applications, *Materials Advances* 6 (2025) 3546-3560. <https://doi.org/10.1039/d5ma00092k>.



Cite this: DOI: 10.1039/d5ma00092k

Microstructural, mechanical, corrosion, and biological behavior of spark plasma sintered commercially pure zinc for biomedical applications

Mayank Kumar Yadav,^a Riddhi Hirenkumar Shukla,^a K. Praveenkumar,^b Sagar Nilawar,^c Chandra Sekhar Perugu,^d Prabhukumar Sellamuthu,^e Kaushik Chatterjee,^f Satyam Suwas,^c J. Jayaraj^g and K. G. Prashanth^h  [★] 

This study investigates the microstructural, mechanical, corrosion, and biological behaviors of spark plasma sintered (SPS) zinc (Zn) samples for biomedical applications. The findings reveal that SPS significantly refines the grain structure of pure Zn compared to the conventional casting method. The SPS process, conducted at a lower sintering temperature of 300 °C and a high uniaxial pressure of 50 MPa, produces fine and uniform equiaxed grains with an average size of 19 μm. The resulting Zn samples exhibit a calculated density of 7.1 g cc⁻¹ due to complete densification. The sintering process disrupts the initial texture strength, and the uniform grain orientation achieved during SPS contributes to an isotropic microstructure, enhancing the mechanical properties. The compressive yield strength and ultimate strength of the SPS samples are 115 ± 4 MPa and 191 ± 6 MPa, respectively. The long-term biodegradation behavior of SPS Zn in simulated body fluid indicates controlled and gradual corrosion, supporting its potential for biodegradable implant applications, while potentiodynamic polarization analysis further confirms similar corrosion rates compared to cast Zn due to the formation of a stable corrosion product film. *In vitro* studies with MC3T3-E1 preosteoblast cells show healthy proliferation in culture media containing the degradation products of SPS Zn. Due to its unique microstructural, mechanical, and corrosion properties, along with its biocompatibility, SPS-processed Zn is a promising candidate for tissue engineering applications.

Received 2nd February 2025,
Accepted 11th April 2025

DOI: 10.1039/d5ma00092k

rsc.li/materials-advances

A. Introduction

Recent studies have highlighted the growing demand for biodegradable implants in tissue engineering applications.^{1–4} Among various biodegradable materials such as magnesium

(Mg), zinc (Zn), and iron (Fe), Zn and their alloys stand out due to their promising features like biodegradability, biocompatibility, lower energy consumption during sintering, and favorable mechanical properties.^{5–7} However, as-cast Zn often exhibits a coarse microstructure, resulting in low mechanical strength and pronounced anisotropy.⁸ Clinical challenges like stress shielding and the need for secondary surgery make biodegradable materials a viable alternative to permanent materials such as titanium (Ti), stainless steel (SS), and cobalt-chromium (CoCr) alloys in tissue engineering applications.^{9–14} Biodegradable or bioresorbable metals are a special class of materials that gradually degrade or resorb, allowing new cells to form functional tissues when placed at a diseased site.¹ These materials provide initial mechanical support to diseased organs or tissues and are gradually resorbed by biological fluids, facilitating bone tissue regeneration at critical-sized bone defect sites.¹⁵ This approach mitigates issues like long-term damage or the need for secondary surgery associated with permanent metallic implants. Mg, Zn, and Fe are commonly used degradable metals.^{15–18} Among these, Mg has a Young's modulus like natural bone but

^a Department of Mechanical and Industrial Engineering, Tallinn University of Technology, Ehitajate tee 5, 19086 Tallinn, Estonia.

E-mail: kgprashanth@gmail.com, prashanth.konda@taltech.ee

^b Faculty of Materials Science and Technology, VSB—Technical University of Ostrava, 17. listopadu 2172/15, 70 800 Ostrava, Czech Republic

^c Department of Materials Engineering, Indian Institute of Science (IISc), Bangalore 560012, India

^d Emerging Nanoscience Research Institute (EnRI), Nanyang Technological University, 50 Nanyang Avenue, 639798, Singapore

^e Department of Mechanical Engineering, Presidency University, Bangalore, India

^f Materials Technology, Dalarna University, SE-79188, Falun, Sweden

^g Department of Mechanical and Materials Engineering, Karlstad University, SE-65188, Karlstad, Sweden

^h Centre for Biomaterials, Cellular and Molecular Theranostics (CBCMT), Vellore Institute of Technology, School of Mechanical Engineering, Tamil Nadu, 632014, India



degrades rapidly in physiological environments, increasing local alkalinity and forming hydrogen pockets affecting the healing process.^{19–24} Fe, on the other hand, degrades too slowly and remains in the body for extended periods.²⁵ Zn's corrosion potential (-0.8 V) lies between that of Mg (~ -2.4 V) and Fe (-0.4 V), resulting in a degradation rate that aligns well with tissue generation.^{26,27}

As an essential metallic element, Zn plays a crucial role in bone metabolism, to stimulate the formation of osteoblasts and inhibit osteoclast differentiation, thus enhancing bone strength.^{28,29} Consequently, biodegradable Zn alloys offer significant advantages over biodegradable materials (polymers, Mg, and Fe-based alloys) in orthopedic applications.^{30,31} For instance, Bowen *et al.*^{32,33} investigated the *in vivo* biodegradation behavior by inserting pure Zn wire into the arteries of rats, which degraded at an optimal rate ($20 \mu\text{m}$ per year) for biodegradable stents during the initial three months. Despite Zn's numerous suitable properties for biomedical applications, its use is limited due to the coarse microstructure of as-cast pure Zn offering poor mechanical strength and strong anisotropy.^{34,35} Researchers have attempted to enhance Zn's properties through mechanical alloying or other similar processing techniques to reduce grain size and improve strength and ductility. Forming techniques such as rolling, forging, equal channel angular pressing (ECAP), high-pressure torsion (HPT), and additive manufacturing (AM) have been employed to refine Zn's microstructure.^{36–39} For example, Wen *et al.*¹⁸ optimized the selective laser melting (SLM) processing parameters to produce high-density pure Zn with enhanced mechanical properties (hardness of 46 ± 2 HV, Young's modulus of 20 ± 6 GPa, yield strength of 122 ± 3 MPa, ultimate strength of 138 ± 3 MPa, and elongation of $8 \pm 1\%$). Similarly, Salehi *et al.*⁴⁰ used a two-step 3D printing technique to create Mg–5.9Zn–0.13Zr components, achieving functional parts with increased relative density ($69 \pm 0.5\%$) and compressive yield strength (31 ± 3 MPa) through liquid phase sintering. Lu and Li *et al.*^{41,42} employed a high-pressure phase transition method to enhance the mechanical and corrosion behavior of Zn–1.5Mn and Zn–Li alloys through solid solution strengthening. Lin *et al.*⁴³ fabricated Mg₂Zn₃/Zn composites *via* accumulative roll bonding (ARB), achieving enhanced mechanical properties, along with an enhanced elongation of 12%, and improved corrosion resistance after 15 cycles. Demirtas *et al.*⁴⁴ demonstrated that multiple equal channel extrusions reduced the grain size (2.0 mm) of Zn–0.3 wt% Al and the presence of Al-enriched precipitates, ranging from 50 to 200 nm, significantly enhancing the alloy's superplasticity at room temperature. Yang *et al.*³¹ developed binary zinc-based materials with elements like Ca, Mg, Li, Sr, Fe, Mn, Ag, and Fe improving cytocompatibility, osteogenesis, and osseointegration. However, the selection and proportion of alloying elements must be carefully considered to achieve good biocompatibility.

Given the challenges of developing defect-free, fine microstructured pure Zn for tissue engineering applications, this research employs the spark plasma sintering (SPS) technique to produce dense and fine micro-structured Zn without alloying or

mechanical processing. SPS is an advanced sintering methodology that applies uniaxial pressure and pulsed current to heat the powder, facilitating rapid densification at lower sintering temperatures.^{45–49} The relatively fast cooling rate of SPS (compared to conventional cast) results in a refined, non-textured microstructure.⁵⁰ Capek *et al.*⁵¹ developed porous Zn for implantation into trabecular bone using SPS, achieving a compressive yield strength (~ 31 MPa) like that of trabecular bone (1–12 MPa). Based on earlier investigations, various studies have improved the mechanical and biological properties of Zn and its alloys using SPS.^{52,53} However, a comprehensive study that examines the microstructural, textural, mechanical, corrosion, and biological behavior of SPS-processed Zn has yet to be reported. To address this research gap, the present investigation aims to thoroughly understand these properties in SPS-processed pure Zn and compare them systematically with cast Zn samples. This comparison will help assess the effectiveness of the SPS process for the fabrication of Zn for biomedical applications.

B. Materials and methods

Commercially pure gas atomized Zn powder with a particle size ranging between $10 \mu\text{m}$ and $25 \mu\text{m}$ was used in the present study. A commercially pure Zn block ($>99.9\%$) from Vedanta Ltd. (Mumbai, India) was used in the present study as the cast sample. To achieve microstructural homogenization, cast Zn material was recrystallized at 300°C for 4 h under ambient conditions. Zn powders were compacted in the form of cylinders of $\sim 6\text{--}7$ mm by SPS (HP D10 FCT system, GmbH, Germany) using a graphite die of 20 mm inner diameter. To prevent Zn from sticking with the die and to maintain electrical conductivity during sintering, 0.5 mm thick graphite paper was placed between the graphite punches and the Zn powder. The sintering was performed in a vacuum at 300°C (temperature) under a uniaxial pressure of 50 MPa. The sintering process involves three distinct stages: initial pressing from 5 MPa to 50 MPa, followed by increasing the temperature from 50°C to 300°C at a rate of $50^\circ\text{C min}^{-1}$ with a dwell time of 10 min; and finally, the cooling stage, where the temperature decreases from 300°C to 50°C at the same rate of $50^\circ\text{C min}^{-1}$. The structural characterization of the powder and the bulk samples was carried out using a Rigaku Smart Lab X-Ray diffractometer (fitted with Cu-K α radiation ($\lambda = 1.5406 \text{ \AA}$)) between the 2θ range of 30° and 80° with a scan rate and step size of 3° min^{-1} and 0.01° , respectively in Bragg–Brentano mode. The bulk texture of the processed samples was analyzed by using an X-ray goniometer with Schulz reflection geometry (Rigaku Smartlab XRD) and a Cu-K α source operated at 45 kV and 30 mA on the XY surface.

The microstructural characterization of the samples including optical microscopy (OM) and scanning electron microscopy (SEM) fitted with electron backscattered diffraction (EBSD) was carried out after the samples were subjected to standard metallographic procedures. After mounting the sample, they



are subjected to grinding (sequentially varied up to 4000 μm grit paper) followed by electropolishing and etching. The electropolishing of the samples was performed to obtain a mirror-like surface finish operating under 20 V for 35 s in an electrolyte consisting of orthophosphoric acid and ethanol (3:5 ratio). The polished surface was etched for 10 s in 10% nitral to characterize the grain morphology using an OM (Leica Microsystem) and SEM (Zeiss Gemini SEM 450) equipped with an EDAX EBSD detector. The room temperature compressive strength of the samples was tested by using an Instron 5567 screw-driven universal testing machine at a strain rate of 10^{-3} s^{-1} . The *in vitro* biodegradation behavior of the samples was assessed by immersing them in simulated body fluid (SBF) for 7, 14, and 21 days, respectively. The SBF solution was prepared according to the method outlined elsewhere but in.⁵⁴ Before immersion, all samples were polished using the previously described procedure and subsequently ultrasonicated for 30 min to eliminate any surface contaminants. The samples were then incubated at 37 °C with a 5% CO_2 supply for the specified durations. The mass change was recorded to determine the degradation rate. The electrochemical corrosion behavior of the as-cast and SPS Zn samples was studied using a standard 3-electrode cell setup using a potentiostat (C.H. Instruments, CHI604E, Texas, USA) with standard calomel and platinum (Pt) as the reference and counter electrodes, respectively. Zn samples with an exposure area of 1 cm^2 were used as the working electrode, and simulated body fluid (SBF) was employed as the electrolyte.^{55,56} All the samples were mechanically ground up to #4000 grit followed by cloth polishing to obtain scratch-free surfaces of an average roughness of 0.08 μm . The open circuit potential (OCP) for the Zn samples was continuously monitored for 1 h. To understand the corrosion behavior, the samples were covered by the SBF solution for 1 h and 24 h, respectively. After 1 h and 24 h, the electrochemical impedance spectroscopy (EIS) information was recorded. The EIS measurement was performed in the frequency range of 10 kHz to 0.01 Hz by applying 10 mV perturbation to OCP values. Similarly, the potentiodynamic polarization (PDP) tests were carried out for 1 h under the potential range of -0.3 V vs. SCE to 0.3 V vs. SCE offset to the rest potential with a scan rate of 1 mV s^{-1} . All these studies were repeated three times to ensure repeatability. After PDP and EIS, all the samples were cleaned according to ISO 8407:2009,³³ and the surface morphology of the corroded surface was observed *via* SEM (Model – Zeiss Gemini SEM 450). The corrosion rate (CR) was calculated according to eqn (1).

$$\text{CR} = \frac{I_{\text{corr}} \cdot 1000}{n \cdot F \cdot A} \quad (1)$$

where I_{corr} represents the current density, n denotes the number of electrons (2 in the present case), F signifies the Faraday's constant (96500 C mol^{-1}), and A stands for the atomic weight of the metal (65.38 g mol^{-1}).

The *in vitro* cytocompatibility of the SPS Zn samples was studied by indirect method by using MC3T3-E1 cells (the MC3T3-E1 preosteoblast cells were obtained from an established commercial

supplier, meeting all necessary regulatory and quality standards), and the results were compared with the as-cast Zn samples. Initially disc shaped Zn samples (20 mm diameter and 2 mm thickness) were polished uniformly followed by sterilizing in ethanol and exposed to UV for 1 h. To remove residual ethanol, the samples were further washed thrice using a mixture of phosphate buffer saline solution and 1% antibiotic. Since Zn degrades in the solution media, the effect of leaching out from the material on the cellular response was observed by using conditioned media. Conditioned media was prepared by incubating the sterilized samples in a complete culture medium, *i.e.*, the mixture of α -MEM (minimum essential medium), 10% fetal bovine serum (FBS, Gibco, Life technologies) and 1% antibiotic (Sigma Aldrich) for 24 h and 72 h at 37 °C in the presence of 5% CO_2 . A constant amount of $15 \mu\text{L mm}^{-2}$ of complete media was used to prepare the conditioned media. After the mentioned incubation period, the samples were removed. The conditioned medium was centrifuged (5000 rpm for 20 min) to remove the presence of any debris.

MC3T3-E1 cells were cultured in complete media using a 48-well plate with 3×10^3 cells per well and allowed to attach for 24 h at 37 °C with 5% CO_2 . After 24 h of incubation, the media was replaced with a conditioned medium and further incubated for 24 h and 72 h separately. The condition media of the as-cast and SPS Zn were used at two different dilutions: $1 \times$ (*i.e.*, 100% conditioned medium) and $8 \times$ (*i.e.*, 12.5% concentration of the condition medium and the remaining complete medium). For the positive control, cells were cultured in fresh media and incubated for the same period as that for the conditioned media sample. After the incubation period (1 day and 3 days), the conditioned medium was aspirated, and the cells were rinsed with PBS. Subsequently they were incubated in complete media containing WST-1 (Invitrogen) solution with 1:10 dilution for 3 h to measure the cell viability. The optical density of the resultant medium was analyzed using a plate reader (Biotek Gen 5, Santa Clara, CA, USA) at 440 nm. The cell viability was reported in the form of relative growth rate (RGR), which can be calculated using eqn (2)

$$\text{GR} = \left(\frac{\text{OD}_{\text{sample}}}{\text{OD}_{\text{control}}} \right) \times 100 \quad (2)$$

where $\text{OD}_{\text{sample}}$ and $\text{OD}_{\text{control}}$ are the optical density of the sample, and the control determined with a plate reader. The obtained data from the WST (water-soluble Tetrazolium) assay were subjected to statistical analyses (using standard analytical technique of variance (ANOVA) with Tukey's test). The differences were considered significant at $p < 0.05$. All the data presented are from the results of at least four samples.

The viability of the cells was studied with live/dead assay by staining with Calcein AM (Thermo Fischer Scientific, India) and Ethidium Homodimer dye (Thermo Fischer Scientific, India). This is followed by imaging of the samples using an inverted epi-fluorescence microscope (Olympus IX-53, Tokyo, Japan). The cell morphology was visualized by fixing the cells with 3.7% formaldehyde in PBS solution at room temperature for 30 min, followed by PBS washing. The cell membrane was



permineralized by incubating in a 0.2% Triton X-100 solution (Sigma, Germany) for 8 min at room temperature, followed by PBS washing. The washed cells were incubated with 25 $\mu\text{g mL}^{-1}$ Alexa Fluor 488 (Invitrogen) for 30 min at room temperature for actin staining. The cell nuclei were stained by incubating in 0.2 $\mu\text{g mL}^{-1}$ DAPI (Invitrogen) for 3 min at room temperature. The stained cells were examined using an inverted epifluorescence microscope.

C. Results and discussion

C.1 Powder characterization

Fig. 1(a) and (b) depict the SEM images of the Zn powder at different magnifications, showcasing the nearly spherically shaped powder particles with faceted surfaces surrounded by numerous satellites (small particles surrounding the larger ones). The formation of satellites is attributed to the collision between solidifying droplets caused by turbulent flow inside the atomization chamber.^{57,58} The particle size distribution plot (shown in Fig. 1(c)) reveals an average powder particle size in the range of $11 \pm 6 \mu\text{m}$. The X-ray diffraction (XRD) pattern of Zn powder shows the presence of peaks corresponding to the *hcp* (hexagonally closed-packed structure) phase (Fig. 1(d)).

C.2 Sintering and densification

The density of the SPS Zn sample was calculated to be $\sim 7.1 \text{ g cc}^{-1}$, with a relative density of $\sim 99.4\%$. This indicates that the Zn powder was almost fully densified during the sintering process. According to Abedi *et al.*,⁵⁹ in metallic samples, a homogeneous temperature distribution is achieved in all directions, resulting in higher consolidation rates compared to ceramic samples.^{60–62} Fig. 2 shows the sintering cycle plot (in terms of piston displacement vs. time and temperature vs. time). Sintering takes place in distinct stages until final densification of the powders and the sintering

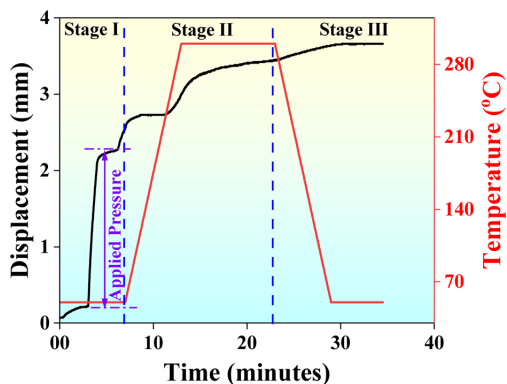


Fig. 2 Plot showing the spark plasma sintering cycles observed due to piston displacement and temperature as a function of time for the Zn samples.

stages are briefly outlined as follows: during stage I, a gradual pressure of 50 MPa was applied to the powder without any increment in temperature. The application of pressure allows the powder particles to rearrange and move closer to each other, leading to a reduction in pore size.

Considerable piston displacement with an average rate of 0.35 mm min^{-1} was observed. In the next stage II, the temperature increased quickly, resulting in the generation of plasma between the powder particles. The particle surface was cleaned, and thermally activated densification takes place.⁶³ A piston displacement of 0.1 mm min^{-1} was observed during this stage. The temperature changes from $50 \text{ }^\circ\text{C}$ to $300 \text{ }^\circ\text{C}$ at the rate of $50 \text{ }^\circ\text{C min}^{-1}$ with a dwell time of 10 min, which leads to grain boundary diffusion, necking, and pore closure. In the last stage III, the cooling stage, the temperature decreases from $300 \text{ }^\circ\text{C}$ to $50 \text{ }^\circ\text{C}$ at a rate of $50 \text{ }^\circ\text{C min}^{-1}$. The piston displacement reduces to 0.01 mm min^{-1} , and this piston motion is attributed to the thermal shrinkage of the sample and this shrinkage doesn't play any role in densification.⁶⁴

C.3 Structural characterization

Fig. 3 illustrates the XRD pattern of pure Zn powder and bulk samples. The XRD patterns show the presence of a single-phased microstructure with the peaks corresponding to the *hcp* phase. No additional peaks corresponding to other phases are observed within the deductible limits suggesting that no oxides are formed during sintering. The peak intensity for the powder is observed at $(10\bar{1}1)$. On the other hand, the peak intensity is observed at (0002) for the bulk samples. The change in the peak's intensity can be attributed to the preferred orientation, where the crystallites (in a polycrystalline material) align in a specific crystallographic plane during the fabrication process, such as casting, sintering, *etc.*^{65–68} During SPS, Zn powder is subjected to high temperature and pressure, and the individual particles start bonding and densifying. During this process, the crystallites may reorient themselves in a specific fashion. Several factors including sintering conditions, particle

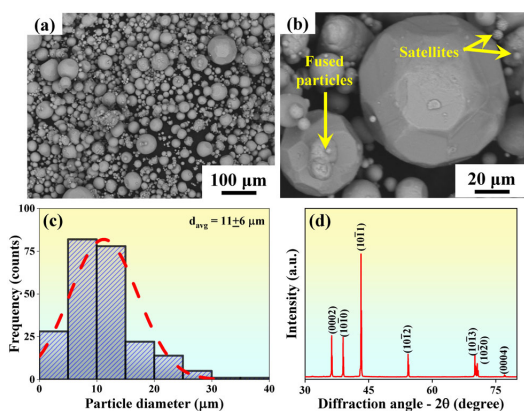


Fig. 1 Scanning electron microscopy images showing the morphology of the Zn powder at (a) lower and (b) higher magnifications. (c) Particle size distribution plot showing the average powder density of the Zn powders, and (d) X-ray diffraction pattern of the Zn powder showing the presence of the hexagonally closed packed structure.



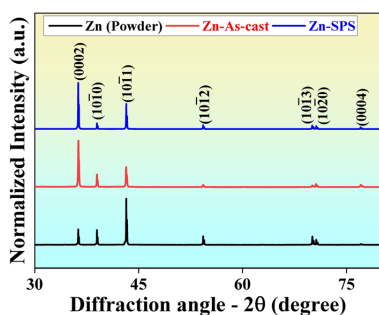


Fig. 3 The X-ray diffraction patterns for the as-received zinc powder and the bulk Zn samples fabricated by both casting and SPS processes.

morphology, mechanical deformation, cooling rate, *etc.*, can affect the preferred orientation during processing. Similarly, during casting, when molten material solidifies into a polycrystalline structure, the cooling rate and solidification conditions can influence the alignment of crystallographic planes within the newly formed grains. In materials with a *hcp* structure, the grains preferred orientation is based on their *c/a* ratio, and Zn has a *c/a* ratio greater than 1.633. Therefore, the basal plane [0002] is parallel to the surface.⁶⁹

C.4 Bulk texture studies

The X-ray texture goniometer was utilized to measure the bulk texture of both the as-cast and SPS samples. The Schulz reflection method was used to measure the total six pole figures. The basal (0002), prismatic (1010), and (1120) pole figures are shown in Fig. 4. The (0002) pole figure shows the highest misorientation random distribution (MRD) value of ~ 17 for the cast sample, but it reduces to ~ 3 for the SPS Zn sample. In the as-cast condition, the (0002) pole figure shows slightly off-basal orientation with other texture components, whereas in the SPS sample, centered basal orientation with lower intensity is observed. During SPS, the rapid heating and cooling cycle, along with the application of pressure, leads to recrystallization, grain growth, and plastic deformation. These processes tend to disrupt any initial texture present in the starting powder. The uniform orientation achieved during SPS can

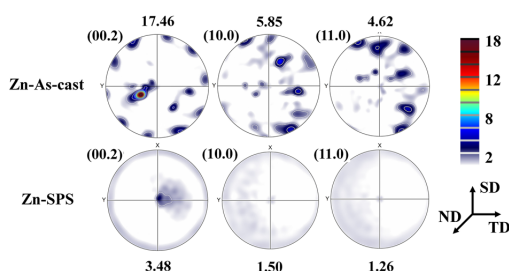


Fig. 4 Pole figures measured by X-ray texture goniometer for the as-cast and spark plasma sintered Zn samples along the following planes: planes (0002), (1010), and (1120).

contribute to a more isotropic microstructure and mechanical properties. The interdependence theory suggests that fine and equiaxed grains obtained due to grain refinement during sintering show a weak texture.^{35,70}

C.5 Microstructural characterization

The surface morphology of the as-cast and SPS samples was characterized through optical and scanning electron microscopy, and the corresponding images are presented in Fig. 5. A non-uniform microstructure, along with a significant number of twins (yellow arrows), is observed in the as-cast samples (Fig. 5(a) and (b)). Furthermore, some fine grains are observed within the coarse grains (red arrows) in Fig. 5(b), which may be due to recrystallization. Fig. 5(c) and (d) illustrate the microstructure of the SPS Zn samples. The samples were sintered adequately, as there were no visible sintering defects (like cracks and pores at the considered magnification), and thus, the density of the SPS Zn samples should be closer to the theoretical density ($\rho = 7.1 \text{ g cc}^{-1}$). Enhanced densification during the SPS process is attributed to the plastic deformation of powder particles and the application of both temperature and pressure during the sintering process. According to Chaim *et al.*,⁷¹ as the applied stress reaches the yield strength, the densification takes place by plastic deformation. Powder particle size significantly influences densification, with larger particles undergoing plastic deformation under external pressure while smaller particles melt and evaporate locally during the process.⁷² The microstructure appears to be a regular arrangement of large grains (circular shape) of uniform size.⁷³ The larger grain may contain some finer grains along with their boundaries considered to be sub-grain boundaries.

The detailed sintering mechanism and the effect of the process parameter on the microstructure can be explained as follows: the applied heating rate of $50 \text{ }^\circ\text{C min}^{-1}$ during the second stage of sintering (from $50 \text{ }^\circ\text{C}$ to $300 \text{ }^\circ\text{C}$) induces a non-equilibrium condition, promoting the formation of fine recrystallized grains while minimizing the grain growth. Localized Joule

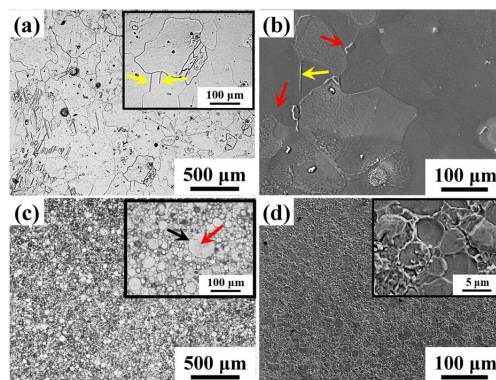


Fig. 5 (a) and (c) Optical and (b) and (d) scanning electron microscopy images of the zinc samples fabricated by (a) and (b) casting and (c) and (d) spark plasma sintering processes.



heating at particle contact points enhances densification by increasing the driving force for diffusion, thereby restricting excessive grain coarsening.^{74–77} Moreover, the pulsed DC current in SPS induces localized heating at grain boundaries promoting sintering through grain boundary diffusion, while the short pulse duration effectively limits grain coarsening. This controlled diffusion mechanism leads to the formation of a finer and more uniform grain structure, further enhancing the material's mechanical properties.⁷⁸ The application of 50 MPa uniaxial pressure throughout the sintering process facilitates plastic deformation, leading to a significant increase in dislocation density at grain boundaries. This, in turn, activates dynamic recrystallization (DRX), where newly nucleated grains replace deformed ones, resulting in a refined microstructure. Additionally, DRX disrupts the initial texture, contributing to a more isotropic grain orientation.⁷⁹ These mechanisms collectively contribute to the superior microstructural characteristics of SPS-processed Zn, distinguishing it from conventionally cast counterparts.

For a better understanding of the crystal orientation and grain boundary characteristics, electron backscatter diffraction (EBSD) analysis was carried out on the Zn samples (Fig. 6). The orientation map developed on the sample surface represents the crystal direction normal to the surface and is referred to as the inverse pole figure (IPF). Most of the grains in the SPS samples are red-colored, suggesting that these grains have their *c*-axes positioned close to the specimen's normal direction, thus indicating that their basal planes {0001} are nearly parallel to the surface. Fig. 6(b) and (e) show the grain boundaries superimposed image quality (IQ) map for the bulk Zn samples. The blue lines in the IQ maps indicate high-angle grain boundaries (HAGBs) with angles exceeding 15°, while red and green lines denote low-angle grain boundaries (LAGBs) characterized by angles below 15°. The as-cast sample displays around 33% LAGBs, while the SPS sample shows ~15% LAGBs. Notably, in the SPS sample, LAGBs primarily appear in sub-grains within coarse grains, while fine grains tend to be relatively free of LAGBs. The SPS samples have smaller grains

(~19 μm) compared to the as-cast sample (~150 μm) with more HAGBs. Areas with fine-grain regions show more HAGBs, possibly due to the strained concentration. The transition from LAGBs to HAGBs is believed to occur mainly during dynamic recrystallization, which is triggered by the combination of applied pressure and temperature observed during the SPS process. Hence, a bimodal grain structure characterized by the coexistence of both coarse and fine grains is observed. On the other hand, the as-cast samples exhibit a predominantly coarser grain with pronounced twin formation. These differences in the microstructural characteristics between the as-cast and SPS samples highlight the distinct variations in the processing methods and thermal conditions/variations observed during the respective manufacturing processes. While the SPS process facilitates dynamic recrystallization and grain refinement, the as-cast samples retain a coarse grain structure with evident twin boundaries.

C.6 Mechanical testing

Fig. 7 depicts the compressive stress–strain and strain–hardening plots of the as-cast and SPS samples. The yield strength (0.2% PS, YS) observed for the SPS sample was significantly higher (115 ± 4 MPa) than that of the cast sample (60 ± 16 MPa). However, the ultimate compressive strength (UCS) observed for the as-cast sample was found to be in the range of 274 ± 37 MPa, which is higher than that of the SPS samples (191 ± 6 MPa). The increase in the YS of the SPS sample is due to the formation of micron and sub-micron grain during the SPS process. The strengthening mechanism during SPS can also be explained with the help of Hall–Petch equation according to which fine and uniform grains offer higher strength as compared to coarse-grained as-cast samples as explained below:

$$\sigma_{\text{yield}} = \sigma_0 + kd^{-1/2} \quad (3)$$

$$\sigma_{\text{yield}} \propto d^{-1/2} \quad (4)$$

where σ_{yield} is the yield strength of the material, σ_0 is the lattice friction stress, k is the Hall–Petch coefficient, and d is the average grain size of the material. The grain size plays a crucial role in determining the yield strength of materials. Specifically, a finer grain size (~19 μm) enhances yield strength (~115 MPa), whereas a coarser grain structure, such as in cast Zn (~150 μm), results in lower yield strength. This occurs because materials with

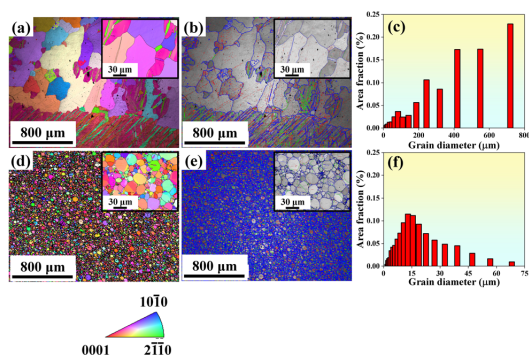


Fig. 6 Electron backscattered diffraction results showing the inverse pole figure (IPF) maps, image quality (IQ) maps, and the grain size distribution plot of the (a)–(c) as-cast and (d)–(f) spark plasma sintered samples, respectively.

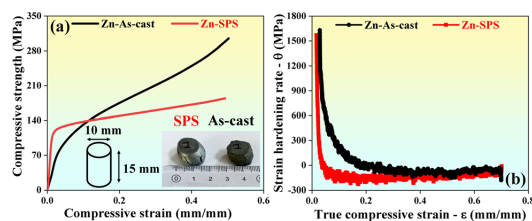


Fig. 7 (a) True compressive stress and strain and (b) strain hardening rate vs. strain plots for the bulk Zn samples fabricated by casting and spark plasma sintering.



smaller grains have a higher density of grain boundaries, which impedes dislocation movement and increases the energy required for dislocations to move into adjacent grains. As a result, the yield strength of SPS samples is higher than that of the cast samples. However, the trend is reversed for ultimate compressive strength; SPS samples exhibit lower strength (~191 MPa), whereas cast samples demonstrate higher strength (~274 MPa). This is because grain boundaries, while restricting dislocation motion, also serve as weak points where cracks initiate, leading to brittle fracture before significant plastic deformation can occur. In hexagonal close-packed (HCP) materials, deformation occurs through a combination of dislocation slip and twinning. In as-cast Zn samples, the presence of larger grains and strong basal texture (as discussed in Section 3.4) facilitates twinning as a dominant deformation mechanism. Twinning allows additional strain accommodation at higher stress levels, leading to an increase in ultimate compressive strength (UCS).⁸⁰ During SPS, recrystallization restricts the twin formation due to the large obstructive effect of grain boundary on the twinning shear.⁸¹ As a result, deformation is primarily accommodated by dislocation slip, which enhances yield strength but limits strain-hardening mechanisms, leading to a lower UCS compared to that for the cast Zn.

Under the SPS condition, the deformed sample showed uniform bulging, whereas in the as-cast condition, irregular deformation is observed (Fig. 7(a) inset). Bulging generally refers to increased absorption of energy due to uniform deformation of load with less twin activity. Fig. 7(b) shows the strain hardening rate (θ) vs. true strain behavior under compression. In the SPS sample, the strain hardening rate decreases rapidly with increasing strain, whereas in the as-cast condition, it reaches the plateau. The extended strain hardening behavior in the as-cast sample might be due to the presence of the

coarse-grained microstructure and the formation of twins. Table 1 summarizes the mechanical properties of SPS Zn, along with a comparison to previously reported studies on pure Zn and its alloys fabricated using various manufacturing methods.

C.7 Immersion study and electrochemical behavior

C.7.1 Immersion study. The immersion behaviors of the as-cast and SPS samples were analyzed according to ASTM G31-72 standards, where polished Zn samples were immersed in simulated body fluid (SBF) under simulated physiological conditions for 7, 14, and 21 days. During the initial 7 days of immersion, a thin, uniform whitish layer formed on the SPS Zn surface. As the immersion time increased, this layer gradually thickened, and degradation products began to accumulate unevenly, as shown in Fig. 8. After 7 days, the degradation rate of the SPS Zn sample was 0.1325 mm per year, which is consistent with previously reported values.⁸² At extended immersion periods of 14 and 21 days, the degradation rates further decreased to 0.0965 mm per year and 0.075 mm per year, respectively. This gradual reduction in degradation rate is attributed to the formation of a thicker protective layer, which acts as a barrier, limiting ion exchange between the sample surface and the surrounding medium. However, in the initial stages, the weaker and unstable oxide layer undergoes continuous breakdown, leading to surface void formation and progressive degradation.

The degradation mechanism of Zn in SBF can be explained as: during the initial stages of electrochemical corrosion, upon exposure to simulated body fluid (SBF), Zn begins to dissolve, initiating oxygen reduction at the cathode according to the following anodic and cathodic reactions (5) and (6):



Table 1 A comparison of the mechanical properties of pure zinc and zinc-based alloys/composites fabricated using different fabrication techniques. MR represents the manufacturing route employed, GM – grain morphology, ρ – density, H – hardness, YS – yield strength in compressive mode unless mentioned as tensile mode, US – ultimate strength in compressive mode unless mentioned as tensile mode, E – elastic modulus (GPa), and Ref. – reference article

Material designation	MR	GM		ρ /porosity	H	YS (MPa)	US (MPa)	E (GPa)	Ref.
		Size (μm)	Shape						
Pure Zn	WAAM	14 \pm 5	Equiaxed	—	35 \pm 2 HV _{0.3}	—	—	—	89
	Wrought	11 \pm 4	—	—	41 \pm 1 HV _{0.3}	—	—	—	—
Ti-5Zn	Hot Pressing	—	—	—	158 \pm 18 HV	651 \pm 3	—	17 \pm 2	90
Ti-10Zn	—	—	—	—	—	934 \pm 32	—	20 \pm 2	—
Ti-20Zn	—	—	—	—	390 \pm 43 HV	1136 \pm 10	—	27 \pm 2	—
Ti-30Zn	—	—	—	—	270 \pm 35 HV	—	—	4 \pm 1	—
Zn-16HAp (wt%)	SPS	—	—	18%	24 \pm 5 HV ₅	46 \pm 3 (Tensile)	65 \pm 4 (Tensile)	—	53
CP Zn	—	—	—	20 \pm 2%	29 HV _{0.3}	43 \pm 2	—	—	51
FP Zn	—	—	—	21 \pm 2%	17 HV _{0.3}	31 \pm 5	—	—	91
Zn	—	—	—	—	43 \pm 2	53 \pm 17	171 \pm 13	—	—
Zn-5Ge	Cast	—	—	—	38 \pm 0.6 HV _{0.1}	29 \pm 3 (Tensile)	34 \pm 6 (Tensile)	—	92
	Hot rolled	—	—	—	39 \pm 1 HV _{0.1}	84 \pm 3	153 \pm 3	—	—
Pure Zn	Cast	150	Coarse	7 g cc ⁻¹	—	60 \pm 16	274 \pm 37	—	Present work
	SPS	19	Fine/equiaxed	7.1 g cc ⁻¹	—	115 \pm 4	191 \pm 6	—	—
Human cortical bone	—	—	—	5–10%	—	80–120	—	3–30	93

WAAM – wire arc additive manufacturing; Hap – hydroxyapatite; SPS – spark plasma sintering; CP – coarse powder (600–850 μm); FP – fine powder (40–100 μm).



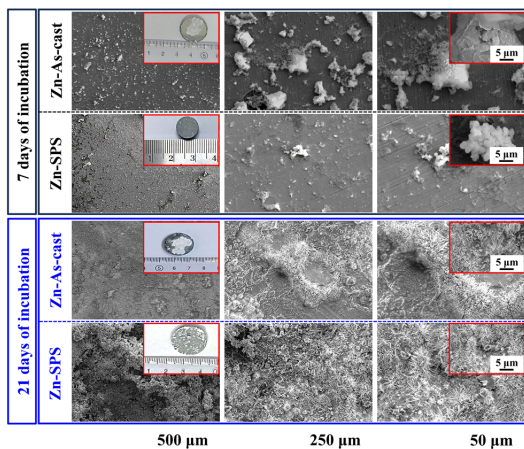
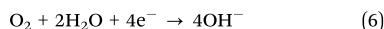
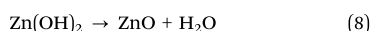
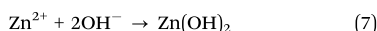


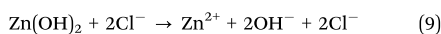
Fig. 8 Scanning electron microscopy images of the spark plasma sintered Zn samples after 7 days and 21 days of immersion in simulated body fluid (SBF). The insets show macroscopic views and high-magnification images. After 7 days of immersion, a thin corrosion layer forms with localized deposits, while after 21 days, a thicker, more uniform degradation layer develops, indicating surface stabilization.



The by-product OH^- of the cathodic reaction increases the pH value, according to the Pourbaix diagram;⁸³ as the pH of the electrolyte increases, zinc ion (Zn^{2+}) reacts with the hydroxide (OH^-) ion by dehydration reaction to form $\text{Zn}(\text{OH})_2$, which further transforms into a thermodynamically stable zinc oxide (ZnO) layer according to reaction (7) and (8):



However, the zinc oxide layer tends to dissolve back into Zn^{2+} due to the leaching action of aggressive Cl^- competing with the surface hydroxyl groups in $\text{Zn}(\text{OH})_2$ according to reaction (9), resulting in the formation of ZnCl_2 :



After 24 h of incubation, a thick corrosion product forms on the sample's surface. The change in surface morphology probably influenced both mass transport and the ionic diffusion. Thus, the corrosion mode varies, and the degradation of pure Zn accelerates progressively with the co-existence of calcium (Ca^{2+}) and phosphate (PO_4^{3-}) ions, leading to the formation of calcium phosphate precipitates according to reactions (10)–(12).⁸⁴ A schematic representation of the corrosion mechanism of pure Zn immersed in a simulated body fluid solution is shown in Fig. 9.

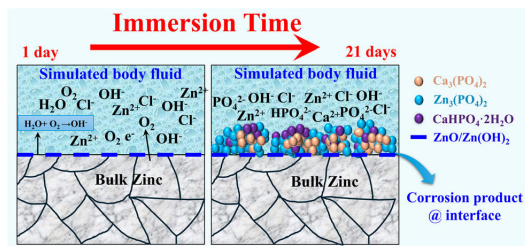
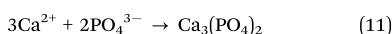
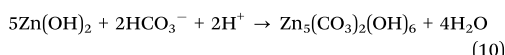
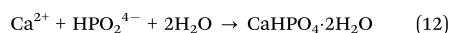


Fig. 9 Schematics illustrating the corrosion mechanism in pure Zn immersed in simulated body fluid for long term degradation studies.



C.7.2 Open circuit potential studies. The bulk Zn samples fabricated by casting and SPS were immersed for 1 h in simulated body fluid (SBF) to examine the potential variation in terms of OCP. From Fig. 10, it is evident that there is a decrease in potential (E_{OCP}) upon initial immersion in the solution and the potential stabilizes between 1400 to 1800 s for both the sample conditions. The SPS Zn sample demonstrated a final OCP value of -1.03 V, which is slightly more active than the as-cast Zn sample (-1.02 V). The active behavior of both samples could be attributed to the deposition of corrosion products in the SBF media and the dissolution of the corrosion film developed on the sample surface.⁸⁵ The variation in the OCP stabilization between the as-cast and SPS Zn samples is mainly due to the microstructural variations among the samples as already discussed in Section 3.5. The refined grain structure of the SPS Zn, with increased grain boundary area, accelerates the initial surface reactions, leading to rapid passivation and earlier stabilization of the OCP.^{86,87} Additionally, the disruption of the initial texture, potentially enhances the uniformity and stability of the passive film.⁸⁸

This, in turn, promotes a more stable electrochemical response compared to as-cast Zn. The formation and stability of surface corrosion products further influence the OCP

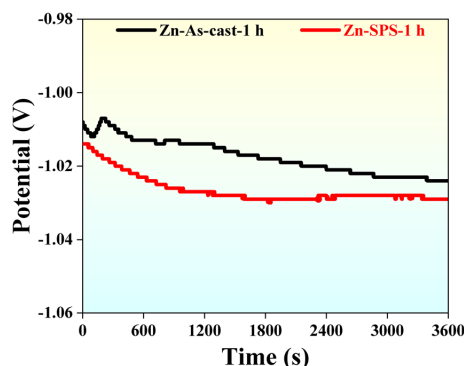


Fig. 10 Open-circuit potential (OCP) behavior of Zn as-cast and SPS samples for an exposure period of 1 h in SBF.



Table 2 Table furnishing the polarization data for the as-cast and SPS zinc samples immersed in simulated body fluid environments

Sample condition	E_{corr} (V) vs. SCE	I_{corr} ($\mu\text{A cm}^{-2}$)	I_{p} ($\mu\text{A cm}^{-2}$)	E_{pp} (V) vs. SCE	E_{pb} (V) vs. SCE	CR (mm per year) $\times 10^{-4}$
As-cast	-1.21 ± 0.02	8.61 ± 0.11	62.0 ± 3.1	-1.16 ± 0.03	-1.06 ± 0.17	0.60 ± 0.08
SPS	-1.20 ± 0.04	12.16 ± 0.90	52.9 ± 1.2	-1.15 ± 0.03	-1.03 ± 0.23	0.88 ± 0.05

behavior, as the SPS Zn surface tends to form a more homogeneous and protective oxide layer at an early stage of immersion (Table 2).

C.7.3 Potentiodynamic polarization studies. Fig. 11 illustrates the potentiodynamic polarization (PDP) curves for the Zn samples (fabricated by casting and SPS). The corrosion parameters such as corrosion current (I_{corr}), and corrosion potential (E_{corr}) were analyzed *via* the Tafel extrapolation method,^{94–96} and the values are tabulated in Table 2. The E_{corr} values of both the as-cast and SPS Zn samples are similar, but the values become significantly active when compared to the OCP values since the Tafel measurements were conducted after the OCP measurements. During the OCP measurements, no external current was supplied, and the equilibrium values were recorded. However, during the Tafel measurements, the samples were already exposed to the SBF environment. In this environment, Zn reacted with Cl, leading to degradation and resulting in a lower potential.

The anodic branch of the Zn samples shows an active-to-passive transition in SBF. Initially, these samples undergo typical active anodic dissolution, followed by passivation at higher potentials. Due to the formation of a passive film, the current density remains constant during the passive region (as seen in Fig. 11). However, after breakdown potential (E_{pb}), the current increases significantly, indicating transpassive corrosion. From the Tafel curve, the corresponding values of I_{corr} , E_{corr} , I_{p} (passivation current density), E_{pp} (passivation potential), E_{bp} (breakdown potential), and corrosion rate (CR)

are calculated and are tabulated in Table 2. The Tafel extrapolation data show that both the as-cast and SPS zinc samples exhibit a similar trend in the cathodic region, with E_{corr} observed to be -1.21 and -1.20 V and I_{corr} measured at 8.61 and $12.16 \mu\text{A cm}^{-2}$, respectively. Upon increasing the potential, a stable oxide layer forms, indicating the passive regime. The passivation potential (E_{ap}) was recorded as -1.16 and -1.15 V for the as-cast and SPS samples, respectively. The passivation current density (I_{p}) was recorded as 62.0 and $52.9 \mu\text{A cm}^{-2}$ for as-cast and SPS samples, respectively. The stable passivation current in this regime suggests the formation of a passivation layer with a lower I_{p} indicating better corrosion resistance. Furthermore, the current starts to increase in both samples at the breakdown of the passive layer. The breakdown potentials (E_{pb}) for the as-cast and SPS samples are observed to be -1.06 and -1.03 V, respectively.

Such differences in potential likely arise from the grain size differences (a smaller grain size of $19 \mu\text{m}$ is observed for the SPS Zn sample leading to a higher density of grain boundaries per unit volume, contrasting with the larger grain size of $150 \mu\text{m}$ observed in the as-cast condition). The grain boundaries, due to their elevated energy state and altered chemical composition, are inherently more susceptible to corrosion than the bulk material. Furthermore, the presence of fine grains facilitates higher hydrophilicity,⁹⁷ increased diffusion, and deeper penetration into the material, potentially leading to localized pitting, as evident from SEM micrographs (Fig. 12). Additionally,

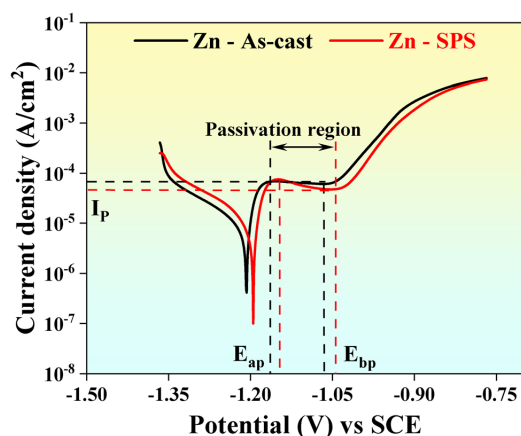


Fig. 11 Potentiodynamic polarization curves obtained after immersion in simulated body fluid for 1 h.

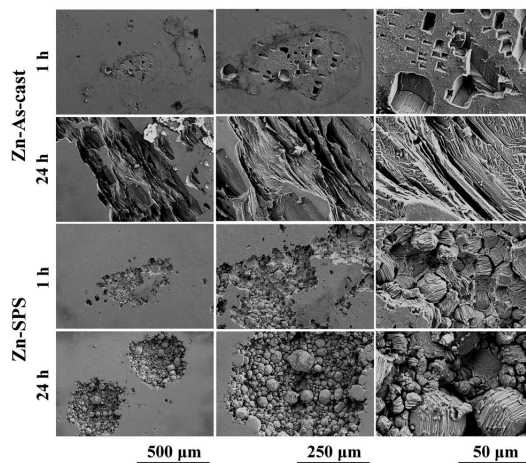


Fig. 12 Scanning electron microscopy images showing the microstructure of the zinc samples after potentiodynamic polarization immersion in simulated body fluid.



Table 3 The polarization data for the as-cast and SPS zinc samples immersed in simulated body fluid as a function of time, compared with other published reports

Material	Manufacturing route	Electrolyte	Degradation parameter				Ref.			
			Corrosion rate (mm per year)	Immersion time (days)	i_{corr} ($\mu\text{A cm}^{-2}$)	E_{corr} (V) vs. SCE				
Pure Zn	Extrusion	SBF	0.048	56	3.241	-1.033	85			
		SBF + Gln	0.023		4.135	-1.055				
		SBF + Glucose	0.014		5.675	-1.099				
		SBF (Tris-HCl)	0.033		4.119	-1.024				
		SBF (Tris-HCl) + Gln	0.034		2.951	-1.004				
		SBF (Tris-HCl) + Glucose	0.027		4.815	-0.999				
Pure Zn	Wrought	SBF	0.30 ± 0.10	—	6 ± 1	-1.13 ± 0.16	98			
Pure Zn	WAAM	—	0.45 ± 0.20	—	9 ± 1	-1.18 ± 0.03				
Zn-1Mg	Cast	SBF	—	—	1.2	-0.98	99			
Zn-1.5Mg			—	—	8.8	-0.93				
Zn-3Mg			—	—	7.4	-0.93				
Mg-0.5Zn			—	—	131 ± 6	-1.87 ± 0.01				
Mg-1Zn	Cast	SBF	—	—	124 ± 10	-1.83 ± 0.01	100			
Mg-2Zn			—	—	115 ± 10	-1.81 ± 0.02				
Mg-3Zn			—	—	102 ± 8	-1.71 ± 0.04				
Ti-5Zn			Hot press sintering	SBF	—	—		0.692	-0.187	101
Ti-10Zn					—	—		0.975	-0.202	
Ti-20Zn	—	—			0.741	-0.178				
Ti-30Zn	Hot press sintering	SBF	—	—	3.631	-0.245	101			
CP Zn			SPS	SBF	0.61 ± 0.11	14		—	—	102
FP Zn	—	—			0.75 ± 0.12		—	—		
Zn16HAP	SPS	SBF	0.41	14	—	—	103			
Zn-0HAP	SPS	Hank solution	0.073 ± 0.042	1.5 h	4.90 ± 2.810	-0.942 ± 0.07	104			
Zn-1HAP			0.327 ± 0.050		21.07 ± 3.25	-1.281 ± 0.03				
Zn-5HAP			0.630 ± 0.011		39.12 ± 0.66	-1.274 ± 0.01				
Zn-10HAP			0.856 ± 0.031		51.04 ± 1.80	-1.290 ± 0.01				
Pure Zn	As-cast	SBF	0.0179 ± 0.002	1 h	9.43 ± 0.11	-1.21	Present work			
			0.0017 ± 0.002	24 h	8.73 ± 0.42	-1.09				
	0.0025 ± 0.001		1 h	12.93 ± 0.9	-1.2					
	0.0016 ± 0.002		24 h	8.43 ± 0.27	-1.07					

WAAM – wire arc additive manufacturing; SBF – simulated body fluid; Gln – glutamine.

it is worth noting that the texture of the samples also plays a significant role in influencing their corrosion behavior.⁸⁸ As discussed above, Fig. 11 indicates the stable passivation layer between -1.15 V to -1.05 V in both the as-cast and SPS Zn samples; beyond that, both the samples indicate the dissolution of the passive layer and the inner material is directly exposed to the corrosive environment increasing the corrosion rate. As indicated above, with a decrease in grain size, an increase in corrosion rate was observed for the SPS sample. This disparity suggests a lower corrosion rate (CR) attributed to the formation of a stable oxide layer, as depicted in Table 2, and the corrosion results of the present work with previously reported work are compared in Table 3.

Fig. 12 shows the SEM images and Fig. 13 shows the EDS images of the corroded Zn samples after 1 h and 24 h immersion time in SBF. The samples, after 1 h of polarization, show the localized form of corrosion with different pit sizes. The as-cast sample shows many pits of the uniform cross-section in a concentrated region/area; however, in the case of the SPS sample the corroded region spreads uniformly with the formation of deep grooves inside the pits (see the higher magnification image in Fig. 12) due to the larger density of grain boundaries. The SEM images reveal that the dissolution is more pronounced at grain boundaries, likely due to their higher

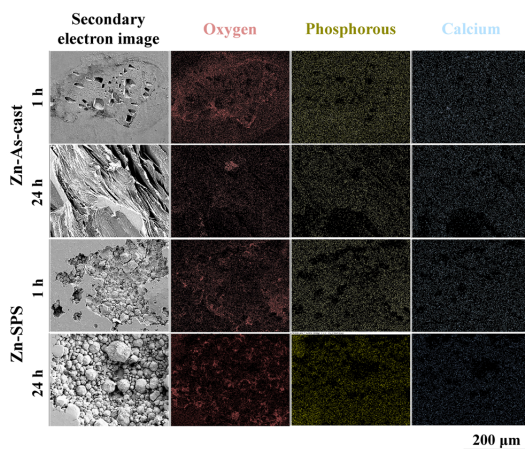


Fig. 13 Energy dispersive spectroscopy images showing the microstructure of the zinc samples after potentiodynamic polarization immersion in simulated body fluid.

activity at these boundaries. The regions adjacent to grain boundaries form micro-level galvanic couples, facilitating



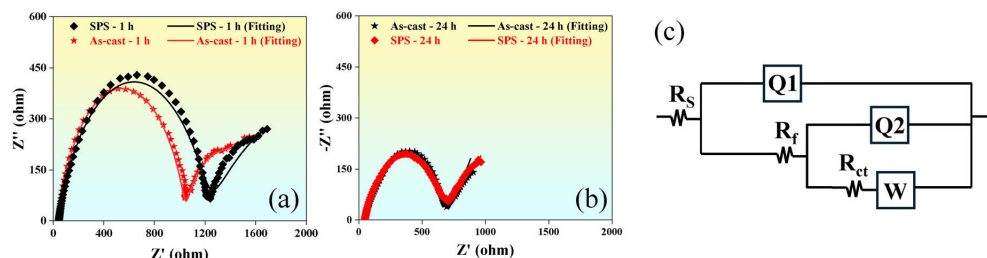


Fig. 14 Plots showing the electrochemical impedance spectroscopy (EIS) result of both the as-cast and SPS zinc samples: Nyquist plots of impedance spectra obtained after (a) 1 h and (b) 24 h of study in SBFs along with (c) the equivalent electrical circuit used to fit the EIS data using Zsimp software.

increased electron transfer and making them more susceptible to activation and localized corrosion.

Both the as-cast and SPS samples display similar electrochemical corrosion behavior but differ in corrosion morphology, likely due to the differences in their microstructural feature (mainly grain morphology), where finer grains are observed in the SPS samples compared to their as-cast counterparts.

C.7.4 Electrochemical impedance spectroscopy. Fig. 14 shows the electrochemical impedance spectroscopy (EIS) results of Zn samples immersed in SBF for 1 h and 24 h. From Fig. 14(a) and (b), all the Nyquist plots exhibited multiple arcs. Furthermore, the impedance response of the Zn samples after 1 h of immersion (Fig. 14(a)) exhibits a semi-circular loop in the high-frequency region followed by a circular arc in the low-frequency region and a straight line with a slope close to 1. Relatively, the impedance of samples after 24 h of immersion (Fig. 14(b)) shows a similar pattern with a varied degree of reaction resistance between the electrolyte and electrode interface. To analyze and fit the electrochemical data, an equivalent electrical circuit model consisting of $[R_s(Q_1(R_f(Q_2[R_{ct}W])))]$ is considered (Fig. 14(c)), where R_s represents the solution resistance, R_f and Q_1 denote the resistance due to the formation of the corrosion product film and the constant phase element for non-ideal capacitance induced by the corrosion product film respectively, R_{ct} is the resistance charge transfer, W represents the Warburg impedance, and Q_2 denotes the constant phase element for non-ideal capacitance induced by the double electrode layer. The values of Q and W can be calculated by using eqn (13) and (14):

$$Q = Y_0^{-1}(j\omega)^{-n} \quad (13)$$

$$W = Y_0^{-1}(j\omega)^{-0.5} \quad (14)$$

where Y_0 is a constant with units of $\Omega^{-1} S^n$ for Q and $\Omega^{-1} S^{0.5}$ for W , Q is used to obtain a better fit of experimental data, and

based on the value of n (-1 , 0 , and 1), it can be treated as the capacitance, resistance, and inductance respectively, ω is the angular frequency, and the j is the imaginary number equal to $\sqrt{-1}$.

According to Huang *et al.*,¹⁰⁵ the corrosion product covering the sample surface changes the surface condition of the electrode and acts as a time constant. Due to the formation of corrosion product (film) on the sample surface, resistance is induced, which effectively impedes the diffusion of ions during the electrochemical process, leading to the development of Warburg impedance.¹⁰⁵ A similar circuit was also used by Huang *et al.*¹⁰⁵ to study the early electrochemical characteristics of pure Zn in SBF. The fitted parameters obtained are shown in Table 4, where the solution resistance (R_s) value of the electrolyte is observed to be the same for all the samples. However, the R_f and R_{ct} values are very high ($1008 \Omega \text{ cm}^2$ and $790 \Omega \text{ cm}^2$, respectively, for the as-cast samples and $1180 \Omega \text{ cm}^2$ and $889 \Omega \text{ cm}^2$, respectively, for the SPS samples) during the first hour of the experiment, but these values decrease significantly after 24 h. Subsequently, the R_f and R_{ct} values reach $600 \Omega \text{ cm}^2$ and $653 \Omega \text{ cm}^2$, respectively, for the as-cast and $658 \Omega \text{ cm}^2$ and $257 \Omega \text{ cm}^2$, respectively, for the SPS Zn samples. The sharp decrease in R_f and R_{ct} values indicates a significant decline in the protective effectiveness of the corrosion product film and the bare metal surface, respectively.

C.8 In vitro bioactivity

Biological analysis is one of the important aspects of the Zn-based biomaterial as it degrades in a biological environment. In this study the cellular response to Zn was assessed by an indirect method wherein the response of cells to the leached degradation products was studied.

C.8.1 Cytocompatibility. The cytocompatibility of the Zn samples was evaluated by incubating cells in a conditioned

Table 4 Equivalent electrical circuit parameters of the as-cast and SPS zinc samples immersed in the simulated body fluid for 1 h and 24 h, respectively

Sample condition	$R_s \Omega \text{ cm}^2$	$R_f \Omega \text{ cm}^2$	$R_{ct} \Omega \text{ cm}^2$	$\text{CPE}_1 (Q_1) \mu\Omega^{-1} \text{ cm}^{-2} \text{ S}^n$	$\text{CPE}_1 (n_1)$	$\text{CPE}_2 (Q_2) \mu\Omega^{-1} \text{ cm}^{-2} \text{ S}^n$	$\text{CPE}_2 (n_2)$	$W \mu\Omega^{-1} \text{ cm}^{-2} \text{ S}^{0.5}$	Error (%)
Zn (as-cast)-1 h	40.39	1008	789.6	2.19×10^{-9}	0.8	2.5×10^{-3}	0.8	0.013	5.8
Zn (SPS)-1 h	41.96	1180	889	7.62×10^{-6}	0.76	6.6×10^{-4}	0.8	0.005	7.9
Zn (as-cast)-24 h	40.68	600	653	7.9×10^{-8}	0.8	2.4×10^{-5}	0.6	0.015	2.8
Zn (SPS)-24 h	42.13	658	257	1.94×10^{-5}	0.6	8.02×10^{-3}	0.72	0.017	7.5



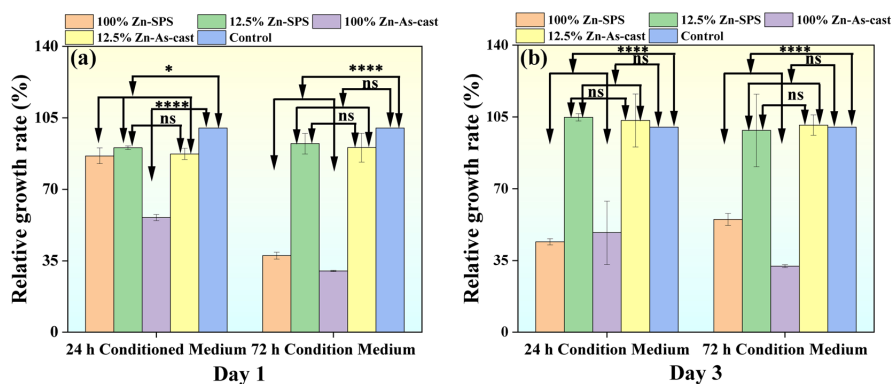


Fig. 15 Relative growth rate measured by WST assay for MC3T3-E1 cells cultured in 24 h and 72 h conditioned media for (a) 1 day and (b) 3 days. The significance level is taken as $p = 0.05$, i.e., $p < 0.05$ (*), $p < 0.01$ (**), $p < 0.001$ (***), $p < 0.0001$ (****) and $p > 0.05$, non-significant (ns), $n = 4$.

medium (indirect method). The growth of MC3T3-E1 pre-osteoblast cells was examined in terms of percentage relative growth rate after incubation in the conditioned medium for 1 day or 3 days, with fresh medium serving as the control. The viability of cells cultured in 1× and 8× extracts (100% and 12.5% concentration of conditioned medium) for 1 day and 3 days is depicted in Fig. 15. Fig. 15(a) illustrates the proliferation rate of cells in 24 h and 72 h conditioned media incubated for 1 day. Following an 8-fold dilution, no toxicity was detected, and the growth rates of both samples exhibited comparable results.¹⁰⁶ However, the response of cells in the 72 h conditioned media varies, demonstrating lower compatibility in the 100% extract. Conversely, the response of cells in the 8-fold dilution was favorable. Fig. 15(b) depicts cell proliferation after 3 days of incubation. The relative growth rate in 100% extract for both 24 h and 72 h conditioned media exhibited a significant decrease.

However, for the 8-fold diluted conditioned media, no toxicity was observed, and the growth rate was comparable to that of the control for both 24 h and 72 h conditioned media.

A live-dead assay was performed to further evaluate toxicity induced by the leachates from samples. Fig. 16 depicts the live-dead assay result, showing live cells in green color and dead cells in red color. 8-Fold dilution of both the samples showed a minimal number of dead cells for both day 1 and day 3 compared to live cells, confirming the cytocompatibility. It also depicts an increased number of cells on day 3 compared to day 1 in both samples confirming cell proliferation. In the case of 100% extract-conditioned media samples, most of the cells were detached after death, which agrees with the WST assay results. Cellular morphology was characterized by using fluorescence microscopy. Micrographs after day 1 and day 3 of incubation in conditioned media are shown in Fig. 17, where a well-developed cellular morphology with uniformly distributed active fibers is seen

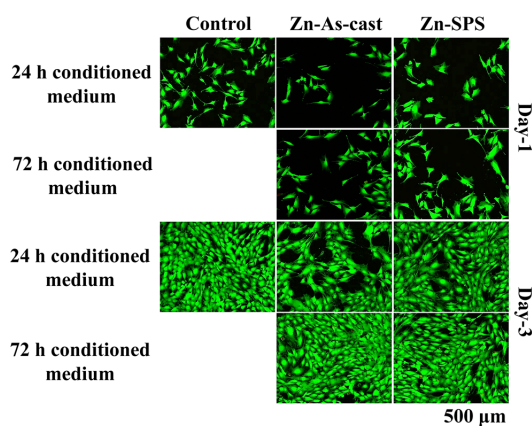


Fig. 16 Representative live/dead stained images of MC3T3-E1 cells treated with conditioned medium (8×) of the as-cast and SPS samples for day 1 and 3 where the live cells are depicted in green while dead cells are depicted in red. Cells cultured in fresh complete media act as the control.

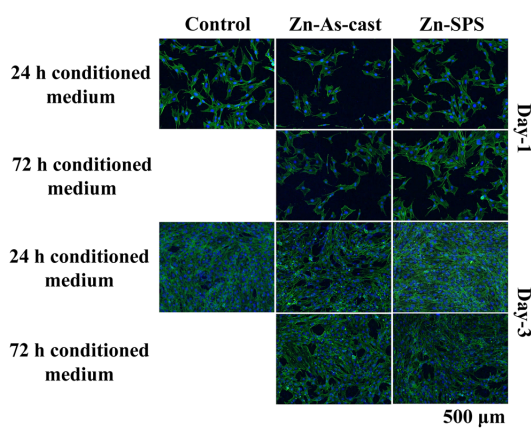


Fig. 17 Representative fluorescent images of MC3T3 cells treated with condition media at day 1 and 3 showing the actin filaments (green) and nuclei (blue) (control represents cell treated with fresh media).



when exposed to 8-fold conditioned media. In both samples, the cellular morphology exhibits good spreading and appears like that of the control samples, which further corroborates the nontoxicity of the 8-fold dilution condition in both samples. In the case of the 100% conditioned samples (both cases), they showed hampered/stressed morphologies. Based on the above study it can be concluded that both the samples exhibited similar and favorable cytocompatibility. At 8-fold dilution, no toxicity was observed, with healthy cell proliferation and morphology comparable to the control. In contrast, 100% of extract-conditioned media showed reduced viability and stressed morphology. These findings confirm that both SPS and as-cast Zn samples exhibit favorable biocompatibility under $8\times$ dilution, making them suitable for potential biomedical applications.

D. Conclusion

The present study systematically compared the microstructural, mechanical, corrosion, and biological properties of SPS-processed Zn with its cast counterpart. Based on this systematic investigation, the following main conclusions are drawn:

- SPS samples have much lower MRD values than their as-cast counterparts. The (0002) pole figure MRD drops from ~ 17 in the as-cast sample to ~ 3 for the SPS condition due to rapid heating, cooling, and pressure, causing recrystallization and grain growth.
- EBSD analysis reveals that the SPS samples have an average grain size of $19\ \mu\text{m}$, much smaller than that of the as-cast samples.
- The compressive yield strength of the SPS Zn samples notably increased to 115 MPa compared to the as-cast samples.
- Electrochemical analysis and long-term immersion studies collectively demonstrate that SPS Zn exhibits controlled and gradual degradation in simulated body fluid, similar to that of the cast-Zn. In addition, the formation of a stable and protective corrosion product layer is exhibited, supporting its suitability for biodegradable implant applications.
- The SPS samples exhibit cell viability and proliferation that are like their as-cast Zn counterparts. When exposed to leachates at a dilute concentration ($8\times$ dilution of conditioned media), the MC3T3 cells exhibited cell viability that was like that of fresh medium but lower viability for undiluted conditioned media.
- Cytocompatibility studies confirmed that both SPS and cast Zn support cell viability and proliferation, particularly at diluted concentrations.
- Given its refined microstructure, enhanced mechanical performance, and stable degradation behavior, SPS Zn emerges as a promising candidate for biomedical applications, particularly in tissue engineering and biodegradable implant development.

Author contributions

Conceptualization – MKY, JJ, KGP; methodology – MKY, RHS, PK, SN, CSP, PS, JJ, KGP; formal analysis – MKY, RHS, PK, SN,

CSP; Investigation – MKY, RHS, PK, SN, CSP, PS; resource – KC, SS, JJ, KGP; writing – original draft preparation – MKY, RHS, PK, SN, CSP, PS; writing – review and editing – MKY, KC, SS, JJ, KGP; supervision – KC, SS, JJ, KGP; project administration – KGP; funding acquisition – KC, SS, KGP.

Data availability

Data may be made available upon reasonable request to the authors.

Conflicts of interest

The authors declare no potential conflicts of interest.

Acknowledgements

The author acknowledges the program for overseas high-level talent's introduction of Henan Province: HNGD2025040 for the financial support.

References

- 1 J. C. C. Paiva, L. Oliveira, M. F. Vaz and S. Costa-de-Oliveira, *Bioengineering*, 2022, **9**, 409.
- 2 M. Prakasam, J. Locs, K. Salma-Ancane, D. Loca, A. Largeteau and L. Berzina-Cimdina, *J. Funct. Biomater.*, 2017, **8**, 44.
- 3 Z. Morsada, M. M. Hossain, M. T. Islam, M. A. Mobin and S. Saha, *Appl. Mater. Today*, 2021, **25**, 101257.
- 4 V. P. M. Rabeeh and T. Hanas, *Progress in Biomaterials*, 2022, **11**, 163–191.
- 5 L. Kong, Z. Heydari, G. H. Lami, A. Saberi, M. S. Baltatu and P. Vizureanu, *Materials*, 2023, **16**, 4797.
- 6 K. Chen, X. Gu and Y. Zheng, *Smart Mater. Manuf.*, 2024, **2**, 100042.
- 7 K. Chen, X. Gu and Y. Zheng, *Smart Mater. Manuf.*, 2024, **2**, 100042.
- 8 B. Hutchinson, J. Komenda, S. Kada, M. Barnett and A. Oskarsson, *Scr. Mater.*, 2019, **166**, 78–80.
- 9 I. D. Engler, P.-A. Hart, D. P. Swanson, J. M. Kirsch, J. P. Murphy, M. A. Wright, A. Murthi and A. Jawa, *Semin. Arthroplasty*, 2022, **32**, 751–756, DOI: [10.1053/J.SART.2022.07.001](https://doi.org/10.1053/J.SART.2022.07.001).
- 10 M. I. Z. Ridzwan, S. Shuib, A. Y. Hassan, A. A. Shokri and M. N. Mohammad Ibrahim, *J. Med. Sci.*, 2007, **7**, 460–467, DOI: [10.3923/jms.2007.460.467](https://doi.org/10.3923/jms.2007.460.467) preprint.
- 11 I. Bendich, C. M. Lawrie, V. Riegler, R. L. Barrack and R. M. Nunley, *J. Arthroplasty*, 2022, **37**, S221–S225.
- 12 K. Praveenkumar, J. Vishnu, A. Raheem, V. Gopal, S. Swaroop, S. Suwas, B. Shankar and G. Manivasagam, *Appl. Surf. Sci.*, 2024, **665**, 160334.
- 13 R. Shukla and K. G. Prashanth, *Trans. Indian Inst. Met.*, 2022, **2022**, 1–11.



- 14 O. O. Salman, F. Brenne, T. Niendorf, J. Eckert, K. G. Prashanth, T. He and S. Scudino, *J. Manuf. Process.*, 2019, **45**, 255–261.
- 15 Y. Li, W. Li, F. S. L. Bobbert, K. Lietaert, J. H. Dong, M. A. Leeflang, J. Zhou and A. A. Zadpoor, *Acta Biomater.*, 2020, **106**, 439–449.
- 16 Q. Chen and G. A. Thouas, *Mater. Sci. Eng., R*, 2015, **87**, 1–57.
- 17 Y. F. Zheng, X. N. Gu and F. Witte, *Mater. Sci. Eng., R*, 2014, **77**, 1–34.
- 18 P. Wen, L. Jauer, M. Voshage, Y. Chen, R. Poprawe and J. H. Schleifenbaum, *J. Mater. Process. Technol.*, 2018, **258**, 128–137.
- 19 H. Pan, K. Pang, F. Cui, F. Ge, C. Man, X. Wang and Z. Cui, *Corros. Sci.*, 2019, **157**, 420–437.
- 20 F. Witte, *Acta Biomater.*, 2010, **6**, 1680–1692.
- 21 Z. Chun-Yan, Z. Rong-Chang, L. Cheng-Long and G. Jia-Cheng, *Surf. Coat. Technol.*, 2010, **204**, 3636–3640.
- 22 M. D. Pereda, C. Alonso, L. Burgos-Asperilla, J. A. Del Valle, O. A. Ruano, P. Perez and M. A. Fernández Lorenzo De Mele, *Acta Biomater.*, 2010, **6**, 1772–1782.
- 23 S. Hiromoto, T. Shishido, A. Yamamoto, N. Maruyama, H. Somekawa and T. Mukai, *Corros. Sci.*, 2008, **50**, 2906–2913.
- 24 J. E. Gray-Munro, C. Seguin and M. Strong, *J. Biomed. Mater. Res., Part A*, 2009, **91A**, 221–230.
- 25 E. Mostaed, M. Sikora-Jasinska, J. W. Drelich and M. Vedani, *Acta Biomater.*, 2018, **71**, 1–23.
- 26 Y. Su, I. Cockerill, Y. Wang, Y. X. Qin, L. Chang, Y. Zheng and D. Zhu, *Trends Biotechnol.*, 2019, **37**, 428–441.
- 27 J. Fu, Y. Su, Y. X. Qin, Y. Zheng, Y. Wang and D. Zhu, *Biomaterials*, 2020, **230**, 119641.
- 28 B. S. Moonga and D. W. Dempster, *J. Bone Miner. Res.*, 1995, **10**, 453–457.
- 29 H.-J. Seo, Y.-E. Cho, T. Kim, H.-I. Shin and I.-S. Kwun, *Nutr. Res. Pract.*, 2010, **4**, 356–361.
- 30 K. Praveenkumar, S. Swaroop and G. Manivasagam, *J. Mater. Eng. Perform.*, 2022, **31**, 6846–6857.
- 31 H. Yang, B. Jia, Z. Zhang, X. Qu, G. Li, W. Lin, D. Zhu, K. Dai and Y. Zheng, *Nat. Commun.*, 2020, **11**, 1–16.
- 32 P. K. Bowen, R. J. Guillory, E. R. Shearier, J. M. Seitz, J. Drelich, M. Bocks, F. Zhao and J. Goldman, *Mater. Sci. Eng., C*, 2015, **56**, 467–472.
- 33 C. K. Patrick Bowen, J. Drelich, J. Goldman, P. K. Bowen, J. Drelich and J. Goldman, *Adv. Mater.*, 2013, **25**, 2577–2582.
- 34 E. Jablonská, D. Vojtěch, M. Fousová, J. Kubásek, J. Lipov, J. Fojt and T. Ruml, *Mater. Sci. Eng., C*, 2016, **68**, 198–204.
- 35 T. Huang, Z. Liu, D. Wu and H. Yu, *J. Mater. Res. Technol.*, 2021, **15**, 226–240.
- 36 Y. Qin, P. Wen, D. Xia, H. Guo, M. Voshage, L. Jauer, Y. Zheng, J. H. Schleifenbaum and Y. Tian, *Addit. Manuf.*, 2020, **33**, 101134.
- 37 Z. Z. Shi, H. Y. Li, J. Y. Xu, X. X. Gao and X. F. Liu, *Materials Science and Engineering: A*, 2020, **771**, 138626.
- 38 Z. Z. Shi, J. Yu, X. F. Liu, H. J. Zhang, D. W. Zhang, Y. X. Yin and L. N. Wang, *Mater. Sci. Eng., C*, 2019, **99**, 969–978.
- 39 Z. Li, Z. Z. Shi, Y. Hao, H. F. Li, X. F. Liu, A. A. Volinsky, H. J. Zhang and L. N. Wang, *J. Mater. Sci. Technol.*, 2019, **35**, 2618–2624.
- 40 M. Salehi, S. Maleksaeedi, M. A. Bin Sapari, M. L. S. Nai, G. K. Meenashisundaram and M. Gupta, *Mater. Des.*, 2019, **169**, 107683.
- 41 G. Lu, Y. Dai, S. He, C. Chen, X. Liu, K. Tang, L. Guo, D. Zhang, J. Lin and C. Wen, *Corros. Sci.*, 2024, **239**, 112399.
- 42 W. Y. Li, Y. L. Dai, W. H. Cai, S. H. Lin, L. Guo, D. C. Zhang, Y. Li and C. Wen, *Rare Met.*, 2024, **43**, 5284–5304.
- 43 J. Lin, Y. Chen, Y. Dai, X. Zhang, D. Zhang, Y. Li and C. Wen, *Acta Biomater.*, 2025, **194**, 514–529.
- 44 M. Demirtas, G. Purcek, H. Yanar, Z. J. Zhang and Z. F. Zhang, *Mater. Sci. Eng., A*, 2015, **644**, 17–24.
- 45 Y. Zhu, J. Qin, J. Wang, P. Jin and P. Li, *Mater. Today Commun.*, 2023, **35**, 105670.
- 46 Q. Yang, D. L. Cheng, F. G. Zhang, Q. W. Shi, Z. Chen, M. L. Wang, S. Y. Zhong, Y. Wu and H. W. Wang, *Mater. Charact.*, 2021, **172**, 110825.
- 47 R. Rahmani, S. I. Lopes and K. G. Prashanth, *J. Funct. Biomater.*, 2023, **14**, 521.
- 48 R. Shukla, R. Sökkalingam and K. G. Prashanth, *J. Alloys Compd.*, 2023, 171079.
- 49 H. S. Maurya, J. Marczyk, K. Juhani, F. Sergejev, R. Kumar, A. Hussain, F. Akhtar, M. Hebda and K. G. Prashanth, *Mater. Today Adv.*, 2025, **25**, 100562.
- 50 L. Li, R. Li, T. Yuan, C. Chen, M. Wang, J. Yuan and Q. Weng, *J. Alloys Compd.*, 2020, **821**, 153520.
- 51 J. Čapek, E. Jablonská, J. Lipov, T. F. Kubatik and D. Vojtěch, *Mater. Chem. Phys.*, 2018, **203**, 249–258.
- 52 F. An, Z. Ma, K. Sun, L. Zhang, S. J. Na, J. Ning and H. Yu, *J. Mater. Res. Technol.*, 2023, **24**, 595–607.
- 53 J. Pinc, J. Čapek, J. Kubásek, F. Průša, V. Hybášek, P. Veřtát, I. Sedlářová and D. Vojtěch, *Metals*, 2020, **10**, 372.
- 54 Z. Zhang, Y. Yang, Y. Guo, Z. Xu, P. Sha, Z. Yu and L. Ren, *Surf. Coat. Technol.*, 2023, **466**, 129653.
- 55 M. K. Yadav, V. Pandey, K. Mohanta and V. K. Singh, *Ceram. Int.*, 2022, **48**(17), 25335–25345.
- 56 M. K. Yadav, V. Pandey, Jyoti, A. Kumar, K. Mohanta and V. K. Singh, *Ceram. Int.*, 2021, **47**(15), 22191–22200.
- 57 V. F. Dunsikii, N. V. Nikitin and N. F. Tonkacheeva, *J. Eng. Phys.*, 1971, **20**, 558–560.
- 58 L. C. Zhang, W. Y. Xu, Z. Li, L. Zheng, Y. F. Liu and G. Q. Zhang, *Powder Technol.*, 2023, **418**, 118162.
- 59 M. Abedi, D. O. Moskovskikh, A. S. Rogachev and A. S. Mukasyan, *Metall. Mater. Trans. B*, 2016, **47**, 2725–2731.
- 60 D. Ovalı, M. Tarraste, M. Kaba, D. Ağaoğulları, L. Kollo, K. G. Prashanth and M. Lütfi Öveçoğlu, *Ceram. Int.*, 2021, **47**, 13827–13836.
- 61 N. Singh, R. Ummethala, P. S. P. S. Karamched, R. Sökkalingam, V. Gopal, G. Manivasagam and K. G. Prashanth, *J. Alloys Compd.*, 2021, **865**, 158875.
- 62 V. V. Patil, K. G. Prashanth and C. P. Mohanty, *J. Alloys Compd.*, 2023, **960**, 170734.



- 63 C. S. Bonifacio, J. F. Rufner, T. B. Holland and K. Van Benthem, *Appl. Phys. Lett.*, 2012, **101**, 093107.
- 64 M. Kermani, M. Razavi, M. R. Rahimpour and M. Zakeri, *J. Alloys Compd.*, 2014, **593**, 242–249.
- 65 D. Kumar, G. Shankar, K. G. Prashanth and S. Suwas, *Mater. Sci. Eng., A*, 2021, **820**, 141483.
- 66 D. Kumar, G. Shankar, K. G. Prashanth and S. Suwas, *J. Alloys Compd.*, 2023, 173040.
- 67 R. J. Vikram, L. Kollo, K. G. Prashanth and S. Suwas, *Metall. Mater. Trans. A*, 2021, **52**, 5329–5341.
- 68 K. G. Prashanth, S. Scudino, H. J. Klauss, K. B. Surreddi, L. Löber, Z. Wang, A. K. Chaubey, U. Kühn and J. Eckert, *Mater. Sci. Eng., A*, 2014, **590**, 153–160.
- 69 B. Hutchinson, J. Komenda, S. Kada, M. Barnett and A. Oskarsson, *Scr. Mater.*, 2019, **166**, 78–80.
- 70 D. H. StJohn, M. A. Easton, M. Qian, P. Cao and M. J. Birmingham, *Mater. Sci. Forum*, 2011, **690**, 206–209.
- 71 R. Chaim, *Mater. Sci. Eng., A*, 2007, **443**, 25–32.
- 72 Y. Cheng, Z. Cui, L. Cheng, D. Gong and W. Wang, *Adv. Powder Technol.*, 2017, **28**, 1129–1135.
- 73 G. Dirras, J. Gubicza, H. Couque, A. Ouarem and P. Jenei, *Mater. Sci. Eng., A*, 2013, **564**, 273–283.
- 74 M. Oghbaei and O. Mirzaee, *J. Alloys Compd.*, 2010, **494**, 175–189.
- 75 Z. A. Munir, U. Anselmi-Tamburini and M. Ohyanagi, *J. Mater. Sci.*, 2006, **41**, 763–777.
- 76 Z. Wang, K. G. Prashanth, K. B. Surreddi, C. Suryanarayana, J. Eckert and S. Scudino, *Materialia*, 2018, **2**, 157–166.
- 77 K. B. Surreddi, S. Scudino, M. Sakaliyska, K. G. Prashanth, D. J. Sordelet and J. Eckert, *J. Alloys Compd.*, 2010, **491**, 137–142.
- 78 G. Liu, R. Li, T. Yuan, M. Zhang and F. Zeng, *Int. J. Refract. Met. Hard Mater.*, 2017, **66**, 68–75.
- 79 A. Flaureau, A. Weibel, G. Chevallier and C. Estournès, *J. Eur. Ceram. Soc.*, 2021, **41**, 3581–3594.
- 80 H. Li, Q. Q. Duan, X. W. Li and Z. F. Zhang, *Mater. Sci. Eng., A*, 2007, **466**, 38–46.
- 81 Y. Xin, X. Zhou, L. Lv and Q. Liu, *Mater. Sci. Eng., A*, 2014, **606**, 81–91.
- 82 S. Yu, H. Chi, P. Li, B. Guo, Z. Yu, Z. Xu, P. Liang, Z. Zhang, Y. Guo and L. Ren, *Addit. Manuf.*, 2024, **93**, 104411.
- 83 P. K. Bowen, E. R. Shearier, S. Zhao, R. J. Guillory, F. Zhao, J. Goldman and J. W. Drelich, *Adv. Healthcare Mater.*, 2016, **5**, 1121–1140.
- 84 L. Liu, Y. Meng, C. Dong, Y. Yan, A. A. Volinsky and L. N. Wang, *J. Mater. Sci. Technol.*, 2018, **34**, 2271–2282.
- 85 X. Liu, Y. Cheng, Z. Guan and Y. Zheng, *Corros. Sci.*, 2020, **170**, 108661.
- 86 Q. Cui, D. Yi, H. Wang, J. Zhang, J. Xu and B. Wang, *J. Rare Earths*, 2019, **37**, 1341–1350.
- 87 P. Wang, L. Ma, X. Cheng, X. Li, L. Wang, C. Dong, C. Man, Y. Hu, Q. Yu, J. Ma, F. Feng, B. Yu, H. Chen, B. Yu, H. Yan, Q. Wu, Z. Hu, F. Chen, Y. Wei, Y. Fu, Z. Pan, Y. Ma, H. Cheng, Q. Zhao, H. Luo, Z. Wang, Z. Zheng, L. Zhao, Y. Lei and K. Yang, *Int. J. Miner., Metall. Mater.*, 2021, **28**, 1112–1126.
- 88 M. Amirnejad, M. Rajabi and R. Jamaati, *Corros. Sci.*, 2021, **179**, 109100.
- 89 R. Soni, S. Jhavar, S. Tyeb, S. K. Gupta, S. Suwas and K. Chatterjee, *J. Funct. Biomater.*, 2022, **13**, 212.
- 90 M. H. Qi, J. L. Xu, T. Lai, J. Huang, Y. C. Ma, J. M. Luo and Y. F. Zheng, *J. Alloys Compd.*, 2023, **931**, 167555.
- 91 H. Yang, X. Qu, W. Lin, C. Wang, D. Zhu, K. Dai and Y. Zheng, *Acta Biomater.*, 2018, **71**, 200–214.
- 92 X. Tong, D. Zhang, X. Zhang, Y. Su, Z. Shi, K. Wang, J. Lin, Y. Li, J. Lin and C. Wen, *Acta Biomater.*, 2018, **82**, 197–204.
- 93 S. C. P. Cachinho and R. N. Correia, *J. Mater. Sci.: Mater. Med.*, 2008, **19**, 451–457.
- 94 M. A. Amin, K. F. Khaled and S. A. Fadl-Allah, *Corros. Sci.*, 2010, **52**, 140–151.
- 95 Z. Shi, M. Liu and A. Atrens, *Corros. Sci.*, 2010, **52**, 579–588.
- 96 E. Poorqasemi, O. Abootalebi, M. Peikari and F. Haqdar, *Corros. Sci.*, 2009, **51**, 1043–1054.
- 97 P. F. Ji, B. Li, B. H. Chen, F. Wang, W. Ma, X. Y. Zhang, M. Z. Ma and R. P. Liu, *Corros. Sci.*, 2020, **170**, 108696.
- 98 R. Soni, S. Jhavar, S. Tyeb, S. K. Gupta, S. Suwas and K. Chatterjee, *J. Funct. Biomater.*, 2022, **13**(4), 212.
- 99 D. Vojtěch, J. Kubásek, J. Šerák and P. Novák, *Acta Biomater.*, 2011, **7**, 3515–3522.
- 100 E. Koç, M. B. Kannan, M. Ünal and E. Candan, *J. Alloys Compd.*, 2015, **648**, 291–296.
- 101 M. H. Qi, J. L. Xu, T. Lai, J. Huang, Y. C. Ma, J. M. Luo and Y. F. Zheng, *J. Alloys Compd.*, 2023, **931**, 167555.
- 102 J. Čapek, E. Jablonská, J. Lipov, T. F. Kubatík and D. Vojtěch, *Mater. Chem. Phys.*, 2018, **203**, 249–258.
- 103 J. Pinc, J. Čapek, J. Kubásek, F. Průša, V. Hybášek, P. Veřtát, I. Sedlářová and D. Vojtěch, *Metals*, 2020, **10**(3), 372.
- 104 H. Yang, X. Qu, W. Lin, C. Wang, D. Zhu, K. Dai and Y. Zheng, *Acta Biomater.*, 2018, **71**, 200–214.
- 105 S. Huang, L. Chen, B. Jiang, L. Qiao and Y. Yan, *J. Electroanal. Chem.*, 2021, **886**, 115145.
- 106 L. Upadhyay, S. Nilawar, C. Kumar, K. Chatterjee and P. Kumar, *J. Mater. Sci.*, 2024, **59**, 5872–5890.



Publication IV

M.K. Yadav, R.H. Shukla, L. Xi, Z. Wang, K.G. Prashanth, Metallic multimaterials fabricated by combining additive manufacturing and powder metallurgy, *Journal of Composites Science* 9 (2025) 80. <https://doi.org/10.3390/jcs9020080>.



Article

Metallic Multimaterials Fabricated by Combining Additive Manufacturing and Powder Metallurgy

Mayank Kumar Yadav ¹, Riddhi Shukla ¹ , Lixia Xi ^{2,*}, Zhi Wang ³ and Konda Gokuldoss Prashanth ^{1,4,*}

- ¹ Department of Mechanical and Industrial Engineering, Tallinn University of Technology, Ehitajate tee 5, 19086 Tallinn, Estonia; mayank.yadav@taltech.ee (M.K.Y.); riddhi.shukla@taltech.ee (R.S.)
 - ² Jiangsu Provincial Engineering Laboratory for Laser Additive Manufacturing of High-Performance Metallic Components, College of Materials Science and Technology, Nanjing University of Aeronautics and Astronautics, Yudao Street 29, Nanjing 210016, China
 - ³ National Engineering Research Center of Near-Net-Shape Forming for Metallic Materials, South China University of Technology, Guangzhou 510640, China; wangzhi@scut.edu.cn
 - ⁴ Centre for Biomaterials, Cellular and Molecular Theranostics (CBCMT), Vellore Institute of Technology, School of Mechanical Engineering, Vellore 632014, Tamil Nadu, India
- * Correspondence: xilixia@880@nuaa.edu.cn (L.X.); kgprashanth@gmail.com (K.G.P.)

Abstract: Nature has created a unique combination of materials, and the design and material compositions used in nature are not successfully employed for industrial applications. Metallic multimaterials (MMMs) are a unique class of materials that combine the properties of various metallic constituents (both matrix and reinforcement(s)) to improve the functionality, performance in real-time, and application spectrum. Accordingly, this study explores the fabrication perspective of MMMs by combining both additive manufacturing (AM) and powder metallurgical (PM) routes. Ti6Al4V structures were fabricated via the laser powder-bed fusion (LPBF) process, and the reinforcement powders were added into the spark plasma sintering (SPS) mold where the Ti6Al4V structures were placed. Different reinforcement compositions including Mg, Al, Fe, Ni, and Cu were explored. Since the present study is focused on the variation of hardness, the hardness profile of the MMM composite was explored showing a sinusoidal trend. This study stands as a testimonial of fabricating MMM composites via a combination of AM and PM processes.

Keywords: composites; metallic multimaterials; powder metallurgy; additive manufacturing



Academic Editor: Jose Manuel Torralba

Received: 31 December 2024

Revised: 28 January 2025

Accepted: 8 February 2025

Published: 10 February 2025

Citation: Yadav, M.K.; Shukla, R.; Xi, L.; Wang, Z.; Prashanth, K.G. Metallic Multimaterials Fabricated by Combining Additive Manufacturing and Powder Metallurgy. *J. Compos. Sci.* **2025**, *9*, 80. <https://doi.org/10.3390/jcs9020080>

Copyright: © 2025 by the authors. Licensee MDPI, Basel, Switzerland. This article is an open access article distributed under the terms and conditions of the Creative Commons Attribution (CC BY) license (<https://creativecommons.org/licenses/by/4.0/>).

1. Introduction

The design and composition of materials observed in nature is based on their applications and the properties needed for those applications. On this account, unique composite materials are observed in nature with optimized design and composition [1]. Some of the nature-inspired multimaterials are as follows: (a) bones: soft collagen with hard minerals for energy dissipation applications [2]; (b) mollusk shells: metal in calcium carbonate shells offer excellent mechanical and tribological properties [3]; (c) deer antlers: calcium phosphate covered with keratin and traces of Fe or Zn for improving toughness and fracture resistance [4]; (d) certain fungi create composite-like structures of fungal mycelium and metal nanoparticles (like Ag, Cu, Fe, etc.) by absorbing metals from their environment. These composite structures offer unique antimicrobial and electrical properties [5]. However, most of the materials designed and fabricated by humans exhibit simple structures using single materials or simple combinations of materials as composites. Hence, they are not completely optimized for unique/specific applications due to unique challenges and limitations w.r.t. design and traditional manufacturing technologies [6].

Thanks to the introduction of additive manufacturing (AM) technologies and the introduction of design for additive manufacturing (DfAM) offering unlimited design freedom with layer-by-layer deposition and fabrication mechanism [7–14], using AM, materials with complex structures and theoretically any design may be fabricated [15–17]. Recent technological innovations and advancements have offered the advantages of fabricating functionally graded materials either of single materials or multiple materials [15,18–24] and multimaterials [25–28]. The metallic multimaterials (MMMs) fabricated by LPBF are conventionally made of two materials in the form of structures or solids [29]. MMMs with multiple compositions were also fabricated via the LPBF process but in a graded fashion. However, it is difficult to fabricate MMMs in the form of composites, where one or multiple materials (reinforcements) are periodically placed or randomly distributed within the matrix. This is where interpenetrating composites (IPCs) are fabricated, where the LPBF fabricates the structure matrix, and the second material (generally a low-temperature material) is introduced via casting, which is often a low melting reinforcement [30–40]. When the IPCs are fabricated with the help of AM and casting, only one type of reinforcement may be introduced into the AM-made precursor, and it is impossible to add multiple reinforcements to the precursor [41–45]. To overcome such disadvantages and to fabricate MMMs with one type of matrix and several reinforcements, an AM-made precursor may be added with multiple reinforcements through a powder metallurgical (PM) approach. Accordingly, this manuscript stands as a testimony for fabricating MMMs by combining AM and PM approaches, where the Ti6Al4V honeycomb structure (precursor) is fabricated via the LPBF process, and one or multiple reinforcements are added through a PM approach to reap the benefits of MMMs.

MMMs have impacted industry in almost every sector (including aerospace, automotive, energy, industrial, medical, etc.) by extending both the capabilities and functionality of components matching the specific needs of the working environment [46–48]. More efficient parts may be fabricated by combining different materials (Table 1). Some examples are: (1) Materials with insulating properties are combined with conductors for reducing energy consumption in building and/or automotive industries [49]. (2) Material combinations where high strength and toughness are combined with functional properties (thermal and electrical conductivity) [50,51]. (3) In addition, MMM parts can help improve components life span, promoting a more green and sustainable future. Lightweight and functionally active MMMs in the automobile and aerospace sectors can help in increasing the life span of the vehicle and at the same time help in energy and fuel savings and reducing CO₂ emissions [52–54].

Combining two unique processes (AM and PM) offers the following specific advantages: (1) flexible and enhanced material design—offering the possibility of fabricating tailored and gradient structures; (2) improved properties including mechanical properties; (3) reduced material defects; (4) optimized material utilization; (5) application-specific properties by tuning the material additions; (6) cost-efficiency; and (7) versatility in manufacturing. In addition, for the fabrication of MMMs (interpenetrating composites), the combination of AM and casting approaches may be utilized. However, if more than one reinforcement is required to be added to the matrix, the casting-based approach may not be feasible and hence the novel approach of introducing PM to AM will be highly beneficial. Accordingly, this manuscript proposes a novel combination of manufacturing processes (by combining AM and PM) to fabricate MMMs with different material combinations.

Table 1. Table illustrating the reported multimaterials along with their industrial applications and a brief rationale on the material combinations.

Material Combination	Industry	Description	References
IN 718—316L Stainless steel (SS)	Nuclear fission applications	<p>Applications: Pressure tubes, reactor head (pressurized light-water reactors) or bottom (boiling light-water reactors), and the reactor pressure vessel of the nuclear reactor</p> <p>Material 1: Nickel alloys ensure resistance to extreme chemical environments (corrosion resistance) and high temperatures—especially high-temperature corrosion resistance.</p> <p>Material 2: Stainless steel provides mechanical strength and corrosion resistance.</p> <p>Material combination: The combination of these materials (IN718 and 316L SS) offers both high-temperature resistance and structural integrity, ensuring safe and efficient reactor operation.</p>	[51,55–57]
316L SS—Oxygen-free high conductivity (OHFC) Cu	Nuclear fusion applications	<p>Applications: Plasma-facing surfaces of divertor plates and first wall components in tokamaks (fusion reactors) like ITER.</p> <p>Material 1: Copper provides excellent thermal conductivity, which is crucial for efficiently removing heat from the reactor surface exposed to high plasma temperatures.</p> <p>Material 2: Stainless steel offers structural integrity and corrosion resistance, essential for withstanding the demanding reactor environment.</p> <p>Material combination: The plasma-facing components (PFCs) are exposed to extremely high heat fluxes, requiring materials that can handle both high temperatures and the erosive effects of plasma.</p>	[58,59]
H360LA—EN AW-5128/EN AW-6016	Chemical processing applications	<p>Applications: Adapters in oxygen regenerators.</p> <p>Material 1: Steel ensures mechanical strength and durability.</p> <p>Material 2: Aluminum forms a protective alumina layer, ensuring high corrosion resistance in oxygen-rich environments.</p> <p>Material combination: Combines corrosion resistance with structural support.</p>	[60]
Ti6Al4V—IN718	Nuclear fusion/ aerospace applications	<p>Applications: Gas turbine blades and shafts.</p> <p>Material 1: Titanium is lightweight with a high strength-to-weight ratio, making it ideal for cooler sections of the turbine to reduce overall weight.</p> <p>Material 2: Inconel, a nickel-based superalloy, exhibits excellent creep and oxidation resistance, enabling it to perform in high-temperature regions exposed to hot gases.</p> <p>Material combination: Enhances turbine efficiency with reduced weight and improved durability in varying thermal zones.</p>	[61]
C18400 Cu alloy—AlSi10Mg	Electrical applications	<p>Applications: Electrical connectors and heat exchangers.</p> <p>Material 1: Copper offers excellent electrical conductivity and heat dissipation.</p> <p>Material 2: Aluminum provides lightweight and corrosion-resistant properties, making it suitable for large structures.</p> <p>Material combination: Combines high conductivity and lightweight characteristics for efficient energy systems.</p>	[62]
316L SS—CuSn10	Marine/industrial applications	<p>Applications: Heat exchanger components and corrosion-resistant structures.</p> <p>Material 1: SS316L provides corrosion resistance and mechanical strength in marine environments.</p> <p>Material 2: CuSn10 ensures superior thermal and electrical conductivity, alongside excellent wear resistance.</p> <p>Material combination: Combines structural integrity and conductivity for demanding environments.</p>	[63,64]

Table 1. Cont.

Material Combination	Industry	Description	References
AlSi10Mg—C18400 Cu alloy	Lightweight components	<p>Applications: Lightweight structural and thermal management components.</p> <p>Material 1: A lightweight aluminum alloy commonly used in additive manufacturing (AM) for its excellent mechanical properties, high strength-to-weight ratio, and corrosion resistance.</p> <p>Material 2: A high-conductivity copper alloy primarily used for thermal management applications due to its superior electrical and thermal conductivity.</p> <p>Material combination: Provides lightweight structures with efficient thermal management.</p>	[62]
Cu—H13 tool steel	Die casting applications	<p>Applications: Bi-metallic die for the pressure die-casting industry.</p> <p>Material 1: Core would be from copper to reduce thermal resistance, thus encouraging the flow of heat energy from the cavity to the cooling channels.</p> <p>Material 2: H13 tool steel to provide structural strength.</p> <p>Material combination: Combines thermal management with structural integrity for effective die-casting operations.</p>	[65]
Tool steel—ceramic (80%ZrO ₂ + 20% Al ₂ O ₃ —tool steel	Tooling applications	<p>Applications: Tools and dies.</p> <p>Material 1: Tool steel provides structural strength and toughness.</p> <p>Material 2: Ceramic offers high hardness and wear resistance.</p> <p>Material combination: Combines toughness and wear resistance for extended tool life in demanding applications.</p>	[60]
SiC—316L	Advanced manufacturing applications	<p>Applications: Support structures for SLM.</p> <p>Material 1: Silicon carbide enhances wear resistance and thermal conductivity.</p> <p>Material 2: Stainless steel ensures corrosion resistance and structural integrity.</p> <p>Material combination: Facilitates easy support removal and high-performance structural compatibility.</p>	[66]
Ti6Al4V—Cu	Biomedical/aerospace applications	<p>Applications: Implants and components requiring thermal management.</p> <p>Material 1: Titanium ensures biocompatibility and structural strength in biomedical and aerospace applications.</p> <p>Material 2: Copper provides excellent thermal conductivity for heat management.</p> <p>Material combination: Combines biocompatibility and efficient thermal management for biomedical and aerospace uses.</p>	[67]

2. Experimental Details

The Ti6Al4V honeycomb structures were fabricated using a laser powder-bed fusion (LPBF) SLM280 device from SLM Solutions GmbH (Luebeck, Germany) from commercially available Ti6Al4V atomized powders. The Ti6Al4V samples were fabricated using the following laser parameters: laser power ‘W’: 400 W, laser scan rate ‘v’: 1000 mm/s, hatch distance ‘h’: 0.12 mm, and layer thickness ‘t’: 0.05 mm, leading to an energy density of 66.67 J/mm³ [68]. The Ti6Al4V structures were fabricated over a Ti-based substrate under an Ar atmosphere to avoid possible oxidation of the melt during the LPBF process. Similarly, the 316L stainless steel (SS) sample was fabricated using the following process parameters: laser power ‘W’: 62.5 W, laser scan rate ‘v’: 1000 mm/s, hatch distance ‘h’: 0.060 mm, and layer thickness ‘t’: 0.025 mm, leading to an energy density of 42.00 J/mm³. A hatch-style rotation of 90° was employed between the layers to minimize possible thermal gradients arising during extreme solidification conditions [69–72]. The composite samples were prepared using the spark plasma sintering (SPS) HPD 10-GB device from FCT System GmbH (Effelder-Rauenstein, Germany). The matrix (Ti6Al4V struts) is placed inside a

graphite mold and the reinforcement particles (commercially available powders of appx. 50 μm diameter from Al, Mg, Fe, Ni, and Cu) are added to the struts in the required portions. The composites are then consolidated to form metallic multimaterials. The sintering parameters are furnished in Table 2. The composite manufacturing steps are furnished in Figure 1.

Table 2. Table furnishing the process parameters employed during the spark plasma sintering process to fabricate the metallic multimaterials.

S. No.	Composition	Temperature (°C)	Load (MPa)	Time (min)
1	Ti–Mg	550	50	10
2	Ti–Mg–Al	550	50	10
3	Ti–Mg–Al–Fe	550	50	10
4	SS(Hexagon)—Ti–Cu–Ni	1000	50	5

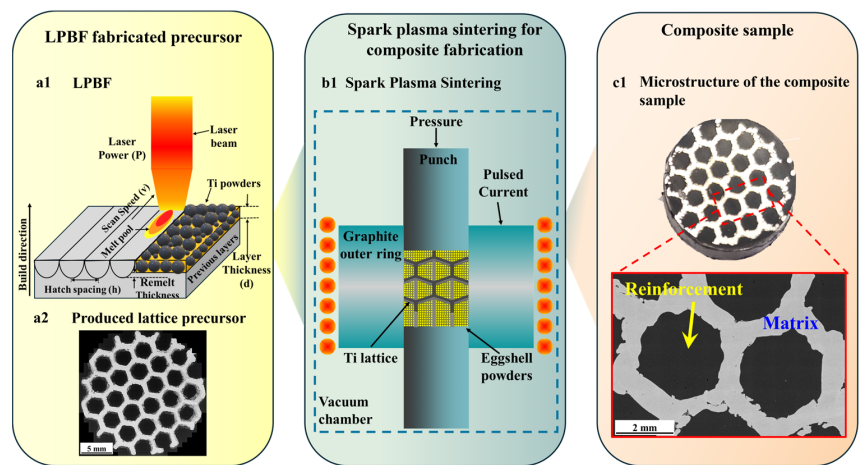


Figure 1. Schematic illustration of the composite manufacturing process: (a1) additive manufacturing of the lattice using LPBF process, (a2) fabricated metal lattice precursor, (b1) spark plasma sintering of the composite by placing the precursor inside the spark plasma sintering mold, and (c1) structure of the fabricated metallic bimetal.

The structural characterization of the samples was carried out using X-ray diffraction (XRD) by a Panalytical X’Pert PRO Diffractometer (Malvern Panalytical GmbH, Kassel, Germany) with Cu Kα ($\lambda = 1.54 \text{ \AA}$) radiation at 40 kV and 30 mA. The scanning was performed within the 2θ range 20° and 100° with a step size of 0.01° and scan speed of $1^\circ/\text{min}$. The microstructural characterization was carried out using a scanning electron microscope (SEM) from Zeiss Gemini SEM 450, Zeiss GmbH, Oberkochen, Germany integrated with Apex energy dispersive spectroscopy (EDS). Both secondary (SE) and backscatter (BSD) SEM images were recorded. The mechanical testing of the samples was carried out using a Future-Tech Corp microhardness tester (FM-810), Future Tech GmbH, Quierschied, Germany. A test load of 0.1 kgf and a dwell time of 10 s were employed for all the hardness measurements.

3. Results and Discussion

Figure 2 shows the SEM–EDS maps of the metallic multimaterials (Ti6Al4V–Mg–bimetal, Ti6Al4V–Mg–Al–trimetal, and Ti6Al4V–Mg–Al–Fe–MMM). It can be observed from Figure 2a—Ti6Al4V–Mg MMM composite that the Ti6Al4V matrix lattice is not distorted and almost maintains its structure/dimensions after the SPS process. The Mg

reinforcement is sintered and shows a distinct interface with the matrix. However, no interfacial reaction between the matrix (Ti) and the reinforcement (Mg) may be observed. On the other hand, in the case of the Ti6Al4V–Mg–Al MMM composite (where two reinforcements Mg and Al are added to the Ti6Al4V matrix) (Figure 2b), both Al and Mg reinforcements are sintered without introducing porosity and maintain a good interface with the lattice. No material reaction is observed at the matrix–reinforcement interface (from Figure 2b). In addition, both the reinforcements are distributed evenly except at the boundary, where there is a mixture of both Mg and Al (as marked in Figure 2b). This mixing of Al and Mg may have happened during the addition of the reinforcement powders to the Ti6Al4V lattice precursor. The Ti6Al4V lattice shows signs of distortion, where the compression of the lattice is observed. In Figure 2c, three different reinforcements (Mg, Al, and Fe) were added to the Ti6Al4V matrix. This MMM composite shows severe lattice distortion like the Ti6Al4V–Mg–Al composite. The reinforcement particles are sintered well, and no visible interfacial reaction is observed between the reinforcement particles and the Ti6Al4V precursor interface. Like the previous counterpart (Ti6Al4V–Mg–Al composite), the mixing of reinforcement powders may be observed near the interface and are marked by blue areas in Figure 2c.

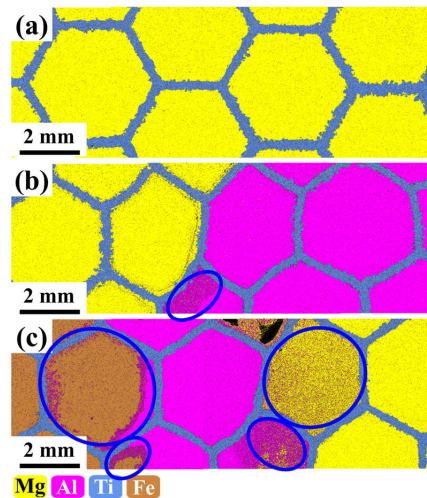


Figure 2. Scanning electron microscopy–energy dispersive spectroscopy area maps showing the individual constituents present in the metallic multimaterials (MMMs): (a) Ti6Al4V–Mg MMM composite—bimetal composite, (b) Ti6Al4V–Mg–Al composite—trimetal composite, and (c) Ti6Al4V–Mg–Ti–Fe composite—multimaterial composite.

XRD measurements were conducted on these MMM composites to evaluate the reaction between the different reinforcement powders at their interface and the reinforcement–matrix interface. The XRD diffraction patterns of these MMM composites (Ti6Al4V–Mg, Ti6Al4V–Mg–Al, and Ti6Al4V–Mg–Al–Fe) are shown in Figure 3. The Ti6Al4V structure fabricated by LPBF shows the presence of α' -Ti—martensitic microstructure, even though Ti6Al4V is an $\alpha + \beta$ composition [73–79]. The complex interplay during heat extraction along different directions (including conduction, convection, and radiation) with different rates leads to a complex and anisotropic microstructure in the LPBF-processed materials [80–83]. The diffraction pattern of the Ti6Al4V–Mg MMM shows the diffraction peaks of Mg and α/α' -Ti phases, both showing *hcp* crystal structure. Thermal energy supplied during the SPS process may partially relax the Ti6Al4V microstructure, where partial transformation of α' phase to α phase may take place. Hence both α and α' phases coexist after

the SPS process. No additional peaks other than the Mg and α/α' -Ti phases are observed within the deductible limits of the XRD suggesting no interfacial reaction taking place during the fabrication process.

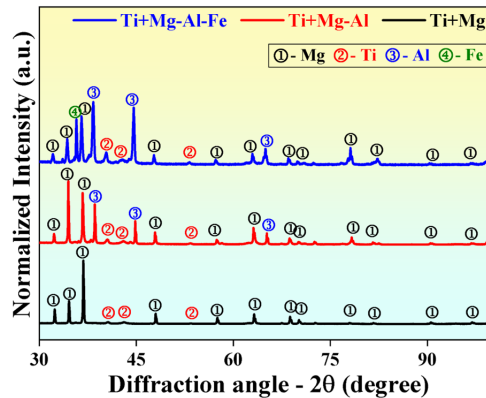


Figure 3. X-ray diffraction patterns of the different metallic multimaterial composites fabricated by the combination of additive manufacturing and powder metallurgical processes.

The diffraction pattern of the Ti6Al4V–Mg–Al MMM shows the peaks of *hcp* Mg and α/α' -Ti phases and *fcc* α -Al corresponding to the matrix and the two reinforcements in the MMM composites. No additional peaks other than the Mg, Al, and α/α' -Ti phases are observed suggesting no interfacial reaction. Similarly in the case of the third composite, where three different reinforcements are added (Mg, Al, and Fe), four phases are observed, namely, *hcp* Mg, α/α' -Ti, *fcc* α -Al, and α -Fe. Even in this case, no additional phases are observed corroborating that no intermetallic phases form at the interface due to interfacial reaction within the XRD deductible limits. The results suggest that the sintering conditions (time, pressure, and temperature and their combination) are insufficient to initiate interfacial diffusion between the matrix and interface.

The SEM (BE and BSD) images of the MMM composites are shown in Figure 4. The microstructures of the LPBF Ti6Al4V structures transform from a predominantly α' -Ti—martensitic microstructure to a α/α' -Ti microstructure after sintering. This is due to the thermal energy offered to the structures during sintering that relaxes the Ti6Al4V microstructure. In addition, the internal defects like dislocation density reduce from $\sim 3.5 \times 10^{15} \text{ m}^{-3}$ to $\sim 4.8 \times 10^{14} \text{ m}^{-3}$ due to structural relaxation of the structure with the supplied thermal energy during the SPS process. It may be observed from Figure 4 that the reinforcement particles (Mg/Al/Fe) do not form any reaction at the interface. However, there may be a chance of reaction between the reinforcements observed at the reinforcement boundaries due to particle mixing that may have occurred during the fabrication process (during powder addition to the Ti6Al4V precursor). The BSD images show the material contrast between the different reinforcement compositions and the matrix. Near the Al/Fe reinforcement boundary mixing of powder is observed. However, no concrete evidence of intermetallic phase formation can be ascertained from the SEM image corroborating the XRD patterns. The SE images show that both Mg and Al particles diffuse well during the sintering process (sintering temperature— $550 \text{ }^\circ\text{C} > 0.7T_m$) since the particle boundaries almost disappear. However, in the case of the Fe particles, the particle boundaries still exist, suggesting the diffusion between the particles is incomplete due to the employed sintering temperature ($550 \text{ }^\circ\text{C}$), which is less than $0.7T_m$.

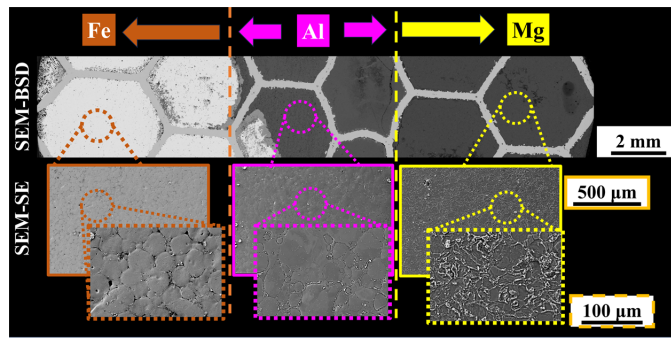


Figure 4. Scanning electron microscopy images (both secondary electron (BE) and back-scattered (BSD) modes) showing the microstructure of the Ti6Al4V–Mg–Al–Fe metallic multimaterial composite.

The hardness profile observed for the Ti6Al4V–Mg–Al–Fe MMM composite is shown in Figure 5. Since the LPBF Ti6Al4V results in α' -Ti martensitic microstructure, it offers very high hardness (~480 HV). However, after the SPS process, the hardness relaxes and hardness values of ~460 HV were observed for the Ti6Al4V structure. The reinforcement (since sintered) shows lower hardness than the solidified Ti6Al4V structure. Sintered Fe shows the highest hardness of ~110 HV, Mg showing intermediate hardness (~75 HV), and Al the least hardness (~40 HV). Since the reinforcements and the matrix lattice are placed uniquely, the hardness profile shows variation in a sinusoidal fashion (Figure 5). Such a unique hardness profile can be observed only for the novel MMM composites fabricated by combining both AM and PM processes.

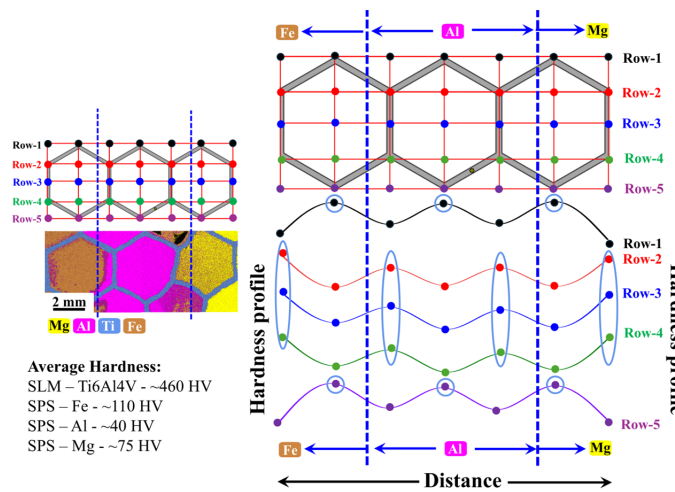


Figure 5. Hardness profile plot observed for the Ti6Al4V–Mg–Al–Fe metallic multimaterial composite fabricated by combining additive manufacturing and powder metallurgical processes.

To illustrate the feasibility of fabricating different compositions, another MMM composite with three different reinforcement compositions and matrix precursor has been manufactured. The three different reinforcement compositions are CP–Ti, CP–Ni, and CP–Cu. The matrix precursor used was 316L SS (Figure 6). Since the LPBF 316L SS shows austenitic microstructure (exhibiting *fcc* crystal structure, which is soft in nature [84–92]) and the employed sintering temperature was 1000 °C (which is ~0.7 T_m), the precursor structure was severely deformed/distorted along the CP–Ti side (which is harder as com-

pared to Ni and Cu). Since Ti is hard, it can resist the load and distort the precursor structure. However, along the Cu and Ni sides, the distortion of 316L SS was not pronounced due to the soft nature of the reinforcement and the reinforcement particles can observe the load during the SPS process. In addition, like the Ti6Al4V–Mg–Al–Fe composite, the reinforcement powders Ni and Cu were missing near their interface. However, no distinct interfacial reaction between the reinforcements and reinforcement–matrix interface is observed.

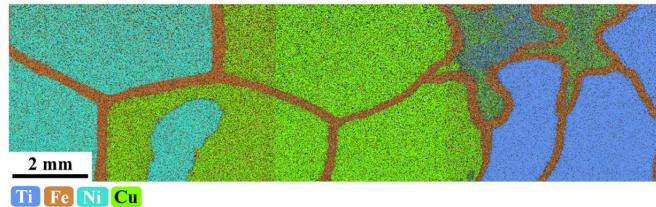


Figure 6. Scanning electron microscopy–energy dispersive spectroscopy area maps showing the individual constituents present in the 316L SS–Ti–Cu–Ni metallic multimaterial composite.

These MMM composites are subjected to sintering after the reinforcement particles are introduced to the matrix precursor (typically fabricated using AM-based processes) [93–98]. In general, no interfacial reaction between the matrix and the reinforcement particles is observed. The absence of reinforcement reaction between the matrix and interface in MMM composites may be attributed to the following: The reinforcement particles introduced into the matrix precursor are loosely packed and most of the pressure applied during the sintering process is utilized for the consolidation of the powder particles. In addition, the temperature applied during the sintering process will be quite low and the time of sintering is too short to form any reaction between the powder reinforcement particles and the matrix at the interface. The interfacial reaction may be pronounced if an extended sintering time may be offered with very high sintering temperatures (close to the melting point of the reinforcement material) [99–105]. In this study, the feasibility of manufacturing MMM composites by combining AM (LPBF) and PM (SPS) was demonstrated. Several MMM composites (bimetal—Ti6Al4V–Mg, trimetal—Ti6Al4V–Mg–Al, and multimaterials—Ti6Al4V–Mg–Al–Fe and 316L SS—Cu–Fe–Ti) were fabricated. In all these combinations, hardness was taken as the varying factor and sinusoidal hardness variation can be observed in the Ti6Al4V–Mg–Al–Fe MMM. Similarly, MMMs with other varying properties (like conductivity, corrosion, tribology, etc.) may be fabricated by carefully selecting the composition of the reinforcement(s) and matrix. The structure of the matrix may also be modified depending on the real-time application. Hence, the present study is a testimony of fabricating next-generation and novel MMM composites with multiple compositions.

4. Conclusions

The present manuscript deals with the fabrication of Ti6Al4V–Mg/Al/Fe and 316L SS/Ti/Cu/Ni MMMs by combining AM (LPBF) and PM (SPS) techniques. The results show that there is no interfacial reaction between the matrix and the reinforcement and between the different reinforcement compositions. Occasionally between the two reinforcement interfaces mixing of powder particles may be observed that arises during the powder introduction process before consolidation. The hardness profile shows a sinusoidal variation in hardness due to the distribution of the different reinforcement particles and the matrix precursor. The present study opens the avenue of fabricating MMMs with different compositions, where a diverse material property is required.

Author Contributions: Conceptualization, L.X., Z.W. and K.G.P.; methodology, M.K.Y., R.S. and K.G.P.; validation, L.X., Z.W. and K.G.P.; formal analysis, M.K.Y., R.S. and K.G.P.; investigation, M.K.Y., R.S., L.X., Z.W. and K.G.P.; resources, L.X. and K.G.P.; data curation, M.K.Y. and R.S.; writing—original draft preparation, M.K.Y., R.S., L.X. and Z.W.; writing—review and editing, K.G.P.; supervision, K.G.P.; project administration, K.G.P.; funding acquisition, L.X., Z.W. and K.G.P. All authors have read and agreed to the published version of the manuscript.

Funding: The present research was partially supported by the National Natural Science Foundation of China (52205382) and special fund of Jiangsu Province Science and Technology Plan (BZ2024019).

Data Availability Statement: Data may be shared on reasonable requests.

Conflicts of Interest: The authors declare no conflicts of interest.

References

1. Katiyar, N.K.; Goel, G.; Hawi, S.; Goel, S. Nature-Inspired Materials: Emerging Trends and Prospects. *NPG Asia Mater.* **2021**, *13*, 56. [[CrossRef](#)]
2. Li, Y.; Liu, Y.; Li, R.; Bai, H.; Zhu, Z.; Zhu, L.; Zhu, C.; Che, Z.; Liu, H.; Wang, J.; et al. Collagen-Based Biomaterials for Bone Tissue Engineering. *Mater. Des.* **2021**, *210*, 110049. [[CrossRef](#)]
3. Le Vay, L.; Egan, B. SHELLFISH (MOLLUSCS AND CRUSTACEA) | Characteristics of the Groups. In *Encyclopedia of Food Microbiology*; Elsevier: Amsterdam, The Netherlands, 1999; pp. 1993–2001. [[CrossRef](#)]
4. Kierdorf, U.; Stoffels, D.; Kierdorf, H. Element Concentrations and Element Ratios in Antler and Pedicle Bone of Yearling Red Deer (*Cervus Elaphus*) Stags—A Quantitative X-Ray Fluorescence Study. *Biol. Trace Elem. Res.* **2014**, *162*, 124–133. [[CrossRef](#)]
5. Moghaddam, A.B.; Namvar, F.; Moniri, M.; Tahir, P.M.; Azizi, S.; Mohamad, R. Nanoparticles Biosynthesized by Fungi and Yeast: A Review of Their Preparation, Properties, and Medical Applications. *Molecules* **2015**, *20*, 16540. [[CrossRef](#)]
6. Bandyopadhyay, A.; Traxel, K.D.; Bose, S. Nature-Inspired Materials and Structures Using 3D Printing. *Mater. Sci. Eng. R Rep.* **2021**, *145*, 100609. [[CrossRef](#)] [[PubMed](#)]
7. Herzog, D.; Seyda, V.; Wycisk, E.; Emmelmann, C. Additive Manufacturing of Metals. *Acta Mater.* **2016**, *117*, 371–392. [[CrossRef](#)]
8. DebRoy, T.; Wei, H.L.; Zuback, J.S.; Mukherjee, T.; Elmer, J.W.; Milewski, J.O.; Beese, A.M.; Wilson-Heid, A.; De, A.; Zhang, W. Additive Manufacturing of Metallic Components—Process, Structure and Properties. *Prog. Mater. Sci.* **2018**, *92*, 112–224. [[CrossRef](#)]
9. Aboulkhair, N.T.; Simonelli, M.; Parry, L.; Ashcroft, I.; Tuck, C.; Hague, R. 3D Printing of Aluminium Alloys: Additive Manufacturing of Aluminium Alloys Using Selective Laser Melting. *Prog. Mater. Sci.* **2019**, *106*, 100578. [[CrossRef](#)]
10. Li, S.; Yuan, S.; Zhu, J.; Wang, C.; Li, J.; Zhang, W. Additive Manufacturing-Driven Design Optimization: Building Direction and Structural Topology. *Addit. Manuf.* **2020**, *36*, 101406. [[CrossRef](#)]
11. Korpela, M.; Riikonen, N.; Pili, H.; Salminen, A.; Nyrhilä, O. Additive Manufacturing—Past, Present, and the Future. In *Technical, Economic and Societal Effects of Manufacturing 4.0*; Palgrave Macmillan: Cham, Switzerland, 2020; pp. 17–41. [[CrossRef](#)]
12. Gibson, I.; Rosen, D.; Stucker, B. *Additive Manufacturing Technologies: 3D Printing, Rapid Prototyping, and Direct Digital Manufacturing*, 2nd ed.; Springer: Berlin/Heidelberg, Germany, 2015; pp. 1–498. [[CrossRef](#)]
13. Lalegani Dezaki, M.; Serjouei, A.; Zolfagharian, A.; Fotouhi, M.; Moradi, M.; Ariffin, M.K.A.; Bodaghi, M. A Review on Additive/Subtractive Hybrid Manufacturing of Directed Energy Deposition (DED) Process. *Adv. Powder Mater.* **2022**, *1*, 100054. [[CrossRef](#)]
14. Yoo, D.J. Recent Trends and Challenges in Computer-Aided Design of Additive Manufacturing-Based Biomimetic Scaffolds and Bioartificial Organs. *Int. J. Precis. Eng. Manuf.* **2014**, *15*, 2205–2217. [[CrossRef](#)]
15. Mahmoud, D.; Elbestawi, M. Lattice Structures and Functionally Graded Materials Applications in Additive Manufacturing of Orthopedic Implants: A Review. *J. Manuf. Mater. Process.* **2017**, *1*, 13. [[CrossRef](#)]
16. Cann, J.L.; De Luca, A.; Dunand, D.C.; Dye, D.; Miracle, D.B.; Oh, H.S.; Olivetti, E.A.; Pollock, T.M.; Poole, W.J.; Yang, R.; et al. Sustainability through Alloy Design: Challenges and Opportunities. *Prog. Mater. Sci.* **2021**, *117*, 100722. [[CrossRef](#)]
17. Bertol, L.S.; Júnior, W.K.; da Silva, F.P.; Aumund-Kopp, C. Medical Design: Direct Metal Laser Sintering of Ti-6Al-4V. *Mater. Des.* **2010**, *31*, 3982–3988. [[CrossRef](#)]
18. Tan, C.; Zhou, K.; Kuang, T. Selective Laser Melting of Tungsten-Copper Functionally Graded Material. *Mater. Lett.* **2019**, *237*, 328–331. [[CrossRef](#)]
19. Wang, S.; Liu, L.; Li, K.; Zhu, L.; Chen, J.; Hao, Y. Pore Functionally Graded Ti6Al4V Scaffolds for Bone Tissue Engineering Application. *Mater. Des.* **2019**, *168*, 107643. [[CrossRef](#)]
20. Vijayavenkataraman, S.; Kuan, L.Y.; Lu, W.F. 3D-Printed Ceramic Triply Periodic Minimal Surface Structures for Design of Functionally Graded Bone Implants. *Mater. Des.* **2020**, *191*, 108602. [[CrossRef](#)]

21. Baskaran, J.; Muthukannan, D.; Shukla, R.; Konda Gokuldoss, P. Manufacturability and Deformation Studies on a Novel Metallic Lattice Structure Fabricated by Selective Laser Melting. *Vacuum* **2024**, *222*, 113065. [[CrossRef](#)]
22. Han, J.C.; Wang, B.L. Thermal Shock Resistance Enhancement of Functionally Graded Materials by Multiple Cracking. *Acta Mater.* **2006**, *54*, 963–973. [[CrossRef](#)]
23. Feng, H.; Meng, Q.; Zhou, Y.; Jia, D. Spark Plasma Sintering of Functionally Graded Material in the Ti-TiB₂-B System. *Mater. Sci. Eng. A* **2005**, *397*, 92–97. [[CrossRef](#)]
24. Zhang, X.Y.; Fang, G.; Xing, L.L.; Liu, W.; Zhou, J. Effect of Porosity Variation Strategy on the Performance of Functionally Graded Ti-6Al-4V Scaffolds for Bone Tissue Engineering. *Mater. Des.* **2018**, *157*, 523–538. [[CrossRef](#)]
25. Wei, C.; Li, L. Recent Progress and Scientific Challenges in Multi-Material Additive Manufacturing via Laser-Based Powder Bed Fusion. *Virtual Phys. Prototyp.* **2021**, *16*, 347–371. [[CrossRef](#)]
26. Verma, A.; Kapil, A.; Klobčar, D.; Sharma, A. A Review on Multiplicity in Multi-Material Additive Manufacturing: Process, Capability, Scale, and Structure. *Materials* **2023**, *16*, 5246. [[CrossRef](#)]
27. Chen, D.; Zheng, X. Multi-Material Additive Manufacturing of Metamaterials with Giant, Tailorable Negative Poisson's Ratios. *Sci. Rep.* **2018**, *8*, 9139. [[CrossRef](#)]
28. Nazir, A.; Gokcekaya, O.; Md Masum Billah, K.; Ertugrul, O.; Jiang, J.; Sun, J.; Hussain, S. Multi-Material Additive Manufacturing: A Systematic Review of Design, Properties, Applications, Challenges, and 3D Printing of Materials and Cellular Metamaterials. *Mater. Des.* **2023**, *226*, 111661. [[CrossRef](#)]
29. Prashanth, K.G. Interpenetrating Composites: A Nomenclature Dilemma. *Materials* **2025**, *18*, 273. [[CrossRef](#)]
30. Zhang, Z.; Wang, Z.; Zhao, Q.; Prashanth, K.G. Metal-Metal Interpenetrating Phase Composites: A Review. *J. Alloys Compd.* **2024**, *1009*, 176951. [[CrossRef](#)]
31. Liu, Y.; Chen, B.; Liu, Z.; Zhang, Z.; Ritchie, R.O. Bioinspired Interpenetrating-Phase Metal Composites. *Prog. Mater. Sci.* **2024**, *144*, 101281. [[CrossRef](#)]
32. Zhang, M.; Yu, Q.; Liu, Z.; Zhang, J.; Tan, G.; Jiao, D.; Zhu, W.; Li, S.; Zhang, Z.; Yang, R.; et al. 3D Printed Mg-NiTi Interpenetrating-Phase Composites with High Strength, Damping Capacity, and Energy Absorption Efficiency. *Sci. Adv.* **2020**, *6*, 5581–5589. [[CrossRef](#)]
33. Zhang, M.; Zhao, N.; Yu, Q.; Liu, Z.; Qu, R.; Zhang, J.; Li, S.; Ren, D.; Berto, F.; Zhang, Z.; et al. On the Damage Tolerance of 3-D Printed Mg-Ti Interpenetrating-Phase Composites with Bioinspired Architectures. *Nat. Commun.* **2022**, *13*, 3247. [[CrossRef](#)]
34. Mattern, A.; Huchler, B.; Staudenecker, D.; Oberacker, R.; Nagel, A.; Hoffmann, M.J. Preparation of Interpenetrating Ceramic-Metal Composites. *J. Eur. Ceram. Soc.* **2004**, *24*, 3399–3408. [[CrossRef](#)]
35. Merzkirch, M.; Blümel, C.; Rössler, R.; Schell, K.G.; Bucharsky, E.C.; Weidenmann, K.A. Manufacturing and Characterization of Interpenetrating SiC Lightweight Composites. *Procedia CIRP* **2014**, *18*, 102–107. [[CrossRef](#)]
36. Wang, B.; Zhao, S.; Ojima, F.; Yang, J.F.; Ishizaki, K. Pulse Electric Current Sintering of 3D Interpenetrating SiC/Al Composites. *Ceram. Int.* **2017**, *43*, 2867–2870. [[CrossRef](#)]
37. Moon, R.J.; Tilbrook, M.; Hoffman, M.; Neubrand, A. Al-Al₂O₃ Composites with Interpenetrating Network Structures: Composite Modulus Estimation. *J. Am. Ceram. Soc.* **2005**, *88*, 666–674. [[CrossRef](#)]
38. Prielipp, H.; Knechtel, M.; Claussen, N.; Streiffer, S.K.; Müllejans, H.; Rühle, M.; Rödel, J. Strength and Fracture Toughness of Aluminum/Alumina Composites with Interpenetrating Networks. *Mater. Sci. Eng. A* **1995**, *197*, 19–30. [[CrossRef](#)]
39. Drotárová, L.; Slámečka, K.; Balint, T.; Remešová, M.; Hudák, R.; Živčák, J.; Schnitzer, M.; Čelko, L.; Montufar, E.B. Biodegradable WE43 Mg Alloy/Hydroxyapatite Interpenetrating Phase Composites with Reduced Hydrogen Evolution. *Bioact. Mater.* **2024**, *42*, 519–530. [[CrossRef](#)]
40. Guo, X.; Ding, J.; Li, X.; Qu, S.; Hsi Fuh, J.Y.; Lu, W.F.; Song, X.; Zhai, W. Interpenetrating Phase Composites with 3D Printed Triply Periodic Minimal Surface (TPMS) Lattice Structures. *Compos. B Eng.* **2023**, *248*, 110351. [[CrossRef](#)]
41. Mortensen, A. Melt Infiltration of Metal Matrix Composites. *Compr. Compos. Mater.* **2000**, *3*, 521–554. [[CrossRef](#)]
42. Sasaki, G.; Adachi, J.; Choi, Y.B.; Pan, J.; Fujii, T.; Matsugi, K.; Yanagisawa, O. Fabrication of the Aluminum Matrix Composite by Ultrasonic Infiltration Technique. *Mater. Sci. Forum* **2005**, *475–479*, 921–924. [[CrossRef](#)]
43. Sampath, V.; Ramanan, N.; Palaninathan, R. Modeling of Liquid Metal Infiltration of Porous Fiber Preform During Squeeze Casting. *Mater. Manuf. Process.* **2006**, *21*, 495–505. [[CrossRef](#)]
44. Travitzky, N.A. Microstructure and Mechanical Properties of Alumina/Copper Composites Fabricated by Different Infiltration Techniques. *Mater. Lett.* **1998**, *36*, 114–117. [[CrossRef](#)]
45. Srinivasa Rao, B.; Jayaram, V. Pressureless Infiltration of Al-Mg Based Alloys into Al₂O₃ Preforms: Mechanisms and Phenomenology. *Acta Mater.* **2001**, *49*, 2373–2385. [[CrossRef](#)]
46. Hinojos, A.; Mireles, J.; Reichardt, A.; Frigola, P.; Hosemann, P.; Murr, L.E.; Wicker, R.B. Joining of Inconel 718 and 316 Stainless Steel Using Electron Beam Melting Additive Manufacturing Technology. *Mater. Des.* **2016**, *94*, 17–27. [[CrossRef](#)]
47. Mei, X.; Wang, X.; Peng, Y.; Gu, H.; Zhong, G.; Yang, S. Interfacial Characterization and Mechanical Properties of 316L Stainless Steel/Inconel 718 Manufactured by Selective Laser Melting. *Mater. Sci. Eng. A* **2019**, *758*, 185–191. [[CrossRef](#)]

48. Sagong, M.J.; Kim, E.S.; Park, J.M.; Karthik, G.M.; Lee, B.J.; Cho, J.W.; Lee, C.S.; Nakano, T.; Kim, H.S. Interface Characteristics and Mechanical Behavior of Additively Manufactured Multi-Material of Stainless Steel and Inconel. *Mater. Sci. Eng. A* **2022**, *847*, 143318. [[CrossRef](#)]
49. Zinkle, S.J.; Was, G.S. Materials Challenges in Nuclear Energy. *Acta Mater.* **2013**, *61*, 735–758. [[CrossRef](#)]
50. Leedy, K.D.; Stubbins, J.F. Copper Alloy–Stainless Steel Bonded Laminates for Fusion Reactor Applications: Crack Growth and Fatigue. *Mater. Sci. Eng. A* **2001**, *297*, 19–25. [[CrossRef](#)]
51. Liu, Z.H.; Zhang, D.Q.; Sing, S.L.; Chua, C.K.; Loh, L.E. Interfacial Characterization of SLM Parts in Multi-Material Processing: Metallurgical Diffusion between 316L Stainless Steel and C18400 Copper Alloy. *Mater. Charact.* **2014**, *94*, 116–125. [[CrossRef](#)]
52. Schimek, M.; Springer, A.; Kaierle, S.; Kracht, D.; Wesling, V. Laser-Welded Dissimilar Steel-Aluminum Seams for Automotive Lightweight Construction. *Phys. Procedia* **2012**, *39*, 43–50. [[CrossRef](#)]
53. Scaramuccia, M.G.; Demir, A.G.; Caprio, L.; Tassa, O.; Previtali, B. Development of Processing Strategies for Multigraded Selective Laser Melting of Ti6Al4V and IN718. *Powder Technol.* **2020**, *367*, 376–389. [[CrossRef](#)]
54. Sing, S.L.; Lam, L.P.; Zhang, D.Q.; Liu, Z.H.; Chua, C.K. Interfacial Characterization of SLM Parts in Multi-Material Processing: Intermetallic Phase Formation between AlSi10Mg and C18400 Copper Alloy. *Mater. Charact.* **2015**, *107*, 220–227. [[CrossRef](#)]
55. Chen, K.; Wang, C.; Hong, Q.; Wen, S.; Zhou, Y.; Yan, C.; Shi, Y. Selective Laser Melting 316L/CuSn10 Multi-Materials: Processing Optimization, Interfacial Characterization and Mechanical Property. *J. Mater. Process Technol.* **2020**, *283*, 116701. [[CrossRef](#)]
56. Wei, C.; Li, L.; Zhang, X.; Chueh, Y.H. 3D Printing of Multiple Metallic Materials via Modified Selective Laser Melting. *CIRP Ann.* **2018**, *67*, 245–248. [[CrossRef](#)]
57. Al-Jamal, O.M.; Hinduja, S.; Li, L. Characteristics of the Bond in Cu–H13 Tool Steel Parts Fabricated Using SLM. *CIRP Ann.* **2008**, *57*, 239–242. [[CrossRef](#)]
58. Wei, C.; Chueh, Y.H.; Zhang, X.; Huang, Y.; Chen, Q.; Li, L. Easy-To-Remove Composite Support Material and Procedure in Additive Manufacturing of Metallic Components Using Multiple Material Laser-Based Powder Bed Fusion. *J. Manuf. Sci. Eng. Trans. ASME* **2019**, *141*, 071002. [[CrossRef](#)]
59. Terrazas, C.A.; Gaytan, S.M.; Rodriguez, E.; Espalin, D.; Murr, L.E.; Medina, F.; Wicker, R.B. Multi-Material Metallic Structure Fabrication Using Electron Beam Melting. *Int. J. Adv. Manuf. Technol.* **2014**, *71*, 33–45. [[CrossRef](#)]
60. McDonnell, B.; Errico, V.; Posa, P.; Angelastro, A.; Furman, A.; O’Hara, E.; Campanelli, S.L.; Harrison, N. Bi-Metallic Lattice Structures Manufactured via an Intralayer Multi-Material Powder Bed Fusion Method. *Addit. Manuf.* **2024**, *89*, 104301. [[CrossRef](#)]
61. Roach, D.J.; Hamel, C.M.; Dunn, C.K.; Johnson, M.V.; Kuang, X.; Qi, H.J. The M4 3D Printer: A Multi-Material Multi-Method Additive Manufacturing Platform for Future 3D Printed Structures. *Addit. Manuf.* **2019**, *29*, 100819. [[CrossRef](#)]
62. Benyahia, K.; Seriket, H.; Prod’hon, R.; Gomes, S.; André, J.C.; Qi, H.J.; Demoly, F. A Computational Design Approach for Multi-Material 4D Printing Based on Interlocking Blocks Assembly. *Addit. Manuf.* **2022**, *58*, 102993. [[CrossRef](#)]
63. Chueh, Y.H.; Zhang, X.; Ke, J.C.R.; Li, Q.; Wei, C.; Li, L. Additive Manufacturing of Hybrid Metal/Polymer Objects via Multiple-Material Laser Powder Bed Fusion. *Addit. Manuf.* **2020**, *36*, 101465. [[CrossRef](#)]
64. Ritchie, R.O. The Conflicts between Strength and Toughness. *Nat. Mater.* **2011**, *10*, 817–822. [[CrossRef](#)] [[PubMed](#)]
65. Rocha, V.G.; Saiz, E.; Tirichenko, I.S.; García-Tuñón, E. Direct Ink Writing Advances in Multi-Material Structures for a Sustainable Future. *J. Mater. Chem. A Mater.* **2020**, *8*, 15646–15657. [[CrossRef](#)]
66. Czerwinski, F. Current Trends in Automotive Lightweighting Strategies and Materials. *Materials* **2021**, *14*, 6631. [[CrossRef](#)] [[PubMed](#)]
67. Shukla, R.; Yadav, M.K.; Madruga, L.Y.C.; Jayaraj, J.; Popat, K.; Wang, Z.; Xi, L.; Prashanth, K.G. A Novel Ti-Eggshell-Based Composite Fabricated by Combined Additive Manufacturing–Powder Metallurgical Routes as Bioimplants. *Ceram. Int.* **2025**, *51*, 6281–6291. [[CrossRef](#)]
68. Singh, N.; Hameed, P.; Ummethala, R.; Manivasagam, G.; Prashanth, K.G.; Eckert, J. Selective Laser Manufacturing of Ti-Based Alloys and Composites: Impact of Process Parameters, Application Trends, and Future Prospects. *Mater. Today Adv.* **2020**, *8*, 100097. [[CrossRef](#)]
69. Kumar, D.; Shankar, G.; Prashanth, K.G.; Suwas, S. Control of Texture and Microstructure in Additive Manufacturing of Stainless Steel 316 L. *J. Alloys Compd.* **2023**, *976*, 173040. [[CrossRef](#)]
70. Kumar, D.; Shankar, G.; Prashanth, K.G.; Suwas, S. Texture Dependent Strain Hardening in Additively Manufactured Stainless Steel 316L. *Mater. Sci. Eng. A* **2021**, *820*, 141483. [[CrossRef](#)]
71. Kumar, D.; Jhavar, S.; Arya, A.; Prashanth, K.G.; Suwas, S. Mechanisms Controlling Fracture Toughness of Additively Manufactured Stainless Steel 316L. *Int. J. Fract.* **2021**, *235*, 61–78. [[CrossRef](#)]
72. Zhao, C.; Wang, Z.; Li, D.; Kollo, L.; Luo, Z.; Zhang, W.; Prashanth, K.G. Cu-Ni-Sn Alloy Fabricated by Melt Spinning and Selective Laser Melting: A Comparative Study on the Microstructure and Formation Kinetics. *J. Mater. Res. Technol.* **2020**, *9*, 13097–13105. [[CrossRef](#)]
73. Karimi, J.; Suryanarayana, C.; Okulov, I.; Prashanth, K.G. Selective Laser Melting of Ti6Al4V: Effect of Laser Re-Melting. *Mater. Sci. Eng. A* **2020**, *805*, 140558. [[CrossRef](#)]

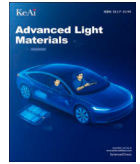
74. Prashanth, K.G.; Damodaram, R.; Maity, T.; Wang, P.; Eckert, J. Friction Welding of Selective Laser Melted Ti6Al4V Parts. *Mater. Sci. Eng. A* **2017**, *704*, 66–71. [[CrossRef](#)]
75. Karimi, J.; Kollo, L.; Prashanth, K.G. Tailoring Anisotropy and Heterogeneity of Selective Laser Melted Ti6Al4V Alloys. *Trans. Indian Natl. Acad. Eng.* **2023**, *8*, 245–251. [[CrossRef](#)]
76. Wang, F.; Mei, J.; Wu, X. Direct Laser Fabrication of Ti6Al4V/TiB. *J. Mater. Process Technol.* **2008**, *195*, 321–326. [[CrossRef](#)]
77. Liu, S.; Shin, Y.C. Additive Manufacturing of Ti6Al4V Alloy: A Review. *Mater. Des.* **2019**, *164*, 107552. [[CrossRef](#)]
78. Yadroitsava, I.; Grewar, S.; Hattingh, D.; Yadroitsev, I. Residual Stress in SLM Ti6Al4V Alloy Specimens. In *Materials Science Forum*; Trans Tech Publications Ltd.: Wollerau, Switzerland, 2015; Volume 828–829, pp. 305–310. [[CrossRef](#)]
79. Onuikwe, B.; Bandyopadhyay, A. Additive Manufacturing of Inconel 718—Ti6Al4V Bimetallic Structures. *Addit. Manuf.* **2018**, *22*, 844–851. [[CrossRef](#)]
80. Wang, Z.; Xie, M.; Li, Y.; Zhang, W.; Yang, C.; Kollo, L.; Eckert, J.; Prashanth, K.G. Premature Failure of an Additively Manufactured Material. *NPG Asia Mater.* **2020**, *12*, 30. [[CrossRef](#)]
81. Zhao, C.; Wang, Z.; Li, D.; Kollo, L.; Luo, Z.; Zhang, W.; Prashanth, K.G. Selective Laser Melting of Cu–Ni–Sn: A Comprehensive Study on the Microstructure, Mechanical Properties, and Deformation Behavior. *Int. J. Plast.* **2021**, *138*, 102926. [[CrossRef](#)]
82. Jung, H.Y.; Choi, S.J.; Prashanth, K.G.; Stoica, M.; Scudino, S.; Yi, S.; Kühn, U.; Kim, D.H.; Kim, K.B.; Eckert, J. Fabrication of Fe-Based Bulk Metallic Glass by Selective Laser Melting: A Parameter Study. *Mater. Des.* **2015**, *86*, 703–708. [[CrossRef](#)]
83. Zhao, C.; Wang, Z.; Li, D.; Xie, M.; Kollo, L.; Luo, Z.; Zhang, W.; Prashanth, K.G. Comparison of Additively Manufacturing Samples Fabricated from Pre-Alloyed and Mechanically Mixed Powders. *J. Alloys Compd.* **2020**, *830*, 154603. [[CrossRef](#)]
84. Bedmar, J.; Riquelme, A.; Rodrigo, P.; Torres, B.; Rams, J. Comparison of Different Additive Manufacturing Methods for 316L Stainless Steel. *Materials* **2021**, *14*, 6504. [[CrossRef](#)]
85. Chen, S.; Ma, G.; Wu, G.; Godfrey, A.; Huang, T.; Huang, X. Strengthening Mechanisms in Selective Laser Melted 316L Stainless Steel. *Mater. Sci. Eng. A* **2022**, *832*, 142434. [[CrossRef](#)]
86. Suryawanshi, J.; Prashanth, K.G.; Ramamurthy, U. Mechanical Behavior of Selective Laser Melted 316L Stainless Steel. *Mater. Sci. Eng. A* **2017**, *696*, 113–121. [[CrossRef](#)]
87. Zhang, S.Y.; Compagnon, E.; Godin, B.; Korsunsky, A.M. Investigation of Martensite Transformation in 316L Stainless Steel. In *Proceedings of the Materials Today: Proceedings*; Elsevier Ltd.: Amsterdam, The Netherlands, 2015; Volume 2, pp. S251–S260.
88. Zhai, W.; Zhu, Z.; Zhou, W.; Nai, S.M.L.; Wei, J. Selective Laser Melting of Dispersed TiC Particles Strengthened 316L Stainless Steel. *Compos. B Eng.* **2020**, *199*, 108291. [[CrossRef](#)]
89. Brytan, Z. Comparison of Vacuum Sintered and Selective Laser Melted Steel AISI 316L. *Arch. Metall. Mater.* **2017**, *62*, 2125–2131. [[CrossRef](#)]
90. Wang, C.; Lin, X.; Wang, L.; Zhang, S.; Huang, W. Cryogenic Mechanical Properties of 316L Stainless Steel Fabricated by Selective Laser Melting. *Mater. Sci. Eng. A* **2021**, *815*, 141317. [[CrossRef](#)]
91. Shamsujjoha, M.; Agnew, S.R.; Fitz-Gerald, J.M.; Moore, W.R.; Newman, T.A. High Strength and Ductility of Additively Manufactured 316L Stainless Steel Explained. *Metall. Mater. Trans. A Phys. Metall. Mater. Sci.* **2018**, *49*, 3011–3027. [[CrossRef](#)]
92. Li, Z.; Yang, Z.; Liu, B.; Yang, S.; Kuai, Z.; Li, J.; Li, H.; Chen, Y.; Wu, H.; Bai, P. Microstructure and Mechanical Properties of CNC-SLM Hybrid Manufacturing 316L Parts. *J. Manuf. Process* **2022**, *79*, 432–441. [[CrossRef](#)]
93. Tang, S.H.; Cheng, C.W.; Yeh, R.Y.; Hsu, R.Q. Direct Joining of 3D-Printed Thermoplastic Parts to SLM-Fabricated Metal Cellular Structures by Ultrasonic Welding. *Int. J. Adv. Manuf. Technol.* **2018**, *99*, 729–736. [[CrossRef](#)]
94. Yang, E.; Leary, M.; Lozanovski, B.; Downing, D.; Mazur, M.; Sarker, A.; Khorasani, A.M.; Jones, A.; Maconachie, T.; Bateman, S.; et al. Effect of Geometry on the Mechanical Properties of Ti-6Al-4V Gyroid Structures Fabricated via SLM: A Numerical Study. *Mater. Des.* **2019**, *184*, 108165. [[CrossRef](#)]
95. Ge, J.; Huang, J.; Lei, Y.; O'Reilly, P.; Ahmed, M.; Zhang, C.; Yan, X.; Yin, S. Microstructural Features and Compressive Properties of SLM Ti6Al4V Lattice Structures. *Surf. Coat. Technol.* **2020**, *403*, 126419. [[CrossRef](#)]
96. Moniruzzaman, M.; O'neal, C.; Bhuiyan, A.; Egan, P.F. Design and Mechanical Testing of 3d Printed Hierarchical Lattices Using Biocompatible Stereolithography. *Designs* **2020**, *4*, 22. [[CrossRef](#)]
97. Mulhi, A.; Dehgahi, S.; Waghmare, P.; Qureshi, A. Dimensional Assessment of Uniformly Periodic Porosity Primitive TPMS Lattices Using Additive Manufacturing Laser Powder Bed Fusion Technique. *Int. J. Adv. Manuf. Technol.* **2023**, *124*, 2127–2148. [[CrossRef](#)]
98. De Wild, M.; Ghayor, C.; Zimmermann, S.; Rüegg, J.; Nicholls, F.; Schuler, F.; Chen, T.H.; Weber, F.E. Osteoconductive Lattice Microarchitecture for Optimized Bone Regeneration. *3d Print. Addit. Manuf.* **2019**, *6*, 40–49. [[CrossRef](#)]
99. Guo, R.F.; Wang, Y.; Shen, P.; Shaga, A.; Ma, Y.H.; Jiang, Q.C. Influence of Matrix Property and Interfacial Reaction on the Mechanical Performance and Fracture Mechanism of TiC Reinforced Al Matrix Lamellar Composites. *Mater. Sci. Eng. A* **2020**, *775*, 138956. [[CrossRef](#)]
100. Xiong, B.; Zheng, F.; Cheng, D.; Zhu, Q.; Niu, Z.; Wang, Z.; Chen, Y.; Li, Y.; Liu, Z.; Wang, Z.; et al. Interfacial Reaction Induced Mechanical Behaviors in Graphene Reinforced Nb/Nb5Si3 Composites. *Mater. Today Commun.* **2024**, *39*, 109014. [[CrossRef](#)]

101. Bai, Y.; Zhou, J.; Zhao, C.; Yun, K.; Qi, L. Inhibition of Interfacial Reaction and Enhancement of Mechanical Properties of CF/Al Composite. *Mater. Charact.* **2024**, *216*, 114258. [[CrossRef](#)]
102. Liu, Z.; Bao, J.; Hu, W.; Yan, H. Microstructure, Interfacial Reaction Behavior, and Mechanical Properties of Ti₃AlC₂ Reinforced Al6061 Composites. *Trans. Nonferrous Met. Soc. China* **2024**, *34*, 2756–2771. [[CrossRef](#)]
103. Jiang, J.; Wang, Y.; Yang, L.; Jia, Q.; Zhang, Y.; Li, M.; Zhang, X.; Kong, X.; Zhang, G.; Yang, Q.; et al. Interfacial Reaction and Matrix Microstructure Evolution of SiCf/Ti₂AlNb Composites Induced by Hot Isostatic Pressing. *J. Alloys Compd.* **2024**, *1008*, 176554. [[CrossRef](#)]
104. Wang, X.; Wang, Y.; Zhang, T.; Liu, X. Flash Joining of C/C Composite with Ag-Cu-Ti Filler by Spark Plasma Sintering: The Promoting and Inhibiting Effects on the Interfacial Reactions. *Ceram. Int.* **2024**. *in press*. [[CrossRef](#)]
105. Hu, Q.; Chen, H.; Fu, W.; Zhou, L.; Deng, Y. Effect of Titanium Element on the Interfacial Reactions and Properties of B₄C/Al Composites Fabricated by Selective Laser Melting. *Mater. Chem. Phys.* **2025**, *333*, 130385. [[CrossRef](#)]

Disclaimer/Publisher’s Note: The statements, opinions and data contained in all publications are solely those of the individual author(s) and contributor(s) and not of MDPI and/or the editor(s). MDPI and/or the editor(s) disclaim responsibility for any injury to people or property resulting from any ideas, methods, instructions or products referred to in the content.

Publication V

M.K. Yadav, K. Praveenkumar, R.H. Shukla, S. Nilawar, C.S. Perugu, K. Chatterjee, S. Suwas, J. Jayaraj, K.G. Prashanth, Novel partially biodegradable Ti-6Al-4V/Zn composites fabricated through hybrid additive manufacturing and powder metallurgy, *Advanced Light Materials* 1 (2026) 1-18. <https://doi.org/10.1016/j.almate.2026.03.001>



Novel partially biodegradable Ti-6Al-4V/Zn composites fabricated through hybrid additive manufacturing and powder metallurgy

Mayank Kumar Yadav^a, K. Praveenkumar^b, Riddhi Hirenkumar Shukla^c, Sagar Nilawar^d, Chandra Sekhar Perugu^e, Kaushik Chatterjee^d, Satyam Suwas^d, J. Jayaraj^{f,g}, K.G. Prashanth^{a,h,i,*}

^a Department of Mechanical and Industrial Engineering, Tallinn University of Technology, Ehitajate tee 5, Tallinn 19086, Estonia

^b Faculty of Materials Science and Technology, VSB-Technical University of Ostrava, 17. listopadu 2172/15, Ostrava 70 800, Czech Republic

^c Multifunctional Materials Manufacturing Laboratory, Wolfson School of Mechanical, Electrical and Manufacturing Engineering, Loughborough University, Loughborough LE11 3TU, UK

^d Department of Materials Engineering, Indian Institute of Science, Bangalore 560012, India

^e Emerging Nanoscience Research Institute (EnRI) Nanyang Technological University, 50 Nanyang Avenue, 639798, Singapore

^f Materials Technology, School of Information and Engineering, Dalarna University, Falun, Sweden

^g Department of Mechanical and Materials Engineering, Karlstad University, Karlstad SE-65188, Sweden

^h Department of Biosciences, Saveetha School of Engineering, Saveetha Institute of Medical and Technical Sciences, Chennai 602117, India

ⁱ National Engineering Research Center of Near-net-shape Forming for Metallic Materials, South China University of Technology, Guangzhou 510641, China

ARTICLE INFO

Keywords:

Metallic Bi-metal composite
Additive manufacturing
Spark plasma sintering
Biodegradation
In-vitro biocompatibility

ABSTRACT

This study reports the development of a Ti6Al4V-Zn metallic bi-metal composite (Ti64-Zn MBMC) engineered for biodegradable biomedical applications. The composite features a continuous additively manufactured (AM) Ti64 hexagonal lattice that provides a three-dimensional structural framework, while Zn infiltrates and occupies the interconnected pore network. Fabrication was achieved through a hybrid route combining AM and powder metallurgy, wherein the Ti64 lattice was first produced by AM, followed by Zn incorporation and consolidation via spark plasma sintering. The tomography results reveal that the composite consists of approximately 27% Ti64 reinforcement phase and 73% Zn matrix phase, confirming successful introduction of Zn within the architected Ti64 honeycomb scaffold. Microstructural characterization confirmed a crack-free interface with no detectable interfacial reactions between Ti64 and Zn. The Ti64-Zn MBMC exhibited a compressive strength of 292 ± 25 MPa, surpassing that of both pure Zn and the Ti64 lattice. Potentiodynamic polarization in simulated body fluid (SBF) revealed corrosion behavior comparable to pure Zn, with post-corrosion microscopy showing selective dissolution of Zn while Ti64 struts remained intact. *In-vitro* biodegradation tests indicated an initial degradation rate of 0.1577 mm/year in SBF. Cytocompatibility assessments using MC3T3-E1 pre-osteoblasts demonstrated healthy cell proliferation in media conditioned with composite leachates. Collectively, these results establish the Ti64-Zn MBMC as a promising candidate for next-generation biodegradable implants and tissue-engineering scaffolds.

1. Introduction

The growing demand for bone implants, driven largely by an aging global population, has intensified efforts to develop reliable, biocompatible materials that closely replicate the mechanical and biological characteristics of natural bone [1]. Metallic implants remain widely used due to their superior mechanical performance, including high fracture toughness, excellent fatigue resistance, and good machinability [2–5]. Among these, titanium (Ti) and its alloys, stainless

steel (SS), and cobalt-chromium (CoCr) alloys are the most established choices in clinical practice [6–10]. However, their significantly higher stiffness compared to bone, combined with their non-degradable nature, can lead to long-term complications such as implant failure and the need for revision surgeries. A major concern is stress shielding, a phenomenon in which the stiffer implant absorbs a disproportionate share of the mechanical load, thereby reducing the stress transmitted to the surrounding bone [11–13]. Because bone remodels in response to mechanical stimuli, insufficient loading can trigger bone resorption and

Peer review under responsibility of Editorial Office of Advanced Light Materials

* Corresponding author at: Department of Mechanical and Industrial Engineering, Tallinn University of Technology, Ehitajate tee 5, Tallinn 19086, Estonia.

E-mail addresses: kgprashanth@gmail.com, prashanth.konda@taltech.ee, kgp@scut.edu.cn (K.G. Prashanth).

<https://doi.org/10.1016/j.almate.2026.03.001>

Received 2 February 2026; Received in revised form 25 February 2026; Accepted 1 March 2026

3117-3144/© 2026 The Authors. Publishing services by Elsevier B.V. on behalf of KeAi Communications Co. Ltd. This is an open access article under the CC BY license (<http://creativecommons.org/licenses/by/4.0/>).

loss of bone density, resulting in implant loosening and failure [14]. Although the precise mechanical cues governing this process remain under debate, parameters such as stress, strain, and strain energy density are commonly used to evaluate the severity of stress shielding [15]. To address the limitations of conventional metallic implants, two major strategies have gained prominence: the design of porous metallic scaffolds and the development of biodegradable metallic systems [16–18]. Introducing controlled porosity enables tailoring of the implant's elastic modulus, thereby mitigating stress shielding while simultaneously promoting bone ingrowth and long-term fixation through mechanical interlocking. Studies indicate that pore sizes around 300 μm are optimal for facilitating bone tissue infiltration and fluid transport [19,20]. However, increasing porosity typically compromises mechanical integrity, particularly fatigue resistance [15,21]. For example, Wang et al [22] demonstrated that a TiNbZr alloy with 74% porosity exhibited a compressive strength below 50 MPa, whereas reducing porosity to 42% increased strength to approximately 500 MPa.

Biodegradable metallic implants represent another promising pathway for achieving biocompatibility and bioactivity while maintaining adequate mechanical performance. Magnesium (Mg), zinc (Zn), and iron (Fe) are the leading candidates in this category [23–25]. Mg is especially attractive due to its high specific strength and an elastic modulus of 41 GPa, which closely matches that of natural bone [26–28]. Nevertheless, its rapid corrosion in physiological environments leads to excessive Mg^{2+} release, premature loss of mechanical integrity, and the formation of hydrogen gas pockets that can impede bone regeneration [29–31]. Fe and its alloys also exhibit biodegradability but corrode too slowly for most clinical applications due to the formation of a stable passive oxide layer [32,33]. This slower degradation is attributed to the formation of a stable oxide layer, which limits the dissolution rate. Studies on Fe-based stents have reported incomplete corrosion over extended periods, emphasizing the need for alloying strategies to enhance degradation rates [32]. Prolonged persistence of Fe-based implants has been reported in stent applications, highlighting the need for alloying strategies to accelerate degradation. Additionally, the ferromagnetic nature of Fe complicates magnetic resonance imaging (MRI), limiting its clinical utility [23]. Among biodegradable metals, Zn has emerged as a particularly compelling option due to its moderate degradation rate, favorable biocompatibility, and ability to support bone regeneration [34–37]. As an essential trace element involved in DNA synthesis, apoptosis regulation, and enzymatic activity, Zn plays a vital physiological role, with recommended daily intakes of 11 mg/day for men and 8 mg/day for women [32,38]. However, despite its biological advantages, the mechanical strength of pure Zn remains insufficient for load-bearing orthopedic applications [39,40].

To address these challenges, researchers have increasingly focused on developing next-generation metallic implants known as interpenetrating phase composites (IPCs). IPCs are a unique class of multi-material composites in which at least one phase forms a topologically continuous network, while the second phase is uniformly distributed throughout the structure [41]. A key advantage of IPCs is their inherent structural redundancy: even if one phase undergoes degradation, the remaining continuous phase can maintain mechanical integrity and load-bearing capability [42–45]. Drawing inspiration from natural materials, bio-inspired IPC architectures have been proposed to enhance strength, toughness, and damage tolerance [46–48]. Although such architectures have been successfully realized in polymer-based systems due to their fabrication flexibility [49–51], replicating similar complex designs in metallic systems remains a significant challenge.

Additive manufacturing (AM) offers a promising pathway for producing intricate metallic architectures with controlled porosity and geometry mimicking biological structures [52–56]. By enabling layer-by-layer fabrication, AM allows tailoring pore size, shape, and interconnectivity to match the mechanical, and biological requirements of load-bearing implants. This level of architectural control is difficult to achieve with conventional manufacturing routes and makes AM particularly well suited for creating biomimetic scaffolds that balance

mechanical strength, permeability, and tissue-integration potential [57–61]. However, the development of multi-phase IPCs via AM is still in its early stages, as most efforts have focused on single-material or single-alloy systems, and integrating multiple metallic phases substantially increases processing complexity. This study introduces a viable strengthening strategy by integrating a Ti64 structural framework with Zn to create a Ti64-Zn MBMC using a hybrid AM and PM approach, following a design philosophy analogous to IPCs. Based on the fabrication routes and phase topologies, MBMCs can be clearly distinguished from IPCs. IPCs are defined as bi-continuous composites in which both constituent phases form fully interconnected three-dimensional networks and are independently load-bearing. Scientifically, IPCs represent a class of heterogeneous materials composed of multiple topologically continuous, 3D-interconnected phases that mutually interpenetrate. Such systems are typically achieved through infiltration-based approaches, where a secondary phase penetrates a pre-existing porous precursor matrix, resulting in genuine three-dimensional interconnectivity of both phases. In contrast, when the secondary phase is introduced into the precursor matrix via powder metallurgy-based consolidation routes, such as pressureless sintering, SPS, hot pressing, or extrusion, the processing mechanism differs fundamentally from infiltration. In these cases, the added phase does not interpenetrate the matrix in a topological sense but is externally incorporated and consolidated, akin to conventional composite processing. Consequently, such materials do not strictly meet the architectural and fabrication criteria of IPCs and may instead be classified as metallic multimaterials. When only two metallic phases are involved, these systems may be more specifically described as metallic bimaterials; accordingly, when both the matrix and reinforcement are metallic, the composite is categorized as an MBMC 17951[41,62].

In the present study a Ti64 hexagonal honeycomb structure with continuous walls was fabricated to encapsulate Zn within its interconnected porous network [63]. The continuous-wall architecture was specifically selected to ensure structural integrity, enhance load transfer, and enable effective Zn retention throughout the composite. Inspired by natural bee-comb geometries, the honeycomb design offers an exceptional strength-to-weight ratio, superior energy absorption, and high structural stability [64,65]. Its interconnected hexagonal topology promotes efficient load distribution, improves impact resistance, and minimizes material usage while maintaining mechanical robustness [64–67]. Although honeycomb structures have traditionally been employed in engineering applications for their energy-absorbing and structural efficiency [68,69], they have recently gained traction in biomedical implant design due to their biomechanical relevance [70,71]. The hexagonal honeycomb geometry closely mimics the load-transfer behavior of trabecular bone, providing an advantageous balance between stiffness and strength [72]. Compared with rod-based lattices, continuous-wall honeycomb architectures exhibit enhanced stability, reduced susceptibility to localized failure, and maintain interconnected porosity conducive to bone ingrowth and nutrient transport. Furthermore, their inherent mechanical anisotropy, characterized by higher stiffness and strength along the primary loading direction, can be strategically leveraged to achieve load-bearing capability while reducing the effective modulus in non-critical directions, thereby mitigating stress shielding. These attributes make honeycomb architectures particularly suitable for partially biodegradable load-bearing implants, motivating their selection in the present work.

Although the present work incorporates the non-degradable Ti64 alloy, the goal is not complete implant resorption but the development of a partially biodegradable system. By combining the excellent biocompatibility and mechanical robustness of Ti64 with the controlled biodegradability of Zn, this study aims to engineer a Ti64-Zn MBMC with a bio-inspired architecture that balances long-term structural stability with localized, time-dependent degradation. In this design, Zn functions as a sacrificial phase that gradually dissolves *in vivo*, facilitating bone ingrowth, enhancing biological fixation, and reducing

Table 1

Optimized process parameters used to fabricate Ti6Al4V-Zn metallic bi-metal composites using the combination of additive manufacturing and spark plasma sintering processes.

Selective laser melting (SLM) parameters					
	Laser power (W)	Laser scan rate (mm/sec)	Hatch distance (mm)	Layer thickness (mm)	Energy density (J/mm ³)
Ti64 Bulk	400	1000	0.12	0.05	66.67
Ti64 Hexagons	400	1000	0.12	0.05	66.67
Spark plasma sintering (SPS) parameters					
	Sintering temperature (°C)		Holding time (min)		Compaction load (MPa)
Pure Zinc	300		10		50
Ti64-Zn (MBMC)	375		30		50

stress shielding, while the Ti64 framework ensures sustained mechanical support. The architected hexagonal Ti64 structure further reduces the effective elastic modulus of the composite, bringing it closer to that of natural bone and thereby mitigating stress-shielding-induced bone resorption. This strategy provides a synergistic combination of mechanical reliability and controlled biodegradation, minimizes complications associated with fully degradable implants, and reduces the likelihood of revision surgeries.

2. Materials and methods

2.1. Development of Ti64 hexagonal lattice

The Ti64 honeycomb structure was fabricated using a laser powder bed fusion (LPBF) process, also referred to as selective laser melting (SLM). Fabrication was carried out on an SLM280 system (SLM Solutions GmbH, Lübeck, Germany) using commercially available gas-atomized Ti64 powder. The optimized LPBF processing parameters are summarized in Table 1. Printing was performed on a Ti-based substrate under an argon atmosphere to prevent oxidation. To reduce thermal gradients and mitigate residual stresses associated with rapid solidification, a 90° hatch rotation strategy was applied between successive layers. Following fabrication, the AM Ti64 hexagonal lattice was manually filled with spherical Zn powder and placed inside a 20 mm diameter graphite die. Consolidation was performed using spark plasma sintering (SPS) in an HPD 10-GB system (FCT System GmbH, Effelder-Rauenstein, Germany). A 0.5 mm thick graphite spacer sheet was inserted between the metallic sample and the die to prevent undesired bonding during sintering. The optimized SPS parameters are also listed in Table 1.

2.2. Structural and microstructural characterization

The phase composition of the feedstock powder and consolidated composites was examined using X-ray diffraction (XRD) (Rigaku SmartLab) equipped with Cu-K α radiation ($\lambda = 1.5406 \text{ \AA}$). Scans were conducted in Bragg-Brentano geometry over a 2θ range of 30°–80°, with a scan rate of 3°/min and a step size of 0.01°. For microstructural characterization, including scanning electron microscopy (SEM) and electron backscatter diffraction (EBSD), samples were prepared following standard metallographic procedures. After mounting, the specimens were sequentially ground up to 4000 grit and subsequently electropolished. The Zn rich regions were electropolished at 20 V for 35 s using an electrolyte composed of orthophosphoric acid and ethanol in a 3:5 ratio to achieve a mirror-like finish. The Ti64 rich regions were electropolished using a standard A3 electrolyte for 20 s, followed by rinsing in deionized water. SEM observations were performed using a Zeiss Gemini SEM 450 equipped with an EDAX EBSD detector.

2.3. Mechanical testing

The surface hardness of all samples was measured using a Vickers micro-indentation tester (Future-Tech FM-810, Future Tech GmbH) with a

0.1 kgf load and a dwell time of 10 s. Compressive strength testing was conducted at room temperature using an Instron 5567 screw-driven universal testing machine, operated at a constant strain rate of 10^{-3} /s.

2.4. Corrosion and biological characterization

The invitro biodegradation behavior of the composite was assessed by immersing samples in SBF for 7, 14, and 21 days. The SBF solution was prepared following the procedure described in [73]. Prior to immersion, all samples were polished using the procedure outlined earlier and ultrasonicated for 30 min to remove surface contaminants. The specimens were then incubated at 37 °C in a 5% CO₂ environment for the designated durations. After immersion, samples were cleaned in a 200 g/L CrO₃ solution for 10 min to remove surface oxides and corrosion products, followed by ultrasonic cleaning in alcohol for 30 min. After drying, mass loss was recorded to determine the degradation rate. The surface morphology of the degraded samples was also examined to evaluate structural changes induced by immersion.

Electrochemical corrosion behavior of the Ti64-Zn MBMC, SPS Zn, and SLM Ti64 was evaluated using a standard three-electrode cell connected to a potentiostat (C.H. Instruments, CHI604E, Texas, USA). A standard calomel electrode (SCE) and a platinum electrode served as the reference and counter electrodes, respectively, while the polished composite samples (exposed area: 1 cm²) acted as the working electrode. SBF was used as the electrolyte to simulate physiological conditions. Potentiodynamic polarization (PDP) tests were conducted over a potential range of –2000 mV to +2000 mV vs. SCE at a scan rate of 1 mV/s. All electrochemical measurements were performed in triplicate to ensure reproducibility. Following PDP testing, samples were cleaned according to ISO 8407:2009 and examined using scanning electron microscopy (Zeiss Gemini SEM 450) to analyze corrosion morphology.

Cytotoxicity of the developed Ti64-Zn MBMC, SPS Zn, and SLM Ti64 samples was evaluated using an indirect method with MC3T3-E1 subclone 4 mouse calvarial pre-osteoblast cells. The cell line was originally sourced from the American type of culture collection (ATCC, USA; catalogue number CRL-2593) and supplied by Chromachemie laboratory private limited, India. Disc-shaped samples (20 mm diameter, 2 mm thickness) were uniformly polished, sterilized in ethanol, and exposed to UV radiation for 1 h. Residual ethanol was removed by washing the samples three times with phosphate-buffered saline (PBS) containing 1% antibiotics. Because Zn undergoes degradation in aqueous media, the cellular response to material leachates was assessed using a conditioned medium. Sterilized samples were incubated in complete culture medium (α -MEM supplemented with 10% fetal bovine serum (FBS, Gibco, Life Technologies) and 1% antibiotics (Sigma Aldrich)) at 37 °C and 5% CO₂ for 24 h and 72 h, using a fixed medium volume of 15 μ L/mm². After incubation, the conditioned medium was centrifuged at 5000 rpm for 20 min to remove debris.

MC3T3-E1 cells were seeded in 48 well plates at a density of 3 times 10³ cells per well and allowed to adhere for 24 h. The culture medium was then replaced with either undiluted conditioned medium (1x, 100%) or an 8x dilution (12.5% conditioned medium supplemented with complete medium), and cells were incubated for an additional 24 h and 72 h. Fresh medium

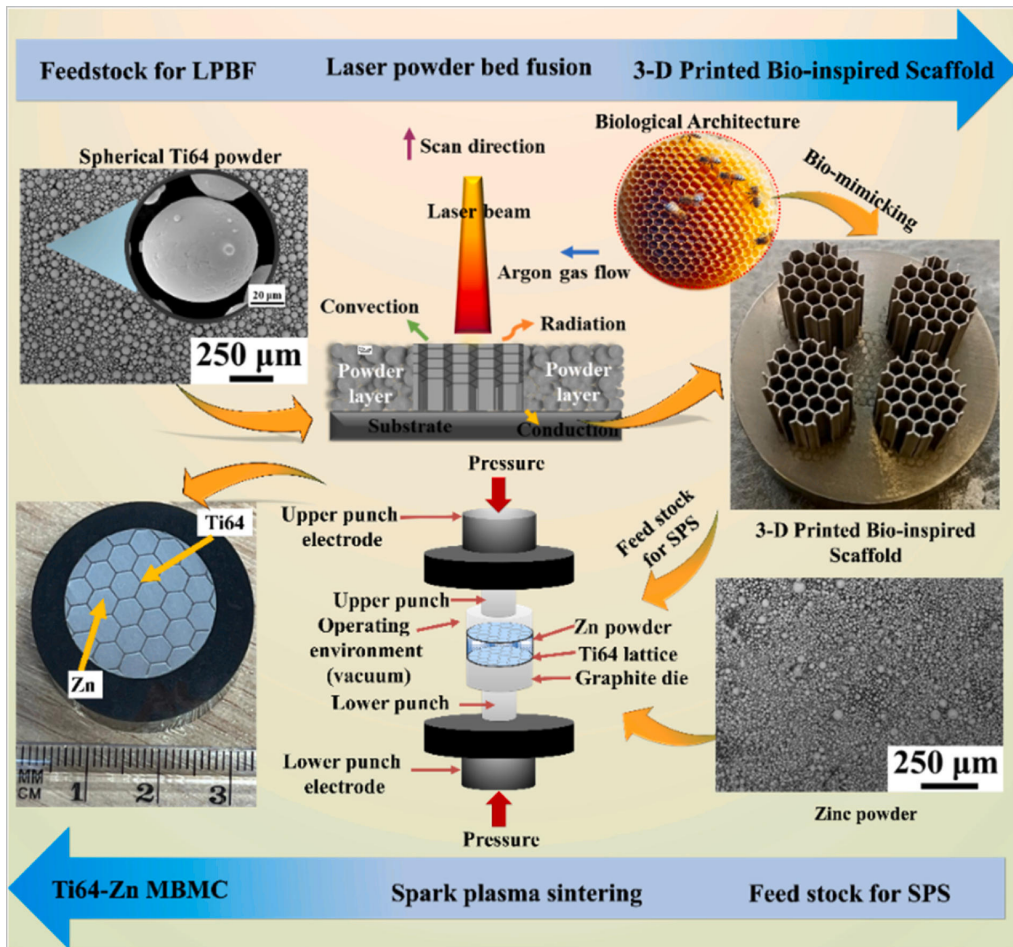


Fig. 1. Schematic illustration of Ti6Al4V-zinc (Ti64-Zn) metallic bi-metal composite (MBMC) manufacturing process in two different steps. Step 1 involves the development of bio-inspired Ti64-based hexagonal lattice architecture using a laser powder bed fusion process. Step 2 involves addition of Zn powder to the hexagonal lattice within a graphite die, followed by spark plasma sintering at optimized temperature and pressure resulting in the development of Ti64-Zn MBMCs.

served as the positive control. After 1 and 3 days, the conditioned medium was aspirated, and cells were rinsed with PBS. Cell viability was quantified using the water-soluble tetrazolium-1 (WST-1) assay (Invitrogen) by incubating cells with WST-1 reagent (1:10 dilution) for 3 h. The optical density (OD) was measured at 440 nm using a microplate reader (Biotek Gen 5, Santa Clara, CA, USA). The relative growth rate (RGR) was calculated as follows:

$$RGR = \left(\frac{OD_{sample}}{OD_{control}} \right) \cdot 100. \quad (1)$$

where OD_{sample} is the optical density of the test group and $OD_{control}$ is the optical density of the control measured using the plate reader. Data from the WST-1 assay were analyzed using one-way analysis of variance (ANOVA) followed by Tukey's post-hoc test, with statistical significance set at $p < 0.05$. All results are reported as mean \pm standard deviation from at least four independent samples.

To further assess cell viability, a live/dead assay was performed using Calcein-AM (Thermo Fisher Scientific, India) to stain viable cells and Ethidium Homodimer to stain non-viable cells. Stained cells were visualized using an inverted epi-fluorescence microscope (Olympus IX-53, Tokyo, Japan). For cell morphology analysis, cells were fixed with

3.7% formaldehyde in PBS for 30 min at room temperature and washed with PBS. Membrane permeabilization was achieved by incubating the cells in 0.2% Triton X-100 (Sigma, Germany) for 8 min, followed by PBS washing. Actin filaments were stained with 25 $\mu\text{g}/\text{mL}$ Alexa Fluor 488 (Invitrogen) for 30 min at room temperature, and nuclei were counterstained with 0.2 $\mu\text{g}/\text{mL}$ DAPI (Invitrogen) for 3 min. The stained cells were examined using an inverted epi-fluorescence microscope.

3. Results and discussion

3.1. Development of MBMC

MBMCs represent a specialized class of metallic multimaterials engineered to integrate and enhance the distinct properties of two constituent metals, thereby achieving superior overall performance. In this study, a novel bio-inspired, partially biodegradable Ti64-Zn MBMC was developed using a two-step advanced manufacturing strategy that combines SLM and SPS [41]. The complete manufacturing workflow, along with representative results from both AM and SPS processing, is illustrated in Fig. 1. In Step 1, a Ti64 honeycomb-inspired hexagonal bio-architecture

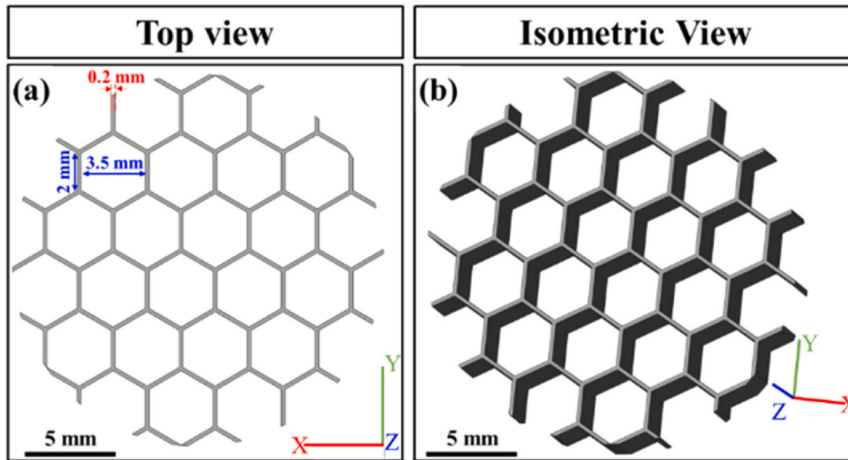


Fig. 2. Computer-aided design of the bio-inspired hexagonal lattice micro-architecture shown in two different projections: (a) Top view illustrating the overall geometry with detailed cell and strut dimensions; (b) Isometric view providing a clearer representation of the three-dimensional structure.

was fabricated using LPBF/SLM, with the optimized printing parameters summarized in Table 1 below. The CAD model of the hexagonal structure, including cell geometry and strut dimensions, is shown in Fig. 2. The strut thickness was fixed at 0.2 mm corresponding to the lower printing limit of the machine while the distance between two parallel struts was set at 3.5 mm to ensure adequate structural integrity. This reduction in strut size was intentionally implemented to minimize the overall Ti64 volume fraction within the composite, thereby reducing the potential for stress shielding [74]. The outer wall of the structure was designed to be continuous to maintain mechanical stability and ensure effective retention of Zn within the porous network [63]. In Step 2, commercially pure Zn powder was introduced into the Ti64 hexagonal scaffold (20 mm diameter, 5 mm thickness). Field-assisted spark plasma sintering (SPS), conducted under optimized pressure, temperature, and dwell time, facilitated the formation of the bio-inspired Ti64-Zn MBMC. The optimized SPS parameters [35] are listed in Table 1. For comparison, pure Zn pellets and Ti64 pellets were also fabricated using SPS and SLM, respectively, to benchmark the performance of the developed composite.

The architecture, phase distribution, and microstructural characteristics of the Ti64-Zn MBMC were examined using 3D X-ray tomography (Micro-CT), as shown in Fig. 3(a,b). The reconstructed Ti64 framework, obtained by thresholding the Zn sub-volume signals, is presented in Fig. 3(b). The resulting structure exhibits a honeycomb-like spatial arrangement, consistent with the intended bio-inspired design despite differences in composition and local morphology. Volume-rendering analysis revealed that the Ti64 hexagonal phase constitutes approximately $27 \pm 1.5\%$ of the total composite volume. Using the

rule of mixtures, the theoretical density of the composite was calculated to be $\sim 6.65 \pm 0.05 \text{ g/cm}^3$, which is in close agreement with the experimentally measured density of $6.63 \pm 0.06 \text{ g/cm}^3$ obtained via Archimedes' method. This close agreement confirms that the composite achieved near-full densification, corresponding to a relative density of approximately 100%, indicating negligible porosity. As illustrated in Fig. 3(a,b), the Ti64 phase forms a continuous three-dimensional load-bearing framework, while Zn uniformly occupies the interconnected lattice network. This integrated yet phase-distinct configuration supports the classification of the material as a MBMC.

3.2. Phase analysis

Fig. 4 shows the XRD patterns of SPS Zn, SLM Ti64 hexagonal structures, and the Ti64-Zn MBMC, along with their corresponding feedstock powders. The diffraction peaks of both Zn and Ti64 powders confirm single-phase structures with no detectable impurities within the resolution limits of XRD. The SLM Ti64 lattice exhibits characteristic peaks of the α/α' martensitic microstructure, consistent with the rapid cooling rates inherent to the SLM process [7,75]. The SPS Zn samples display a single-phase hexagonal close-packed (HCP) structure, with no additional peaks corresponding to oxides or secondary phases, indicating that oxidation was effectively suppressed during sintering. A noticeable difference in peak intensities between Zn powder and SPS-Zn, particularly for the most intense reflections, suggests the presence of preferred crystallographic orientation, as reported in our earlier work [35].

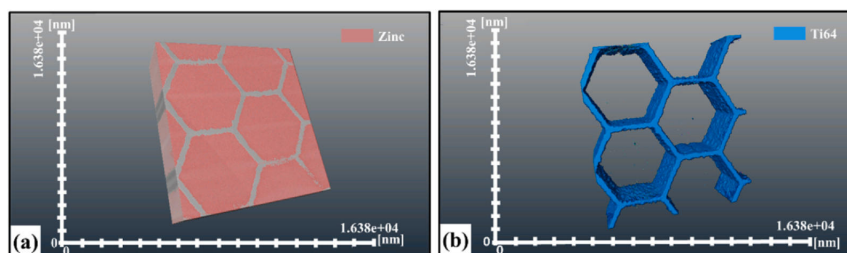


Fig. 3. Micro-computed tomography (μ CT) volume rendering of Ti64Al4V-zinc (Ti64-Zn) metallic bi-metal composite (MBMC). CT images highlighting the volume fraction of (a) Zn in the composite, obtained by thresholding the sub-volume signals of Ti64 constituents, and (b) bio-inspired Ti64 hexagon structure in the composite, processed by thresholding the sub-volume signals of Zn constituents. The volume fraction of the bio-inspired hexagonal Ti64 phase in the composite, as determined by X-ray tomography, is $\sim 27\%$.

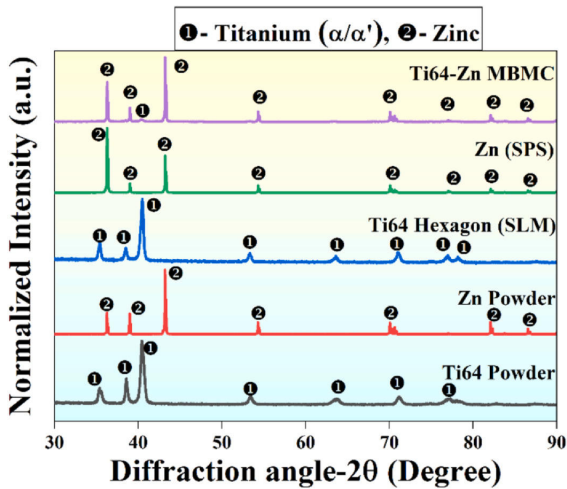


Fig. 4. The X-ray diffraction (XRD) patterns of feed stock powders zinc (Zn) and Ti6Al4V (Ti64), spark plasma sintered Zn, selective laser melted fabricated Ti64 hexagonal lattice structure, and the Ti64-Zn metallic bi-metal composite (MBMC) are shown. The Ti64-Zn MBMC reveals the presence of α/α' -Ti and Zn as the primary phases, indicating the absence of interfacial reactions between Ti64 and Zn during the fabrication process.

For the Ti64-Zn MBMC, the diffraction pattern clearly shows peaks corresponding to *HCP*-Zn and the α/α' phases of Ti. Due to the relatively low volume fraction of Ti64 in the composite, the Ti peaks appear with lower intensity compared to those in the standalone SLM Ti64 structure. Importantly, no additional peaks beyond those of Zn and α/α' -Ti are observed within the measurable limits of XRD, confirming the

absence of significant interfacial reactions or the formation of inter-metallic phases during composite fabrication.

3.3. Microstructural analysis

The surface morphology and microstructural features of the Zn and Ti64 regions within the Ti64Zn MBMC are presented in Fig. 5 and Fig. 6. As shown in Fig. 5, the Ti64 hexagonal architecture remains uniformly distributed throughout the composite and retains its original lattice geometry without noticeable distortion after SPS processing, indicating that the optimized sintering parameters are well-suited for composite fabrication. SEM images at multiple magnifications (Fig. 5(a-c)) together with EDS elemental mapping (Fig. 5(d)) reveal two distinct, well-bonded interfaces between Ti64 and Zn that are free of cracks and pores. The EDS results further confirm the absence of interfacial reaction products between the Zn matrix and the Ti64 reinforcement, consistent with the XRD findings.

EBSD analysis of the Ti64-Zn MBMC is presented in Fig. 6. The Zn region exhibits a bimodal grain structure composed of both coarse and fine grains. The microstructure contains a regular distribution of large, circular grains with relatively uniform size, some of which contain finer grains within them, features likely corresponding to sub-grain boundaries. To further elucidate crystallographic orientation and grain boundary characteristics, SEM-EBSD mapping was performed, as shown in Fig. 6(b,c). The inverse pole figure (IPF) map reveals a predominance of red-colored grains, indicating that the *c*-axes of many Zn grains are aligned with the specimen's normal direction. This suggests that the basal planes {0001} are oriented nearly parallel to the polished surface.

The Ti64 region displays a fine acicular α/α' martensitic microstructure, consistent with the XRD results (Fig. 6(d)). The presence of needle-like features is attributed to the rapid cooling inherent to the SLM process, which promotes the formation of secondary and tertiary martensite [76,77]. This microstructural evolution plays a significant role in governing the mechanical behavior of the composite and is discussed further in 3.4. The high cooling rates during SLM act as the driving force

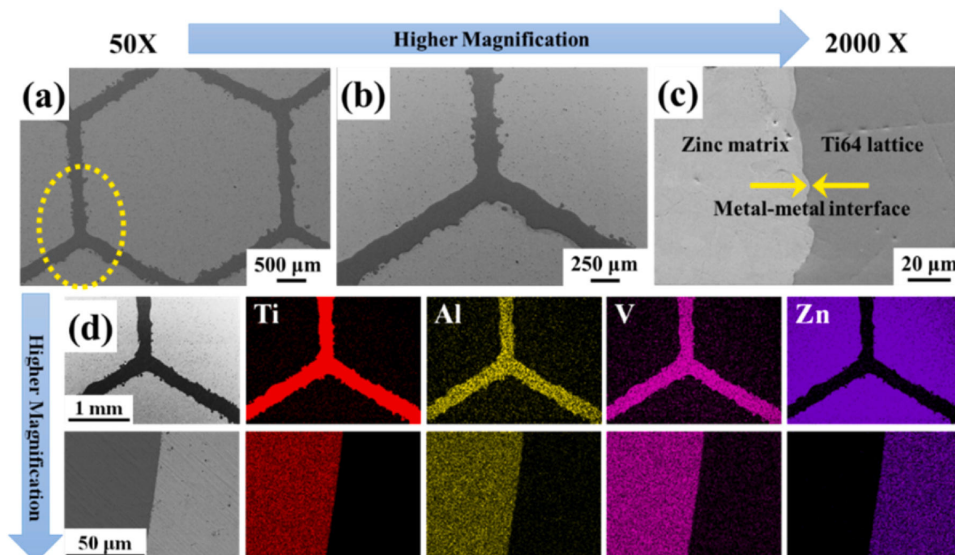


Fig. 5. (a-c) Scanning electron microscopy (SEM) images of the fabricated Ti6Al4V-zinc (Ti64-Zn) metallic bi-metal composite (MBMC). (a) SEM micrograph depicting the surface morphology of a single hexagon unit, highlighting the positions of the matrix and reinforcement phases. (b) Higher magnification image of the highlighted region in (a), revealing the topography at the triple junction interface. (c) High-magnification micrograph illustrating the metal-metal interface, showing no evidence of defects like cracks. (d) Energy dispersive spectroscopy mapping of the MBMC at two different magnifications, demonstrating the elemental distribution of the matrix and reinforcement phases.

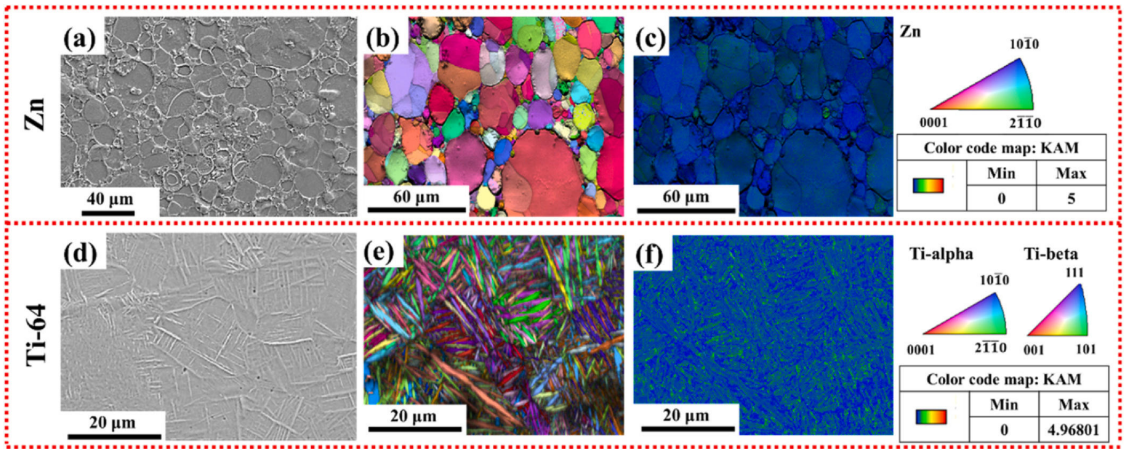


Fig. 6. Scanning electron microscopy images, and electron backscatter diffraction analysis of (a-c) zinc (Zn) and (d-f) Ti6Al4V (Ti64) struts taken from random regions of the Ti64-Zn metallic bi-metal composite.

for the transformation of the prior β phase into α/α' laths following the Burgers orientation relationship [78]. Additionally, the IPF map in Fig. 6(e) shows no strong preferred orientation among the α' laths, indicating a largely random crystallographic distribution. This lack of texture likely arises from the highly dynamic thermal gradients and rapid solidification conditions characteristic of SLM, which promote heterogeneous nucleation and growth of martensitic laths [79].

The kernel average misorientation (KAM) maps of the SLM Ti64 regions exhibit elevated local misorientations, particularly near the interfaces between fine martensitic laths (Fig. 6(d-f)). The rapid and repeated thermal cycling inherent to the SLM process promotes coarsening of the α' martensitic laths [80]. The substantial transformation strain associated with the $\beta \rightarrow \alpha/\alpha'$ phase transformation leads to increased KAM values, reflecting a high density of geometrically necessary dislocations. These dislocations form to accommodate the transformation-induced strain during martensite formation [81] and play a significant role in influencing the mechanical response of the alloy. In contrast, the SPS Zn region exhibits relatively uniform strain distribution within its sub-grain structure (Fig. 6(a-c)), indicating a more homogeneous deformation behavior.

These lower KAM values indicate that only minimal plastic strain was introduced during the SPS process. This suggests that densification in the Zn alloy was primarily governed by diffusion-controlled mechanisms and grain-boundary sliding rather than dislocation-mediated plastic deformation. The relatively low processing temperature, combined with the intrinsic softness of Zn, likely facilitated stress relaxation and limited the accumulation of geometrically necessary dislocations. Overall, the contrast in KAM values, higher in SLM Ti64 (~ 4.96) and lower in SPS Zn (~ 3.1), highlights the greater degree of localized strain and dislocation density generated in Ti64 during rapid solidification compared to the more uniform strain distribution in SPS-consolidated Zn.

3.4. Mechanical properties

The mechanical properties of the Ti64-Zn MBMC were assessed through Vickers microhardness and compression testing. Fig. 7(a-c) shows representative Vickers indents on the Ti64 and Zn regions, along with the corresponding hardness profile and indentation map,

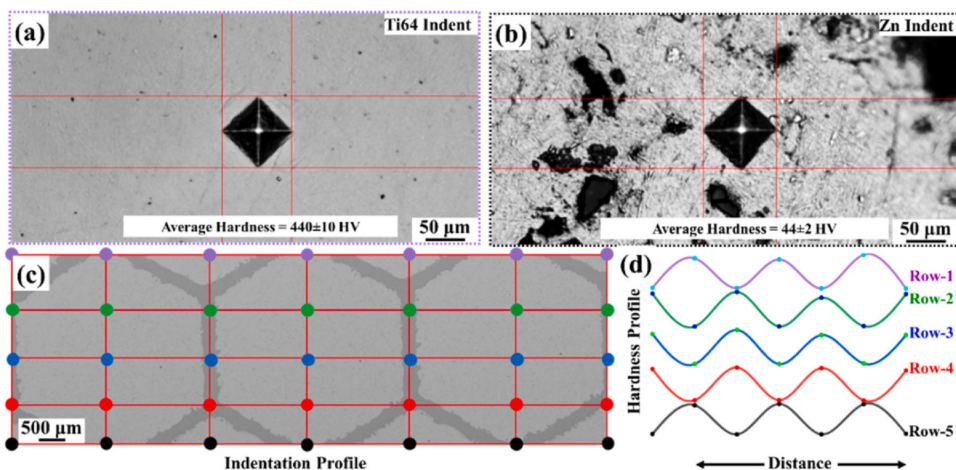


Fig. 7. Hardness plot for Ti6Al4V-zinc (Ti64-Zn) metallic bi-metal composite (MBMC). Microstructure representative of the Vickers microhardness indents on (a) Ti64 and (b) Zn surface at 0.1 kgf load, (c) microstructural area displaying the indentation profile pattern followed to make the indents i.e. the approximate position of indents over the surface of composite, and (d) hardness profile map for MBMC showing the variation in hardness over the composite surface.

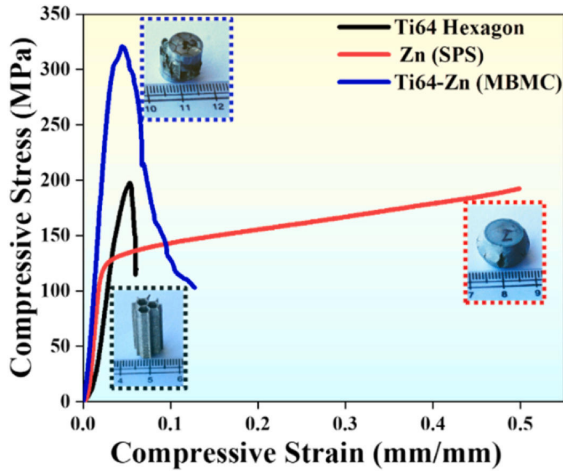


Fig. 8. Uniaxial compressive engineering stress-strain plot for Ti6Al4V-Zn metallic bi-metal composite (MBMC) compared to selective laser melted Ti64-Hexagon without any infiltration, and the spark plasma sintered Zn. Representative images of the fractured samples are shown alongside their respective graphs as insets.

Table 2

Comparison of compressive properties of the Ti6Al4V-zinc (Ti64-Zn) metallic bi-metal composites, spark plasma sintered Zn, and selective laser melted Ti64 hexagonal structures.

Sample composition	Yield compressive strength (MPa)	Ultimate compressive strength (MPa)
Ti64 Hexagon	165 ± 2	182 ± 13
Zn (SPS)	115 ± 5	191 ± 6
Ti64-Zn (MBMC)	265 ± 25	292 ± 25

highlighting the spatial variation in hardness across the composite. The Ti-rich regions exhibit an average hardness of 440 ± 10 HV0.1, whereas the Zn-rich regions show a significantly lower hardness of 44 ± 2 HV0.1. The dark regions observed in Fig. 7(b) arise from microstructural heterogeneity and differential reflectivity of the Zn phase rather than from porosity. The elevated hardness of the Ti64 phase is attributed to the presence of the α' -Ti martensitic microstructure formed during the rapid cooling inherent to the AM process. A linear hardness scan across multiple repeating Ti64-Zn units reveal a periodic alternation between high- and low-hardness values, directly reflecting the architected distribution of the Ti64 framework and Zn matrix. This oscillatory pattern arises from the geometric periodicity and intrinsic hardness contrast between the two phases, rather than from any mathematically fitted sinusoidal function Fig. 7(b). Such spatially patterned hardness variation is a defining characteristic of MBMCs fabricated through the combined AM + PM route.

Fig. 8 shows the compressive engineering stress-strain curves of the Ti64-Zn MBMC, along with SPS pure Zn and the AM porous Ti64 hexagonal lattice for comparison. The corresponding fracture surfaces are included as insets. The Ti64-Zn MBMC exhibits a yield compressive strength of 265 ± 25 MPa and an ultimate compressive strength of 292 ± 25 MPa, both substantially higher than those of SPS Zn and the SLM Ti64 lattice, as summarized in Table 2. The fracture surfaces reveal interfacial cracking between the two constituent phases, suggesting that crack propagation is influenced by the mutual partitioning of Ti64 and Zn. This indicates effective load sharing within the composite architecture.

Upon implantation, the biodegradable nature of the Ti64-Zn MBMC implies that the Zn phase will gradually degrade in physiological environments, leading to a progressive reduction in composite strength. This degradation-induced evolution of mechanical properties, along with the re-exposure of hexagonal pores that promote osseointegration, is consistent with recent findings on Ti64-Zn based composite. Yu et al. reported that Zn acts as a sacrificial, degradable phase whose dissolution during in-vitro and in-vivo studies leads to a controlled decrease in composite stiffness, enabling gradual load transfer to the Ti64 scaffold [34]. As Zn degrades, the previously filled pores reopen, forming interconnected pathways that facilitate bone ingrowth and vascularization, as confirmed by micro-CT and histological analyses showing enhanced new bone formation around the Ti64 framework [34]. Furthermore, in-vivo implantation studies demonstrated that Zn degradation proceeds in synchrony with bone regeneration, allowing newly formed bone to occupy the recovered pore spaces while the Ti64 scaffold maintains structural integrity throughout healing [82,83]. These observations provide strong experimental support for the design rationale of the present MBMC, where controlled Zn degradation simultaneously reduces stiffness over time and promotes osseointegration.

The interfacial cracking observed after compression is attributed to strain incompatibility arising from the substantial mechanical mismatch between Ti64 and Zn, as Zn undergoes plastic deformation at much lower stresses. Such debonding reflects damage evolution under high compressive strain rather than inadequate initial interfacial bonding. While limited interfacial separation can facilitate progressive deformation and energy dissipation, excessive debonding could diminish load-sharing efficiency. In the present Ti64-Zn composite, the enhanced compressive strength relative to the individual constituents indicates that the interface remains sufficiently effective to support cooperative deformation.

The compressive fracture morphology of the Ti64-Zn MBMC is presented in Fig. 9. The macroscopic post-compression appearance (Fig. 9(a)) shows shear-dominated deformation, with fracture planes inclined at approximately 45° to the loading axis, typical of compressive failure in metallic materials. The absence of complete disintegration indicates that the continuous Ti64 honeycomb framework maintains global structural integrity even beyond the peak load. As shown in Fig. 9(b), the crack path is non-planar and slightly deflected, suggesting mechanical interaction between the Ti64 scaffold and the Zn matrix during deformation. The high-magnification fracture image of the Ti64-rich region (Fig. 9(c)) reveals a well-developed dimpled surface. The fine, equiaxed dimples confirm a ductile fracture mechanism governed by microvoids nucleation and coalescence within the additively manufactured Ti64 struts. This demonstrates that the Ti64 framework undergoes localized plastic deformation prior to failure rather than brittle cleavage, contributing to enhanced damage tolerance and preventing abrupt structural collapse. In contrast, the Zn-rich region (Fig. 9(d)) exhibits clear evidence of void nucleation and growth, hallmarks of ductile failure in Zn. Microvoids likely initiate at microstructural heterogeneities and near Ti64-Zn interfaces where stress concentrations and strain incompatibilities arise. Progressive void growth and coalescence ultimately lead to localized separation within the Zn phase. Compared with the Ti64 struts, the Zn matrix displays more pronounced plastic flow, consistent with its lower strength and modulus.

The interfacial cracking observed after compression arises from the elastic-plastic mismatch between the stiff Ti64 scaffold and the more compliant Zn phase. Notably, this interfacial damage develops progressively rather than catastrophically, indicating that it contributes to energy dissipation instead of triggering premature failure. The continuous Ti64 honeycomb framework effectively arrests crack propagation across the structure, thereby preserving load-bearing capacity even after localized Zn degradation. Upon implantation, the continuous-wall Ti64 honeycomb architecture governs load transfer by providing uninterrupted compressive load paths along the hexagonal walls. In this

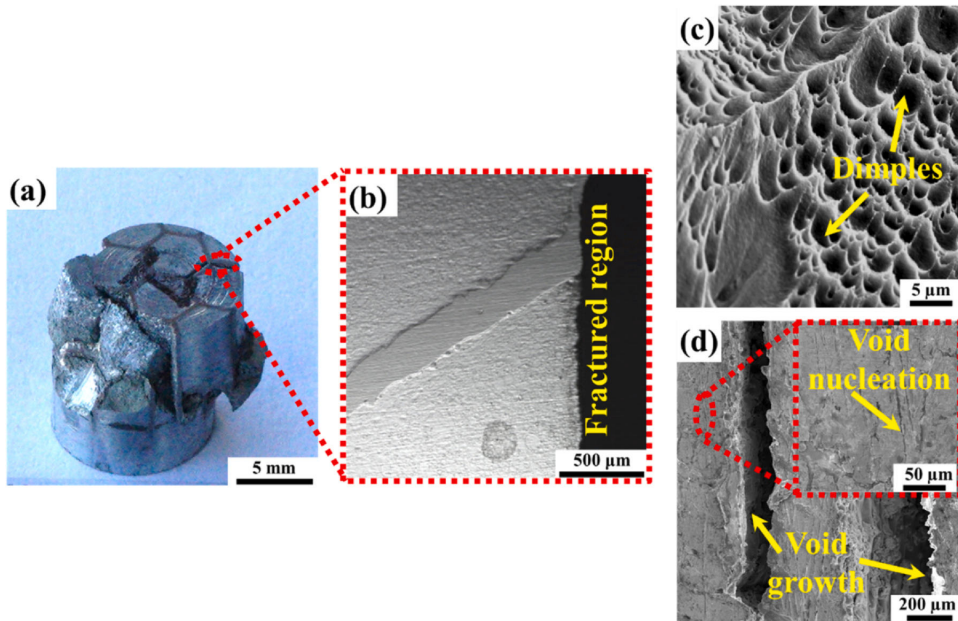


Fig. 9. Compressive fracture morphology of the Ti6Al4V-Zn (Ti64-Zn) metallic bi-metal composite (MBMC). (a) Macroscopic view of the specimen after compression, showing shear-dominated failure, (b) low-magnification scanning electron microscopy (SEM) image highlighting the crack propagation path, (c) high-magnification SEM fracture surface of the Ti64-rich region exhibiting a dimpled morphology characteristic of ductile fracture, and (d) SEM fracture surface of the Zn-rich region showing pronounced void nucleation and growth.

configuration, the Ti64 phase functions as a fully percolating load-bearing framework, while the infiltrated Zn phase undergoes constrained deformation and contributes to stiffness through cooperative load sharing. Unlike node-based lattices, where stresses concentrate at junctions, the planar wall continuity distributes stresses over extended segments, reducing stress concentrations and stabilizing the composite response. Under these conditions, the initial composite exhibits a compressive yield strength of 265 ± 25 MPa, exceeding that of cortical bone (~ 100 – 230 MPa), ensuring sufficient early-stage mechanical support.

We further hypothesize that progressive Zn dissolution leads to a gradual reduction in composite stiffness and yield strength by diminishing the effective load-sharing area of the Zn phase and shifting stresses toward the Ti64 walls, consistent with the observations of Yu et al. [34]. Because the Ti64 framework remains fully continuous in three dimensions, degradation does not disrupt load-path connectivity, preventing catastrophic collapse. Even in the limiting case of complete Zn removal, the remaining Ti64 scaffold retains a compressive yield strength of 165 ± 2 MPa, which remains within the load-bearing range of cortical bone. Consequently, the mechanical response is expected to evolve monotonically from cooperative Ti64-Zn load sharing to Ti64-dominated load bearing as the Zn volume fraction decreases. Simultaneously, Zn degradation reopens the originally infiltrated hexagonal porosity, enabling bone ingrowth while the Ti64 framework preserves structural continuity. This establishes a coupled degradation-regeneration mechanism in which mechanical load transfer transitions progressively from the sacrificial Zn phase to the Ti64 skeleton and ultimately to newly formed bone occupying the restored pore space [82,83].

The progressive degradation or biological replacement of one phase while maintaining overall mechanical stability is a defining characteristic of the Ti64-Zn MBMC. This behavior is evaluated in relation to the mechanical properties of the developed composites, summarized in Table 3 and compared with previously reported interpenetrating and

multi-material systems fabricated through various manufacturing routes. The comparative analysis highlights how different processing strategies influence the mechanical response of multi-material composites. Notably, systems incorporating bio-inspired architectures such as honeycomb, TPMS, and brick-and-mortar designs consistently demonstrate enhanced mechanical strength, improved load distribution, and superior energy absorption capabilities. These trends underscore the advantages of architected multimaterials designs in achieving balanced mechanical performance and functional adaptability.

While full fatigue testing may be beyond the scope, expected fatigue performance is discussed based on the present experimental evidence: The material (Ti64-Zn MBMC) would be expected to exhibit moderate to good fatigue performance for a biodegradable load-bearing implant. This is due to the:

- Absence of brittle intermetallics: The XRD results indicate a two-phase Ti64-Zn system without hard, crack-susceptible intermetallic compounds. This typically delays crack initiation under cyclic loading and improves fatigue endurance.
- Homogeneous phase distribution: A uniform microstructure reduces local stress concentrations, which are common sites for fatigue crack nucleation.
- Lack of significant internal defects: Micro-CT analysis shows no large pores or inclusions. Since fatigue life in titanium alloys is strongly defect-controlled, the absence of such flaws suggests a more stable cyclic response.

Overall, the experimental evidence suggests that the Ti64-Zn alloy should exhibit fatigue resistance comparable to other defect-free titanium-based biomaterials, with delayed crack initiation and stable cyclic deformation behavior. While the exact fatigue limit cannot be quantified without testing, the microstructure does not present characteristics typically associated with poor fatigue performance.

Table 3
Summary of multi-metallic composites fabricated using different manufacturing routes and their properties.

System	MR	LS	Bio-architecture	YS/UTS	E	DR	Application	Ref.
Mg-Ti	AM + pressureless infiltration	Rhombic dodecahedron	Cellular	64/275	47.3	-	Biomedical applications	[83]
Mg-Ti	Ti woven 3D mesh + pressureless infiltration	Bioinspired orthogonal plywood	Fish-scale-like architectures	~210 UTS	-	-	Architectural design for composite	[84]
Mg-Ti	AM + pressureless infiltration	Bioinspired double-Bouligand	H. Rufescens O. Scyllarus S. Purpuratus	169.7 ± 7.9 (UTS) 156.6 ± 8.6 (UTS) 226.6 ± 5 (UTS)	58.2 ± 4.6 54.0 ± 5.1 55.5 ± 6.3	-	Architectural design for composite	[85]
Ti64 + CaSiO3	AM + SPS	TPMS scaffolds	Rectangular	100 ± 5 (RN)	-	-	Biomedical applications	[86]
Mg-Ti	Ti wire + pressureless infiltration	-	Primitive	52 ± 2	-	-	-	-
Ti-Eggshell	AM + SPS	Hexagonal prism	Lattice	12 ± 1	47 ± 2	-	-	[87]
Ti64-Zn	AM + casting	Rhombic dodecahedron	Gyroid	35 ± 2	1.54 (C)	0.1550	-	[88]
Ti64-Zn MBMC	AM + SPS	Continuous hexagonal wall	Honeycomb Wired mesh Honeycomb Cellular	70 ± 4 86 123 ± 34 91.06 ± 3.21 (OYS) 97.97 ± 5.42 (TYS)	3.021 (T)	-	-	[34]
			Honeycomb	265 ± 25/292 ± 25	-	0.1577	-	*

Abbreviations:

Ti64 – Ti6Al4V alloy; TPMS – Triply periodic minimal surfaces; AM – Additive Manufacturing; SPS – Spark Plasma Sintering; MR – Manufacturing route; YS/US – yield strength/ultimate strength (MPa) in compression, unless otherwise specified as tensile mode; C – Compressive mode; T – Tensile mode; LS – lattice structure; E – elastic modulus (GPa); DR – degradation rate (mm/year); Ref. – reference article

* - Present work

3.5. Potentiodynamic polarization (PDP) behaviour of Ti64-Zn MBMC

To assess the corrosion behavior of the developed composite, potentiodynamic polarization (PDP) tests were conducted in simulated body fluid (SBF) to replicate physiological conditions. The corrosion response of the Ti64-Zn MBMC was compared with SPS Zn and SLM bulk Ti64, which served as control samples. Fig. 10 presents the PDP curves of Ti64-Zn MBMC, SPS Zn, and SLM Ti64, providing insight into their electrochemical characteristics. Corrosion potential (E_{corr}) and corrosion current density (I_{corr}) were determined using the Tafel extrapolation method, and the corresponding values are summarized in Table 4. E_{corr} reflects the thermodynamic tendency of a material to corrode, where a more negative E_{corr} indicates higher electrochemical activity and greater susceptibility to corrosion. In contrast, I_{corr} represents the kinetic rate of material degradation, with lower I_{corr} values corresponding to improved corrosion resistance and slower dissolution. In this study, the primary comparison focuses on the corrosion behavior of pure Zn and the Ti64-Zn MBMC. Although Ti64 is well known for its bio-inert and non-degradable nature, evaluating its electrochemical response remains essential for biomedical implant applications, particularly in multi-material systems where interfacial stability and galvanic interactions may influence long-term performance [89].

The bulk SLM Ti64 exhibits an E_{corr} of -264 mV and I_{corr} of $3.35 \mu\text{A}/\text{cm}^2$, values that align well with those typically reported for Ti64 alloys. Similar E_{corr} and I_{corr} values for SLM Ti64 immersed in SBF were also reported by Chen et al. [90]. The SPS Zn samples show an E_{corr} of -1180 mV and an I_{corr} of $0.045 \mu\text{A}/\text{cm}^2$. When exposed to the same SBF environment, the Ti64-Zn MBMC displays an E_{corr} of -1185 mV, slightly more negative than that of SPS Zn, indicating a comparable electrochemically active surface. Notably, the I_{corr} of the Ti64-Zn MBMC is $0.027 \mu\text{A}/\text{cm}^2$, which is lower than that of SPS Zn. This reduced I_{corr} suggests a slower degradation rate for the composite despite its more negative E_{corr} . To further elucidate the corrosion mechanism and surface degradation behavior, SEM analysis was performed on the tested samples.

Fig. 11 presents SEM images of the corroded Ti64-Zn MBMC and SPS Zn samples after exposure to SBF. As established in previous studies, bulk SLM Ti64 exhibits excellent corrosion resistance due to the formation of a stable TiO_2 passive film that effectively suppresses pitting and surface degradation [89,91]. Given this well documented behavior, SEM images of Ti64 are not included. In contrast, both the Ti64-Zn MBMC and SPS Zn samples display similar degradation features, characterized by localized corrosion and variations in pit morphology, as shown in Fig. 11. High-magnification SEM images of the Zn-rich regions within the MBMC (Fig. 11(e,f)) reveal uniformly distributed corroded areas accompanied by pit formation. This behavior is likely associated with the high density of grain boundaries, which serve as energetically favourable sites for dissolution [35]. Fig. 11(g) highlights the corroded interface between the Ti64 and Zn phases. Notably, the Ti64 surface remains smooth and free of visible corrosion or pitting, as confirmed by the high-magnification image in Fig. 11(i), reinforcing its bio-inert and passive nature. However, active corrosion is evident at the interface (Fig. 11(g)), reaffirming its bio-inert and passive nature. However, active corrosion is evident at the Ti64-Zn interface, driven by galvanic coupling between the two phases. The substantial potential difference, Ti64 at ~ -250 mV acting as the cathode and Zn at ~ -1200 mV acting as the anode [89] creates a strong galvanic driving force that accelerates Zn dissolution at the interface.

Ti64 exhibits excellent corrosion resistance due to the formation of a stable TiO_2 passive film, as demonstrated by Chen et al. [90]. This protective layer effectively shields the alloy surface from aggressive Cl^- ions present in SBF. In contrast, Zn and its alloys are more anodic and readily undergo corrosion in chloride-containing environments, leading to the release of Zn^{2+} ions. Consequently, the Ti64-Zn composite shows a lower corrosion potential (E_{corr}) and a higher passivation current (I_p), reflecting the electrochemical activity of the Zn phase. The formation of

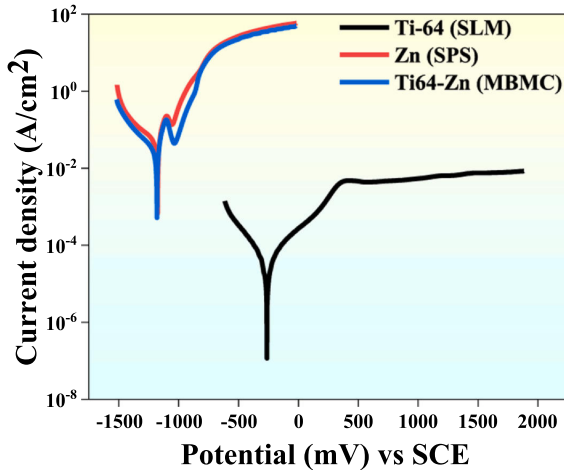


Fig. 10. Potentiodynamic polarisation curve of Ti6Al4V-zinc (Ti64-Zn) metallic bi-metal composite (MBMC) compared to selective laser melted Ti64, and spark plasma sintered Zn for an exposure period of 1 h in simulated body fluid.

a distinct interfacial gap likely indicates intensified ion exchange between Zn and Ti64 during galvanic coupling. Despite this, the lower I_{corr} value of the composite suggests that its overall degradation rate remains relatively controlled, making the Ti64-Zn MBMC a promising candidate for biomedical applications where moderate, time-dependent degradation is desirable. The subsequent sections further examine this behavior through detailed immersion studies, which reinforce the trends observed in the electrochemical analysis and confirm the controlled degradation characteristics of the Ti64-Zn MBMC.

3.6. In-Vitro bio-degradation analysis

The degradation behavior and rate of the Ti64-Zn MBMC were evaluated by incubating the composite in SBF for varying durations, with weight measurements recorded every 7 days. The biodegradation behavior of the composite was evaluated following ASTM G31–72, which recommends short-term immersion testing (typically 7–28 days) for preliminary assessment of corrosion mechanisms and quantification of degradation rates. Accordingly, the degradation performance of the Ti64-Zn MBMC was examined by immersing samples in simulated body fluid (SBF) for predetermined time intervals, with specimen mass recorded at 7-day increments to calculate the corresponding degradation rate. For comparison, SPS Zn and bulk SLM Ti64 were also incubated under identical conditions. During the initial stages of immersion, a thin white layer formed uniformly on the MBMC surface. As immersion time increased, this layer thickened and degradation products accumulated unevenly, as shown in Fig. 12. After 7 days, the degradation rate of the Ti64-Zn MBMC was calculated to be 0.1577 mm/year, whereas SPS Zn exhibited a slightly lower rate of 0.1325 mm/year. As expected, bulk SLM Ti64 being bio-inert showed negligible weight loss during the same period.

Table 4

Polarization data of the Ti6Al4V-zinc (Ti64-Zn) metallic bi-metal composite in comparison to the spark plasma sintered Zn and selective laser melted Ti64 bulk sample immersed in simulated body fluid for 1 h.

Samples	E_{corr} (mV) vs SCE	I_{corr} ($\mu\text{A}/\text{cm}^2$)	I_p ($\mu\text{A}/\text{cm}^2$)	E_{pp} (mV) vs SCE
Ti64-Zn MBMC	-1185 ± 60	0.027 ± 0.010	7.50 ± 1.01	-754 ± 7
Zn (SPS)	-1180 ± 48	0.046 ± 0.010	6.66 ± 0.89	-774 ± 5
Ti64 bulk (SLM)	-264 ± 10	3.355 ± 0.600	4.68 ± 0.24	429 ± 7

The degradation rate of the composite is lower than that reported for pure Mg and Mg-based composites [92,93], which is advantageous for biomedical applications requiring controlled, moderate degradation. The slightly higher degradation rate of the MBMC compared to SPS Zn is attributed to galvanic coupling between Ti64 and Zn, as discussed earlier. The weaker, less stable oxide layer formed on Zn during early immersion undergoes continuous breakdown, leading to surface void formation and progressive dissolution. At extended immersion times of 14 and 21 days, the degradation rate of the Ti64-Zn MBMC decreases to 0.0872 mm/year and 0.0845 mm/year, respectively. This reduction is attributed to the formation of a thicker degradation layer that acts as a diffusion barrier, limiting ion exchange between the composite and the surrounding medium. A similar trend is observed for SPS Zn, while bulk SLM Ti64 continues to exhibit negligible degradation, as summarized in Table 5.

SEM images of the Ti64-Zn MBMC surface after 21 days of immersion in SBF, captured at different locations and magnifications, are shown in Fig. 12(a–f). The overall surface morphology (Fig. 12(a)) reveals a uniformly distributed oxide layer, accompanied by the agglomeration and accumulation of degradation products along the composite periphery. Higher magnification images taken from the central region and near the Ti64-Zn interface Fig. 12(b, c), show an oxide-rich surface layer. In certain regions, circular patches are observed (highlighted in yellow), as shown in Fig. 12(d). The magnified view in Fig. 11(e) displays a regular petal-like, floral microstructure, characteristic of apatite formation. Apatite, primarily composed of calcium phosphate, closely resembles natural hydroxyapatite ($\text{Ca}_{10}(\text{PO}_4)_6(\text{OH})_2$) found in human bone [94]. Bioactive materials typically form such fine apatite crystals when exposed to physiological environments, indicating their ability to support biological mineralization.

The high-magnification image in Fig. 12(f) further reveals multiple rectangular and irregularly shaped crystals, reinforcing the likelihood of apatite layer formation. EDS elemental maps for a single hexagonal unit and the Ti64-Zn interface (Fig. 13(a,b)) confirm the presence of a uniform oxide layer enriched with calcium (Ca) and phosphorus (P). Additionally, point EDS analysis of the region shown in Fig. 12(f) yields a Ca/P atomic ratio of 0.96. Although lower than the ideal ratio of 1.67 for stoichiometric hydroxyapatite, this value still indicates the formation of a calcium-phosphate-based apatite layer. Collectively, these observations demonstrate that the Ti64-Zn MBMC exhibits clear bioactivity under simulated physiological conditions.

Fig. 14(a–f) presents SEM images of the Ti64-Zn MBMC surface after removal of the oxide film and accumulated degradation products, revealing the underlying morphology of the degraded structure. The overall view of a single hexagonal unit Fig. 14(a) shows uniform and controlled degradation across the Zn-rich regions. A higher magnification image of this area Fig. 14(b) highlights widespread surface dissolution, while Fig. 14(c) reveals deep grooves within corrosion pits, suggesting that degradation progresses preferentially along grain boundaries. This behavior is consistent with the higher electrochemical activity at grain boundaries, where micro-galvanic coupling and localized electron transfer accelerate dissolution. Fig. 14(d–f) show the Ti64-Zn interfacial region, where uneven degradation is evident. The interfacial gap appears to have widened, indicating accelerated Zn dissolution at the junction, while the Ti64 surface remains stable and

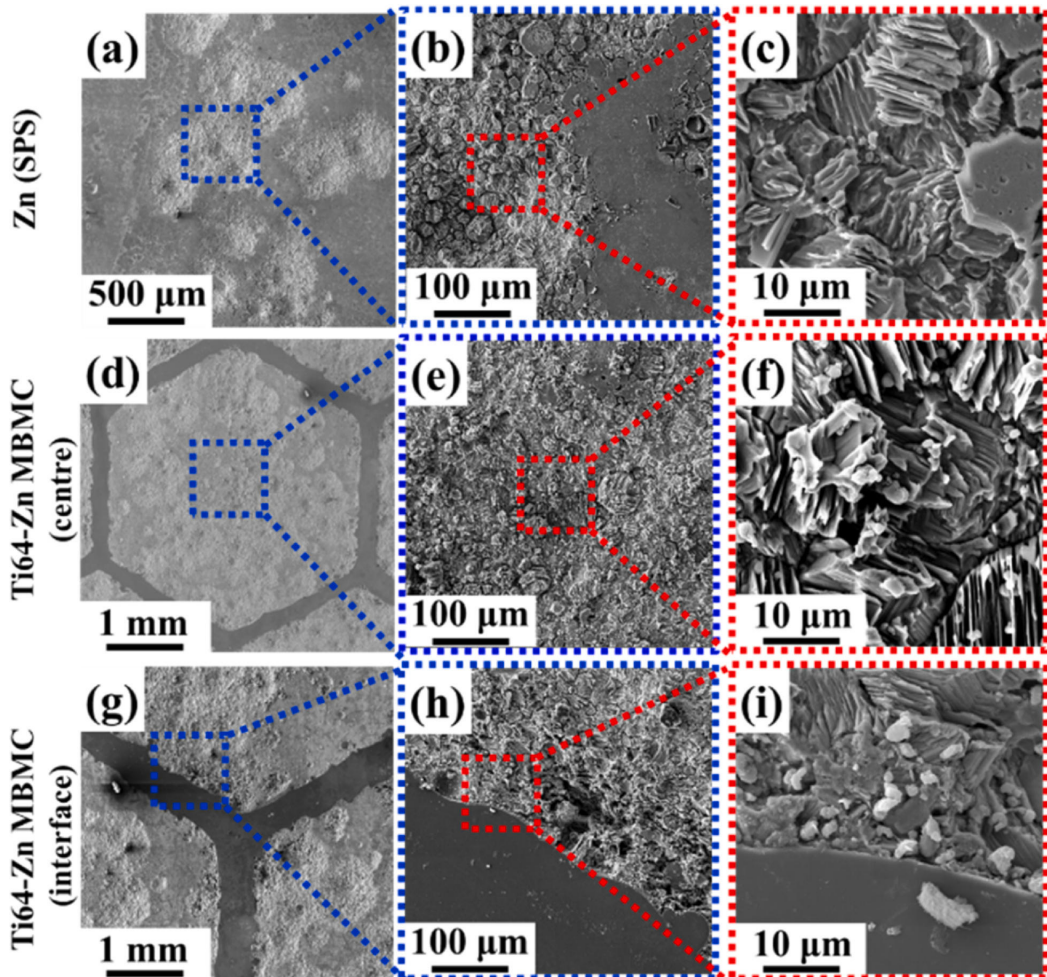


Fig. 11. Scanning electron microscopy images of the corroded samples following potentiodynamic polarization immersion in simulated body fluid (SBF) solution for 1 h, comparing spark plasma sintered (SPS) Zn and Ti6Al4V-zinc (Ti64-Zn) metallic bi-metal composite (MBMC). (a-c) Surface morphology of SPS Zn at varying magnifications, revealing a uniformly distributed corroded region with deep grooves inside the pits, as observed in the higher magnification images. (d-e) Surface morphology of Ti64-Zn MBMC, displaying a complete hexagonal unit and a higher magnification image highlighting the corrosion behavior at the center of the hexagon, away from the Ti64-rich region. (g-i) Surface morphology at the Ti64-Zn interface, showing a corrosion pattern like SPS Zn while demonstrating the stability of Ti64 in the corrosive environment.

largely unaffected. This behavior is attributed to galvanic coupling between the two phases, which enhances ion exchange and drives preferential corrosion of Zn adjacent to Ti64. Similar interfacial degradation patterns have been reported in other dissimilar metal systems, including Ti-Mg and Ti-Zn composites [95,96], supporting the mechanism observed in the present study.

3.7. In-vitro cytotoxicity

The in-vitro biological evaluation of the biodegradable Ti64-Zn MBMC was performed using an indirect cytocompatibility method, in which the cellular response to degradation products released into the conditioned medium was assessed. MC3T3-E1 pre-osteoblast cells were cultured in extracts prepared according to the procedure described in Section 2.8, and cell growth was quantified using the relative growth rate (RGR) after 1 and 3 days of incubation. Fresh medium served as the

control, and the RGR values obtained for the composite were compared with those of SPS Zn and SLM Ti64 under identical conditions. The viability of MC3T3-E1 cells cultured in 1x and 8x extracts (corresponding to 100% and 12.5% conditioned medium) after 1 and 3 days is shown in Fig. 15.

Cells exposed to the 1x extract of the Ti64-Zn MBMC exhibited reduced viability compared with SLM Ti64, while SPS Zn showed a similar response likely due to the higher Zn ion concentration in the undiluted medium. However, upon 8-fold dilution, no cytotoxic effects were observed, and cell viability became comparable to that of both Ti64 and Zn. A similar trend was observed for the 72 h conditioned medium: 8x dilutions supported normal cell growth, whereas 1x extracts of both the composite and SPS Zn resulted in decreased proliferation. Fig. 15(b) shows the cell proliferation after 3 days of incubation. The RGR values for the 100% extracts of both 24 h and 72 h conditioned media showed a marked decline. In contrast, the 8x diluted

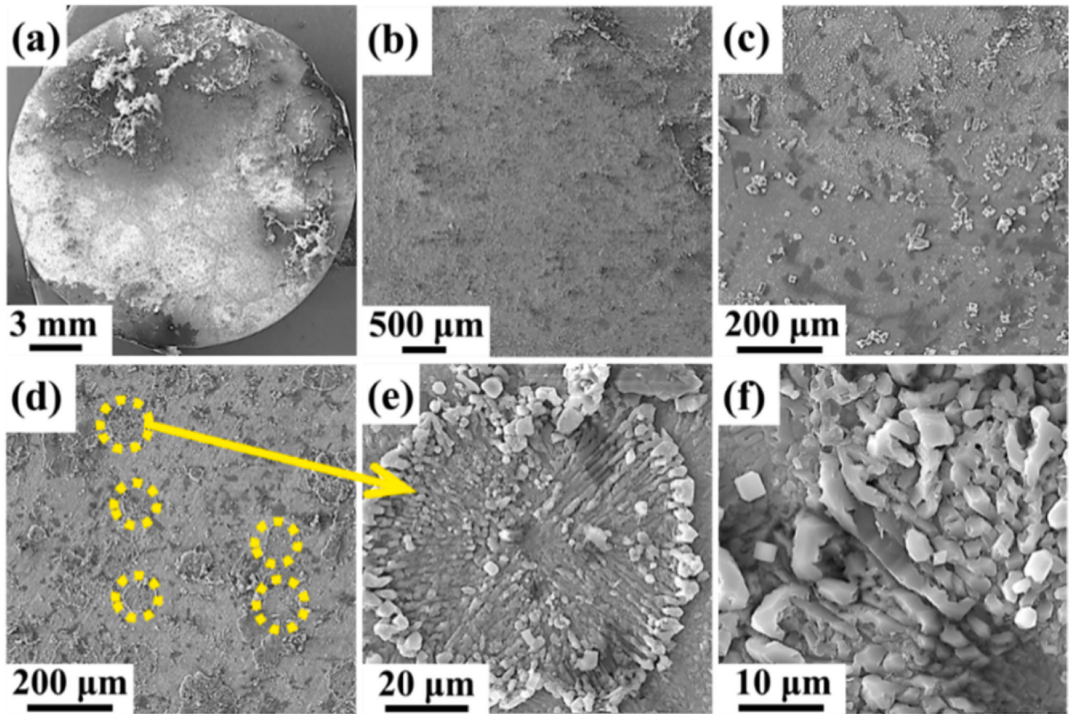


Fig. 12. Scanning electron microscopy images showing the surface morphology of Ti6Al4V-Zn metallic bi-metal composites after 21 days of immersion in simulated body fluid. (a) overall surface image, (b) and (c) higher magnification images from the centre and at the interfacial region, (d) presence of circular patches on the surface; (e) magnified view of patches showing petal-like structures suggestive of apatite layer formation. (f) High-magnification image revealing rectangular and irregularly shaped crystals, possibly indicating the apatite crystallization.

Table 5

Table furnishing the degradation data in mm/year for Ti6Al4V-zinc (Ti64-Zn) metallic bi-metal composite, spark plasma sintered Zn, and bulk selective laser melted Ti64 after incubating the samples in simulated body fluid as a function of varying time.

Samples	After 7 days	After 14 days	After 21 days
Ti64-Zn (MBMC)	0.1577 ± 0.0100	0.0872 ± 0.0100	0.0845 ± 0.0300
SPS Zn	0.1325 ± 0.0800	0.0965 ± 0.1000	0.0858 ± 0.0500
SLM bulk Ti64	0	0.0072 ± 0.0100	0.0004 ± 0.0100

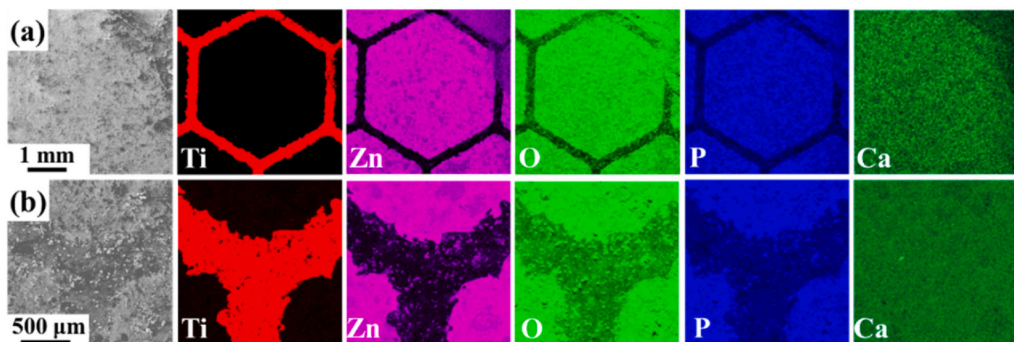


Fig. 13. Energy dispersive spectroscopy mapping of the Ti6Al4V-zinc (Ti64-Zn) metallic bi-metal composite surface after 21 days of immersion in simulated body fluid. (a) Elemental distribution across a single hexagonal unit, (b) elemental mapping at the Ti64-Zn interfacial region.

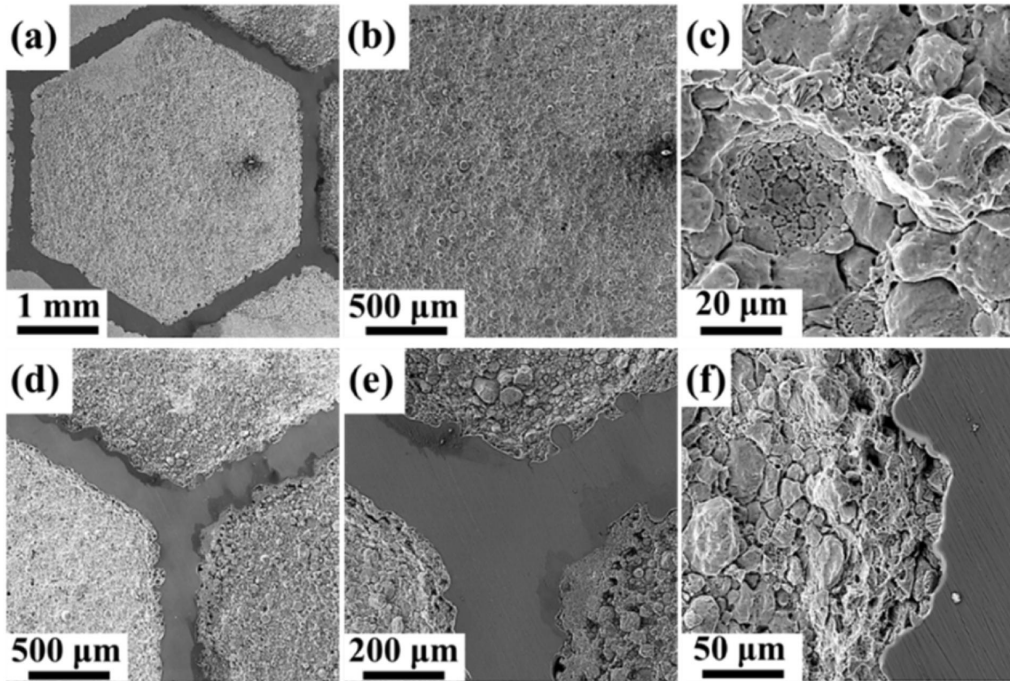


Fig. 14. Scanning electron microscopy images illustrating the degraded surface of the Ti6Al4V-zinc (Ti64-Zn) metallic bi-metal composite (MBMC) after removal of the oxide film and degradation products. (a) Overall view of a single hexagonal unit, (b) a magnified image of the Zn-rich region, (c) higher magnification image highlighting the presence of deep grooves within corrosion pits, (d–f) Ti64-Zn interface at different magnifications.

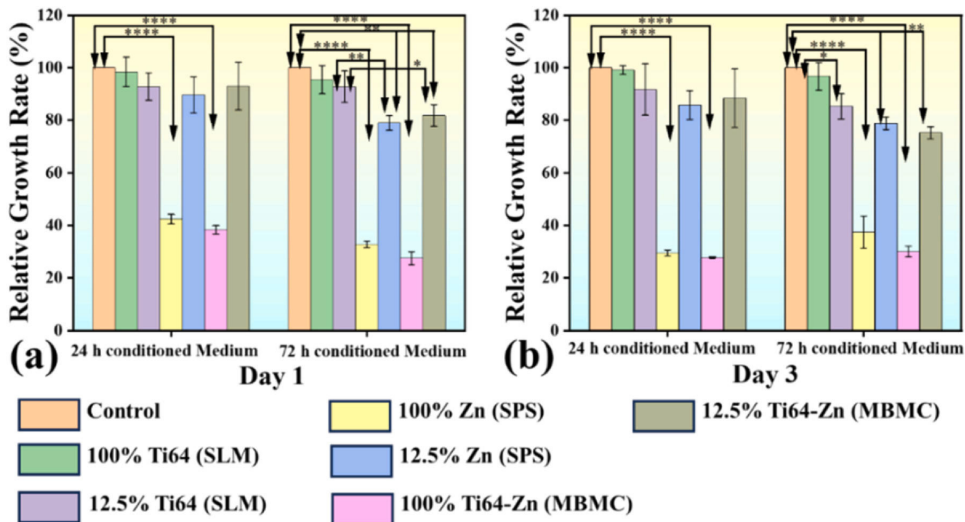


Fig. 15. Relative growth rate measured by water-soluble tetrazolium (WST) assay for MC3T3-E1 cells cultured in 24 h and 72 h conditioned medium for (a) 1 and (b) 3 days, respectively. Cells in fresh medium were taken as the control for each day. The significance level is taken as $p = 0.05$, i.e., $p < 0.05$ (*), $p < 0.01$ (**), $p < 0.001$ (***), $p < 0.0001$ (****) and $p > 0.05$, non-significant (ns), $n = 3$.

extracts exhibited no cytotoxicity, and the growth rates were comparable to the control group for both extraction times. Importantly, samples incubated in 8x diluted conditioned medium for both 1 and 3 days demonstrated cell viability above 75%, which according to established

cytotoxicity classification standards indicates that the Ti64-Zn MBMC is non-cytotoxic [97,98].

Fig. 16 presents the Live–Dead assay results used to assess potential cytotoxicity arising from the composite’s degradation products. Green

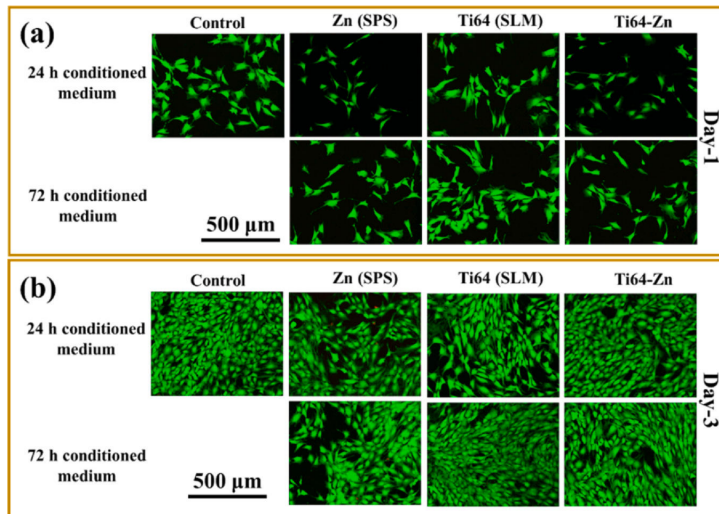


Fig. 16. Representative live/dead stained images of MC3T3-E1 cells cultured in 8x diluted conditioned medium of spark plasma sintered Zn, selective laser melted Ti6Al4V, and Ti6Al4V-Zn metallic bi-metal composites (MBMC) after 1 and 3 days of incubation. Live cells are depicted in green while dead cells appear in red. Cells cultured in fresh complete medium act as the control. The scale bar is 500 μm.

fluorescence corresponds to live cells, while red fluorescence indicates dead cells after 1 and 3 days of exposure to an 8-fold diluted extract. As shown in Fig. 16(a,b), all samples exhibit only a minimal number of dead cells at both time points, comparable to the control group, confirming the cytocompatibility of the Ti64Zn MBMC. Moreover, Fig. 16(b) shows an increase in the number of live cells over time, indicating continued cell proliferation. In contrast, exposure to the undiluted (1x) extract resulted in extensive cell detachment following cell death, consistent with the observations from the WST assay.

To further examine cellular morphology, fluorescence microscopy was performed at different incubation periods, and the corresponding micrographs are shown in Fig. 17. The composite samples exhibit well-spread cells with morphology comparable to that of the control. SPS Zn and SLM Ti64 also demonstrate favourable cell attachment and spreading like the MBMC. However, in the 100% conditioned medium,

both the composite and SPS Zn show signs of stressed cellular morphology, likely due to the elevated concentration of Zn ions in the undiluted extract. Overall, the results demonstrate that the Ti64-Zn MBMC exhibits favourable cytocompatibility. Under 8x dilution, no cytotoxic effects were observed, and cells displayed healthy proliferation and morphology comparable to the control group. At low concentrations, Zn²⁺ ions have been reported to enhance cellular activity in human vascular cells [99–102]. Although Zn can modulate pro-inflammatory responses, it also plays an essential role in maintaining normal immune function [103]. In contrast, exposure to the undiluted (100%) conditioned medium resulted in reduced cell viability and clear signs of cellular stress. Collectively, these findings confirm that the bio-inspired, partially biodegradable Ti64-Zn MBMC exhibits excellent biocompatibility at 8x dilution, supporting its potential for biomedical applications.

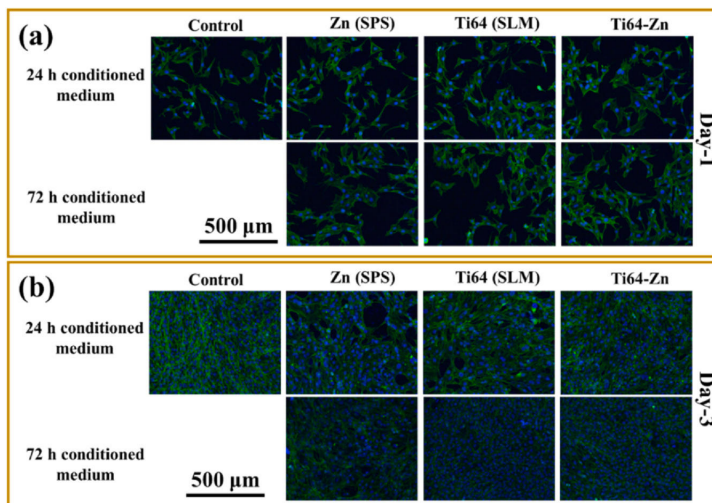


Fig. 17. Representative fluorescence images of MC3T3-E1 cells cultured in conditioned medium after 1 and 3 days of incubation, showing actin filaments (green) and nuclei (blue). The control represents cells treated with fresh complete medium.

4. Conclusions

This study reports the successful development of a bio-inspired, partially biodegradable Ti64-Zn MBMC using a combined additive manufacturing and powder metallurgy approach. The Ti64 hexagonal lattice provides structural integrity, while the incorporated Zn phase enables controlled degradation. Microstructural analysis confirmed a defect-free Ti64-Zn interface with no detectable interfacial reactions, ensuring mechanical stability. The composite achieved an ultimate compressive strength of 292 ± 25 MPa, significantly exceeding that of pure Zn and the standalone Ti64 lattice. In-vitro biodegradation tests revealed a degradation rate of 0.1577 mm/year, and electrochemical analysis indicated a moderate corrosion rate governed by galvanic interactions between Ti64 and Zn. Cytocompatibility studies demonstrated healthy cell proliferation with no cytotoxic effects at optimized dilution levels. The bio-inspired architecture further supports bone ingrowth, positioning the Ti64-Zn MBMC as a promising candidate for next-generation biodegradable implants that effectively balance mechanical stability, controlled degradation, and reduced stress shielding for biomedical applications.

CRedit authorship contribution statement

Kaushik Chatterjee: Writing – review & editing, Supervision, Resources, Methodology. **Satyam Suwas:** Writing – original draft, Supervision, Resources. **J. Jayaraj:** Writing – review & editing, Writing – original draft, Supervision, Methodology, Investigation, Formal analysis, Data curation. **Prashanth Konda Gokuldoss:** Writing – review & editing, Validation, Supervision, Resources, Project administration, Investigation, Funding acquisition, Formal analysis, Conceptualization. **Mayank Kumar Yadav:** Writing – original draft, Visualization, Methodology, Investigation, Formal analysis, Data curation. **K. Praveenkumar:** Writing – original draft, Methodology, Investigation, Formal analysis, Data curation. **Riddhi Hirenkumar Shukla:** Writing – original draft, Methodology, Investigation, Formal analysis, Data curation. **Sagar Nilawar:** Writing – original draft, Methodology, Investigation, Data curation. **Chandra Sekhar Perugu:** Writing – original draft, Investigation, Formal analysis, Data curation.

Funding

Funding from the European Union's Horizon 2020 Research and Innovation programme under Grant Agreement No 101004730 is acknowledged.

Data availability

Data will be made available on request.

Declaration of Competing Interest

The authors declare the following financial personal relationships which may be considered as potential competing interests: The corresponding author and the last author (Prashanth Konda Gokuldoss) is one of the Associate-Editors of this journal - Advanced Light Materials. If there are other authors, they declare that they have no known competing financial interests or personal relationships that could have appeared to influence the work reported in this paper.

Acknowledgments

Funding from the European Union's Horizon 2020 Research and Innovation programme under Grant Agreement No 101004730 is acknowledged. This article has been produced with the financial support of the European Union under the REFRESH–Research Excellence For REgion Sustainability and High-tech Industries project number

CZ.10.03.01/00/22.003/0000048 via the Operational Programme Just Transition. This work was also supported as part of the project No. CZ.02.01.01/00/22.008/0004631; Materials and technologies for sustainable development within the Jan Amos Komensky Operational Program financed by the European Union and from the state budget of the Czech Republic, Ministry of education, youth and sports.

References

- [1] M. Geetha, A.K. Singh, R. Asokamani, A.K. Gogia, Ti based biomaterials, the ultimate choice for orthopaedic implants - a review, *Prog. Mater. Sci.* 54 (2009) 397–425, <https://doi.org/10.1016/j.pmatsci.2008.06.004>.
- [2] Q. Chen, G.A. Thouas, Metallic implant biomaterials, *Mater. Sci. Eng. R Rep.* 87 (2015) 1–57, <https://doi.org/10.1016/j.mser.2014.10.001>.
- [3] M. Saini, Y. Singh, P. Arora, V. Arora, K. Jain, Implant biomaterials: A comprehensive review, *World J. Clin. Cases* 3 (2015) 52–57, <https://doi.org/10.12998/wjcc.v3.i1.52>.
- [4] M.K. Yadav, A. Yarlapaty, Y.N. Aditya, P. Kesavan, V. Pandey, C.S. Perugu, A. Nain, K. Chatterjee, S. Suwas, J. Jayamani, P.K. Gokuldoss, Processing and Development of Porous Titanium for Biomedical Applications: A Comprehensive Review, *J. Manuf. Mater. Proc.* 9 (2025) 401, <https://doi.org/10.3390/JMMP9120401>.
- [5] K. Chen, J. Dong, N.E. Putra, L.E. Fratila-Apachitei, J. Zhou, A.A. Zadpoor, Additively manufactured function-tailored bone implants made of graphene-containing biodegradable metal matrix composites, *Prog. Mater. Sci.* 155 (2026) 101517, <https://doi.org/10.1016/j.pmatsci.2025.101517>.
- [6] S. Subramanian, M.K. Yadav, J. Jayaraj, F. Yangyang, L. Xi, K.G. Prashanth, Microstructural homogenization through laser remelting in an additively manufactured Ti–40Nb sample from elemental feedstock powders, *J. Mater. Res. Technol.* 38 (2025) 4305–4320, <https://doi.org/10.1016/j.jmrt.2025.08.203>.
- [7] K. Praveenkumar, J. Vishnu, C. Samuel S, V. Gopal, M. Arivarasu, J.M. Lackner, B. Meier, D. Karthik, S. Suwas, S. Swaroop, K.G. Prashanth, M.K. Yadav, G. Manivasagam, High temperature dry sliding wear behaviour of selective laser melted Ti-6Al-4V alloy surfaces, *J. Mater. Process. Technol.* 329 (2024) 118439, <https://doi.org/10.1016/j.jmatprotec.2024.118439>.
- [8] X. Gong, Y. Li, Y. Nie, Z. Huang, F. Liu, L. Huang, L. Jiang, H. Mei, Corrosion behaviour of CoCrMo alloy fabricated by electron beam melting, *Corros. Sci.* 139 (2018) 68–75, <https://doi.org/10.1016/j.corsci.2018.04.033>.
- [9] A. Bandyopadhyay, A. Shivaram, M. Isik, J.D. Avila, W.S. Dernell, S. Bose, Additively manufactured calcium phosphate reinforced CoCrMo alloy: Bio-tribological and biocompatibility evaluation for load-bearing implants, *Addit. Manuf.* 28 (2019) 312–324, <https://doi.org/10.1016/j.addma.2019.04.020>.
- [10] Y.S. Hedberg, B. Qian, Z. Shen, S. Virtanen, I. Odnevall Wallinder, vitro biocompatibility of CoCrMo dental alloys fabricated by selective laser melting, *Dent. Mater.* 30 (2014) 525–534, <https://doi.org/10.1016/j.dental.2014.02.008>.
- [11] M. Geetha, A.K. Singh, R. Asokamani, A.K. Gogia, Ti based biomaterials, the ultimate choice for orthopaedic implants - A review, *Prog. Mater. Sci.* 54 (2009) 397–425, <https://doi.org/10.1016/j.pmatsci.2008.06.004>.
- [12] S. Arabnejad, B. Johnston, M. Tanzer, D. Pasini, Fully porous 3D printed titanium femoral stem to reduce stress-shielding following total hip arthroplasty, *J. Ortho. Res.* 35 (2017) 1774–1783, <https://doi.org/10.1002/jor.23445>.
- [13] M.I.Z. Ridzwan, S. Shuib, A.Y. Hassan, A.A. Shokri, M.N. Mohammad Ibrahim, Problem of stress shielding and improvement to the hip implant designs: A review, *J. Med. Sci.* 7 (2007) 460–467, <https://doi.org/10.3923/jms.2007.460.467>.
- [14] D.R. Sumner, Long-term implant fixation and stress-shielding in total hip replacement, *J. Biomech.* 48 (2015) 797–800, <https://doi.org/10.1016/j.jbiomech.2014.12.021>.
- [15] A.A. Zadpoor, Open forward and inverse problems in theoretical modeling of bone tissue adaptation, *J. Mech. Behav. Biomed. Mater.* 27 (2013) 249–261, <https://doi.org/10.1016/j.jmbbm.2013.05.017>.
- [16] P. Hameed, C.F. Liu, R. Ummethala, N. Singh, H.H. Huang, G. Manivasagam, K.G. Prashanth, Biomimetic porous Ti6Al4V gyroid scaffolds for bone implant applications fabricated by selective laser melting, *Prog. Addit. Manuf.* 6 (2021) 455–469, <https://doi.org/10.1007/s40964-021-00210-5>.
- [17] J. Lv, Z. Jia, J. Li, Y. Wang, J. Yang, P. Xiu, K. Zhang, H. Cai, Z. Liu, Electron Beam Melting Fabrication of Porous Ti6Al4V Scaffolds: Cytocompatibility and Osteogenesis, *Adv. Eng. Mater.* 17 (2015) 1391–1398, <https://doi.org/10.1002/adem.201400508>.
- [18] G.E. Ryan, A.S. Pandit, D.P. Apatsidis, Porous titanium scaffolds fabricated using a rapid prototyping and powder metallurgy technique, *Biomaterials* 29 (2008) 3625–3635, <https://doi.org/10.1016/j.biomaterials.2008.05.032>.
- [19] Q. Ran, W. Yang, Y. Hu, X. Shen, Y. Yu, Y. Xiang, K. Cai, Osteogenesis of 3D printed porous Ti6Al4V implants with different pore sizes, *J. Mech. Behav. Biomed. Mater.* 84 (2018) 1–11, <https://doi.org/10.1016/j.jmbbm.2018.04.010>.
- [20] B.V. Krishna, S. Bose, A. Bandyopadhyay, Low stiffness porous Ti structures for load-bearing implants, *Acta Biomater.* 3 (2007) 997–1006, <https://doi.org/10.1016/j.actbio.2007.03.008>.
- [21] Y.J. Liu, H.L. Wang, S.J. Li, S.G. Wang, W.J. Wang, W.T. Hou, Y.L. Hao, R. Yang, L.C. Zhang, Compressive and fatigue behavior of beta-type titanium porous structures fabricated by electron beam melting, *Acta Mater.* 126 (2017) 58–66, <https://doi.org/10.1016/j.actamat.2016.12.052>.
- [22] X. Wang, Y. Li, J. Xiong, P.D. Hodgson, C. Wen, Porous TiNbZr alloy scaffolds for biomedical applications, *Acta Biomater.* 5 (2009) 3616–3624, <https://doi.org/10.1016/j.actbio.2009.06.002>.

- [23] K. Prasad, O. Bazaka, M. Chua, M. Rochford, L. Fedrick, J. Spoor, R. Symes, M. Tieppo, C. Collins, A. Cao, D. Markwell, K. Ostrikov, K. Bazaka, *Metallic Biomaterials: Current Challenges and Opportunities*, *Materials* 10 (2017) 884, <https://doi.org/10.3390/ma10080884>.
- [24] M. Prakasam, J. Locs, K. Salma-Ancane, D. Loca, A. Largeteau, L. Berzina-Cimdina, *Biodegradable Materials and Metallic Implants—A Review*, *J. Funct. Biomater.* 8 (2017) 44, <https://doi.org/10.3390/jfb8040044>.
- [25] G. Song, S. Song, A possible biodegradable magnesium implant material, *Adv. Eng. Mater.* 9 (2007) 298–302, <https://doi.org/10.1002/adem.200600252>.
- [26] T.S. Shih, W.S. Liu, Y.J. Chen, Fatigue of as-extruded AZ61A magnesium alloy, *Mater. Sci. Eng. A* 325 (2002) 152–162, [https://doi.org/10.1016/s0921-5093\(01\)01411-3](https://doi.org/10.1016/s0921-5093(01)01411-3).
- [27] D. Persaud-Sharma, A. Mgoron, *Biodegradable Magnesium Alloys: A Review of Material Development and Applications*, *J. Biomim. Biomater. Tissue Eng.* 12 (2011) 25–39, <https://doi.org/10.4028/www.scientific.net/jbte.12.25>.
- [28] L. Drotárová, K. Slámečka, T. Balint, M. Remešová, R. Hudák, J. Živčák, M. Schnitzer, L. Čelko, E.B. Montufar, *Biodegradable WE43 Mg alloy/hydroxyapatite interpenetrating phase composites with reduced hydrogen evolution*, *Bioact. Mater.* 42 (2024) 519–530, <https://doi.org/10.1016/j.bioactmat.2024.08.048>.
- [29] N.T. Kirkland, N. Birbilis, M.P. Staiger, *Assessing the corrosion of biodegradable magnesium implants: A critical review of current methodologies and their limitations*, *Acta Biomater.* 8 (2012) 925–936, <https://doi.org/10.1016/j.actbio.2011.11.014>.
- [30] A. Atrens, M. Liu, N.I. Zainal Abidin, *Corrosion mechanism applicable to biodegradable magnesium implants*, *Mater. Sci. Eng. B* 176 (2011) 1609–1636, <https://doi.org/10.1016/j.mseb.2010.12.017>.
- [31] M.A. Hussein, M.A. Azeem, A.M. Kumar, N.M. Emara, *Processing and in vitro corrosion analysis of sustainable and economical eggshell reinforced Mg and Mg-Zr matrix composite for biomedical applications*, *Mater. Today Commun.* 32 (2022) 103944, <https://doi.org/10.1016/j.mtcomm.2022.103944>.
- [32] P.K. Bowen, E.R. Shearier, S. Zhao, R.J. Guillory, F. Zhao, J. Goldman, J.W. Drellich, *Biodegradable Metals for Cardiovascular Stents: from Clinical Concerns to Recent Zn-Alloys*, *Adv. Healthc. Mater.* 5 (2016) 1121–1140, <https://doi.org/10.1002/adhm.201501019>.
- [33] V.P.M. Rabeeh, T. Hanas, *Progress in manufacturing and processing of degradable Fe-based implants: a review*, *Prog. Biomater.* 11 (2022) 163–191, <https://doi.org/10.1007/s40204-022-00189-4>.
- [34] S. Yu, H. Chi, P. Li, B. Guo, Z. Yu, Z. Xu, P. Liang, Z. Zhang, Y. Guo, L. Ren, *Interpenetrating phase composites Ti6Al4V/Zn as partially degradable biomaterials to improve bone-implant properties*, *Addit. Manuf.* 93 (2024) 104411, <https://doi.org/10.1016/j.addma.2024.104411>.
- [35] M. Yadav, R. Shukla, P. Kesavan, S. Nilavar, C. Perugu, P. Sellamuthu, K. Chatterjee, S. Suwas, J. Jayamani, K. Prashanth, *Microstructural, mechanical, corrosion, and biological behavior of spark plasma sintered commercially pure zinc for biomedical applications*, *Mater. Adv.* 6 (2025) 3546–3560, <https://doi.org/10.1039/d5ma00092k>.
- [36] H. Kabir, K. Munir, C. Wen, Y. Li, *Recent research and progress of biodegradable zinc alloys and composites for biomedical applications: Biomechanical and bio-corrosion perspectives*, *Bioact. Mater.* 6 (2021) 836–879, <https://doi.org/10.1016/j.bioactmat.2020.09.013>.
- [37] Y. Su, I. Cockerill, Y. Wang, Y.X. Qin, L. Chang, Y. Zheng, D. Zhu, *Zinc-Based Biomaterials for Regeneration and Therapy*, *Trends Biotechnol.* 37 (2019) 428–441, <https://doi.org/10.1016/j.tibtech.2018.10.009>.
- [38] P. Trumbo, A.A. Yates, S. Schlicker, M. Poos, *Dietary reference intakes: vitamin A, vitamin K, arsenic, boron, chromium, copper, iodine, iron, manganese, molybdenum, nickel, silicon, vanadium, and zinc*, *J. Am. Diet. Assoc.* 101 (2001) 294–301, [https://doi.org/10.1016/s0002-8223\(01\)00078-5](https://doi.org/10.1016/s0002-8223(01)00078-5).
- [39] C. Wang, C. Lan, X. Lin, Y. Hu, *Effect of laser power on microstructure and mechanical properties of pure Zn fabricated via laser powder bed fusion*, *J. Mater. Res. Technol.* 28 (2024) 2523–2534, <https://doi.org/10.1016/j.jmrt.2023.12.159>.
- [40] X. Tong, X. Hong, L. Chen, Y. Zhang, Y. Wang, Y. Chen, Y. Zhu, C. Wang, L. Zhu, J. Lin, S. Huang, J. Ma, P. Luo, *Degradable Zn–5Ce alloys with high strength, suitable degradability, good cytocompatibility, and osteogenic differentiation fabricated via hot-rolling, hot-extrusion, and high-pressure torsion for potential load-bearing bone-implant application*, *J. Mater. Res. Technol.* 28 (2024) 1752–1763, <https://doi.org/10.1016/j.jmrt.2023.12.098>.
- [41] K.G. Prashanth, *Interpenetrating Composites: A Nomenclature Dilemma*, 18, *Materials* 2025 18 (273) (2025) 273, <https://doi.org/10.3390/ma18020273>.
- [42] Z. Zhang, Z. Wang, Q. Zhao, K.G. Prashanth, *Metal-metal interpenetrating phase composites: A review*, *J. Alloy. Compd.* 1009 (2024) 176951, <https://doi.org/10.1016/j.jallcom.2024.176951>.
- [43] O. Al-Ketan, R.K.A. Al-Rub, R. Rowshan, *Mechanical properties of a new type of architected interpenetrating phase composite materials*, *Adv. Mater. Technol.* 2 (2017) 1600235, <https://doi.org/10.1002/admt.201600235>.
- [44] Y. Liu, B. Chen, Z. Liu, Z. Zhang, R.O. Ritchie, *Bioinspired interpenetrating phase metal composites*, *Prog. Mater. Sci.* 144 (2024) 101281, <https://doi.org/10.1016/j.pmatsci.2024.101281>.
- [45] L. Zeng, C. You, X. Zhang, T. Liang, S. Miao, B. Liu, *Preparation of bulk Cu-W interpenetrating-phase composites by liquid metal dealloying*, *Int. J. Refract. Met. Hard Mater.* 97 (2021) 105503, <https://doi.org/10.1016/j.jrmhm.2021.105503>.
- [46] U.G.K. Wegst, H. Bai, E. Saiz, A.P. Tomsia, R.O. Ritchie, *Bioinspired structural materials*, *Nat. Mater.* 14 (2014) 23–36, <https://doi.org/10.1038/nmat4089>.
- [47] D. Kokkinis, M. Schaffner, A.R. Studart, *Multimaterial magnetically assisted 3D printing of composite materials*, *Nat. Comm.* 6 (2015) 1–10, <https://doi.org/10.1038/ncomms9643>.
- [48] L.Y. Chen, S.X. Liang, Y. Liu, L.C. Zhang, *Additive manufacturing of metallic lattice structures: Unconstrained design, accurate fabrication, fascinated performances, and challenges*, *Mater. Sci. Eng. R* 146 (2021) 100648, <https://doi.org/10.1016/j.mser.2021.100648>.
- [49] F. Liu, T. Li, Z. Jia, L. Wang, *Combination of stiffness, strength, and toughness in 3D printed interlocking nacre-like composites*, *Extrem. Mech. Lett.* 35 (2020) 100621, <https://doi.org/10.1016/j.eml.2019.100621>.
- [50] E.E. de Obaldia, C. Jeong, L.K. Grunenfelder, D. Kisailus, P. Zavattieri, *Analysis of the mechanical response of biomimetic materials with highly oriented microstructures through 3D printing, mechanical testing and modeling*, *J. Mech. Behav. Biomed. Mater.* 48 (2015) 70–85, <https://doi.org/10.1016/j.jmbmb.2015.03.026>.
- [51] A. Velasco-Hogan, J. Xu, M.A. Meyers, A. Velasco-Hogan, M.A. Meyers, J. Xu, *Additive Manufacturing as a Method to Design and Optimize Bioinspired Structures*, *Adv. Mater.* 30 (2018) 1800940, <https://doi.org/10.1002/ADMA.201800940>.
- [52] L. Bai, C. Gong, X. Chen, Y. Sun, J. Zhang, L. Cai, S. Zhu, S.Q. Xie, *Additive manufacturing of customized metallic orthopedic implants: Materials, structures, and surface modifications*, *Metals* 9 (2019) 1004, <https://doi.org/10.3390/met9091004>.
- [53] A.A. Raheem, P. Hameed, R. Whenish, R.S. Elsen, G. Aswin, A.K. Jaiswal, K.G. Prashanth, G. Manivasagam, *A review on development of bio-inspired implants using 3D printing*, *Biomimetics* 6 (2021) 65, <https://doi.org/10.3390/biomimetics6040065>.
- [54] P.A. Khan, A. Raheem, C. Kalirajan, K.G. Prashanth, G. Manivasagam, *Vivo Assessment of a Triple Periodic Minimal Surface Based Biomimetic Gyroid as an Implant Material in a Rabbit Tibia Model*, *ACS Mater. Au* 4 (2024) 479–488, <https://doi.org/10.1021/acsmaterials.4c00016>.
- [55] J.B. Jin, S. Zhou, H. Yang, J. Yang, Z. Zhang, B. Guo, L.C. Zhang, *Breaking through the strength-ductility trade-off of LPBF-produced Ti-xNb alloys from mixed powders via ω -phase induced heterostructure*, *Int. J. Ext. Manuf.* 7 (2025) 065003, <https://doi.org/10.1088/2631-7990/aded4e>.
- [56] K. Li, J. Yang, Y. Yi, X. Liu, Y. Liu, L.C. Zhang, W. Zhang, W. Li, D. Chen, S. Zhou, *Enhanced strength-ductility synergy and mechanisms of heterostructured Ti6Al4V-Cu alloys produced by laser powder bed fusion*, *Acta Mater.* 256 (2023) 119112, <https://doi.org/10.1016/j.actamat.2023.119112>.
- [57] S. Limmahakun, A. Oloyede, K. Sithiseripatip, Y. Xiao, C. Yan, *3D-printed cellular structures for bone biomimetic implants*, *Addit. Manuf.* 15 (2017) 93–101, <https://doi.org/10.1016/j.addma.2017.03.010>.
- [58] M. Cerea, G.A. Dolcini, *Custom-Made Direct Metal Laser Sintering Titanium Subperiosteal Implants: A Retrospective Clinical Study on 70 Patients*, *Biomed. Res. Int.* 2018 (2018) 5420391, <https://doi.org/10.1155/2018/5420391>.
- [59] J.M. Cordeiro, T. Beline, A.L.R. Ribeiro, E.C. Rangel, N.C. da Cruz, R. Landers, L.P. Faverani, L.G. Vaz, L.M.G. Fais, F.B. Vicente, C.R. Grandini, M.T. Mathew, C. Sukotjo, V.A.R. Barão, *Development of binary and ternary titanium alloys for dental implants*, *Dent. Mater.* 33 (2017) 1244–1257, <https://doi.org/10.1016/j.dental.2017.07.013>.
- [60] S. Tunchel, A. Blay, R. Kolerman, E. Mijiritsky, J.A. Shibli, *3D Printing/Additive Manufacturing Single Titanium Dental Implants: A Prospective Multicenter Study with 3 Years of Follow-Up*, *Int. J. Dent.* 2016 (2016) 8590971, <https://doi.org/10.1155/2016/8590971>.
- [61] Q. Ran, W. Yang, Y. Hu, X. Shen, Y. Yu, Y. Xiang, K. Cai, *Osteogenesis of 3D printed porous Ti6Al4V implants with different pore sizes*, *J. Mech. Behav. Biomed. Mater.* 84 (2018) 1–11, <https://doi.org/10.1016/j.jmbmb.2018.04.010>.
- [62] Z. Zhang, Z. Wang, Q. Zhao, K.G. Prashanth, *Metal-metal interpenetrating phase composites: A review*, *J. Alloy. Compd.* 1009 (2024) 176951, <https://doi.org/10.1016/j.jallcom.2024.176951>.
- [63] M.K. Yadav, R. Shukla, L. Xi, Z. Wang, K.G. Prashanth, *Metallic multimaterials fabricated by combining additive manufacturing and powder metallurgy*, *J. Comp. Sci.* 9 (2025) 80, <https://doi.org/10.3390/jcs9020080>.
- [64] L.J. Gibson, M.F. Ashby, *Cellular solids: Structure and properties, second edition, Cellular Solids: Structure and Properties, Second Ed.* (2014) 1–510, <https://doi.org/10.1017/cbo9781139878326>.
- [65] S.D. Papka, S. Kyriakides, *In-plane compressive response and crushing of honeycomb*, *J. Mech. Phys. Solids* 42 (1994) 1499–1532, [https://doi.org/10.1016/0022-5096\(94\)90085-X](https://doi.org/10.1016/0022-5096(94)90085-X).
- [66] Z. Zhang, Z. Shi, B. Yang, B. Ge, X. Zhang, Y. Guo, *Preparation and anisotropic thermophysical properties of SiC honeycomb/Al-Mg-Si composite via spontaneous infiltration*, *Prog. Nat. Sci. Mater. Int.* 29 (2019) 177–183, <https://doi.org/10.1016/j.pnsc.2019.02.004>.
- [67] L. Zhang, B. Song, A. Zhao, R. Liu, L. Yang, Y. Shi, *Study on mechanical properties of honeycomb pentamode structures fabricated by laser additive manufacturing: Numerical simulation and experimental verification*, *Compos. Struct.* 226 (2019) 111199, <https://doi.org/10.1016/j.compstruct.2019.111199>.
- [68] P. Xia, Q. Liu, H. Fu, Y. Yu, L. Wang, Q. Wang, X. Yu, F. Zhao, *Mechanical properties and energy absorption of 3D printed double-layered helix honeycomb under in-plane compression*, *Compos. Struct.* 315 (2023) 116982, <https://doi.org/10.1016/j.compstruct.2023.116982>.
- [69] S. Xu, N. Chen, H. Qin, M. Zou, J. Song, *Biomimetic Study of a Honeycomb Energy Absorption Structure Based on Straw Micro-Porous Structure*, *Biomimetics* 9 (2024) 60, <https://doi.org/10.3390/biomimetics9010060>.
- [70] D.W. Hutmacher, *Scaffolds in tissue engineering bone and cartilage*, *Biomaterials* 21 (2000) 2529–2543, [https://doi.org/10.1016/s0142-9612\(00\)00121-6](https://doi.org/10.1016/s0142-9612(00)00121-6).
- [71] D.W. Hutmacher, *Scaffold design and fabrication technologies for engineering tissues — state of the art and future perspectives*, *J. Biomater. Sci. Polym. Ed.* 12 (2001) 107–124, <https://doi.org/10.1163/156856201744489>.

- [72] Q. Zhang, X. Yang, P. Li, G. Huang, S. Feng, C. Shen, B. Han, X. Zhang, F. Jin, F. Xu, T.J. Lu, Bioinspired engineering of honeycomb structure – Using nature to inspire human innovation, *Prog. Mater. Sci.* 74 (2015) 332–400, <https://doi.org/10.1016/j.pmatsci.2015.05.001>.
- [73] Z. Zhang, Y. Yang, Y. Guo, Z. Xu, P. Sha, Z. Yu, L. Ren, The corrosion resistance and biomineralization of the DCPD-PCL coating on the surface of the additively manufactured TiTi alloy, *Surf. Coat. Technol.* 466 (2023) 129653, <https://doi.org/10.1016/j.surfcoat.2023.129653>.
- [74] H.I. K ok, M. Kick, O. Akbas, S. Stammk otter, A. Greuling, M. Stiesch, F. Walther, P. Junker, Reduction of stress-shielding and fatigue-resistant dental implant design through topology optimization and TPMS lattices, *J. Mech. Behav. Biomed. Mater.* 165 (2025) 106923, <https://doi.org/10.1016/j.jmbbm.2025.106923>.
- [75] J. Karimi, M. Antonov, L. Kollo, K.G. Prashanth, Role of laser remelting and heat treatment in mechanical and tribological properties of selective laser melted Ti6Al4V alloy, *J. Alloy. Compd.* 897 (2022) 163207, <https://doi.org/10.1016/j.jallcom.2021.163207>.
- [76] J. Karimi, C. Zhao, K.G. Prashanth, Massive transformation in dual-laser powder bed fusion of Ti6Al4V alloys, *J. Manuf. Process* 119 (2024) 282–292, <https://doi.org/10.1016/j.jmapro.2024.03.083>.
- [77] Z. Zhou, Y. Liu, X. Liu, Q. Zhan, K. Wang, Microstructure evolution and mechanical properties of in-situ Ti6Al4V–TiB composites manufactured by selective laser melting, *Compos. B Eng.* 207 (2021) 108567, <https://doi.org/10.1016/j.compositesb.2020.108567>.
- [78] S.C. Wang, M. Aindow, M.J. Starink, Effect of self-accommodation on α/α' boundary populations in pure titanium, *Acta Mater.* 51 (2003) 2485–2503, [https://doi.org/10.1016/S1359-6454\(03\)00035-1](https://doi.org/10.1016/S1359-6454(03)00035-1).
- [79] C. Zhao, Z. Wang, D. Li, L. Kollo, Z. Luo, W. Zhang, K.G. Prashanth, Cu-Ni-Sn alloy fabricated by melt spinning and selective laser melting: a comparative study on the microstructure and formation kinetics, *J. Mater. Res. Technol.* 9 (2020) 13097–13105, <https://doi.org/10.1016/j.jmrt.2020.09.047>.
- [80] C. Tan, Y. Chew, F. Weng, S. Sui, Z. Du, F.L. Ng, G. Bi, Superior strength-ductility in laser aided additive manufactured high-strength steel by combination of intrinsic tempering and heat treatment, *Virtual Phys. Prototyp.* 16 (2021) 460–480, <https://doi.org/10.1080/17452759.2021.1964268>.
- [81] J. Su, X. Ji, J. Liu, J. Teng, F. Jiang, D. Fu, H. Zhang, Revealing the decomposition mechanisms of dislocations and metastable α' phase and their effects on mechanical properties in a Ti-6Al-4V alloy, *J. Mater. Sci. Technol.* 107 (2022) 136–148, <https://doi.org/10.1016/j.jmst.2021.07.048>.
- [82] S. Yu, Y. Yang, P. Li, C. Jiang, Z. Xu, R. Liu, Y. Guo, Z. Yu, P. Liang, Z. Zhang, Z. Xu, J. Wang, L. Ren, Tuning mechanical, degradation and biological properties of interpenetrating phases composites Ti6Al4V/Zn bone implant by interface modification, *Chem. Eng. J.* 523 (2025) 168728, <https://doi.org/10.1016/j.cej.2025.168728>.
- [83] C. Dou, M. Zhang, D. Ren, H. Ji, Z. Yi, S. Wang, Z. Liu, Q. Wang, Y. Zheng, Z. Zhang, R. Yang, Bi-continuous Mg-Ti interpenetrating-phase composite as a partially degradable and bioactive implant material, *J. Mater. Sci. Technol.* 146 (2023) 211–220, <https://doi.org/10.1016/j.jmst.2022.11.011>.
- [84] Y. Liu, Q. Yu, G. Tan, M. Zhang, E. Tang, S. Wang, Z. Liu, Q. Wang, Z. Zhang, R.O. Ritchie, Bioinspired fish-scale-like magnesium composites strengthened by contextures of continuous titanium fibers: Lessons from nature, *J. Magnes. Alloy.* 11 (2023) 869–881, <https://doi.org/10.1016/j.jma.2021.06.023>.
- [85] M. Zhang, N. Zhao, Q. Yu, Z. Liu, R. Qu, J. Zhang, S. Li, D. Ren, F. Berto, Z. Zhang, R.O. Ritchie, On the damage tolerance of 3-D printed Mg-Ti interpenetrating-phase composites with bioinspired architectures, *Nat. Comm.* 13 (2022) 1–13, <https://doi.org/10.1038/s41467-022-30873-9>.
- [86] R. Rahmani, M. Antonov, L. Kollo, Y. Holovenko, K.G. Prashanth, Mechanical behavior of Ti6Al4V scaffolds filled with CaSiO₃ for implant applications, *Appl. Sci.* 9 (2019) 3844, <https://doi.org/10.3390/app9183844>.
- [87] Q. Li, G. Jiang, C. Wang, J. Dong, G. He, Mechanical degradation of porous titanium with entangled structure filled with biodegradable magnesium in Hanks' solution, *Mater. Sci. Eng. C* 57 (2015) 349–354, <https://doi.org/10.1016/j.msec.2015.08.008>.
- [88] R. Shukla, M.K. Yadav, L.Y.C. Madruga, J. Jayaraj, K. Popat, Z. Wang, L. Xi, K.G. Prashanth, A novel Ti-eggshell-based composite fabricated by combined additive manufacturing-powder metallurgical routes as bioimplants, *Ceram. Int.* 51 (2025) 6281–6291, <https://doi.org/10.1016/j.ceramint.2024.12.073>.
- [89] A.N. Aufa, M.Z. Hassan, Z. Ismail, Recent advances in Ti-6Al-4V additively manufactured by selective laser melting for biomedical implants: Prospect development, *J. Alloy. Compd.* 896 (2022) 163072, <https://doi.org/10.1016/j.jallcom.2021.163072>.
- [90] X. Chen, Q. Liao, M. Gong, Q. Fu, Corrosion Performances of Selective Laser Melting Ti6Al4V Alloy in Different Solutions, *Metals* 13 (2023) 192, <https://doi.org/10.3390/met13020192>.
- [91] A. Sharma, M.C. Oh, J.T. Kim, A.K. Srivastava, B. Ahn, Investigation of electrochemical corrosion behavior of additive manufactured Ti-6Al-4V alloy for medical implants in different electrolytes, *J. Alloy. Compd.* 830 (2020) 154620, <https://doi.org/10.1016/j.jallcom.2020.154620>.
- [92] M.Q. Cheng, T. Wahafu, G.F. Jiang, W. Liu, Y.Q. Qiao, X.C. Peng, T. Cheng, X.L. Zhang, G. He, X.Y. Liu, A novel open-porous magnesium scaffold with controllable microstructures and properties for bone regeneration, *Sci. Rep.* 6 (2016) 1–14, <https://doi.org/10.1038/srep24134>.
- [93] Y. Xin, T. Hu, P.K. Chu, Degradation behaviour of pure magnesium in simulated body fluids with different concentrations of HCO₃⁻, *Corros. Sci.* 53 (2011) 1522–1528, <https://doi.org/10.1016/j.corsci.2011.01.015>.
- [94] M. Kumar Yadav, R. Hireen Shukla, K.G. Prashanth, A comprehensive review on development of waste derived hydroxyapatite (HAP) for tissue engineering application, *Mater. Today Proc.* (2023), <https://doi.org/10.1016/j.matpr.2023.04.669>.
- [95] X. Yang, W. Huang, D. Zhan, D. Ren, H. Ji, Z. Liu, Q. Wang, N. Zhang, Z. Zhang, Biodegradability and Cytocompatibility of 3D-Printed Mg-Ti Interpenetrating Phase Composites, *Front. Biotechnol.* 10 (2022) 891632, <https://doi.org/10.3389/fbioe.2022.891632>.
- [96] X. Han, L. Zhou, Z. Liu, S. Zhang, Q. Wang, X. Lu, M. R.I. Abueida, Q. Wang, Z. Zhang, D. Zhang, Degradation behavior of biomedical partially degradable Ti–Mg composite fabricated by 3D printing and pressureless infiltration, *J. Mater. Res. Technol.* 29 (2024) 3192–3204, <https://doi.org/10.1016/j.jmrt.2024.02.059>.
- [97] R. Liu, K. Memarzadeh, B. Chang, Y. Zhang, Z. Ma, R.P. Allaker, L. Ren, K. Yang, Antibacterial effect of copper-bearing titanium alloy (Ti-Cu) against *Streptococcus mutans* and *Porphyromonas gingivalis*, *Sci. Rep.* 6 (2016) 1–10, <https://doi.org/10.1038/srep29985>.
- [98] J. Luo, S. Guo, Y. Lu, X. Xu, C. Zhao, S. Wu, J. Lin, Cytocompatibility of Cu-bearing Ti6Al4V alloys manufactured by selective laser melting, *Mater. Charact.* 143 (2018) 127–136, <https://doi.org/10.1016/j.matchar.2017.12.003>.
- [99] J. Ma, N. Zhao, D. Zhu, Endothelial cellular responses to biodegradable metal zinc, *ACS Biomater. Sci. Eng.* 1 (2015) 1174–1182, <https://doi.org/10.1021/acsbiomaterials.5b00319>.
- [100] E.R. Shearier, P.K. Bowen, W. He, A. Drelich, J. Drelich, J. Goldman, F. Zhao, Vitro Cytotoxicity, Adhesion, and Proliferation of Human Vascular Cells Exposed to Zinc, *ACS Biomater. Sci. Eng.* 2 (2016) 634–642, <https://doi.org/10.1021/acsbiomaterials.6b00035>.
- [101] Y. Yao, P. Zhang, Y. Gao, High corrosion resistance and cytocompatibility of zinc phosphate coating on pure zinc achieved by incorporating a trace amount of MXene nanosheets for orthopedic implants, *Mater. Today Commun.* 51 (2026) 114814, <https://doi.org/10.1016/j.mtcomm.2026.114814>.
- [102] S.V. Kellesarian, M. Yunker, R. Ramakrishnaiah, H. Malmstrom, T.V. Kellesarian, V. Ros Malignaggi, F. Javed, Does incorporating zinc in titanium implant surfaces influence osseointegration? A systematic review, *J. Prosthet. Dent.* 117 (2017) 41–47, <https://doi.org/10.1016/j.prosdent.2016.06.003>.
- [103] N.Z. Gammoh, L. Rink, Zinc in infection and inflammation, *Nutrients* 9 (2017) 624, <https://doi.org/10.3390/nu9060624>.

Curriculum vitae

Personal data

Name: Mayank Kumar Yadav
Date of birth: 11/08/1992
Place of birth: India
Citizenship: Indian

Contact data

E-mail: mayankky45@gmail.com

Education

2022–2026 Tallinn University of Technology, PhD
2016–2018 Masters of Technology (Material Science and Engineering)
2010–2014 Bachelor of Technology (Mechanical Engineering)
2005–2009 High school

Language competence

English: Fluent
Hindi: Mother Tongue

Research Visits

10/01/2023 to 09/07/2023: Indian Institute of Science, Bengaluru (ERASMUS+ student mobility)
15/10/2023 to 15/04/2024: Presidency University, Bengaluru ERASMUS+ student mobility)

Elulookirjeldus

Isikuandmed

Nimi: Mayank Kumar Yadav
Sünniaeg: 11/08/1992
Sünnikoht: India
Kodakondsus: Indialane

Kontaktandmed

E-post: mayankky45@gmail.com

Hariduskäik

2022–2026 Tallinna Tehnikaülikool, PhD
2016–2018 Tehnikateaduste magister (Materjaliteadus ja tehnika)
2010–2014 Tehnikateaduste bakalaureus (Masinaehitus)
2005–2009 Keskkharidus

Keelteoskus

Inglise keel: Kõrgtase
Hindi: emakeel

Uurimiskülastused

10/01/2023 to 09/07/2023: Indian Institute of Science (ERASMUS+ Üliõpilaste mobiilsus)
15/10/2023 to 15/04/2024: Presidency University (ERASMUS+ Üliõpilaste mobiilsus)

ISSN 2585-6901 (PDF)
ISBN 978-9916-80-452-0 (PDF)